UCRL--53689-88

DE89 012801

I • R • & • D

Institutional Research and Development

Lawrence Livermore National Laboratory

UCRL-53689-88 • Distribution Categories UC-700

Acknowledgments

The Institutional Research and Development (IR&D) Program for FY88 was directed by John Holzrichter, Assistant to the Director for IR&D. Jeannie Maniz served as Research Manager for the IR&D Program. The following people formed the publication staff for the FY88 IR&D report:

Scientific Editor	Gordon L. Struble
Publication Editor	Lauren de Vore
Editors	A. Paul Adye Robert D. Kirvel Gloria M. Lawler Coralyn K. McGregor Timothy M. Peck Judyth K. Prono Sondra Reid Palmer T. Van Dyke
Designer	John M. Zych
Artists	Robert Caldwell John Danielson Lynn M. Costa Julia Z. Deal Barbara Edwards Kirk Hadley Kathryn C. House George A. Kitrinos Frank Marquez Merry Oman Phyllis Thomas
Composition	Louisa Cardoza
Cover Photograph	Don Gonzalez

We thank George F. Bing, Jane T. Staehle, and Mary Ann Esser for careful reading of the entire manuscript.

Contents

Exploratory Research

Director's Initiatives

Individual Awards

University of California Institutes

IR&D Resource Requirements

Author Index

Introduction

J. F. Holzrichter

The Laboratory's Institutional Research and Development (IR&D) Program was established in 1984 to foster exploratory work to advance science and technology, disciplinary research to develop innovative solutions to problems in various scientific fields, and long-term interdisciplinary research to support our national defense and energy missions. In FY88, the IR&D Program was funded by a 2% assessment on the Laboratory's operating budget. Our policy is to use these funds for researching innovative ideas in LLNL's areas of expertise and for developing new areas of expertise that we perceive to be in the national interest.

We support four categories of research. The first, Exploratory Research, is managed by Laboratory departments and divisions to promote pioneering work in the various scientific disciplines (biomedical and environmental sciences, chemistry and materials science, computations, earth sciences, engineering, nuclear chemistry, and physics). The second, Director's Initiatives, is devoted to a few larger projects selected by the Laboratory Director.

The third, Individual Awards, supports promising research outside the usual programmatic channels; funds are awarded on the basis of scientific excellence, potential impact, and leverage for future funding. In FY88, 151 applications for individual grants were submitted, and 26 were funded.

The fourth category, University of California (UC) Institutes, arises from the Laboratory's role in the nation's academic and research establishment and our collaboration with many UC campuses and universities nationwide. The IR&D Program has provided support to begin several joint Laboratory-University research groups that enable bring LLNL and UC scientists together to focus effort on important scientific problems of mutual interest.

The IR&D Program is managed for the Laboratory Director by a special assistant who chairs the IR&D Review Committee. The other members of the Review Committee are senior LLNL scientists, engineers, and managers with areas of expertise that span the range of scientific disciplines pursued at the Laboratory. The Individual Award proposals and projects are evaluated by the IR&D Review Committee, a group of prominent Laboratory scientists and engineers.

For FY88, the total IR&D budget was $18 million: $6 million for Exploratory Research, $6.5 million for Director's Initiatives, $3.2 million for Individual Awards, and $2 million for the UC Institutes.

The technical and scientific accomplishments of each project and of each institute funded this year are presented in this report. The projects were selected because they are expected to advance research in important areas that are too basic or too time consuming to be funded by the developmental programs or because they are somewhat risky projects that have the promise of high payoff.

We are continually reappraising the IR&D Program. In particular, we seek new candidates for the Director's Initiatives, and we constantly reassess the work in progress. Each year, we make adjustments to further the Laboratory's policy of using the IR&D Program to fund innovative ideas with high potential for enhancing programmatic activities of national importance.

I ◆ R ◆ & ◆ D

Exploratory Research

Lawrence Livermore National Laboratory

Biotechnology

M. L. Mendelsohn

IR&D funds for the Biomedical and Environmental Research Program were allocated to six innovative projects, three in exploratory research and three under the Director's Initiatives. Here, we summarize the main thrust of each of these activities.

Exploratory research was conducted to develop a plant molecular genetics capability at LLNL. We established a small facility for studying plant molecular genetics that includes rooms for plant growth, areas for plant culture, and the beginnings of a recombinant DNA laboratory. The basic techniques for handling and culturing plants, for isolating DNA, and for creating genetic variants are now operational.

We are also doing innovative work with the scanning tunneling microscope to image biological molecules, particularly DNA. We have already obtained dramatic, previously unattainable, high-resolution images showing the three-dimensional atomic structure of double-stranded DNA. This new ability to obtain atomic-level images of biological structures promises to greatly advance the field of molecular research.

In our third exploratory research project, we are applying the technique of post-labeling with phosphorus-32 for the detection of DNA adducts (building blocks of DNA that have been modified by the binding of electrophilic chemical species). This method results in distinctive spot patterns or fingerprints for the compounds of interest that are of great value in studying the genotoxicity of exotic chemicals. We are applying the post-labeling assay to the potent, mutagenic, heterocyclic amines found in cooked foods, such as fried ground beef, that are typical of the Western human diet.

For the Director's Initiatives, we are studying the biological and ecological effects of nuclear war. Specifically, we are using experimental data and model simulations to examine the combined effects of low temperature and low levels of light, which have been projected to follow a nuclear exchange, at the plant, community, and regional levels. For some of the plants studied, computer simulations correctly predict the experimentally observed effects. For others, predictions have failed because the plants have discontinuous or switch-like mechanisms that were not previously known. Research at the regional level of resolution for both agricultural and natural ecosystems comprises a new field in ecology and should yield large returns.

For our research on monoclonal antibodies, we are pursuing two approaches to develop new immunochemical sensors for environmental monitoring. The first makes use of the surface acoustic (or Lamb) wave to detect oscillatory changes in thin films secondary to the binding of antibody molecules; we are testing such devices that have been designed onto silicon chips. The second approach exploits the evanescent wave to quantify antibody fluorescence in the zone immediately adjacent to the surface of an optical fiber; our goal in this project is to fabricate real-time, portable assay systems for detecting environmental pollutants.

In our last IR&D project, we have used recombinant DNA techniques to transfer the gene responsible for the first enzymatic step in the assimilation of sulfur from one bacterium, *Thiobacillus ferrooxidans*, into another, *Escherichia coli*. This gene has now been made to function in the new setting, and we are developing a plasmid for gene transfer back into *T. ferrooxidans*. We have used a similar technique for the gene that converts toxic selenate into nontoxic selenium. This gene has been transferred from *Clostridium pasteurianum* into *E. coli* and has been characterized and made to function in the new setting.

In FY88, the Biomedical and Environmental Research Program received a total of $810,000, $100,000 for exploratory research and $710,000 for Director's Initiatives projects.

Plant Molecular Genetics Capability at LLNL

We are applying recent advances in plant molecular genetics and biotechnology to minimize the impact of energy-related stressors on plants. One application is the development of plants that are resistant to or tolerant of specific air pollutants.

Principal Investigators: Y. Y. Marchant and J. H. Shinn

We have created a small facility for studying plant molecular genetics in the Environmental Sciences Division. Our facility includes rooms for plant growth and laboratories for tissue culture and recombinant DNA research. In initial work, we used *Arabidopsis thaliana*, a small annual weed, as a model test organism. This year, we established basic techniques for handling this plant in culture and for isolating and separating DNA, and we began work on creating phenotypic and genotypic variants. Our long-term objective is to genetically engineer enhanced tolerance to environmental stressors, such as ozone, in economically important plants.

In general, mutants have been used by researchers as experimental tools to probe the relation between protein structure and function, to determine the order of events during differentiation and morphogenesis, and to define the roles of specific proteins and protein assemblies in the cell. In particular, mutants from algae and higher plants have been important in recent studies of biochemical, biophysical, and structural aspects of photosynthetic phenomena. The *in vivo* efficacy of an appropriate mutation can be determined by *in vitro* assays of the gene product, making possible the comparison of two organisms that differ by only one protein. Once the role of the mutation has been characterized, the properties of a mutant can then be reproduced consistently.

The first step of our project involving *A. thaliana* was to screen mutagen-exposed seed populations and identify mutant individuals that can withstand constant exposure to high levels of ozone by some biochemical mechanism (such as an increase in the relative isozyme proportions of superoxide dismutase). We then screened presumptive mutants for several generations to ensure homozygosity of the mutation and thereby eliminate spurious genetic diversity. We have adopted a procedure for growing *A. thaliana* based on standardized techniques, and we have tested and modified various methods for handling this plant as genetic material.

We successfully transformed sterile plants of *A. thaliana* by *Agrobacterium rhizogenes* and obtained hairy root cultures (Marchant, 1988; Flores *et al.*, 1988). *A. rhizogenes* is a bacterium closely related to the causative agent of crown gall disease. Virulence is conferred by large plasmids, which have been extensively investigated as vectors for use in plant genetic engineering because of their natural ability to insert DNA into whole plants. Genetically transformed hairy roots readily regenerate into whole plants that transmit the DNA to their progeny. We are attempting to regenerate whole plants from transformed *A. thaliana*.

Finally, we isolated *A. thaliana* DNA according to published procedures and repeated the procedures for characterizing its relatively small haploid genome, which consists of approximately 7×10^7 base pairs.

References

Flores, H. E., J. J. Pickard, and M. Hoy (1988), "Production of Polyacetylenes and Thiopenes in Heterotrophic and Photosynthetic Root Cultures in Asteraceae," *Intl. Conf. on the Chemistry and Biology of Naturally Occurring Acetylenes and Related Compounds* (Elsevier Publishing Co., NY).

Marchant, Y. Y. (1988), "*Agrobacterium rhizogenes*-Transformed Root Cultures for the Study of Polyacetylene Metabolism and Biosynthesis," *Intl. Conf. on the Chemistry and Biology of Naturally Occurring Acetylenes and Related Compounds* (Elsevier Publishing Co., NY).

Scanning Tunneling Microscopy of Biological Samples

We are developing the instrumentation and methodologies needed to apply scanning tunneling microscopy to the analysis of biological materials at the atomic level of resolution.

Principal Investigator: R. Balhorn
Co-Investigator: W. Siekhaus

The recent development of the scanning tunneling microscope (STM) and the demonstration of its capabilities for imaging molecular structures with atomic resolution provide tremendous promise for future studies in molecular biology. Investigators who have used this microscope have finally succeeded in visualizing individual metallic atoms and organic molecules. The process is accomplished by locating the atomically sharp tip of the STM probe a few tenths of a nanometer above a sample, scanning the area containing atoms or molecules, and measuring the current produced as electrons tunnel across the gap between the tip and the outer electronic surface of a sample's atoms.

When we began our project, the only biological samples that had been examined with the STM were virus particles and isolated, double-stranded DNA. Neither study, however, provided images even approaching the atomic level of resolution. The primary goal of our study was to prepare biological samples relevant to ongoing studies in the Biomedical Sciences Division and to devise methods for imaging the atomic structure of these samples using the STM constructed by researchers in LLNL's Chemistry and Materials Science Department. We also sought to identify and solve special problems that might be encountered in imaging samples on conventional graphite surfaces.

We prepared samples for analysis that varied in both size and complexity, including a single-stranded fragment of DNA, a folded protamine molecule containing 50 amino acids, high-molecular-weight double-stranded DNA, and a sperm chromatin particle several micrometers long and two micrometers wide. The bulk of our effort, however, was directed toward imaging the atomic structure of double-stranded DNA. We realized that once the capability for imaging the nucleotide subunits of DNA was attained, an entirely new "electronic" approach for sequencing DNA could be developed, automated, and applied to the analysis of very long DNA fragments.

We used a simple approach for drying DNA on the surface of graphite to prepare double-stranded DNA for scanning tunneling microscopy. We have now successfully scanned these samples using a tapered, atomically sharp probe. Although we have only begun to learn what factors control optimal sample and tip preparation, our current methods have produced images of DNA at near-atomic resolution (see Figure 1) that are the best in the world. In future efforts, we expect to provide enhanced images at the atomic level of resolution that can be used to identify individual base pairs.

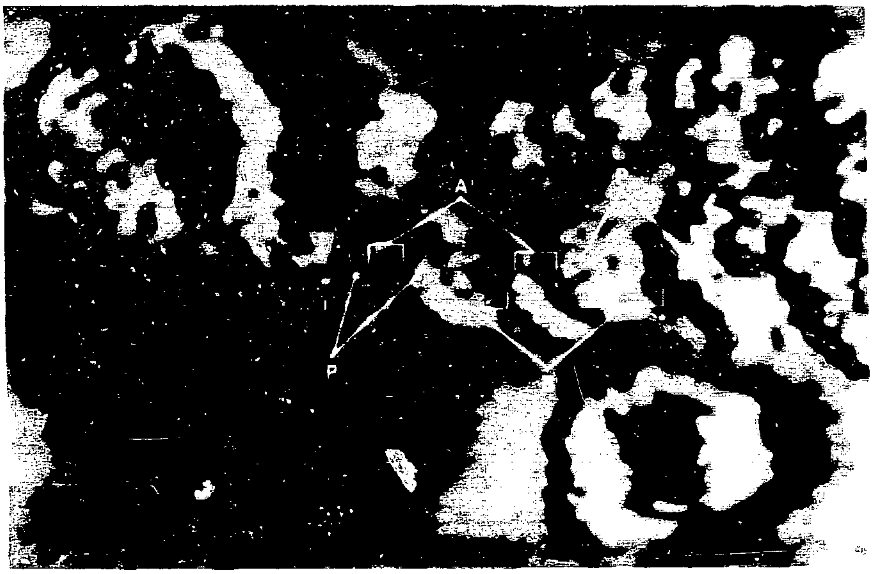

Figure 1. DNA image of calf thymus obtained using scanning tunneling microscopy. This image clearly resolves the two individual phosphodiester strands (P) of DNA as well as the major (A) and minor (B) grooves produced by the helical coiling of the two strands.

Post-Labeled DNA Adducts

Principal Investigators: K. W. Turteltaub and J. S. Felton

We are attempting to assess the extent of DNA damage caused through exposure to a group of heterocyclic amines found in cooked foods typical of the Western diet.

Our objective is to adapt the phosphorous-32 (^{32}P) post-labeling assay so that we can resolve DNA adducts formed through exposure to heterocyclic amines in the diet. The term DNA adduct refers to nucleosides, the building blocks of DNA, which have been modified by the binding of electrophilic chemical species. DNA adducts can lead to mutations that are associated with cell death and cancer. More specifically, we are interested in studying DNA adducts of the amino imidazoazaarene (AIA) family of cooked meat mutagens.

Figure 1. DNA from *Salmonella* bacteria modified by the IQ mutagen. This DNA was digested to nucleotides, labeled with ^{32}P, and resolved using four-dimensional thin-layer chromatography. Under such conditions, only DNA adducts remain. The visible, overlapping spots correspond to the adducts. The intensity of such spots can be quantified and then used to study the relations among adducts, exposure, and disease.

The ^{32}P post-labeling assay for DNA adducts is a new technique that exploits the ability of specific enzymes to digest DNA and to label the resultant nucleoside monophosphates with ^{32}P after exposure to genotoxic chemicals (Gupta *et al.*, 1982). Labeled DNA adducts are then isolated using multidimensional thin-layer chromatography. The end result is the detection of specific adducts as spots on x-ray film by means of autoradiography. The advantages offered by this technique are high sensitivity and the ability to analyze DNA that has been exposed to non-radioactively labeled and unknown chemicals. Such advantages make the technique especially useful for studying the effects of interactions among chemicals present in complex environmental mixtures on DNA and for monitoring human exposure to these mixtures. Because the diet is a complex mixture, this technique is ideally suited to studying the effects of diet on human genetic material and the relationship between diet and cancer.

Our initial studies involved comparison of DNA adducts of the two AIA mutagens often referred to by their short names, MeIQx and PhIP. These compounds can be isolated from fried ground beef. The MeIQx and PhIP DNA adducts can be formed *in vitro* from synthetically derived azido forms of the mutagens. Different spot patterns result for each compound. We have found four distinct adduct spots for MeIQx and three spots for PhIP, each having different fingerprints or spot profiles. We have also looked at DNA adducts formed in *Salmonella typhimurium* exposed to the IQ mutagen (see Figure 1). We found several distinct adduct spots with a pattern distinct from the *in vitro*-formed azido-MeIQx and azido-PhIP adduct standards.

We are trying to determine whether the mechanisms of DNA modification in mammals, bacteria, and purified DNA are related by comparing spot patterns from mice, *Salmonella* bacteria, and DNA modified *in vitro*. The differing spot patterns may indicate different types of genetic damage and may help to explain the varying potency of the compounds under investigation.

Our future plans are to compare the results obtained in our current studies to those for humans, with the hope of identifying appropriate models to study the effects of these and other mutagens on human DNA. In addition, the methodology should be extremely useful for other studies in the Laboratory's biomedical and environmental research program. For example, one area of current application is a study of the effects of pollutants, particularly polycyclic aromatic hydrocarbons, on fish from San Francisco Bay.

Reference

Gupta, R. C., M. V. Reddy, and K. Randerath (1982), *Carcinogenesis* 3(9), 1081-1092.

Chemistry and Materials Science

T. T. Sugihara

The Chemistry and Materials Science Department conducts exploratory research to support various Laboratory programs. In FY88, we began challenging new experimental projects in high-temperature superconductors and in interface science, together with an associated theoretical effort. In addition, studies in synchrotron-related materials science and photoactivated hydrogenation reactions were continued from FY87.

IR&D-supported research in superconductivity was begun in late FY87. This work concentrated on the synthesis and initial characterization of the Y-Ba-Cu-O superconducting compounds. In FY88, the focus shifted to the use of positrons to investigate electronic structure in the vicinity of localized positrons in perovskites, whose chemical structure is similar to that of the new superconductors. Our first experiments investigated positron lifetime as a function of temperature and the angular correlation of annihilation radiation. Results show that changes in electron density accompany the normal-to-superconducting transition in the high-temperature superconductors.

To improve our understanding of adhesion and bonding of materials, we are investigating the properties of interfaces. In FY88, we initiated a new project to study the diffusion of oxygen anions in the lattice and along grain boundaries in sintered polycrystals of metal oxides. In contrast to initial expectations, anions were found to diffuse significantly more rapidly than cations.

A first-principles theoretical study, directly related to both superconductors and interfacial phenomena, was initiated to describe the electronic structure of systems with reduced symmetry, such as surfaces and interfaces. This year, we developed a formalism that exploits the properties of systems with semi-infinite periodicity.

In synchrotron-related science, the capabilities developed in FY87 for high-resolution x-ray absorption studies (extended x-ray absorption fine structure or EXAFS, and x-ray absorption near-edge structure or XANES) were used to investigate superconductor properties and to probe interfaces of near-monolayer thickness. In another synchrotron-related project, multilayer diffraction gratings were found to be well suited for use as high-resolution monochromators in the experimentally difficult energy region of a few hundred to a few thousand eV (electron volts).

Also in FY88, a proof-of-principle experiment was conducted to demonstrate that carbon monoxide (plus hydrogen gas) can be catalytically converted to hydrocarbon at room temperature by photoactivation. This new process involves the use of an aerogel doped with uranyl ion.

The Chemistry and Materials Science Department received $1,003,000 in IR&D funds in FY88.

Positron Studies of High-Temperature Superconductors

We studied the temperature dependence of the positron lifetime and the spatially averaged electron-momentum distribution in one-, two-, and three-layered perovskite superconductors. These experiments revealed that, at the onset of superconductivity, the electronic structure of each material undergoes similar changes attributable to a common characteristic of the superconducting mechanism in this class of materials.

Principal Investigators: M. J. Fluss and Y. C. Jean
Co-Investigators: P. E. Turchi, R. H. Howell, C. W. Chu, and A. L. Wachs

There is no universally accepted mechanism to explain the observation of superconducting materials with critical temperatures greater than 30 K, the upper limit that can be attributed to conventional electron-phonon interaction. The positron is particularly useful for probing the changes in electronic structure that may be associated with the superconducting mechanism.

Positrons are easily implanted into samples by the use of radioisotopic sources. We studied the annihilation properties of positrons from a sodium-22 acetate source sandwiched between various samples of high-critical-temperature (T_c), superconducting perovskite materials. Positrons from sodium-22 are rapidly thermalized (~2 ps) in the solid sample, where they either propagate as delocalized particles (analogous to electrons in their ground state) or become trapped in regions where there is a potential minimum (such as oxygen vacancies or vacancy clusters). Our objective was to determine how the positron might be sensitive to changes accompanying the onset of superconductivity in the perovskite materials.

Our work consisted of two types of experiments: determining the positron lifetime, and measuring the electron-momentum distribution for those electrons sampled by the positron-electron annihilation process. The experiments were carried out as a function of temperature for three materials: $(La_{1-x}Sr_x)_2CuO_4$, $YBa_2Cu_3O_7$, and $Tl_2Ca_2Ba_2Cu_3O_{12}$. They are representative of one-, two-, and three-layer perovskite materials, respectively. The two types of experiments provided different but complementary information.

To measure the positron lifetime, we used the 1.28-MeV gamma ray from the excited state of neon-22 (the positron-decay product of sodium-22) to start an ultrafast clock, which was then stopped by the detection of the annihilation event (the 511-keV gamma ray). To measure the spatially averaged momentum distribution of the annihilating positron-electron pairs, we used a solid-state intrinsic germanium detector in Doppler-broadening experiments.

In the lifetime measurements, the different states of the positron can be resolved because they appear as terms in the data, which are represented as a sum of exponentials analogous to parent-daughter decay schemes. In the momentum measurements, however, different states of the positron appear as a sum of linear terms, yielding an overall average momentum distribution.

Figure 1 shows the temperature variation of the deduced positron Bloch-state lifetime for the three high-T_c materials studied. The intensity of the short-lived component from which these data are derived was found to vary only a few percent over the entire temperature range. The positron lifetime exhibits a strong temperature dependence for $T < T_c$ but not for $T > T_c$. This temperature dependence appears to increase systematically from the one-layer to the three-layer material. Also noteworthy is the similarity of the temperature dependence of the positron lifetime to that of the superconducting gap. The relatively large lifetime change observed for the three-layer $Tl_2Ca_2Ba_2Cu_3O_{12}$ material appears to indicate that there is a significant change in the charge distribution associated with the onset of superconductivity. Since almost all theories make predictions about the nature and location of the charge carriers (usually holes) in these materials, we hope that the predictions of such theories will translate into specific, testable models regarding corresponding changes in the positron wavefunction itself.

Our measurement of the electron-momentum distribution obtained from Doppler-broadening experiments provided complementary evidence for the observed coupling of the positron to the superconducting phase transformation (see Figure 2). The temperature dependence of the electron-momentum distribution, measured by a peak-counting rate parameter of the 511-keV gamma-ray line (the S parameter), is almost identical in the $(La_{1-x}Sr_x)_2CuO_4$ and $Tl_2Ca_2Ba_2Cu_3O_{10}$ materials. Most notable is the behavior in the vicinity of T_c, where the results indicate an increase in the high-momentum electrons, coincident with the initial increase in the positron lifetime.

Our results support earlier suggestions of a positron-superconductivity interaction mechanism common to the

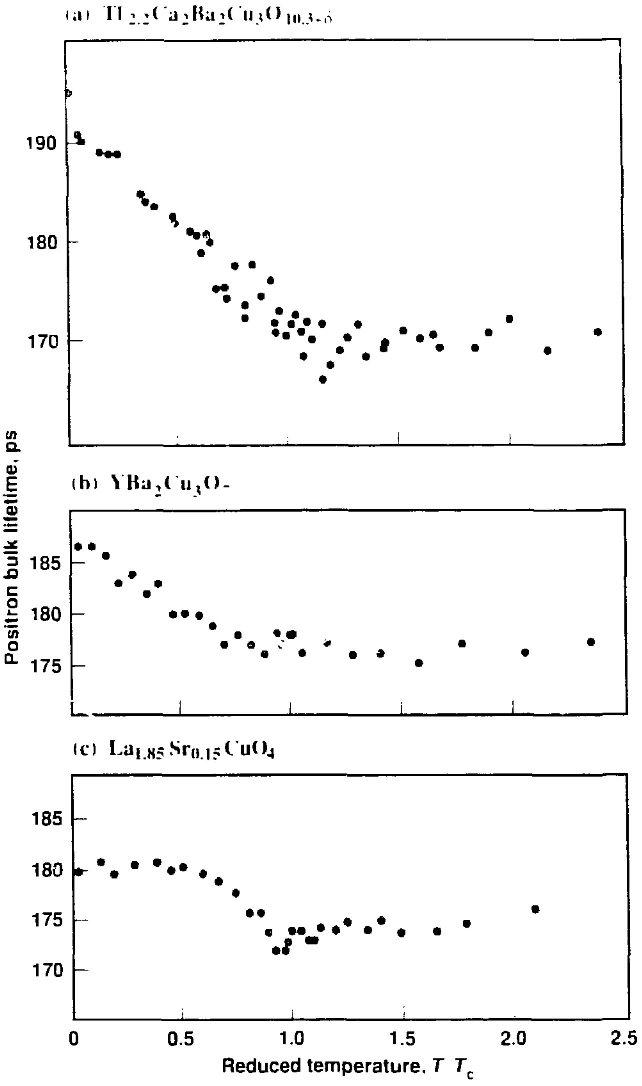

Figure 1. A comparison of the positron Bloch-state lifetimes for three classes of perovskite superconductors.

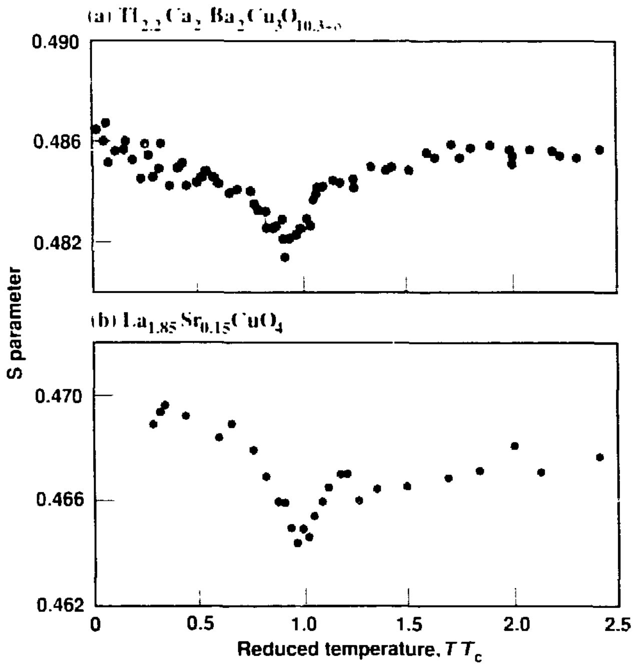

Figure 2. Doppler-broadening S parameter as a function of temperature in $Tl_{2.2}Ca_2Ba_2Cu_3O_{10.3+\delta}$ and $La_{1.85}Sr_{0.15}CuO_4$.

perovskite materials. Consideration of both the lifetime and Doppler data suggests an anticorrelation of positrons with electrons as well as a possible coincident redistribution of electronic structure as T decreases below T_c. Any present or future theory of superconductivity will probably have to account for these data, and, in this sense, our experiments should help to guide the development of a theoretical understanding of superconductivity at high temperatures.

References

Harshman, D. R., L. F. Schneemeyer, J. V. Waszczak, Y. C. Jean, M. J. Fluss, R. H. Howell, and A. L. Wachs (1988), "Temperature Dependence of the Positron Annihilation Lifetime in Single-Crystal $YBa_2Cu_3O_7$," *Phys. Rev. B* **38**, 848.

Jean, Y. C., J. Kyle, H. Nakanishi, P. E. A. Turchi, R. H. Howell, A. L. Wachs, M. J. Fluss, R. L. Meng, H. P. Hor, J. Z. Huang, and C. W. Chu (1988), "Evidence for a Common High-Temperature Superconducting Effect in $La_{2-x}Sr_xCuO_4$ and $YBa_2Cu_3O_7$," *Phys. Rev. Lett.* **60**, 1069.

Jean, Y. C., H. Nakanishi, M. J. Fluss, A. L. Wachs, P. E. A. Turchi, R. H. Howell, Z. Z. Wang, R. L. Meng, P. H. Hor, J. Z. Huang, and C. W. Chu (1988), *A Comparison of the Temperature Dependence of Electron Positron Momentum Density Characteristics in Tl(2223), Y(123), and La(214) Superconductors*, Lawrence Livermore National Laboratory, Preprint UCRL 99081; accepted for publication in J. Phys. Chem.

Jean, Y. C., S. J. Wang, H. Nakanishi, W. N. Hardy, M. E. Hayden, R. F. Kiefl, R. L. Meng, H. P. Hor, J. Z. Huang, and C. W. Chu (1987), "Positron Annihilation in the High-Temperature Superconductor $YBa_2Cu_3O_{7-x}$," *Phys. Rev. B* **36**, 3994.

Reactive-Element Effect Studied Using Ion Implantation

Principal Investigator: W. E. King
Co-Investigator: K. S. Grabowski

Naval Research Laboratory,
Washington, DC

We have investigated the effect of yttrium-ion implantation on the high-temperature oxidation of Fe–24Cr using Rutherford backscattering spectroscopy, secondary-ion mass spectroscopy, and electron microscopy. We have applied analytical tools to determine the spatial distribution of yttrium, the microstructure of the oxide, and the contribution of oxygen transport to the oxidation process.

Ion implantation is an important technique for treating metal surfaces subjected to high-temperature oxidizing environments. Ion implantation of reactive elements, such as yttrium, cerium, thorium, and hafnium, can give rise to a larger reduction in oxide growth rate than that observed in materials alloyed with reactive elements. This technique is also ideal for investigating mechanisms that result in the reactive-element effect.

We have investigated the effect of reactive-element ion implantation on high-temperature oxidation of high-purity metal alloys that form Cr_2O_3 layers. Previous reports suggest that such implantation yields three beneficial effects: stimulation of the early formation of a continuous, single-phase protective oxide layer, reduction in the growth rate of chromia, and enhanced oxide adhesion compared to addition-free materials.

We used Rutherford backscattering spectroscopy, electron microscopy, and secondary-ion mass spectroscopy (SIMS) to investigate the oxidation kinetics and elemental distributions that evolve during oxidation of Fe–24 wt% Cr implanted with yttrium ion doses of $1 \times 10^{[illegible]}$, $3 \times 10^{[illegible]}$, and $1 \times 10^{[illegible]}$ ions/cm[illegible]. We investigated microstructural and microchemical evidence of the location and chemical state of the reactive element both in the oxide and in the metal. We then compared the effects of ion implantation of reactive elements with the effects of alloying and studied the impact of ion implantation on the elucidation of reactive-element mechanisms.

Three regions of a sample were implanted with 150-keV yttrium ions at the Naval Research Laboratory, each with one of the three ion doses. Rutherford backscattering spectroscopy was carried out at the tandem accelerator facility at Argonne National Laboratory using 1.770-MeV, singly charged ^3He ions before oxidation and after incremental oxidation times of 5, 10, and 45 min at 1000°C in flowing oxygen.

Our results indicate that ion implantation affects oxidation behavior in two ways. When the near-surface concentration of implanted reactive element in the alloy is below a critical level, most of the implanted element will be found near the oxide/metal interface following oxidation. Above this critical level, most of the implanted element will be found near the oxide/gas interface. The critical concentration is probably related to formation of a second phase in the scale, which may be related to formation of a second phase in the alloy either during implantation or on heating the sample for oxidation.

The near-surface concentration of implanted atoms is a function of both ion dose and ion energy. From the literature, we established the ion dose required to produce the critical level of yttrium for several ion-implantation energies. This relation is plotted in Figure 1. Evaluation of yttrium composition profiles calculated for each of the experimental cases indicates that the critical concentration could be a yttrium concentration at the surface of about 1 at.% or a peak yttrium concentration of about 6 at.%. Curves for both of these criteria calculated for yttrium implantation of Fe–24Cr are shown in Figure 1. Beyond these concentrations, either precipitation at the surface could begin, or nearly 50 vol% of the intermetallic yttride could form beneath the surface. Formation of these precipitates in the alloy depends on the thermal history of the implanted samples and the opportunity for internal oxidation of yttrium. We propose that, for doses above the critical dose, the effect that is observed is not the reactive-element effect by its most strict definition. At these high doses, we believe that second-phase formation in the oxide is likely, an occurence that is not observed in alloy systems

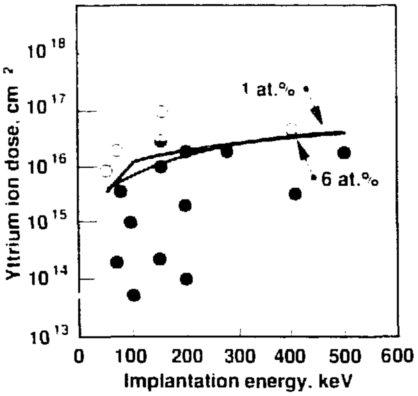

Figure 1. Yttrium ion dose as a function of implantation energy. Solid points indicate that the implant was found at the oxide/metal interface; open points indicate the implant was found near the oxide/gas interface. The black curve shows the ion dose needed to produce a peak yttrium concentration of 6 at.%; the colored curve shows the dose required to produce a surface yttrium concentration of 1 at.%

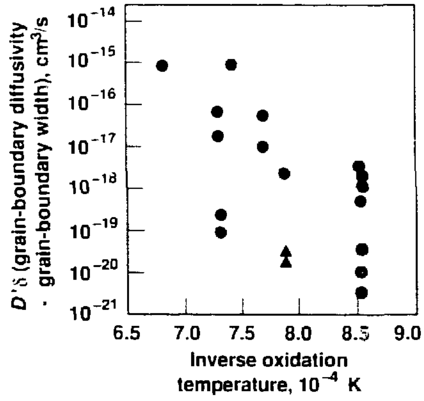

Figure 2. $D'\delta$ values deduced from previous experiments (black data points) and from our work (colored data points) plotted as a function of inverse oxidation temperature. The text gives a detailed discussion of this figure.

and that is not required for the reactive-element effect to be operative.

To compare our results for oxide growth kinetics and literature data on the growth of Cr_2O_3 with cation and anion diffusion measurements, we converted the experimental values of k_p, the parabolic rate constant, to values of $D'\delta$, the product of grain boundary diffusivity and grain boundary width, using the procedure described by Park *et al.* (1987). Those researchers assumed that the contribution of anion diffusion to the growth of Cr_2O_3 films was negligible. In a recent study by King and Park (1988), anion diffusivities in the lattice and along grain boundaries were measured on sintered polycrystals of Cr_2O_3 and Cr_2O_3 doped with 0.09 wt% Y_2O_3 at 1100°C and at the oxygen partial pressure corresponding to that of the Cr/Cr_2O_3 equilibrium at that temperature. Results demonstrated that under the same conditions, anion diffusion is significantly faster than cation diffusion.

Figure 2 shows $D'\delta$ versus inverse temperature from the available literature, including the $D'\delta$ values from cation (Park *et al.*, 1987) and anion (King and Park, 1988) tracer diffusion studies. The values for $D'\delta$ deduced from k_p measurements are spread over two orders of magnitude. All values for $D'\delta$, except those deduced from the current implantation experiment and the experiments of Pivan *et al.* (1980), are higher than the values measured for cation grain boundary transport in Cr_2O_3 and Cr_2O_3 doped with Y_2O_3 at 1100°C. This indicates that cation grain boundary diffusion is far too slow to explain observed oxide growth rates in unimplanted samples. These data are consistent with the anion grain boundary diffusion data of King and Park (1988). The oxidation rates of the implanted samples in this study and in that of Pivan *et al.* (1980) are consistent with rate control by cation diffusion.

There appears to be a critical implantation dose above which a change in the oxidation behavior of the alloy is observed. Below the critical dose, the implant is located near the oxide/metal interface. In this regime, the reactive-element effect due to implantation with energetic ions seems to be similar to effects observed due to alloying with reactive elements. However, in alloys, the reactive element is not found in such high concentrations in the oxide layers (except over yttrides) as in implanted samples, and implantation gives rise to a larger reduction in growth rate compared to alloying. Ion implantation produces a uniform distribution of reactive element whereas alloying often results in second-phase formation in the base metal. Uniform distribution of a reactive element does not appear to be necessary for the alloy to exhibit the reactive-element effect. Above the critical dose, the implant is located near the gas/oxide interface. Chromia on unimplanted alloys grows at rates consistent with anion grain boundary diffusion. Chromia on implanted alloys grows at rates consistent with cation grain boundary diffusion. SIMS data suggest that yttrium reduces the inward transport of oxygen through a chromia scale, and at high enough concentrations, it can trap a significant portion of the inwardly migrating oxygen.

References

Park, J. H., W. E. King, and S. J. Rothman (1987), *J. Amer. Ceram. Soc.*, **70**, 880.

Pivan, J. C., C. Roques-Carmes, J. Chaumont, and H. Bernas (1980), *Corros. Sci.* **20**, 947–962.

King, W. E., and J. H. Park (1988), "Anion Grain Boundary Diffusion in Cr_2O_3 and Cr_2O_3 Doped with Y_2O_3," presented at *Mat. Res. Soc.*, Reno, NV.

New Method for Calculating the Electronic Structure of Solids

We are developing a computer code to determine the electronic structure of materials with full or low symmetry (e.g., surfaces and interfaces). This information will help us understand the role played by the electronic structure in such complex phenomena as corrosion, ductility, adhesion, and bonding.

Principal Investigator: A. Gonis

The calculation of the electronic structure of matter for the study of material properties has been developed almost exclusively on the basis of Bloch's theorem, which assumes the existence of full translational invariance. However, use of this method for materials with broken or low symmetry (e.g., impurities, surfaces, grain boundaries) requires either the imposition of approximate and ill-defined boundary conditions on the corresponding Schrödinger equation (supercells, slabs) or extreme computational complexity.

We are develoing an alternative approach based on the concept of semi-infinite periodicity (Zhang and Gonis, 1988) instead of translational invariance. Our new method replaces expansions in reciprocal space and the associated integrations with a self-consistent equation to determine electronic structure. Semi-infinite periodicity is defined as the periodic repetition of a basic unit or set of units along a given direction starting at a given point. Examples of systems with semi-infinite periodicity include a linear, semi-infinite periodic arrangement of atoms (where the basic repeating unit is an atom), or one of the two parts formed upon severing of a periodic material along a cleavage plane (where the repeating unit is either an atomic monolayer or a set of such layers). A broad range of systems, from periodic bulk materials to twist-and-tilt grain boundaries, can be viewed as having parts characterized by semi-infinite periodicity; in fact, this view encompasses all structures except those characterized by structural disorder (i.e., amorphous materials) or quasi-periodicity.

Our new approach, called real-space, multiple scattering theory (RS-MST) (Zhang and Gonis, 1988), is based on a reformulation of ordinary scattering theory developed originally by Gonis (1986). It is rigorously applicable to all systems consisting of parts with semi-infinite periodicity, including, for example, surfaces, grain boundaries, and pure translationally invariant materials. It is not confined to cells of spherical symmetry but can treat potential cells of arbitrary shape (Gonis and Zhang, 1988). The RS-MST is straightforward to program and prescribes a well-defined process for achieving and testing convergence. However, it is also computationally intensive, requiring the storage capabilities of Cray-type supercomputers.

This year, we developed the computer code to the point that we can reproduce, for a given potential, the electronic structures of pure bulk materials obtained by conventional theories. With this code, we were also able to determine, for the first time ever, the electronic structures of certain surface and interface systems. Typical results of RS-MST calculations are shown in Figure 1. The solid black curves show the electronic density of states (DOSs) for bulk elemental copper as calculated with a commonly used Bloch's-theorem method (Moruzzi *et al.*, 1978), and the shaded regions represent the DOSs obtained using RS-MST (a) for bulk copper and (b) at a (100)/(111) planar copper interface. The RS-MST calculation in (a) closely reproduces the reciprocal-space calculations; differences are attributed to a lack of convergence. The interface DOS (b) shows a nearly complete loss of structure and has a somewhat narrower bandwidth than the DOS for the bulk material (a). The first effect is due to an expected loss of translational invariance, and the second effect reflects the decreased coordination at the site at which the DOS was calculated.

Athough the RS-MST needs to be improved and refined, it does provide an answer to a long-standing problem in electronic-structure calculations, namely how to determine boundary conditions on a cluster of sites to represent properly the infinite medium surrounding the

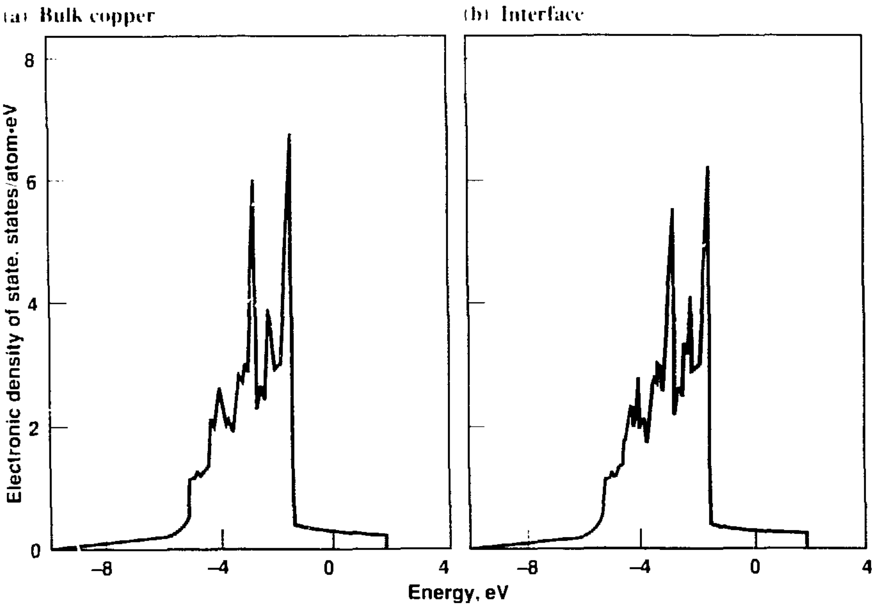

Figure 1. Local electronic density of states (DOSs) of bulk elemental copper calculated with a commonly used Bloch's-theorem method (solid black curves) and with our RS-MST method (shaded areas) for bulk copper (a) and at a (100)/(111) planar copper interface (b).

cluster. Our goal for next year is to extend the code to allow the self-consistent determination of charges, potentials, and total energies. We are also working to reduce the storage and computing times required.

References

Gonis, A. (1986), "Multiple Scattering Treatment of Surfaces and Interfaces," *Phys. Rev. B* **34**, 8313.

Gonis, A., and X.-G. Zhang (1988), "Electronic-Structure Method for General Space-Filling Cell Potentials," *Phys. Rev. B* **38**, 3564.

Moruzzi, V. L., J. F. Frank, and A. R. Williams (1978), *Calculated Electronic Properties of Metals* (Pergamon Press, NY).

Zhang, X.-G., and A. Gonis (1988), *A New, Real Space Multiple Scattering Theory Method for the Determination of Electronic Structure*, Lawrence Livermore National Laboratory, Preprint, UCRL-99819; submitted to *Phys. Rev. B*.

Site-Specific Chemistry Using Synchrotron Radiation

Principal Investigator: J. Wong

We have performed x-ray absorption experiments to study the site-specific chemistry of selected constituent elements in optical materials, laser crystals, high-temperature superconductors, and an ultrathin film on a multilayer structure.

Our studies combine the use of synchrotron radiation as a light source and x-ray absorption spectroscopy as a structural probe. We performed a variety of x-ray absorption experiments on Beamline 10-2 at the Stanford Synchrotron Radiation Laboratory soon after it became operational in November 1987. We will resume running experiments at the Brookhaven National Synchrotron Light Source when that facility returns to normal operation after a phase-II construction upgrade.

Our experiments included:

- Studies of rare-earth substitutions in superconducting $YBa_2Cu_3O_7$ materials.
- Site-selective detection using the technique of optical extended x-ray absorption fine structure (EXAFS).
- Interface structure of a monolayer of Hf on a multilayer structure.
- Investigations of Cr^{3+} ions in fluoride laser crystals.
- Measurement of the wiggler-beam profile with a charge-coupled device imager. Our two-dimensional images, such as that shown in Figure 1, are the first recorded of any synchrotron beam.

Due to space constraints, we highlight only a few of our findings.

Substitution of trivalent rare-earth elements for Y in $YBa_2Cu_3O_7$ has little effect on superconductivity; whereas Pr and Tb, which have an accessible tetravalent state, either lower the critical temperature (T_c) or destroy superconductivity. The question is whether the effect is due to valence. In an attempt to determine valence, we measured *L*-edge spectra for the following compounds:

- $Pr_xY_{1-x}Ba_2Cu_3O_7$ where $x = 0.2$, 0.4, and 0.6.
- $Gd_xY_{1-x}Ba_2Cu_3O_7$ where $x = 0.5$ and 1.0.
- $HoBa_2Cu_3O_7$.

The Gd and Ho compounds were 90-K superconductors, whereas the T_c of the Pr compounds was ~80 K, ~40 K, and nonsuperconducting for $x = 0.2$, 0.4, and 0.6, respectively.

Our results show that in Pr superconductors, the valence is 3+; however, there is evidence of some splitting in the final state. In contrast, there is no such splitting on

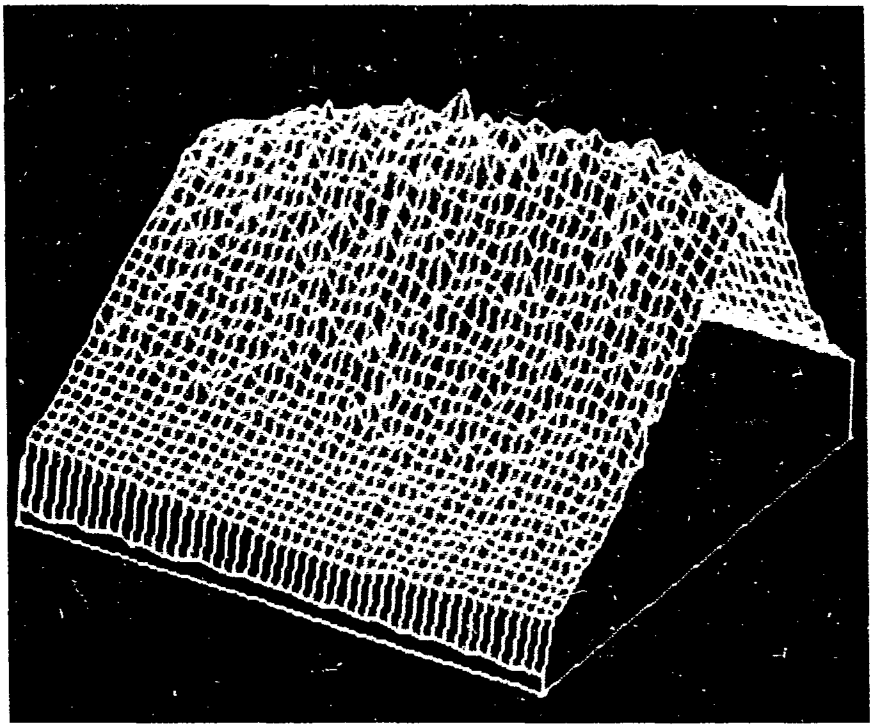

Figure 1. Surface plot of the intensity profile from Beamline 10-2 of the Stanford Synchrotron Radiation Laboratory, operating at a wiggler field strength of 14 kG with focusing. The image span is approximately 1 mm to either side of the horizontal center. This image is the first recorded of any synchrotron beam.

the high-energy side of the white line for the Gd or Ho data. Both L spectra of the Gd- and Ho-substituted superconducting materials were identical to well-known trivalent model compounds of Gd and Ho.

In an exploratory effort, we examined the sensitivity of EXAFS to structures at near-monolayer thickness. We measured the L_3 spectrum of a 0.5-nm-thick Hf film deposited on a Pt/C multilayer with a period of 3.17 nm. Figure 2a shows the experimental spectrum, which is a composite of eight scans of the Hf L_3-edge EXAFS. These data were taken at a grazing angle of 0.5°, resulting in an effective Hf layer thickness of ~57 nm. Figure 2b shows the normalized EXAFS signal, defined as $\chi(k)$. Figure 2c shows the Fourier transform of $\chi(k)$ to yield a radial structure function $\phi(R)$ that reveals a series of radial peaks at various distances R from the central atom. Figure 2d shows the inverse transform in the region around the central-absorbing Hf atom, where $\chi^F(k)$ refers to the filtered data.

Our results indicate that the nearest neighbors of the Hf atoms are low-Z species. The atomic species is probably carbon because the Hf layer was overcoated with 1.0 nm of amorphous carbon to stabilize the metal against oxidation. The position of the radial peak at $R = 0.17$ nm indicates that there is no Hf-Hf correlation (in the pure metal, the Hf-Hf distance is 0.32 nm). Our main conclusion is that high-quality EXAFS spectra may be obtained at monolayer coverages on moderately large-area samples. The intensity available at Beamline 10-2 allows us to project measurements to a fraction of a monolayer.

In the coming year, we will use synchrotron radiation to investigate the bonding and local atomic structure of several advanced materials. Our studies will include valence and site occupancy of 3d metal ions in high-T_c superconductors, Cr^{3+} and Nd^{3+} ions in laser crystals and glasses, sol-gel intermediates and products, fossil fuels and catalysts, optical detection for valence selectivity, and excited-state structures. We also plan to use time-resolved x-ray diffraction and/or energy-dispersive EXAFS to investigate chemical dynamics and phase transformation on a subsecond time scale. We will investigate solid-state reactions at high temperature and *in situ* structures of thin films and interfaces.

(a) Original data (b) Normalized signal

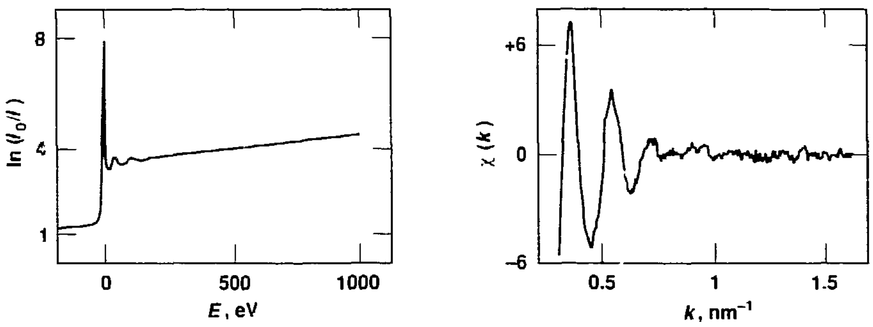

(c) Fourier transform (d) Inverse transform

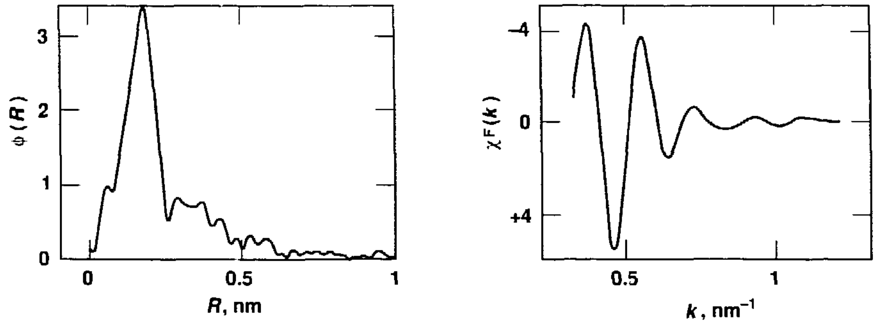

Figure 2. (a) Experimental scan of hafnium L_3-edge EXAFS for 0.5 nm of hafnium on a Pt/C multilayer. The energy scale is plotted with respect to the hafnium L_3-edge's first inflection of Hf metal at 9561 eV as zero. (b) The normalized EXAFS signal. (c) Fourier transform and (d) inverse transform of the normalized signal in the region from 0.02 to 0.24 nm about the central absorbing Hf atom.

Reference

Stanford Synchrotron Radiation Laboratory Activity Report (1987), Stanford Synchrotron Radiation Laboratory, Stanford, CA, Report 88/01, pp. 67, 104, 120, and 121.

X-Ray Thin Films

Principal Investigator: T. W. Barbee, Jr.

Multilayers are man-made microstructures that are periodic in depth and can be applied as x-ray, soft-x-ray, and extreme-ultraviolet optics; diffraction gratings are man-made microstructures that are periodic in plane and have been used as optical elements for most of this century. We have combined these two optical elements and demonstrated that their unique properties can advance our experimental capabilities in short-wavelength spectral regions.

Multilayer structures, such reflection or antireflection coatings, were developed more than 50 years ago for studying infrared, visible, and ultraviolet light. However, multilayer structures of sufficient quality for optical applications in the x-ray, soft-x-ray, and extreme-ultraviolet (EUV) ranges, where wavelengths are 10 to 10,000 times shorter, have only been fabricated during the past decade. Simple reflective diffraction gratings were developed in the early 1900s and are now a standard dispersive element used in moderate- to high-resolution optics. The in-plane scale of diffraction gratings ranges from 300 to 5000 nm; in contrast, the in-depth microstructural scale typical of multilayers is from 1 to 40 nm. Our challenge was to design advanced reflective optical elements that focus, disperse, and otherwise manipulate short-wavelength light.

We have prepared multilayer diffraction gratings by multisource magnetron-sputter deposition onto 2000-nm-period laminar amplitude grating substrates. The grating structures were anisotropically etched in (110) single-crystal silicon patterned using standard microlithography techniques. We fabricated multilayers of tungsten/carbon, rhodium/carbon, molybdenum/silicon, and 304 stainless-steel/silicon, with periods of 2.5 to 20 nm, onto these diffraction-grating substrates and characterized them at the Stanford Synchrotron Radiation Laboratory.

Figure 1 is a schematic cross section of a multilayer grating. The grating consists of flat-topped bars with width $d_g^0/2$ and period d_g^0. We deposit multilayers with a geometric period d_0 onto these bars. Light is incident from the left at a grazing angle θ, called the Bragg angle, and is diffracted in a specular manner by the multilayer at an exit angle θ relative to the multilayer in the zero grating order ($m = 0$). Interference of light diffracted by the multilayers on each grating bar results in intensity maxima at angles $m\phi$ relative to the zero order, where $m = \pm1, 2, 3, \ldots$.

The convolution of diffractive properties of the two periodic structures results in a relation between the grating-order dispersion angles $m\phi$ and the geometric parameters of the multilayer and grating structures. The resulting analytical relation is

$$\sin\phi = \frac{2md'}{nd_g^0}\,, \qquad (1)$$

where m is the grating order, d' is the refraction-corrected multilayer

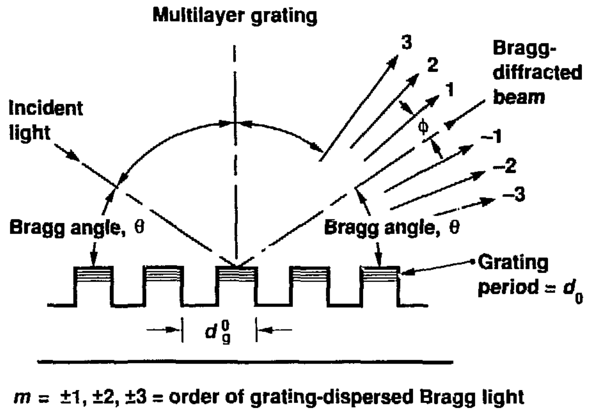

Figure 1. Cross section of a multilayer diffraction grating. Flat-topped grating bars have a width $d_g^0/2$ and a period d_g^0. Multilayers with a geometric period d_0 are deposited onto these bars. Light is incident from the left at a grazing angle θ, typically called the Bragg angle. Diffracted beams are shown on the right.

period, n is the Bragg order of the multilayer-diffracted light, and d is the grating period.

Several unique characteristics of multilayer diffraction gratings are apparent from this result. First, the dispersion angle Θ is constant because it is independent of the angle of incidence θ or the wavelength of light that is Bragg-diffracted by the multilayer. Second, the multilayer grating separates Bragg orders of the multilayer-diffracted light because the dispersion angle Θ is inversely proportional to n. Third, because angle Θ is independent of wavelength, the gratings are constant-resolution dispersion elements for a given geometry. Fourth, the specificity of the relations among Θ, d', and d_g^0 shown in Equation 1 results in design criteria for more complex structures including laminar, blaze, and echelle gratings. Such gratings meeting these criteria will, in general, produce Bragg-reflected light that constructively interferes, greatly extending the range and use of such optical elements. This property makes possible efficient, very-high-resolution dispersion elements in the soft-x-ray and EUV ranges.

We have used a multilayer grating as the second element in a two-parallel-element monochromator to measure the carbon K-absorption edge at 283 eV. The multilayer contained no carbon, was synthesized from 304 stainless steel and silicon, and had a period of 5.5 nm. The period of the grating substrate was 2000 nm. We used a 236 nm thick carbon foil for our transmission measurements. Figure 2 shows our measured mass absorption coefficient for energies of 95 to 1100 eV compared with previous data from the literature. The agreement is good; however, our experiment reveals structure at approximately 330 eV that is not seen in the previous data. This structure is at the same energy as that observed in crystalline graphite and is believed to signify the presence of small microcrystalline regions in carbon foil. These are the first measurements obtained with a multilayer/multilayer grating in a simple, two-parallel-crystal monochromator. Our data demonstrate the unique capabilities of such advanced optics.

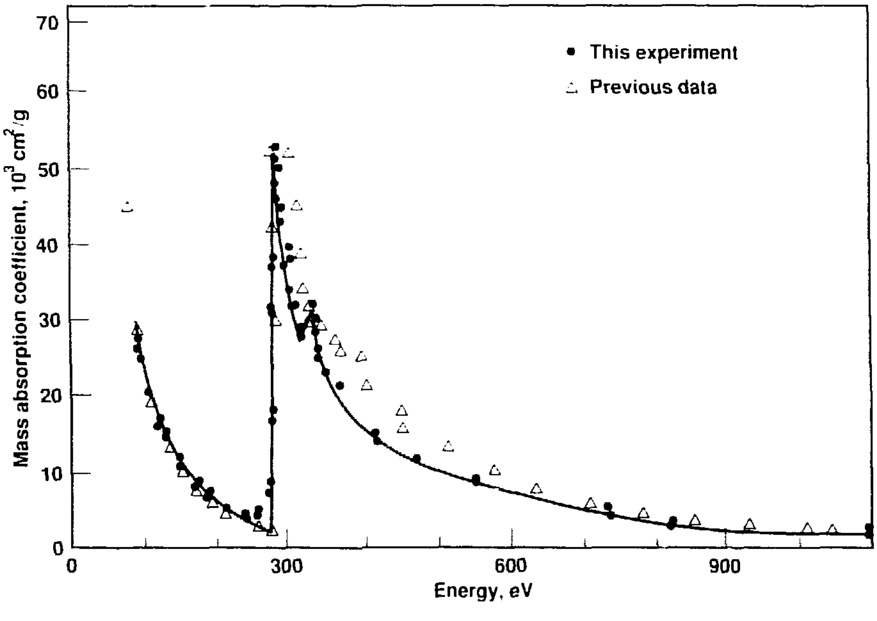

Figure 2. Mass absorption coefficient of carbon measured via a multilayer grating (d_g^0 = 2000 nm) as the second element in a two-parallel-crystal monochromator for energies of 95 to 1100 eV. The experimentally observed structure at approximately 330 eV probably signifies the presence of small microcrystalline regions in the carbon foil. These are the first measurements obtained with a multilayer/multilayer grating in a simple, two-parallel-crystal monochromator.

References

Barbee, T. W., Jr. (1988), "Combined Microstructure X-Ray Optics: Multilayer Diffraction Gratings," in *Materials Research Society Proc.*, T. W. Barbee, Jr., F. Spaepen, and L. Greer, Eds. (Materials Research Society, Pittsburgh, PA), Vol. 103, p. 307.

Barbee, T. W., Jr. (1988), "Multilayer Structures: Atomic Engineering in its Infancy," in *Proc. NATO ASI on Physics, Fabrication, and Applications of Multilayered Structures*, P. Dhez, Ed. (Plenum Corporation, New York, NY).

Barbee, T. W., Jr. (1988), "The Use of Multilayer Diffraction Gratings in the Determination of X-Ray, Soft X-Ray and VUV Elemental Scattering Cross Sections," *SPIE Proc.*, **911**, 169.

Pianetta, P., and T. W. Barbee, Jr. (1988), "Applications of Multilayers to Synchrotron Radiation," *Nucl. Instrum. Methods* **A226**, 441.

Walker, A. B. C., Jr., T. W. Barbee, Jr., R. B. Hoover, and J. F. Lindblom (1988), "Soft X-Ray Images of the Solar Corona with a Normal Incidence Cassegrainian Multilayer Telescope," *Science* **241**, 1781.

Photoactivated Heterogeneous Catalysis on Aerogels

An SiO_2 aerogel doped with 0.45 wt% of uranyl ion (UO_2^{2+}) is an effective photocatalyst for synthesizing C_1 to C_5 hydrocarbons from $2H_2$:1CO and $1H_2$:$1C_2H_4$ gas mixtures. This catalyst also produces ethylene and traces of methane from a $1H_2$:$1C_2H_6$ gas mixture.

Principal Investigator: C. A. Colmenares
Co-Investigators: E. F. See, W. E. Elsholz, C. L. Evans, M. Connor,* and R. Gaver*

University of California, Davis
San Jose State University, San Jose, CA

We have developed an energy-efficient process for synthesizing C_1 to C_5 hydrocarbons. This process uses an SiO_2 aerogel doped with UO_2^{2+} to catalyze the hydrogenation of CO to hydrocarbons; the energy source for the reaction is simulated sunlight. Our goal this year was to reproduce our FY87 results to confirm that our success was not anomalous. We also wanted to study the effect of the same catalyst on $1H_2$:$1C_2H_4$ and $1H_2$:$1C_2H_6$ gas mixtures, to produce SiO_2 and ThO_2 aerogels doped with cerium and europium, and to begin studies to determine the wavelength dependence and energy-transfer mechanism of reactions catalyzed by doped aerogels.

For the catalyst, SiO_2 aerogels with a density of 50–100 mg/cm^3 are produced and doped with 0.45 wt% UO_2^{2+}. These doped aerogels display and maintain an intense fluorescence, indicating the persistence of the uranyl ion. Spectroscopy reveals that the uranium in the aerogel maintains a 6+ oxidation state, confirming the continued presence of the uranyl ion. Thus the catalyst can be used for long periods without deterioration.

To hydrogenate CO to hydrocarbons, ground and sieved (300-mesh) doped aerogel is placed in a fluidized-bed quartz reactor with one of three gas mixtures ($2H_2$:1CO, $1H_2$:$1C_2H_4$, or $1H_2$:$1C_2H_6$). The gas mixtures are continuously circulated while a 1000 W, mercury xenon, solar-simulator lamp illuminates the aerogel particles; the temperature of the fluidized bed reaches ~90°C.

To determine the effect of temperature, we repeated this process with heat alone (no light) at 100 and 200°C. The yields for hydrogenation of CO produced by 0.5 g of catalyst (see Table 1) are virtually identical to those obtained in FY87. The thermal contribution to the product quantities is negligible; in addition, the product distribution of the heated reactions differs from that of the photochemical reaction.

We also confirmed the effect of the uranyl dopant. A photochemical experiment using plain SiO_2 aerogel produced predominantly ethane and methane and an unidentified product in quantities about ten times lower than for the uranyl-doped aerogel.

Lastly, we determined the effect of light intensity on the

Table 1. **Distribution of CO hydrogenation products by weight percent (determined by gas chromatography).**

Products	Light exposure, 54 h	Heat exposure	
		100°C, 21 h	200°C, 24 h
Methane	62.57		3.13
Ethylene	13.41	48.39	22.65
Ethane	9.67	51.61	35.57
Propene*	—	—	—
Propane	9.09	—	—
Methanol	—	—	11.23
Isobutane	2.21	—	—
1-butene	—	—	10.52
***N*-butane**	2.64	—	16.90
***N*-pentane**	0.42	—	—
C_8 hydrocarbons*	—	—	—
%C conversion	~0.1	2×10^{-4}	7×10^{-3}

*Detected but not measured quantitatively.

photochemical reaction. Using uranyl-doped aerogel and a $2H_2:1CO$ gas mixture, we found that an increase in intensity from 60 to 540 W raised the methane yield fivefold but only doubled the yield of the other products.

In other photochemical experiments, we used uranyl-doped aerogel with mixtures of $1H_2:1C_2H_6$ and $1H_2:1C_2H_4$. With the first gas mixture, the main product was ethylene with a small amount of methane. With the second gas mixture, the main products were methane, ethane, propane, butane, pentane, hexane, and an unidentified product believed to be octane. Full quantitative results are not yet available, but we repeated these experiments and obtained identical qualitative results.

After much work, we have developed a process to produce cerium- and europium-doped SiO aerogels. Our most time consuming problem was to separate the dopant from the aerogel in the final stage of the process. We have yet to test these aerogels for catalytic activity.

A study of the energy-transfer mechanism of reactions catalyzed by doped aerogels was adopted as a doctoral project by M. Conner, a co-investigator.

Computation

R. R. Borchers

The overall goal of the Computation Department IR&D projects for FY88 was to give Laboratory scientists more effective means for using supercomputers to solve their research problems. The projects spanned the spectrum from direct applications to basic research. Our researchers strove to understand the nature of the calculations that must be performed and to identify alternate approaches to them that might perform better on specific computer architectures. We also addressed the ways in which scientists interact with computers. The design, writing, and debugging of programs is time-consuming and takes away from a scientist's time to do creative research. We are seeking ways to help them create working programs faster and more reliably. In addition, we are evaluating the difficulties of dealing with new, advanced computer architectures, particularly parallel machines. We are continually working to increase the efficiency with which Laboratory computing resources are used; we have major efforts in optimizing compilers, making libraries efficient, and improving the design of operating systems. An integral part of this work is evaluating the performance of various computer architectures executing specific programs.

In the area of applications, considerable progress has been made in developing a program to model strongly turbulent processes in plasma physics by the methods of fluid-turbulence closure theory. The challenge here is to increase computational efficiency while still considering most of the important physics in these processes.

In two other projects, we are developing knowledge-based engineering techniques to give users a simpler and more powerful way of interacting with computers. In one project, we have developed new schemes, or knowledge bases, for representing information that will simplify the translation of partial differential equations and problem specifications into programs for solving them. The knowledge base being developed for mathematical analysis allows us to represent functions and operators in a deep context, not merely as the solely syntactic objects of traditional symbolic-manipulation systems. In the other project, we are developing the knowledge-based programming techniques that can assume much of the operational and tuning responsibility for such complex experimental facilities as the Laboratory's Advanced Test Accelerator and Experimental Test Accelerator. This project has succeeded not only with traditional heuristic approaches that provide qualitative help but also with approaches that base diagnosis and tuning on conclusions drawn from a quantitative model.

Another pair of projects deals with parallel computing. We report on work toward developing the simulation model needed to explore a wide variety of multiprocessor architectures. Informative execution traces for hypothetical systems are combined with studies on the current SISAL runtime system to help us understand how parallelism works and why it sometimes fails. In the last project, we are working to identify quantitative statistical measures of parallel random number generators and to develop ways of improving these generators for more demanding applications. We can now recommend parallel methods for generating up to several hundred streams of pseudorandom numbers.

In FY88, the Computation Department received $728,000 in IR&D funds.

Closure Modeling of Plasma Turbulence

Turbulence closures can predict turbulent flow properties and aid our understanding of the underlying physics. The goal of our project is to derive and numerically implement closure models for turbulence in tokamak plasmas.

Principal Investigator: A. E. Koniges
Co-Investigators: W. P. Dannevik
and C. E. Leith

Strong turbulence is a leading candidate to explain anomalous transport and thus loss of confinement in tokamak plasmas. Such turbulence can be described by a coupled set of *nonlinear equations* that resemble the Navier-Stokes equations of fluid dynamics. Guided by the success of closure models in fluid problems, we have made a perturbative approximation that models the influence of the nonlinear terms on the statistical (and thus transport-related) properties of the turbulent system. However, fluid theories must be substantially modified and rederived in order to incorporate properties of the plasma equations that are not contained in Navier-Stokes turbulence modeling. These properties include the occurrence of complex field quantities, the presence of linear damping and driving via complex linear terms, and the nondiagonal coupling of two or more field quantities in the system.

In FY88, we concentrated on developing a closure theory that is both applicable to plasma turbulence and amenable to numerical solution. Approximations based on the physics of the turbulent steady state can be useful for simplifying the numerical computation. In particular, through numerical simulations, we showed that the application of the fluctuation-dissipation relation is reasonable for a damped and driven system in steady state (see Figure 1). Our current scheme incorporates this approximation and in so doing *eliminates* a costly *integration* present in full direct-interaction-approximation (DIA) calculations. We also began to develop a procedure based on Pade approximates that further accelerates the computation.

In FY89, we will test these numerical schemes by applying them to tokamak turbulence equations that contain driving and damping.

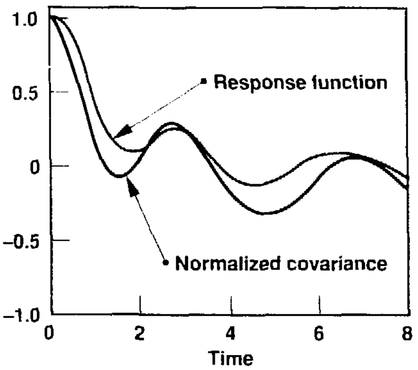

Figure 1. Demonstration of the fluctuation-dissipation relation for a turbulent drift-wave problem. The agreement of the two curves allows us to replace the two-time covariance with the response function.

References

Koniges, A. E., W. P. Dannevik, and C. E. Leith (1988). "Pade Approximant Schemes for Integrating Turbulence Closures of the DIA Type." *Bull. Amer. Phys. Soc.* **33**, 2021.

Koniges, A. E., and C. E. Leith (1987). "Statistical Closure Approximations and the Fluctuation-Dissipation Theorem for Drift-Wave Interaction." *Phys. Fluids* **30**, 3065.

Koniges, A. E., and Leith, C.E. (1988). "Parallel Processing of Random Number Generation for Monte Carlo Turbulence Simulation." *J. Comp. Phys.* **80** (in press).

An Automatic Programming System for Solving Partial Differential Equations

The goal of our project is to improve the productivity of scientists and engineers who develop numerical simulations for physical problems described by partial differential equations (PDEs). This is to be done by first developing a knowledge base for mathematical analysis and then building an automatic programming system on that knowledge base that will create numerical simulators for PDEs.

Principal Investigators: D. Balaban, J. Garbarini, and W. Grieman*

Lawrence Berkeley Laboratory,
Berkeley, CA

Our goal is to create an automatic programming system that generates numerical discretization schemes for partial differential equation (PDE) problems, thus eliminating the tedium and human errors inherent in the mathematical manipulations and programming normally involved in creating PDE simulations. Initially, the system will be useful to engineers who need to simulate well-understood physical problems with discretization schemes that would previously have been too costly to derive. A nonlinear heat equation in spherical coordinates and three space dimensions is one example of such a problem.

To begin with, we want to be able to derive numerical schemes for parabolic equations such as the reaction diffusion equation with complex chemistry, for nonlinear wave equations such as those describing smooth acoustic or seismic waves, and for electromagnetic systems described by Maxwell's equations. Later, as the automatic programming system becomes more sophisticated, it will be useful to engineers and physicists who are developing unusual or complex discretization schemes for less routine problems, such as those defined by Euler's equation or by magnetohydrodynamic equations that may have discontinuous solutions.

There are a variety of ways to create an automatic programming system for PDEs (see the box "Automatic Programming Systems for PDEs" on the following page). We have chosen the following steps to implement our system:

- Develop a uniform scheme for representing continuous-physics problems that can be implemented in a computer program.
- Develop a uniform scheme that represents the process of deriving a discretization scheme from a continuous description.
- Develop advanced symbolic-manipulation capabilities to implement the derivation.

We have developed a relational model of continuous-physics knowledge centered on conserved quantities and conservation laws. Initially, this model defined observables, densities, currents, and sources as well as three fundamental relations of current, density, and the conservation law that related them to one another and contained information about the materials being modeled. All of this knowledge is represented in standard vector calculus form.

The discretization schemes are derived systematically and mechanically. Stokes theorem is used to create discrete forms of the conservation laws. The partitioning of the domain on which the physical problem is defined provides a framework for defining a system of equations from the discrete conservation laws. The discretization scheme is then essentially this system of equations.

Much of the multidimensional calculus in our automatic programming system is represented functionally by the mathematical-analysis knowledge base currently being implemented. (That is, functions and operators are treated much as they are in functional analysis; there are no variables, and expressions are represented as compositions of functions.) This knowledge base is being built as a layer over the traditional symbolic-manipulation system MAPLE. In this way, many new and powerful symbolic-manipulation capabilities are being added without recreating existing ones.

In traditional symbolic-manipulation systems, some constructs such as operators and complicated functions must be expressed as programs in the symbolic-manipulation language. Changing expressions involving these constructs then entails restructuring programs. Our symbolic-manipulation capabilities are powerful enough to allow us to represent these constructs as functions, not programs. Thus, we will be able to manipulate and simplify more complex expressions that contain them.

In FY88, we extended our automatic programming system by placing it in the uniform framework of differentiable manifolds. We did this for four reasons. First, it provides a systematic way to compute high-dimensional surface integrals, which are the basis of our approach to deriving discretization schemes. Second, discretization schemes can then be derived in the same way for many different coordinate systems because manifold theory allows physical systems to be described independently of their coordinates. Third, a wider class of physics problems can be described. Differential manifolds provide the most natural setting for the mathematical objects used to model continuous physical systems. This single formalism can describe such diverse physical systems as electrodynamic, reaction diffusion, quantum mechanic, and fluid systems. Finally, differential manifolds allow us to deal with complex domain geometries. For example, a domain might best be described by a patchwork of different coordinate systems, or it might have a complex boundary.

A new implementation of the mathematical-analysis knowledge base is nearly finished. It has a much more general and complete theoretical foundation, which was needed to handle the more abstract differential geometry formalism that we are now using. A novel scheme based on Currying composition operators was completed for manipulating higher-order functions. This scheme is the basis of our implementation and enables us to systematically represent and manipulate operators (functions of functions).

Significant progress was also made on our relational model for continuous physics. The question of how a PDE corresponds to the tensor of conserved quantities was at least partially solved for the case of

Automatic Programming Systems for PDEs

Current automatic programming systems for PDE problems follow a variety of approaches. Some start with a problem's continuous description; others start with its discrete description. Some systems work from conservation laws; others work from the PDEs derived from those laws. Some use symbolic manipulation to derive all or parts of the discretization scheme; others use artificial intelligence techniques to classify the class of problem being solved and to fill program templates that implement the discretization scheme.

Each approach reflects the desired properties of the simulation that is created by the automatic programming system. Systems that use template filling are likely to produce a very efficient code but one that is applicable only to narrow classes of problems. Systems that start with discrete problem descriptions are also likely to generate efficient codes, but the codes are often complicated to use because the user must deal with both the continuous problem and its discrete approximation. Systems that deal with PDEs directly may have a harder time generating conservative discretization schemes (that is, schemes consistent with conservation laws), whereas systems that deal with conservation laws will not handle more abstract PDEs.

Our automatic programming system starts with a continuous description of a problem in terms of conservation laws and derives its discretization schemes from this description. Consequently, our system is relatively easy to use and is applicable to a wide variety of problems. It always generates conservative discretization schemes. However, these schemes may require some work to make them numerically efficient.

classical field theory. Mathematical models for many continuous systems can be expressed in terms of a manifold, its structure, and the Hodge *-mapping. Examples include Maxwell's equations for electrodynamics, Laplace's equation, and the heat and wave equations.

These models are expressed in terms of differential forms over manifolds that represent conservation laws for the system that are independent of material properties. The properties are expressed by relationships between state variables for the system and conserved currents that appear in conservation laws. In many cases, this relationship can be expressed in the metric structure associated with the manifold's tangent space. This relationship is reflected in the Hodge *-mapping, which is determined by the metric.

A large class of continuous-physics models have the form

$$dF = 0, \; d * F = J \; .$$

These equations are equivalent to a PDE model for the system. The metric structure determines the PDE class (elliptic, parabolic, or hyperbolic). Table 1 gives the relationship between the metric and PDE class for the case where F is the one-form $F = df$ and $J = 0$. A single covariant expression represents all PDE classes.

The highest priority for FY89 will be to upgrade our current implementation of the mathematical-analysis knowledge base to the point where it can compute general surface integrals. To do this, we will have to expand the knowledge base to handle manifolds, tangent bundles, and pull backs. This expansion will delay the automatic derivation of the first discretization schemes a few months. However, being able to do general surface integration will mean that high-dimensionality discretization schemes will be immediately derivable.

We hope to have the implementation ready to derive some schemes for simple electrodynamic systems early in FY89. Discrete approximations for simple fluid dynamics systems should follow shortly. At this point, we will begin using FIDIL (a finite-difference language extension to Fortran) to implement the automatically derived schemes.

Table 1. **The PDE corresponding to the covariant expression $*d*df = 0$ is determined by the metric structure.**

Domain of *f*	Metric on the domain of *f*	Equivalent PDE	PDE class
Space and time	Lorentz	$\frac{\partial^2 f}{\partial t^2} - \Delta f = 0$	Hyperbolic
Space and time	Singular	$\frac{\partial f}{\partial t} - \Delta f = 0$	Parabolic
Space only	Riemannian	$\Delta f = 0$	Elliptic

References

Balaban, D., and J. Garbarini (1988). *An Automatic Programming System for PDEs Based on a Relational Model of Continuous Physics Problems and a Functional Model of Mathematical Analysis*. Lawrence Livermore National Laboratory, Report UCRL-53895.

Greiman, W., D. Balaban, M. Durst, and J. Garbarini (1987). "Knowledge Representations for the Automatic Generation of Numerical Simulators for PDEs." *Proc. IMACS Conference on Expert Systems for Numerical Computing*, Barcelona, Spain, June 2–4.

Olwell, K., D. Balaban, and J. Garbarini (1988). *Discrete Analogs of PDEs Defined on Rectangular Lattices*. Lawrence Livermore National Laboratory, Report UCID-21598.

An Expert System for Tuning Accelerators

Principal Investigators: H. Brand, D. Lager, R. Searfus, W. Maurer, J. Hernandez, and F. Coffield

The machines used for modern experimental research are becoming increasingly complex, and there is a pressing need for automation techniques to provide high-level control of these machines to complement and supplement human control. We are developing a knowledge-based expert system to handle many of the tuning tasks and operational responsibilities for induction linear accelerators. Use of an expert system should greatly increase the available high-quality beam time.

We are applying knowledge-based systems (KBS) techniques to the problem of tuning and controlling an induction linear accelerator and its beam-transport system. Our initial efforts have focused on developing KBS techniques for the beam-transport system of the Advanced Test Accelerator (ATA); this work is also directly applicable to the next-generation machine, the Experimental Test Accelerator (ETA-II). This year, we completed the interface with the ATA's diagnostic subsystem and have nearly completed the interface with the control subsystem.

We are investigating both a heuristic and a model-based approach. The heuristic approach mimics the diagnosis and tuning done by an expert human operator. It can be applied to any instrument for which there is operational and tuning expertise. The model-based approach, on the other hand, operates a numerical simulation code and compares code-simulated results with current machine performance for diagnosis and tuning. This approach holds much promise but is limited to machines whose operations can be simulated by numerical models.

To support both the heuristic and model-based approaches, we have developed a "smart" object-oriented representation of an accelerator and its beam-transport system and have used this representation to model the ATA beamline. This representation is "smart" in that it includes procedural knowledge via the data-driven programming paradigm. For example, it automatically completes the description of the beamline as soon as the minimum required information is available. It also includes procedural knowledge that couples the model to the diagnostic subsystem interface so that data is acquired as required and when requested; a similar coupling exists with the control subsystem interface so that changes to the model can be automatically propagated to the control subsystem.

The heuristic approach uses a hierarchical scheme, dubbed MDS for monitored decision script, to describe the accelerator operation and tuning procedures. Unlike earlier scripts (e.g., Barr and Feigenbaum, 1981) that only permit a linear sequence of events, our MDSs allow decision-based branches and loops. They also allow conditions to be monitored periodically (for exceptions or errors) during execution of the script, and they include an exception/error-handling capability to cope with exceptions from the monitored conditions and errors signaled by the actions taken (or MDSs called) from within the script.

We have built a set of prototype MDSs that can tune part of the ATA beam-transport system. These MDSs use the object-oriented machine representation to reason about the beamline and to identify choices as to which steering magnets to adjust to align the beam. Actual adjustment of the steering magnets is done by a Uniplex optimization algorithm that can operate in the presence of measurement noise. This system has been demonstrated successfully both on the simulator and on the ATA.

Significant work has also been completed in support of the numerical model-based approach. Dr. M. Lee of the Stanford Linear Accelerator Center is assisting us as a consultant. Dr. Lee and his colleague, S. Clearwater, are pioneers in the application of knowledge-based systems that use beamline simulation codes and actual beam-trajectory data in off-line analyses. We have also procured (and are awaiting delivery of) a state-of-the-art accelerator- and beamline-modeling code.

In the mean time, using a simple beamline model, we are extending the work of Lee and Clearwater to two dimensions, an action necessitated by the solenoidal beam-transport system used on the ETA-II and soon to be installed on the ATA. This work differs from that of Lee and Clearwater in that it uses a model with an absolute, instead of a relative, coordinate system. An absolute-coordinate-system model produces results directly comparable to those generated by the beam-position diagnostics; this should make analysis much easier and lead to a powerful system free of many of the mistakes that can be introduced when results from a relative-coordinate-system model are directly compared with measured beam parameters.

We have used the simple beamline model to find regions within the beamline where the model and the beam-diagnostic measurements agree. Figure 1 shows such a region for a simulated section of the ATA beamline. Our next step will be to use the knowledge-based system to search for the areas where regions of good fit abut to identify the faulty part(s) in the beamline that account for discrepancies between the actual beamline and the model. In this way, we will be able to merge multiple regions of good fit into a single region covering the whole beamline.

Increased funding from the Beam Research Project for FY89 will enable us to complete the extension of Lee and Clearwater's work to two dimensions and upgrade the system into an on-line, real-time feedback system. Our goal is to make this system capable of designing, running, and analyzing diagnostic experiments to identify faulty beamline components and to determine the type of fault. This information would then be fed back into the numerical model so that operation and tuning of the accelerator could continue in the degraded environment. At present, the major obstacle appears to be the ability of the numerical model to simulate the many types of possible faults (e.g., misalignment in any or all of six axes, field winding shorts, etc.).

Eventually, the heuristic and model-based approaches will be combined. The heuristic approach using MDSs will exercise high-level operational control and monitoring. The MDSs will prepare the accelerator and beamline for various experiments, monitor its performance, and adjust for part failures when possible. The model-based approach will serve as the tuning and diagnostic "intelligence" in the system. Faulty or misaligned parts and diagnostics will be located by intelligent use of a numerical model, and tuning parameters will be derived directly from the model after it has been updated to account for whatever faults are identified.

Reference

Barr, A., and E. A. Feigenbaum, Eds. (1981), *The Handbook of Artificial Intelligence* (William Kaufmann, Inc., Los Altos, CA), Vol. 1, pp. 158–159, 306–315.

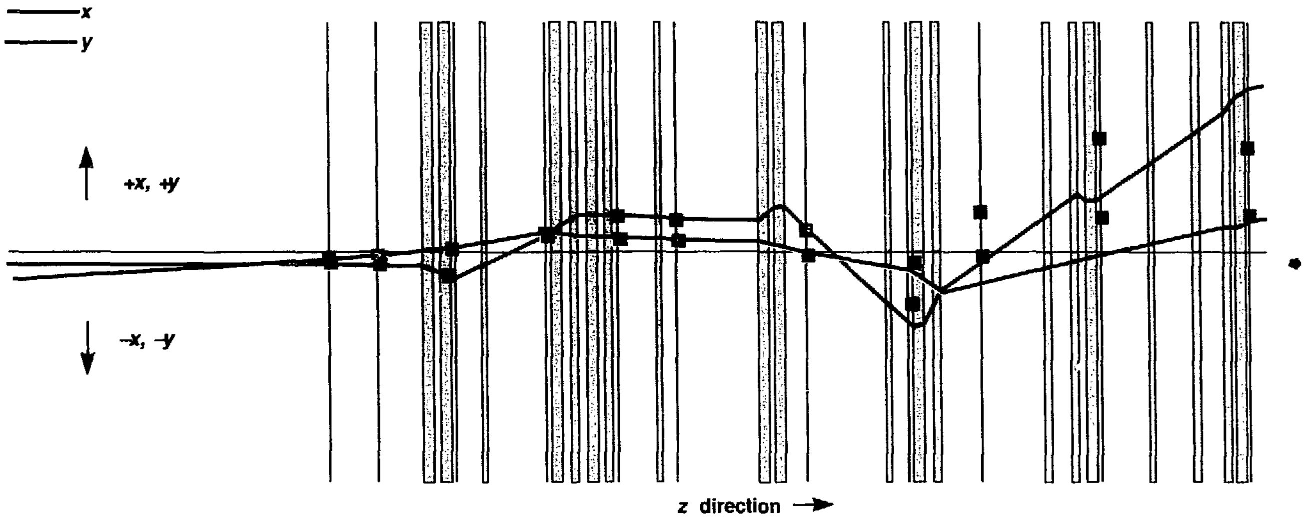

Figure 1. Simulated section of the ATA beamline showing agreement between the model prediction and the measured positions over the first seven beam-position monitors. The beam in both the x and y directions is plotted as a function of position along the beamline (z direction). Tall rectangles represent various beamline components; vertical lines represent beam-position monitors; squares represent the beam-position measurements; the (near-horizontal) colored lines show the modeled beam path.

FY88: $136,000

Architecture Studies with SISAL

Principal Investigator: J. T. Feo

We are evaluating the performance of multiprocessor computer systems for dataflow computing by simulating the execution of programs written in SISAL on such machines. Our goal is to identify the architectural features that abet or hinder the programs' execution. An important spinoff of this project is the development of heuristics to map the tasks of a parallel process onto the resources of a multiprocessor computer system.

The Laboratory has an ongoing program to design and implement SISAL (Streams and Iteration in a Single Assignment Language), a high-level, applicative language for parallel processors. As part of this work, we must understand how different hardware components, such as the Cray-X/MP vector processors, affect the performance of SISAL programs on multiprocessors. The speed of a parallel program depends on the multiprocessor's hardware components, the topology of the interconnection network, and the algorithms used to partition and schedule an application's concurrent computation units onto the processor's resources.

We are evaluating multiprocessor systems for a mode of parallel processing known as dataflow computing. Dataflow differs from conventional parallel processing in that synchronization and communication between concurrent computation units is the sole responsibility of the runtime system. The user does not explicitly encode synchronization and communication primitives in his programs; instead, the compiler realizes the code's implicit dependencies and inserts calls to the appropriate system routines.

Our goal is to develop a dataflow simulator that will take as input a dataflow program and a description of a multiprocessor system. Once a program is mapped, the simulator will logically execute the program and output performance statistics. As part of this work, we are developing heuristics to partition and map dataflow programs to the resources of each system we consider. We are concentrating our initial efforts on systems for which we are developing SISAL compilers and runtime systems.

In FY88 we developed a profile utility and enhanced the SISAL debugger and interpreter (DI) to output execution traces of interpreted SISAL programs. The profiler generates a parallelism profile, which assumes an infinite number of processors, no communication delays, and unit instruction cost (all instructions take one unit of time); it observes all data and logical dependencies. We began upgrading the profiler to simulate execution on a shared-memory architecture with a finite number of processors, nonzero communication delays, and variable instruction costs.

We also completed an extensive study of the current SISAL runtime system. This work led to improving the memory-allocation algorithm and to rewriting certain parts of the runtime system to alleviate bottlenecks. It is important that we understand the characteristics of the current SISAL system, because we plan to establish the correctness of our simulator by comparing the performance it predicts for an application on a particular system with the application's actual execution on that system.

We have three main tasks to complete in FY89:

- Reorganize the project's approach.
- Develop a flexible but comprehensive paradigm to describe parallel architectures.
- Develop mapping heuristics for our initial target machines.

While upgrading the profiler, we realized that DI is an example of the simulator we want to develop. Presently, DI simulates the execution of SISAL programs on a multiprocessor system with infinite resources and zero communication delays; thus we need only to enhance

DI to simulate program execution for an input architecture. Although this is no trivial task, at least we do not have to rewrite the support routines for program execution (input/output, memory management, and instruction scheduling and execution). Moreover, DI works directly with our dataflow graphs, known as IF1 graphs, removing the need for execution trace files that can be very large for even simple programs.

We have decided on a table format to describe multiprocessor computer systems. At the very least, the table will include the number of processors, their type, the amount and layout of memory, instruction costs, network topology, and the communication delays between resources. We plan to consider each memory as a separate resource, thus casting all memory accesses as communication delays between a processor element and a memory resource. Finally, we will develop mapping heuristics for shared-memory multiprocessor systems with both vector and scalar processors and with and without cache (high-speed local memories).

References

Lee, C., S. Skedzielewski, and J. Feo (1988). "On the Implementation of Applicative Languages in Shared-Memory MIMD Multiprocessors." *Proc. ACM SIGPLAN Symposium on Parallel Programming: Experience with Applications, Languages and Systems*, New Haven, CT, July 1988.

Oldehoeft, R., and D. Cann (1988). "Applicative Parallelism—Potential and Challenge." *IEEE Software* **5** (1), 62.

Sarkar, V. (1987), *Partitioning and Scheduling Parallel Programs for Execution on Multiprocessors*, Stanford University, Stanford, CA, Report TR CSL-TR-87-328.

Skedzielewski, S., and J. Glauert (1985), *IF1 — An Intermediate Form for Applicative Languages*, Lawrence Livermore National Laboratory, Manual M-170.

Skedzielewski, S., R. Yates, and R. Oldehoeft (1987). "DI: An Interactive Debugger Interpreter for Applicative Languages." *Proc. ACM SIGPLAN Symposium on Interpreters and Interpretive Techniques*, St. Paul, MN, June 1987.

Parallel Pseudorandom Number Generation

Principal Investigator: M. Durst

We developed ways to reliably generate up to several hundred streams of pseudorandom numbers, with definitive quantitative measures for schemes that split sequences from congruential random number generators. We also created a battery of empirical tests for any parallel random number generator.

Parallel random number generators (PRNGs) can be viewed as algorithms for generating many mutually independent streams of pseudorandom numbers. To generate such streams, one may split the sequence of a single random number generator (RNG) or use a unique generator for each stream. We have completely described the statistical behavior of PRNGs formed by splitting the sequence from a congruential RNG. With a variant of the well-known spectral test, we tested such generators in use on the Cray-X/MP and found their behavior acceptable. We also calculated bounds on their behavior and found that they will not provide thousands of generally reliable streams. These theoretical inadequacies led us to consider unique generators for each stream.

The most promising idea was to use a different multiplier for each stream. Using work done by G. Fishman of the University of North Carolina, we projected that millions of individually acceptable multipliers exist. We developed necessary, but not sufficient, conditions on the interrelationships between multipliers. Combinatorial analysis of these interrelationships suggests that thousands of mutually acceptable streams might be found.

We also studied ways of constructing empirical tests for PRNGs. Fully general PRNGs for as few as a dozen streams must be acceptable in hundreds of dimensions: this makes exhaustive testing difficult. We constructed tests to correlate all streams at various lags. Since these tests study pairwise dependencies, they are necessary but far from sufficient. We provided a preliminary battery of tests (Durst, 1988a) for PRNGs that our Cray-X/MP implementations pass (although some earlier schemes do not). A side benefit of this work is an improved minimal battery of tests for standard RNGs: these tests uncovered defects in a published RNG. We also devised techniques for the *ad hoc* improvement of PRNGs for difficult applications and for comparison purposes when a PRNG is suspect (Durst, 1988b).

Our FY89 plans include a definitive discrepancy calculation for splitting schemes for generalized feedback-shift registers, whose vastly longer period and superior randomness make them more attractive for computations involving thousands of streams. In addition, it may be possible to adapt discrepancy calculations to the scheme involving different multipliers for each stream (currently these calculations are only available as an impractically large discrete summation). Further empirical work should also be done to find best splits for congruentials and to determine when the theoretical failings of congruential splitting schemes actually impinge on calculations. Finally, we intend to implement a functional PRNG for the parallel language SISAL, which should make parallel simulations and Monte Carlo calculations in that language more natural. This could produce a test bed in SISAL for both, which would in turn point out the most important remaining difficulties for PRNGs.

References

Durst, M. (1988a). "Testing Parallel Random Number Generators." *Computer Science and Statistics: Proceedings of the 20th Symposium*, American Statistical Association, Alexandria, VA (in press).

Durst, M. (1988b). "Improving Parallel Random Number Generators." *1988 Proceedings of the Statistical Computing Section*, American Statistical Association, Alexandria, VA (in press).

Earth Sciences

L. Schwartz

The Earth Sciences Department uses IR&D funds to maintain long-range basic research in the earth sciences, to promote collaboration with outstanding scientists at other institutions, to develop new capabilities, and to attract new staff members. The Department provides support in the areas of geochemistry, geophysics, seismology, geological engineering, and hydrology to LLNL programs in Nuclear Test Containment, Treaty Verification, Nuclear Waste Management, and Fossil Energy.

During FY88, we used IR&D funds to establish laboratories with unique capabilities for the study and accurate characterization of earth materials. We completed the installation of a thermal image furnace in our crystal-growth laboratory and successfully grew crystals of olivine, akermanite, spinel, magnetite, rutile, and nickel oxide. The availability of high-quality single crystals of olivine is especially important for studies of the electrical conductivity, diffusion, and deformation properties of the earth's upper mantle. In another effort, we are developing a large-volume, high-pressure facility for which we have designed a split-cone apparatus capable of reaching pressures as high as 250 kbar and temperatures up to 2000°C. When completed, this facility will provide a capability unique in the western U.S., extending the experimentally accessible "depth" to pressures believed to exist in the earth's lower mantle (depths greater than 600 km).

We also improved the computational and measurement techniques that are required to develop and test models of geological processes with realistic complexity. The fluid flow and transport modeling effort continued on a number of related fronts. We enhanced a hydrothermal flow code that enables us to study partially saturated flow in a fractured rock mass subjected to an episodic infiltration event. We are also developing codes to predict changes in fluid composition and mineral zonation as a fluid flows through and reacts with a porous media. In the area of aqueous geochemistry, we demonstrated the feasibility of a new method of determining the hydrogen ion activity in high-ionic-strength solutions. We have also developed optical chemical sensors for an optical-fiber system to measure the properties and composition of fluids in hot, corrosive wells.

To develop and test competing hypotheses on crust-mantle interactions, we are combining seismological and geochemical techniques in a unique tectonic region of northern California. We collected a suite of crustal xenoliths and deployed a portable broadband seismograph at the Clear Lake volcanic field. Initial analysis indicates that the xenoliths record two phases of thermal events, while seismic evidence indicates that the San Andreas Fault is decoupled in this region at mid- to lower crustal levels.

We also co-sponsored efforts in biotechnology and in modeling the equation of state of earth materials. Together with the Energy Program, we sponsored a study of thermophilic microorganisms in geothermal fluids that will eventually allow us to determine which types of these organisms may be useful for the subsurface processing of mineral, organic, or geothermal wastes at temperatures fatal to ordinary bacteria. In addition, we used a small grant, supplemental to our ongoing weapon-support research, to improve numerical simulations of underground nuclear explosions by incorporating a more flexible and accurate equation-of-state model into DYNA2D.

In FY89, the Earth Sciences Department received $876,000 (which includes $102,000 for the biotechnology project).

Single Crystal Synthesis in a Thermal Image Furnace

Principal Investigators: M. S. Young, F. J. Ryerson, and A. G. Duba

Many geochemical and geophysical experiments require well-characterized, high-quality single crystals for measuring phemonena ranging from diffusion and electrical conductivity to seismic attenuation and plastic deformation. Recognizing this need, we have established a crystal-growth laboratory in the Earth Sciences Department. In the past year, we have successfully used a thermal image furnace for growing crystals of olivine, akermanite, spinel, magnetite, rutile, and nickel oxide.

The bulk of the information on which we currently base our understanding of the mechanisms governing creep, diffusion, and electrical conductivity has been provided by measurements made on natural single crystals, which include a large number of components and are rarely of high quality. The thermal image furnace, purchased with funding from the Basic Energy Sciences Program and delivered to our crystal-growth laboratory in October 1987, makes it possible for us to investigate the synthesis of many mineral phases relevant to problems in geochemistry and geophysics.

The thermal image furnace is diagrammed in Figure 1. Two halogen lamps, each placed at one of the focal points of a gold-coated ellipsoidal mirror, provide the heat source for the thermal image furnace. The mirror focuses radiative heat on a small spot, thus generating the high temperature required for melting oxide minerals. A feed rod is made of well-mixed, stoichiometric amounts of chemicals that constitute the desired composition of the crystal. This feed rod is compacted under hydrostatic pressure and sintered 50 to 100 C below the melting point of the crystal compound. Crystal growth is initiated by melting a small section of the feed rod and bringing the molten zone in contact with a seed crystal. Because the feed rod and the crystal-growing assembly are enclosed in a quartz tube, both the crystal-growth atmosphere and the oxidation state of the growing crystal can be controlled by regulating the flow-through gas supply. Single crystals can be obtained by carefully maintaining

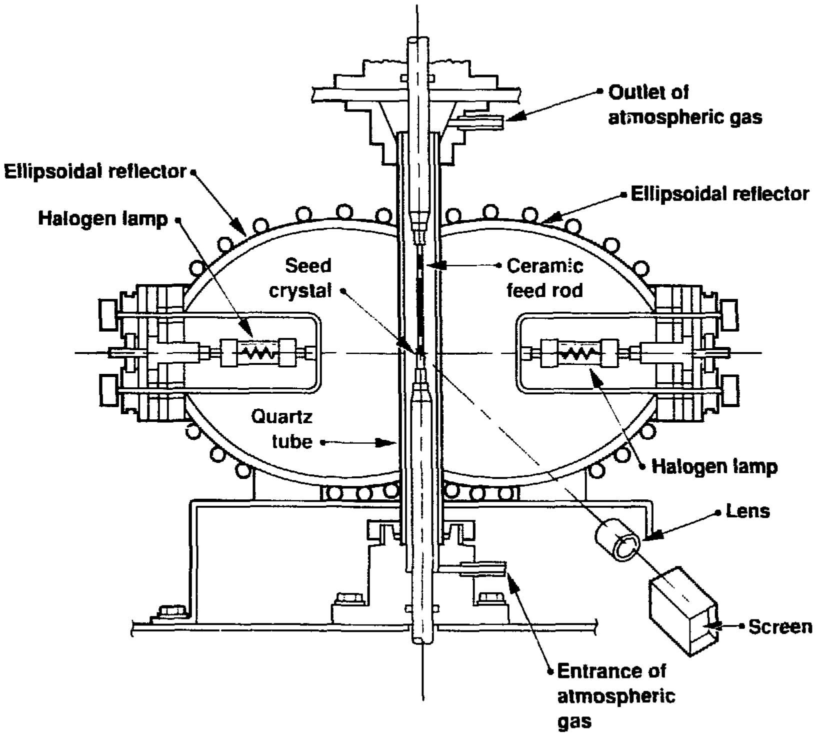

Figure 1. Schematic diagram of a thermal image furnace with two ellipsoidal reflectors.

a stable molten zone and slowly moving it away from the seed crystal.

The thermal image furnace offers several unique advantages for growing high-melting-point, multicomponent crystals. Since the melt zone that connects the growing crystal and the feed rod is held in place by its own surface tension, the float-zone method does not need a crucible to hold the melt, avoiding the crucible contamination problems often encountered in many melt-growth methods. The heating of the melt through the absorption of infrared radiation by the feed rod is another advantage for the various oxide systems of interest to earth scientists, as most of these oxides are electric and magnetic insulators, making induction heating or electron-beam heating impractical. By properly selecting the liquid-zone composition, which can be different from the composition of the feed rod, incongruent melting compounds can also be grown by the float-zone method.

The thermal image furnace is ideally suited for growing olivine, a solid solution of forsterite (Mg_2SiO_4) and fayalite (Fe_2SiO_4). Understanding the electrical conductivity, diffusion, and deformation properties of olivine will help us determine conditions in the earth's upper mantle, of which olivine is the major mineralogical constituent. Although geophysical measurements on natural olivines are abundant, interpretation of the results is often complicated by the presence of minor constituents such as cobalt, manganese, and nickel. The limited compositional range of available natural olivines also constrains our ability to test models of olivine behavior based on their defect chemistry. High-quality synthetic olivine crystals of well-defined composition and structure hold much promise for the refinement of such models.

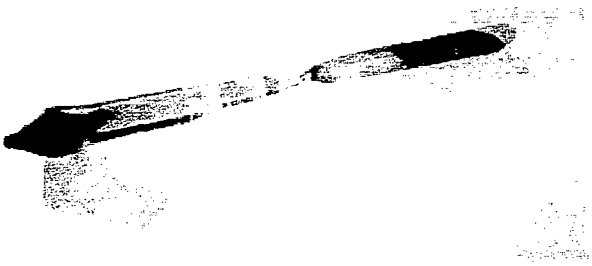

Figure 2. Olivine single crystal grown on a forsterite seed (right). On the average, this crystal is 8 mm in diameter and 50 mm in length.

After initial setup and characterization, we have successfully grown olivine crystals of intermediate composition. A typical as-grown olivine crystal is shown in Figure 2. The transparent, light-green crystal was grown on a forsterite seed in the [100] direction. Two (010) facets can be seen on the sides of the boule. Crystals of other orientations can be grown by selecting different seed orientations. Observation under the optical microscope reveals few growth imperfections such as gas bubbles and inclusions. These laboratory-grown olivine crystals have a density of imperfections of 10^4–10^5/cm^2, an order of magnitude lower than that of natural olivine.

This year, we have successfully grown spinel ($MgAl_2O_4$:1% NiO), rutile (TiO_2:0.5% Cr_2O_3), and forsterite (Mg_2SiO_4) in the thermal image furnace. We have also grown the following scientifically significant crystals:

- Magnetite (Fe_3O_4). Rock magnetists are very interested in understanding how various magnetic properties vary with temperature. Magnetic stability depends critically on defect and impurity effects on the magnetic domain structures in Fe_3O_4 and titanomagnetic ($Fe_{3-x}Ti_xO_4$, $x = 0.6$). The magnetite single crystal we have grown is typically 5 to 6 mm in diameter and 40 mm long; the crystal surface shows pronounced growth facets.
- Nickel oxide (NiO). Nickel oxide has a melting point of 1990°C and is usually difficult to grow by the melt method because of its high reactivity with noble metal crucibles. We obtained a single crystal of NiO in the thermal image furnace using a growth atmosphere of oxygen (200 cm^3/min) and argon (1000 cm^3/min). A self-seeding technique is used to obtain the single crystal by necking down a polycrystalline seed and crowding out the unfavorable slow-growth orientations.
- Akermanite and gehlenite. Melilite crystals (solid solutions of akermanite and gehlenite) are needed for studies of oxygen diffusion. Data from such studies are required for constraining models that attempt to explain the correlated covariations in the $^{18}O/^{16}O$ and $^{17}O/^{16}O$ abundances in the anhydrous minerals found in high-temperature inclusions in meteorites. We have had moderate success in growing an akermanite crystal, although precipitates of a calcium-rich phase have complicated the process. Attempts to grow gehlenite crystals are under way.

Large-Volume, High-Pressure Apparatus for Geophysical Research

We have completed the design of a large-volume, split-cone apparatus capable of reaching pressures as high as 250 kbar and temperatures up to 2000°C. By increasing the upper pressure limit of high-pressure, high-temperature experiments, this apparatus can extend the depth to which we can model the composition, structure, and evolution of the earth.

Principal Investigators: F. J. Ryerson and L. L. Dibley

Experiments at moderately high pressures (up to 40 kbar) have provided an abundance of equilibrium and kinetic data that have been used to define the composition, mineralogy, and structure of the earth's lower crust and upper mantle. Our concepts of magma genesis and the evolution of the upper mantle and lower crust are largely constrained by these data. Such experiments rely on quenching and recovery of high-temperature and pressure run products for subsequent analysis. Over the past two decades, a number of institutions, predominantly in Japan, have successfully increased the applicable pressure range, extending the experimentally accessible depth to pressures appropriate to the earth's lower mantle (depths greater 600 km). The apparatus used in these experiments are known generically as multi-anvil sliding systems (MASS), which consist of a cascading pressure assembly of steel and tungsten carbide (WC) anvils driven by a large uniaxial press.

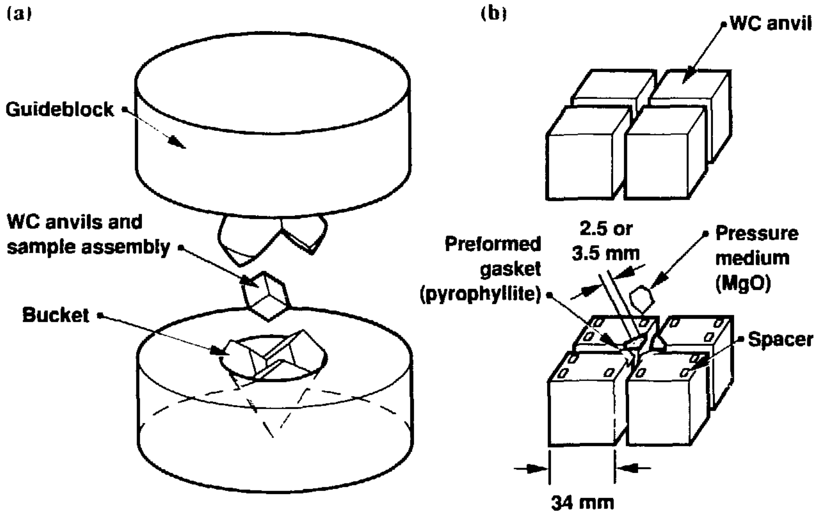

Figure 1. (a) Diagram of the LLNL split-cone multi-anvil sliding system, showing the guideblocks, buckets, and WC anvil sample/assembly; (b) schematic illustration of the pressure assembly.

In FY87, we received funding to investigate the feasibility of constructing a MASS that would be compatible with an existing 1200-ton uniaxial press at LLNL while still permitting access to the press by other apparatus. Having established that adapting our existing equipment was feasible, we received funding to design and fabricate the system in FY88.

The MASS design is based on a split-cone configuration in which six conical steel anvils or buckets are confined in steel guideblocks consisting of two interference-fit rings. This assembly forms the first stage of the pressure system (Figure 1a). The intersection of the upper and lower buckets forms a cubical volume containing the second stage, known as the pressure assembly (Figure 1b), consisting of eight WC anvils with triangular truncations at each corner. When placed together, the assembly of WC anvils has an octahedral volume at its center that accommodates the pressure medium and furnace sample assembly. The furnace sample assembly components are typically manufactured from ceramic materials that are chemically and structurally stable at high pressures and temperatures. The pressure medium and anvil dimensions can be tailored for the desired application and working pressure. The truncated corners of two of the anvils also provide the electrical contacts for the resistance-heated furnaces, typically made of $LaCrO_3$ or graphite.

We completed the design and drafting of plans for the MASS in December 1987. We also visited the high-pressure laboratory at the State University of New York (SUNY) at Stony Brook to investigate the materials and designs used in fabricating that furnace sample assembly. A number of local machine shops bid on the LLNL fabrication contract. Omnitec Corp. was chosen to fabricate the guideblocks, Accurate Machine Engineering the conical anvils, and Kennametal, Inc., the WC anvils; the ceramic materials required for furnace parts were procured from a number of Japanese ceramic manufacturers.

The system will be assembled next year in the 1200-ton press, and we will begin to experiment with various furnace/sample assemblies and the design of furnace power-supply and temperature-control systems. Because the pressure transmission in the MASS depends on mechanical properties of gasket materials extruded during compaction, the pressure scale must be established empirically for each assembly design. At room temperature, this is accomplished by calibrating the uniaxial press force against phase transitions in various metals. At higher temperatures, known (or at least agreed-upon) phase transitions in silicates can be used. This calibration procedure is expected to take at least half the fiscal year to accomplish. We will also make periodic visits to laboratories at SUNY-Stony Brook and the University of Alberta in Edmonton, Canada, to become more familiar with system operations.

Modeling Fluid Flow and Particle Transport in Porous Media

We are tackling the problems involved in modeling the hydrothermal flow and transport of reactive chemicals in porous media. This year, we developed a theory describing infiltration in partially saturated, fractured porous media. We also implemented several reactive-transport codes and began the development of a particle-based simulator for reactive-transport problems in porous media.

Principal Investigators: T. A. Buscheck, R. B. Knapp, J. J. Nitao, and A. F. B. Tompson

The Laboratory's research efforts in nuclear waste isolation, enhanced hydrocarbon recovery, geothermal energy, and groundwater contamination involve the flow of fluids and gases and the transport of reactive chemicals in a variety of complex subsurface environments, including fractured, heterogeneous porous media. Many of the relevant physical processes are interdependent and not yet adequately understood, requiring significant advances in our conceptual and numerical models.

We are working to identify, modify, and develop codes capable of predicting changes in fluid composition and mineral zonation as a fluid flows through and reacts with a porous media. The reactions of interest are irreversible dissolution and precipitation, equilibrium precipitation, adsorption, ion and isotope exchange, and radioactive decay; the transport processes of interest include advection, diffusion, and dispersion. This year, we modified a one-dimensional reactive-transport code MCCTM that has proved to be useful for simplified systems. We are continuing to refine the LLNL-developed EQ6 code for calculating water–rock interactions and to develop a general, finite-element flow and transport code as well as a particle-based simulator for modeling reactive transport in porous media.

LLNL enhancements to the TOUGH code (Preuss, 1985), together with the development of pre- and postprocessors, facilitated several modeling studies in FY88, including an investigation of infiltration in partially saturated, fractured porous media. The system was modeled as a semi-infinite set of parallel vertical fractures. We found that the movement of the infiltration front is governed by the interaction of gravity-dominated flow in the fractures and by capillary imbibition-dominated flow in the matrix. Figure 1 shows the liquid saturation distribution around a 50-µm fracture two days into the infiltration event. We conducted a parameter sensitivity study to identify fundamental relationships among various fracture and matrix properties. In particular,

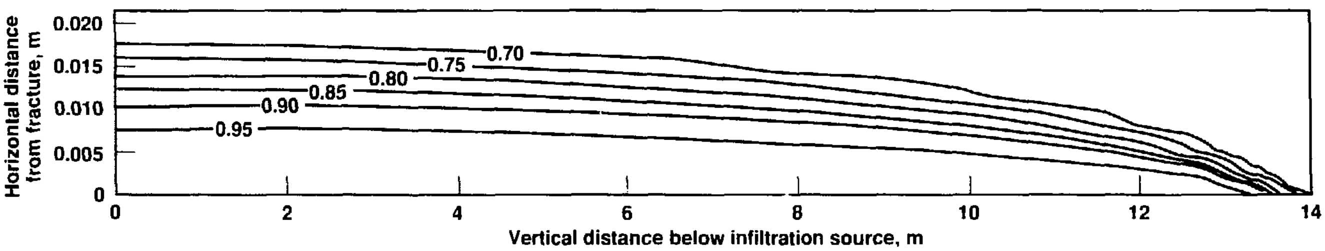

Figure 1. Liquid saturation distribution around a 50-µm fracture two days into the infiltration event. Contour values represent liquid saturation; initial saturation was 0.65. (To distinguish the contours, the distances on the y axis are exaggerated by a factor of 143 relative to the x axis.)

we found that for noninterfering fractures, the depth to which the infiltrating fluid penetrates the fracture varies as the one-half power of time ($t^{1/2}$) for sufficiently large times.

Starting with the class of problems addressed in the modeling study, we derived asymptotic expansions for a range of fracture inclinations, fracture spacings, and boundary conditions at the fracture entrance. A numerical solution to the integro-differential equation was also derived for all cases. Depending on the boundary conditions, the movement of the infiltration front can be shown to experience three to five distinct flow regimes characterized by physically interpretable time scales.

We initiated work on several reactive-transport codes during FY88. We implemented the one-dimensional code MCCTM (Lichtner, 1985) on LLNL computers and modified it to handle more general reactions and to be more computationally efficient in treating reaction fronts. LLNL's EQ6 code has been extensively used in modeling the reaction path of spatially static water–rock interactions. This year, we developed a version of this code (MPEQ6) to simulate one-dimensional, high-Peclet-number reactive transport in a Lagrangian reference frame. Modifications include the incorporation of stationary-state theory. Reaction fronts that develop in natural systems move at a slow rate relative to the transport and reaction rates. Steady-state concentration profiles develop upstream from a reaction front, and precipitation and dissolution rates can be linearly extrapolated for the duration of the stationary state (typically 10^4 years). Thus, we can model these systems with a time step of comparable magnitude, greatly accelerating our computations.

We are also developing a particle-based simulator for general problems of reactive transport in porous media. This simulator is an extension of an earlier particle-tracking solute transport code used to study the dispersion of contaminant plumes in a spatially heterogeneous flow field. Our extended model represents the mass of one or more aqueous chemical components as a large collection of particles, in much the same way as is done in particle-based plasma-dynamics simulators (Tompson and Dougherty, 1988; Tompson *et al.*, 1987). Particles are moved in space over discrete time increments by advective, diffusive, and dispersive forces. Particles can also be selectively removed or added after each time step to accommodate the loss or gain of component mass due to chemical reactions. Particle-based transport models can be extremely efficient in large three-dimensional problems, particularly those involving multiple components. Such models are well suited to parallel computer architectures, allowing for even further increases in computational efficiency.

In FY89, we will continue to develop our general, finite-element flow and transport code. We plan specifically to configure this code for problems in nuclear waste isolation and groundwater contamination. In addition, we will continue our analysis of infiltration in partially saturated, fractured porous media by addressing more complex fracture geometries and boundary conditions. We also plan to apply MPEQ6 and TOUGH to hypothetical nuclear-waste repository environments. We will continue our work on a geochemical reaction module for the particle-based simulator, and we will begin to develop a specialized reactive-transport simulator for fractured porous media.

References

Buscheck, T. A., and J. J. Nitao (1987). *Estimates for the Hydrologic Impact of Drilling Water on Core Samples Taken from Partially Saturated Densely Welded Tuff.* Lawrence Livermore National Laboratory, Report UCID-21294.

Lichtner, P. C. (1985). "Continuum Model for Simultaneous Chemical Reactions and Mass Transport in Hydrothermal Systems," Geochim. *Cosmochim. Acta* **49**, 779–800.

Preuss, K. (1985). *TOUGH User's Guide.* Lawrence Berkeley Laboratory, Berkeley, CA, Report LBL-20700.

Tompson, A. F. B., E. G. Vomvoris, and L. W. Gelhar (1987). *Numerical Simulation of Solute Transport in Randomly Heterogeneous Porous Media: Motivation, Model Development, and Applications,* Lawrence Livermore National Laboratory, Report UCID-21287.

Tompson, A. F. B., and D. E. Dougherty (1988). "On the Use of Particle Tracking Methods of Solute Transport in Porous Media," in *Computational Methods in Water Resources*, M. Celia *et al.*, Eds. (Elsevier, New York, NY).

FY88 $45,000

Measuring pH in Concentrated Electrolytes

Principal Investigators: K. G. Knauss, J. Bennett, T. J. Wolery, J. Harrar, and K. J. Jackson

We have demonstrated the feasibility of a new* in-situ *method for determining the hydrogen ion activity in high-ionic-strength solutions. The results suggest that our proposed operational definition of the measured pH based on high-ionic-strength standard solutions may be applicable in a manner roughly analogous to the IUPAC's recommended definition of pH in dilute solutions.

No method currently exists for directly measuring pH in brines. Although pH may be estimated indirectly by titration, direct measurement using National Bureau of Standards (NBS) conventional or modified procedures is hindered by both theoretical and experimental limitations. If established, a method for direct measurement would benefit energy programs, programs in nuclear waste isolation, and programs in chemistry and materials science that investigate the corrosion of materials in brines.

Our objective was to evaluate a proposed operational definition of measured pH based on high-ionic-strength standards. We used two pH scales: the NBS scale, intended for dilute solutions, and a so-called "rational" scale, which assumes that the hydrogen activity coefficient is 1 and which is more suitable for work in concentrated solutions. We measured the potential difference at 25°C between an H^+ ion-specific electrode (ISE) and both a Cl ISE and a Br ISE in a series of aqueous solutions designed to investigate:

- Nernstian behavior (using Nernst's Law for calculating potential) over a wide range of ionic strength.
- Potential glass electrode/cation interference from Na^+ and K^+.
- Response to H^+ at both low (pH 2) and high (pH 12) rational pH.
- Interchangeability of the HCl and HBr couples as a basis for the proposed method.

We used the Pitzer's equations option in the EQ3NR geochemical modeling code (Wolery, 1983) to calculate the composition of 84 standard solutions used in six series of experiments. Table 1 identifies the compositional range and pH spanned by the calculated standard solutions.

In addition to measuring the potential between the HCl and HBr couples, we measured the NBS pH in all solutions. Our results demonstrate that our proposed ISE method, which is free of liquid-junction problems, works very well, whereas the conventional NBS method fails in all cases above ionic strength of approximately 0.7. The response of the ISE couples is essentially Nernstian in all cases, and the goodness of fit is 0.999 or better. The electrode couples respond linearly to H^+ at both high and low pH activity over an extreme range in stoichiometric ionic strength.

Table 1. Calculated composition of standard solutions.

Electrolyte	Molal concentration	pH	Adjusted by calculation to fix pH
NaC	0.01–4.0	2	HCl
KCl	0.01–3.0	2	HCl
KBr	0.01–3.0	2	HCl
NaCl	0.01–4.0	12	NaOH
KCl	0.01–3.0	12	KOH
KBr	0.01–2.0	12	KOH

Reference

Wolery, T. J. (1983). *EQ3NR, A Computer Program for Geochemical Aqueous Speciation-Solubility Calculations: User's Guide and Documentation*, Lawrence Livermore National Laboratory, Report UCRL-53414.

FY88: $100,000

In-Situ Downhole Measurements

Principal Investigators: S. M. Angel, H. M. Buettner, and P. W. Kasameyer

To understand the* in-situ *conditions in the earth's crust, we must be able to determine the properties of fluids from deep boreholes without changing their chemical state. We are developing candidate optical chemical sensors (optrodes) for an optical-fiber system to measure fluid properties and composition in hot, corrosive wells.

The inability to sample or measure the chemical composition of brines in hot wells limits our understanding of *in-situ* conditions in the earth's crust. Our objective is to develop optical-fiber systems that can expand this capability to temperatures and depths where *in-situ* sampling methods usually fail. In this project, we have identified a number of approaches that use solid-ceramic-matrix and thin-film-matrix materials to produce candidate optical-fiber sensors that will survive in hot, deep wells.

Optrodes are optical transducers placed at the distal end of optical fibers. They produce a signal, usually fluorescence, in response to the parameter being measured. Optrodes have already proven useful at LLNL for remote *in-situ* monitoring of a variety of chemical species and of pH in groundwater. In previous years, we developed a temperature optrode based on a rare-earth-doped, porous ceramic material. This optrode has been successfully tested in a geothermal steam well to a depth of about 150 m (Angel, 1987; Angel *et al.*, 1989). The results obtained during these tests indicated that wells up to 1 km deep can be logged in real time using this device.

We were previously unsuccessful in developing a pH sensor using porous ceramic materials. However, this year we have successfully demonstrated several candidate pH and Eh optrode materials based on an inert polymer electrolyte (Nafion). Although the polymer is stable only to about 250°C, it immobilizes many pH- and Eh-sensitive fluorescent and highly colored dopants. The pH optrode demonstrates a reversible response over a pH range of 1.5 to 10 and has been shown to be stable up to 180°C. Measurements can be made either by absorption or fluorescence.

We checked the pH responses of the doped polymer films by immersing the films in a variety of buffered solutions for at least 15 minutes and then measuring the absorption spectra. We determined stability by heating the films in 180°C water for 24 hours. The fluorescence response was measured at room temperature using a short optical fiber. Figure 1 shows the fluorescence intensity of a Nafion-based pH optrode upon exposure to NH_4OH vapor compared to the fluorescence response in air. These pH optrodes are also sensitive to Eh changes in solution. A number of stable dopants show reversible Eh response in the Nafion films at positive potentials.

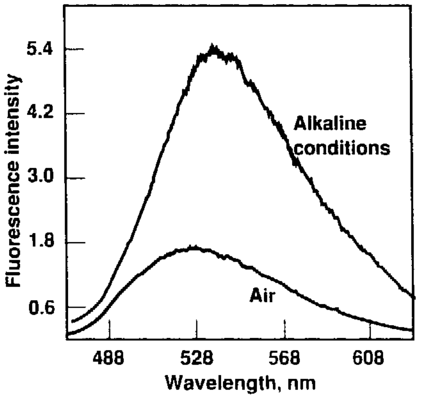

Figure 1. Fluorescence response of a Nafion-based, high-temperature pH optrode in air and under alkaline conditions (exposed to NH_4OH vapor).

Before this measurement approach can be applied in the field, specific optrode designs must be carefully calibrated in a number of solutions to determine whether they are sensitive to more than one property. In addition, our proposed cable termination and protection methods must be tested with a prototype measurement system that can be taken to the field. The system will also have to be operated in wells where adverse conditions exist to demonstrate that optical-fiber systems can indeed provide useful *in-situ* measurements at depth.

References

Angel, S. M. (1987), "Development of Fiber-Optics Sensors for Temperature Measurement and Chemical Analysis in Geothermal Wells," *Transactions, Geothermal Resources Council* **11**, 155.

Angel, S. M., D. G. Garvis, S. K. Sharma, and A. Seki (1989), "Field Applications of Fiber-Optic Sensors: I. Temperature Measurements in a Geothermal Well," *Appl. Spectrosc.* **43** (in press).

Seismological and Geochemical Studies in Northern California

Principal Investigators: G. Zandt and W. E. Glassley

We are combining geochemical and seismological methods to study a unique tectonic regime in northern California where crust and upper mantle interactions are currently generating an active volcanic field with an associated geothermal area. Knowledge about the way heat, fluids, and magma are transported through the continental crust has important implications for both basic and applied science.

The relative motions of three tectonic plates at the Mendocino Triple Junction in northern California (at the juncture of the San Andreas Fault, the Mendocino Fracture Zone, and the Gorda Subduction Zone; see Figure 1) have created an unusual zone of interaction between the crust and upper mantle. As a geometric consequence of the relative plate motions in this region, the California coastal area southeast of the Triple Junction is progressively exposed to hot, upwelling mantle. This upwelling, together with its interaction with the overlying continental crust, is ultimately responsible for several Coast Range volcanic fields, for the Plio-Pleistocene uplift of the Coast Range, and for ongoing seismicity, crustal deformation, and the evolution of ore bodies and geothermal fields in coastal northern California.

We are using seismological and geochemical techniques in this unique tectonic setting to develop and test competing hypotheses on crust-mantle interactions and crustal accretion. We have completed reconnaissance field work at the Clear Lake volcanic field, where we collected a suite of crustal xenoliths and deployed a portable broadband seismograph. Field evidence indicates that the xenoliths are from different eruptive phases, implying that different segments of the crust were sampled. The xenoliths appear to form two distinctive suites, one from a lower crustal suite of gneisses and schists and one from a more mafic suite that may be related to earlier phases of magmatic intrusions. Preliminary results from several gneissic xenoliths indicate that these rocks experienced a complex recrystallization history that is related, at least in part, to decompression. By reaction textures, we recorded recrystallization events in the samples at 18–35 km (lower crust) and at 12–15 km (mid-crustal depths).

To reconstruct the geometry and evolution of the San Andreas Fault zone (Furlong *et al.*, 1988), we mapped crustal and upper mantle heterogeneity by combining teleseismic imaging techniques with thermal-mechanical modeling studies. The results indicate that the surface trace of the fault is offset from a deeper plate boundary parallel to the surface trace but approximately 50 km to the northeast. The deeper boundary appears to form the southwestern boundary of a zone of "warm" mantle and to control the location of young volcanism at Clear Lake. Teleseismic earthquakes recorded at our broadband station at Clear Lake have anomalously large amplitudes on the horizontal components, similar to teleseisms recorded in Long Valley Caldera, supporting the idea that the observed complexity may be due to magmatic structures associated with the Clear Lake magma chamber.

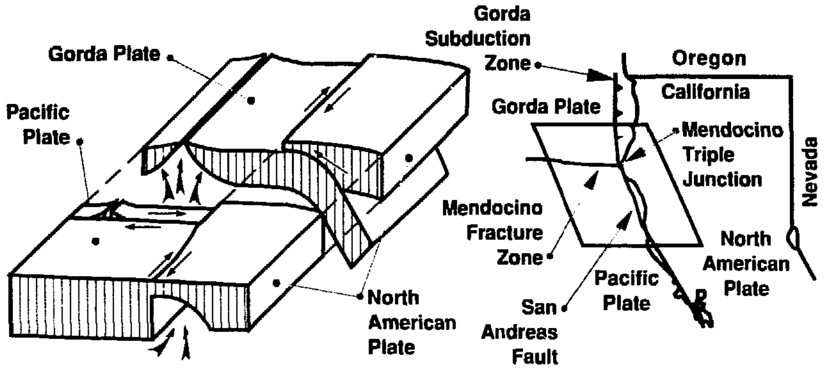

Figure 1. Tectonic plate interactions near Mendocino Triple Junction in northern California. Thin arrows indicate relative plate motions; thick arrows indicate upwelling of "warm" mantle.

Reference

Furlong, K. P., W. D. Hugo, and G. Zandt (1988), "Geometry and Evolution of the San Andreas Fault Zone in Northern California," *J. Geophys. Res.* **94** (in press).

Incorporating Equation-of-State Models in DYNA2D

Principal Investigator: L. A. Glenn

We improved our capability to numerically simulate underground nuclear explosions by incorporating a more flexible and accurate equation-of-state (EOS) model into the DYNA2D code. These improved simulations are essential for ensuring complete containment of underground nuclear tests.

Valid equations of state (EOSs) for rocks of arbitrary consistency are required for numerical simulations of underground nuclear explosions. Last year, we incorporated an EOS model into the DYNA2D code that has greater flexibility and accuracy than the Butkovich rock gas model used in the TENSOR code (which assumes that all rocks are combinations exclusively of silicate, carbonate, water, and air). The Butkovich pressure-density gas tables that are generated are also very sparse, so that large and potentially inaccurate interpolations and extrapolations are required to obtain pressure and energy data. Furthermore, the absence of energy considerations in the Butkovich gas tables is thermodynamically inconsistent.

The DYNA2D model has no restrictions on rock composition, however, and it yields a pressure-density-energy table that is thermodynamically consistent and dense enough to allow reliable interpolations. In developing an EOS table for an arbitrary rock composition, we first generate pressure and energy isotherms using the HQEOS code. These isotherms are then combined to obtain a pressure-density-energy table, the required form of the EOS for DYNA2D. No more than two days are usually required for this process.

We also improved the TENSOR mixture model within DYNA2D. Historically, the TENSOR code addressed the vaporization of nonporous rocks by mixing the Hugoniot with release adiabat tables (which spanned only the gas states of the material) and used the ratio of peak pressure to vaporization pressure as a parameter to interpolate linearly between the Hugoniot and the gas phase. In our adaptation of the TENSOR model, we replaced the release adiabats with the HQEOS tables.

The effect of mixing the Hugoniot with the HQEOS has been evaluated. Figure 1 shows SiO_2 vaporization response as pressure-time histories and energy-density paths, using HQEOS tables alone and using the Hugoniot mixed with the HQEOS tables. Each plot shows two identical pressurization-release curves, indicating that mixing the Hugoniot with the HQEOS tables does not alter the SiO_2 vaporization response obtained by using the HQEOS tables alone. With a three-phase EOS now quickly available for rocks of arbitrary composition, it is no longer necessary to mix the Hugoniot with a gas table in simulating the vaporization of nonporous rocks, as was previously done in TENSOR. The same level of accuracy is provided in less computer time.

Reference

Attia, A. V., and D. A. Young (1988). *Comparison of Two Rock Vaporization Models in DYNA2D*. Lawrence Livermore National Laboratory, Preprint UCRL-99714; presented at *Nuclear Explosives Code Developers Conference*, Boulder, CO, October 11–14.

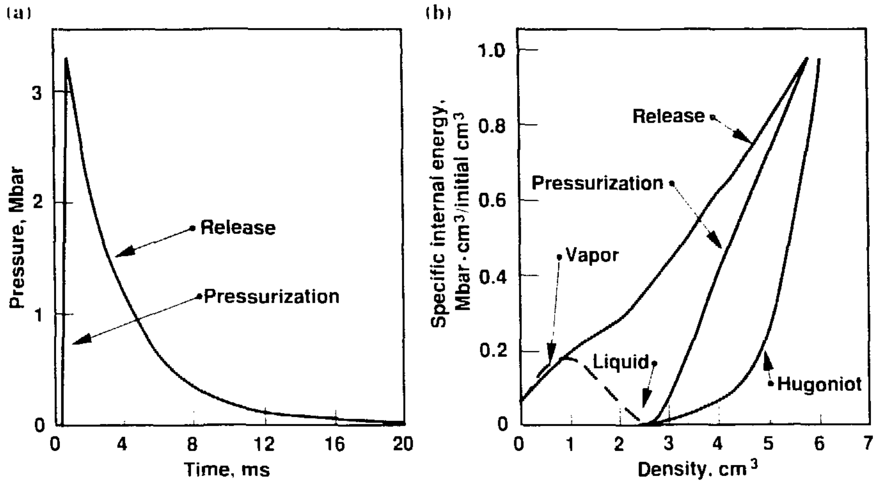

Figure 1. SiO_2 vaporization response, shown as (a) pressure-time histories and (b) energy-density paths. Pressurization-release curve in each plot represents two identical curves, calculations using HQEOS alone and using both the Hugoniot and HQEOS.

Engineering

E. A. Lafranchi

An important mission of the Engineering Department is to identify and develop the emerging technologies that will be needed to meet the future requirements of LLNL programs. Results of the research projects funded by the IR&D Program in FY88 will find immediate application in the Laboratory's weapons, laser, beam research, and precision engineering programs. In addition, since principal investigators often collaborate with scientists at universities, industrial technology centers, and other laboratories, these IR&D projects markedly increase and enhance the spectrum of engineering resources available to LLNL.

The engineering projects funded in FY88 address the need to understand the behavior of materials. In one project, we investigated the breakdown of surfaces subjected to electric and electromagnetic fields and sought to understand the basic physical properties of materials that make them susceptible to surface breakdown. In FY88, we began the development of an experimentally validated model of such surfaces with the study of solid-plasma transitions and bounded plasmas. Our goal is to develop a validated calculational model that can be used to predict surface behavior under large transient fields. This understanding, coupled with a validated model, will have a significant effect on all pulsed-power and high-power-microwave research.

In another project, we studied the ductile grinding of brittle materials, concentrating on the material removal process. The goal of this research is to be able to fabricate components with high precision and excellent surface finish but without subsurface defects. This project requires the integration of theory and experiment as we work to develop a numerical model of the material properties that are dependent on chemical composition and material temperature. This model will help us to understand the transition between ductile and brittle grinding of a material. We have tested the hypothesis that ductile grinding can occur in the region between the yield and fracture envelopes of the material in question. So far, we have only collected preliminary data, and further analysis is required. Once we are satisfied with the validity of our theory, we will need to develop a grinding capability to determine if our theory can be achieved experimentally. Success in this project will have a major impact on the Laboratory's weapons and laser research programs.

The Engineering Department received $498,000 in IR&D funds in FY88.

Surface Breakdown Induced by Large Transient Fields

We are developing experimentally validated, realistic models of the behavior of surfaces when they are subjected to large transient electric, magnetic, or electromagnetic fields. These models are needed because breakdown under such fields is one of the main limiters of pulsed-power and high-power microwave systems.

Principal Investigators: R. Ziolkowski, S. Ray, A. Friedman, and E. Morse*

*University of California, Berkeley

Pulsed-power and high-power microwave sources are used in several important Laboratory programs, and a number of new microwave, laser, accelerator, and simulator concepts are being investigated. A severe obstacle to realizing the full potential of these concepts is the problem of breakdown of the component surfaces. The available information on the behavior of surfaces under large transient electric, magnetic, and/or electromagnetic fields is empirically based and only minimally understood, and existing models of surface breakdown are crude and based on gross dynamical effects. A thorough investigation of field emission and vacuum breakdown and dielectric/insulator breakdown would greatly increase the available database. Several Laboratory and national programs have a need, both current and long-term, for the information that would be gained.

The goal of this project is to investigate, both theoretically (through analysis and computations) and experimentally, the breakdown of surfaces induced by large transient electrical, magnetic, and/or electromagnetic fields. The end product of this work will be a numerical model of surface breakdown with predictive capabilities and the experimental data to confirm it.

In FY88, we studied solid-plasma phase transitions and bounded plasmas using several approaches. These included non-LTE (nonlocal thermodynamic equilibrium), NLGO (nonlinear geometrical optics), and advanced PIC (particle-in-cell) calculations, as well as bounded plasma modeling and multiscale methods. Our objective was to extend current methods and models to more realistic systems than has previously been possible.

Progress was made in several areas. We implemented a variation of the Hunter-Keller NLGO approach (Hunter and Keller, 1983) to describe the interaction of intense microwave fields with nonlinear media. We also constructed a model of the response of a compact toroidal plasma to an intense microwave pulse. The plasma model has a quadratic nonlinearity that is characteristic of many other bounded plasma systems. Combining this model with the NLGO approach, we have begun to study the heating of compact toroidal plasmas (Morse and Ziolkowski, 1988).

Also for bounded plasmas, we developed a new implicit method for analyzing systems with boundaries (Parker *et al.*, 1987). A simple particle injection/absorption model was included that is consistent with the implicit particle advance. An implicit multiscale method was also developed that allows time steps of different sizes to be used in different parts of the plasma (Friedman *et al.*, 1987a, 1987b, 1988). This method makes the calculation considerably more efficient. Quiescent portions of the plasma can be treated with a coarser time resolution and turbulent portions with a finer resolution, allowing computational effort to be spent only where it is needed. Work is under way to merge the bounded implicit and multiscale implicit methods.

Progress is also being made in the development of multiscale methods that vary the spatial grid as well as the time step size. Although we have demonstrated the potential effectiveness of the multiscale implicit PIC method, we have also identified a number of difficulties with the original algorithm. In particular, the particle mover has a number of unexpected sensitivities; we are actively characterizing these in order to alleviate or eliminate them.

In FY89, we will closely couple our theoretical work with experimental efforts. Specifically, we will focus on the breakdown of dielectric surfaces induced by large transient voltages and microwave fields, with characteristic frequencies ranging from quasi-static to microwave. Analytical and numerical techniques similar to those needed for this work have already been developed for gaseous media and verified against experiment (Figure 1). New modeling tools will be developed to compliment and guide the experimental measurements, and experiments will be designed to provide the requisite inputs (such as rate coefficients) to test the models under development. As our modeling capability develops, we will move to progressively more complex environments within the basic configurations. This combined theoretical and experimental program will allow a systematic evaluation of the factors that lead to surface breakdown.

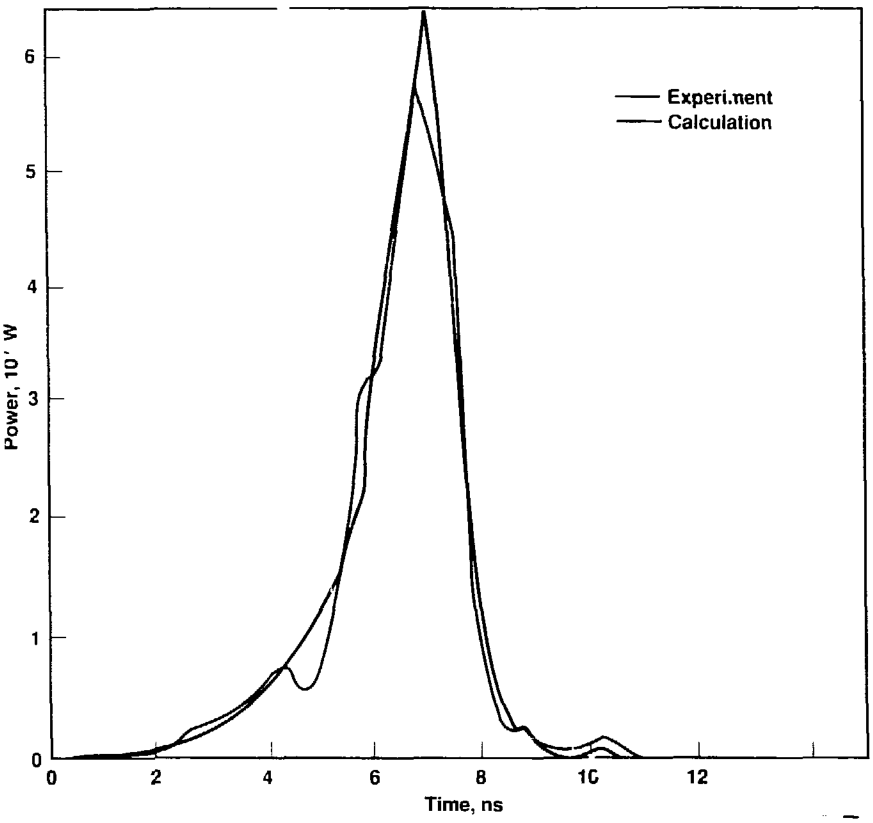

Figure 1. Breakdown of air (300 Torr) in a rectangular waveguide (3.34 × 4 × 7.1 cm) induced by a high-power microwave pulse (75 MW, 15 ns, 2.85 GHz). The results generated by a self-consistent, two-dimensional model based on Maxwell's equations and a fluid model of the resulting electron plasma agree very well with the experimental results. Similar modeling techniques and codes will be used in next year's studies of the initiation and evolution of breakdown on surfaces.

References

Friedman, A., S. L. Ray, C. K. Birdsall, and S. E. Parker (1987a). "Particle-in-Cell Plasma Simulation with a Wide Range of Space and Time Scales," *Proc. 12th Conf. on Numerical Simulation of Plasma* (San Francisco, CA), paper CW-6.

Friedman, A., S. L. Ray, S. E. Parker, and C. K. Birdsall (1987b). "Prospects for Multi-Scale Particle-in-Cell Simulation of Plasmas," *Bull. Amer. Phys. Soc. Division of Plasma Physics, 29th Annual Meeting* (San Diego, CA).

Friedman, A., S. L. Ray, C. K. Birdsall, and S. E. Parker (1988). "Multi-Scale Particle-in-Cell Plasma Simulation: Timestep Control and Some Tests," *Abstracts of IEEE Intl. Conf. on Plasma Science Conf.* (Seattle, WA), p. 119.

Hunter, J. K., and J. B. Keller (1983). *Comm. Pure Appl. Math.* **36**, 547–569.

Morse, E. C., and R. W. Ziolkowski (1988). "Transient Microwave Heating of Compact Toroidal Plasmas," *Fusion Tech.* **14** (3), 1325–1333.

Parker, S. E., C. K. Birdsall, A. Friedman, and S. L. Ray, (1987). "Direct Implicit Simulation of a Bounded Plasma System," *Bull. Amer. Phys. Soc. Division of Plasma Physics, 29th Annual Meeting* (San Diego, CA).

Ductile Grinding of Brittle Materials

Principal Investigator: K. L. Blaedel
Co-Investigators: P. Davis and J. Franse*

*Philips Research Laboratories, Eindhoven, The Netherlands

We are investigating grinding as a material removal process so that we will be able to cost-effectively fabricate workpieces made from brittle materials. Our effort involves both numerical simulation of the process and grinding experiments as we attempt to determine whether material removal occurs by crack propagation into the material or by plastic flow of the material.

Our objectives are to understand theoretically the grinding of brittle materials and to develop a grinding process that removes brittle material in a ductile fashion. In pursuit of these goals, we must acquire the capability to perform ductile grinding for modestly sized glass and ceramic workpieces. Our efforts in FY88 have focused on developing a mechanical model for the transition from brittle to ductile material removal in precision grinding and on devising the machinery and techniques to grind brittle materials.

Previous successful attempts to grind various brittle materials in a ductile manner, both at low and high grinding speeds, indicate that mechanical properties of the material, rather than chemical or thermal effects, predominantly determine the transition between ductile and brittle material removal. Thus, to improve our precision-grinding capabilities, we must develop a mechanical model (in which mechanical properties may be temperature- or chemistry-dependent) for the transition from brittle to ductile behavior. Most needed is a criterion to distinguish the stress states in the material that result in ductile behavior from those that result in crack initiation (brittle behavior).

By reviewing the deformation and fracture patterns in glass under sharp and blunt indenters, we were able to develop such a criterion (Franse and Blaedel, 1988). Sharp indenters cause significant plastic deformation, whereas blunt indenters cause mostly elastic deformation up to the point where crack initiation begins. Our criterion incorporates a region in stress space within which no plastic deformation occurs and outside of which plastic flow takes place; the von Mises criterion (Dieter, 1986) was chosen as an appropriate condition for plastic flow in normal glass materials. Our criterion also includes a region within which cracking occurs and outside of which cracks initiate and propagate. Figure 1 diagrams the yield and fracture regions in principal stress space. We hypothesize that ductile material removal can occur between the umbrella-shaped fracture boundary and the cylindrical yield boundary.

We tested this hypothesis using analytical elastic solutions for the stress distribution under various indenters, both blunt and sharp, and found that our criterion correctly predicts the trends observed in indentation tests. The next step will be to perform finite-element-modeling stress analyses for particular indenters and to corroborate experimentally the criterion for a specific set of brittle

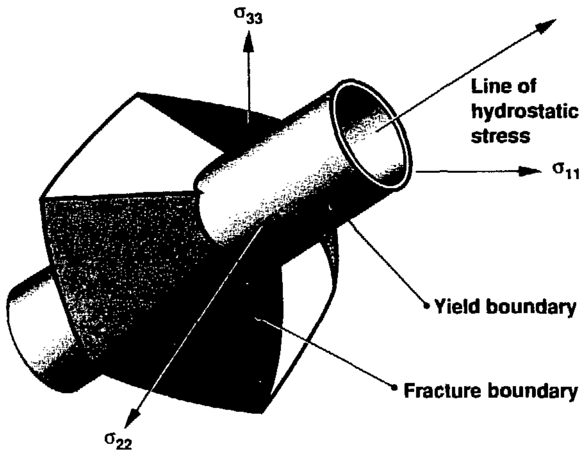

Figure 1. The three-dimensional fracture and the yield criteria in principal stress space.

(a) Top view

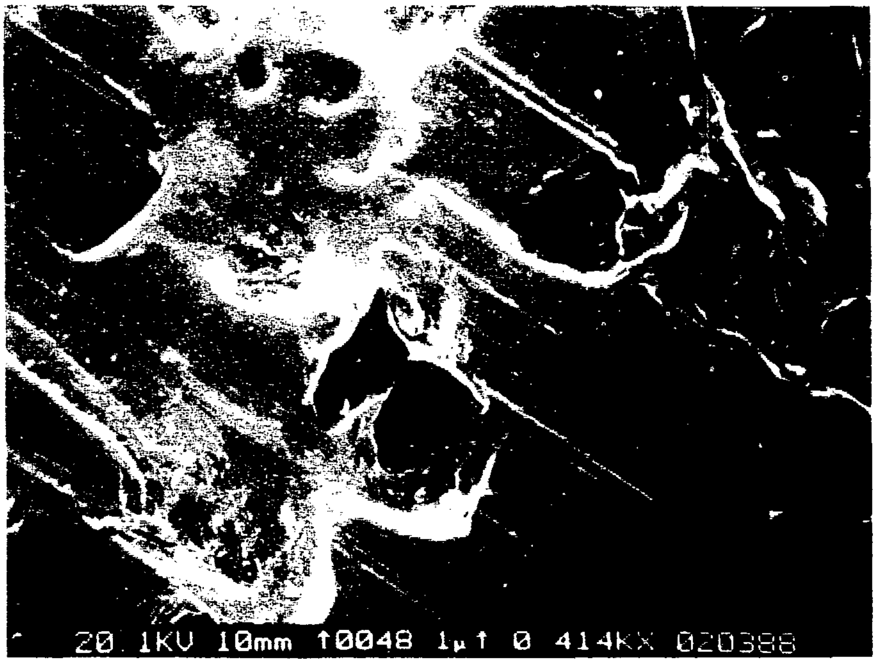

(b) Side view

Figure 2. Top (a) and side (b) views of a precision grinding wheel prepared in such a way that the diamond grits (three dark patches in (a)) protrude uniformly.

[illegible]

W[illegible] dis[illegible] part [illegible] materials [illegible] of the [illegible] techniques. Re[illegible] concentrated [illegible] methods to dress and true the grinding wheel.

Conventional techniques for preparing the surface of a diamond impregnated grinding wheel (i.e., "dressing") leave sharp points of diamond grit exposed at nonuniform heights. From the point of view of the workpiece, each grit that passes by takes a different depth of cut and has a different [illegible]. As a result, some particles remove material in a brittle fashion, thereby causing damage deep into the surface.

An alternative method of dressing the grinding wheel was sought that would leave the grits at a uniform height so that each would take about the same depth of cut. Previous experience of other researchers indicated that fracturing off pieces of the grits was not an appropriate way of dressing the wheel. Hence, we explored several methods to cause the diamond grits to wear down to a uniform height by attrition. The techniques we investigated included using loose abrasive while grinding a sacrificial workpiece and grinding materials known to cause catastrophic wear of diamonds, such as [illegible] carbon steel. Figure 2 shows the grinding wheel surface we were able to produce. The flat topped diamond grits (the dark [illegible] in Figure 2a) [illegible]

For precision grinding, it is imperative that the rotating grinding wheel be as perfectly balanced as possible. The traditional method of balancing grinding wheels uses accelerometers to sense acceleration of the stator and thereby determine the magnitude and location of the imbalance; this method is suitable if the stator is somewhat compliantly mounted on the machine. However, new precision-grinding machines are much more rigid and thus the acceleration of the stator is much less detectable. Therefore, instead of accelerometers, we use displacement transducers located in the gap between the air-bearing spindle rotor and the stator (the most compliant link in the precision grinding machine's structurual loop). We extract the imbalance force from the displacement measurements to balance our grinding wheels more perfectly and thereby achieve a more uniform depth of cut.

The product of our grinding effort is illustrated in Figure 3. This piece of phosphate glass was ground on a computer-controlled machine here at LLNL. It has a very smooth surface of 2.5 nm rms as measured by a WYKO profilometer (with a 20× objective) and 7.5 nm rms as measured by a Talystep profilometer (with a 2.5 µm-radius stylus). The surface finish, however, is not the most important measure of surface quality. We must also consider the extent of damage below the surface.

Determining how damage occurs beneath the surface of a precision-ground workpiece is a topic of our FY89 IR&D proposal. In particular, next year, we will:

- Continue to refine the machinery and techniques required to grind brittle materials in a ductile fashion, with further emphasis on preparing the diamond abrasive (i.e., dressing the grinding wheel).
- Evaluate the surfaces ground by the machinery and use the techniques developed above to assess damage beneath the surface resulting from the grinding process.
- Validate the material failure criterion developed in FY88 through indentation tests.
- Extend the modeling from two to three dimensions, progressing from simulating the indentation of a static diamond grit into the surface of a workpiece to modeling a diamond grit sliding across the workpiece surface. The addition of sliding will give us a more realistic model of the actual process of grinding.

Figure 3. This 5-cm-diam phosphate-glass component was fabricated using our new ductile-grinding techniques. Its has a very smooth surface, measuring between 2.5 and 7.5 nm rms, depending on the type of profilometer used.

References

Dieter, G. E. (1986). *Mechanical Metallurgy* (McGraw-Hill, NY), 3rd ed., pp. 77–78.

Franse, J., and K. L. Blaedel, (1988) "Mechanical Model for the Transition from Ductile to Brittle Material Removal in Precision Grinding," presented at the *ASPE Conference*, Atlanta, GA, October 24

Membership in the NCSU Precision Engineering Center

Principal Investigators: **L. F. Stowers and E. R. McClure**

As members of the Precision Engineering Center at North Carolina State University (NCSU, Raleigh), we have access to the results of their research projects, many of which are similar or related to Laboratory efforts in precision engineering.

High-technology products have been one of the mainstays of the U.S. balance of trade, but lately there has been a drop in demand for these goods as a result of competition from other countries. To reverse this slump, American companies must concentrate on developing new products, boosting productivity, and improving manufacturing processes.

The Laboratory is addressing this need with its Precision Engineering Program. To augment our efforts, we have become members of the NCSU Precision Engineering Center, a multidisciplinary research and graduate program established to provide the new technologies needed by America's high-technology institutions. As members, we have access to and use of the results of their research projects, many of which parallel our precision engineering efforts at LLNL. In FY88, the Precision Engineering Center supported 11 major projects (details are contained in the Center's 1988 annual report):

- Diamond turning of amorphous polymers. The cutting characteristics of polycarbonate, Plexiglas, and polystyrene are being investigated. The surface cutting speed greatly influences the temperature at the cutting tool tip and, correspondingly, the deformation of the polymer.
- Ductile-regime turning of silicon and germanium. A critical chip thickness has been identified for the machining of silicon and germanium. Cutting is ductile (not brittle) if the chip thickness is maintained below this critical thickness.
- Residual stress in machined surfaces. A micro-Raman spectrometric technique has been developed to measure directly the residual stress resulting from cutting.
- Modeling the metal cutting process. A fracture-mechanics model is being incorporated into a eight-node, isoparametric, singularity element to permit simulation of the singularity at the tip of a cutting tool during modeling of the metal cutting process.
- Dynamics of single-point diamond cutting. The cutting tool forces associated with diamond turning are being measured to aid in the development of a numerical model for the servo control system of diamond-turning machines.
- Machining of asymmetric optical surfaces. A high-speed servo controller is being developed for a grinding machine that will be used to fabricate asymmetrically shaped optical surfaces. The controller uses capacitance gauges to sense cutter position and piezoelectric crystals to accurately change the position of the cutter relative to the sample being machined.
- Generic controller for diamond-turning machines. A generic machine-tool controller is being designed and built to control a Rank Pneumo diamond-turning machine recently acquired by the Precision Engineering Center.
- Multiprocessor system for high-speed control. A real-time, multiprocessor, machine-tool controller has been designed and is nearing completion. This controller uses several TI-TMS320C25 processors to control multiple axes of a machine tool at high speed.
- Focused-ion-beam micromachining. An ultrahigh-vacuum subsystem for a focused-ion-beam micromachining system is under construction.
- Elastic emission machining. Work is continuing on a rotary polishing technology, first developed in Japan, that offers great promise for polishing arbitrary contours with nanometer accuracy.
- Design of a scanning tunneling microscope. A scanning tunneling microscope (STM) with a large, 4 × 4-μm scanning range has been designed and constructed. The STM is coupled to a microcomputer-based data-acquisition system for image processing of the data.

Nuclear Chemistry

D. A. Leich

The primary mission of the Nuclear Chemistry Division is to provide diagnostic information on the performance of nuclear explosive devices through the use of radiochemical and isotopic techniques. We combine chemical and physical disciplines, including inorganic and physical chemistry, geochemistry, radiochemistry, and nuclear physics, with such technologies as radiation detection, isotope mass spectrometry, and data analysis. The resulting expertise is applied to meet the needs of Laboratory programs, notably Nuclear Test, Nuclear Waste Management, Treaty Verification, Safeguards Technology, Environmental Protection, and Laser Isotope Separation. As new programs develop, we respond by developing new applications of nuclear science and technology.

Through IR&D-sponsored fundamental research in nuclear science and related disciplines, we build the scientific and technical leadership needed to contribute most effectively to Laboratory programs. With the IR&D support received in FY88, we completed three projects and began the experimental-measurements stage in two others that will continue into FY89.

One of the completed projects was a three-part exploration of new techniques for measuring isotope ratios. One part involved the development of general isotope-ratio measurement capabilities by inductively coupled plasma mass spectrometry (ICP-MS); this investigation is nearly complete, and further developments for specific applications will be supported by Laboratory programs. We also completed the development of techniques for *in situ* oxygen isotopic analyses by secondary ion mass spectrometry (SIMS). In the accelerator mass spectrometry (AMS) part of this project, we used the accelerator at the University of Rochester to develop and test procedures for making AMS measurements of ^{36}Cl and ^{129}I. These experiments have helped to spark widespread interest in AMS at the Laboratory and have contributed to the establishment of a new Center for Accelerator Mass Spectrometry at LLNL.

Our IR&D-sponsored cosmochemistry research was also concluded in FY88. We completed our determination of the ^{187}Re half-life. Our studies of titanium isotopic anomalies in meteorites have led to some interesting conclusions and speculations about chemical and physical processes in the early solar system.

In the ultrasensitive laser spectroscopy project, we completed a two-year evaluation of photothermal spectroscopy techniques for measuring actinide solution speciation. We achieved comparable sensitivities at the submicromolar level for three different photothermal techniques. The technique for a given application may therefore be chosen on the basis of less critical technical criteria.

Also this year, we completed the assembly of a major experiment to measure the mass of the electron antineutrino. This experiment uses a gaseous atomic tritium source to eliminate all known systematic problems associated with the solid-state interactions of the tritium beta-decay process. In FY89, we will finish testing and calibrating the high-resolution magnetic spectrometer and will begin measuring tritium.

During FY88, we also completed the instrumentation for a study of the thermodynamic properties of the actinide elements. We developed and tested a photoacoustic spectrometer for submicromolar detection of the various oxidation states of uranium, neptunium, plutonium, and americium. We also constructed a variable-temperature calorimeter for measuring actinide complexation enthalpies. Thermodynamic investigations using these capabilities will begin next year.

In FY88, the Nuclear Chemistry Division received $750,000 in IR&D funds.

FY88 $124,000

New Techniques for Measuring Isotopic Ratios

Principal Investigators: G. P. Russ, III, and R. C. Finkel
Co-Investigators: D. L. Phinney, K. D. McKeegan, J. M. Bazan, and M. W. Caffee

By the end of this year, we will have demonstrated the isotopic analysis capabilities of two new techniques for high-sensitivity measurements of isotopic ratios in very small samples: inductively coupled plasma mass spectrometry (ICP-MS), and secondary ion mass spectrometry (SIMS). Design and construction of a third technique, accelerator mass spectrometry (AMS), is continuing.

The objectives of this project were to explore ways to increase the sensitivity of ICP-MS for both multielement and isotopic analysis, to develop ion source and detection systems for AMS using LLNL's tandem Van de Graaff accelerator, and to develop SIMS methods for measuring oxygen isotope ratios in solids.

As a result of changes made to the instrument, our ICP-MS is now roughly ten times more sensitive than standard commercial instruments. For many elements in solution, the limit of detection is now in the range of one part per trillion (pptr). Using 1 to 10 ml of solution, we can now determine the concentrations of two-thirds of the elements in the periodic table if they are present in concentrations of 1 ppm to 1 pptr. The enhanced sensitivity of our instrument also reduces the amount of sample required for analysis. For example, we are now using ICP-MS to measure the isotopic composition of uranium in environmental monitoring samples as small as 4 ng. This task was formerly done by thermal ionization mass spectrometry (TIMS). Although TIMS still has better sensitivity than ICP-MS for this particular element, ICP-MS analysis is much faster and requires substantially less sample preparation. We are exploring new sample inlet systems that will allow us to make isotopic analyses on a variety of elements using less than 1 ng of sample.

Until this year, our SIMS instrument could not be tuned accurately and reproducibly enough at the high-mass-resolving power required for isotopic analysis of trace elements. With a specially designed, dual-microchannel plate now in operation, the detector gain on the SIMS instrument has been increased by a factor of 1000. We have completed preparations for oxygen isotope measurements with SIMS at natural levels of ^{17}O (0.04%) and ^{18}O (0.2%). These preparations included improving the tuning in the primary column for the cesium-sputtering source, writing extensive data acquisition and reduction software, and collecting, curating, and preparing samples of oxygen isotope standards.

We have designed the data collection instrumentation for LLNL's AMS and have begun construction of the multiplate gas-ionization detector that we will use for isotope detection. We plan to test the detector and gas control system by the end of 1988. In the interim, we have continued to use the AMS at the University of Rochester, New York, for pilot studies in two areas:

- We have extended our previous work on ^{129}I in groundwater from the Nevada Test Site to include ^{36}Cl, which we have now measured in samples taken near the sites of the Cambric and Cheshire events.
- We have begun analyzing ^{36}Cl in samples of building materials from Hiroshima to determine the neutron dose associated with the Hiroshima atomic bomb. The major uncertainty in the dosimetry for Hiroshima and Nagasaki survivors is the neutron dose. Therefore, we plan to use ^{36}Cl that was produced by neutron activation in building materials to redetermine the neutron doses at Hiroshima and Nagasaki. Because of the low concentrations present, AMS is the only suitable detection technique for determining this isotope. We have measured ^{36}Cl in one roof tile from Hiroshima and we will extend this work to a suite of samples collected in Hiroshima and Nagasaki.

No IR&D funding is requested for FY89. Further development of the ICP-MS and SIMS techniques for specific applications will be supported by Laboratory programs. Continued development of AMS techniques is planned as a new Director's Initiative, with specific aspects also included in a new Nuclear Chemistry proposal.

References

Bazan, J. M., G. F. Hunt, and G. P. Russ (1988). "Isotope Ratio Measurement of Nanogram Sized Samples Using ICP-MS," presented at *First Intl. Conf. on Plasma Source Spectrometry*, University of Durham, England (September 1988); also Lawrence Livermore National Laboratory, Preprint UCRL-98950 (abstract).

Doehne, E., C. Eddy, J. M. Bazan, and G. P. Russ (1988). "Trace Element Analysis on Milligram Sized Geological Samples," presented at *First Intl Conf. on Plasma Source Spectrometry*, University of Durham, England (September 1988); also Lawrence Livermore National Laboratory, Preprint UCRL-98951 (abstract).

Phinney, D. (1988). "Lithium Abundances in Natural Diamonds: An Exploratory Ion-Microprobe Study," *Lunar and Planetary Science* **XIX**, 927.

Russ, G. P. (1988) "Isotope Ratio Measurements Using ICP-MS," *Applications of ICP-MS* (Blackie and Son, Ltd., Glasgow, Scotland).

FY88 $80,000

Cosmochemistry Research

Principal Investigators: S. Niemeyer and M. Lindner
Co-Investigators: J. M. Bazan, D. A. Leich, and G. P. Russ, III

We completed our determination of the half-life of ^{187}Re by measuring the growth rate of ^{187}Os in five rhenium sources over a period of four years. Studies of titanium isotopic anomalies in meteorites have also been completed, with the emphasis this year on interpreting isotopic data in terms of models of early solar system processes.

The goal of this project has been to use measured variations in isotopic abundances to advance our understanding of early solar system and geochemical processes. The ^{187}Re-^{187}Os parent-daughter pair provides a radiometric clock that records the time scale of galactic nucleosynthesis prior to isolation of our solar system and promises to provide a valuable dating scheme for the formation of metallic and sulfide phases in solar system bodies. Isotopic anomalies in meteorites yield clues to stellar nucleosynthetic processes and provide a means of tracing the early history of the solar system. Titanium isotopic anomalies in meteorites have proven to be especially important for constraining models of the evolution of the dust in the early solar nebula.

This year, we completed isotopic analyses of osmium samples isolated from five independent rhenium sources. The osmium samples had been chemically isolated from each of the rhenium sources in approximately six-month intervals over a period of four years. Measurement of the growth rate of ^{187}Os relative to osmium isotope spikes led to direct measurement of the half-life in each of the five sources. The 42-billion-year half-life was determined with a precision of ±3% (95% confidence level) (Lindner, 1988).

We also completed our studies of titanium isotopes. We have published two papers that, together, represent the final and complete report on our investigations of titanium isotopes in the carbonaceous chondrites, a primitive class of meteorite. The first paper (Niemeyer, 1988a) reports our results on titanium isotopic anomalies in chondrules (a type of inclusion in stony meteorites); the second paper (Niemeyer, 1988b) deals with the distribution of titanium isotopic anomalies in carbonaceous chondrites. The highlights of this work include:

- A clear demonstration that the fine-grained matrix in these primative meteorites also carries small excesses of ^{50}Ti.
- The development of a model in which matrix and chondrule precursor assemblages are closely related to one another, whereas the genesis of refractory-rich inclusions involves additional processing in which the ^{50}Ti-rich carrier is enriched relative to normal titanium.
- A suggestion that FUN inclusions (where many elements are isotopically anomalous) represent "snapshots" of a partial melting episode.
- The recognition of an *s*-process (slow-neutron-capture) component in titanium in the mineral hibonite.

References

Niemeyer, S. (1988a). "Titanium Isotopic Anomalies in Chondrules from Carbonaceous Chondrites," *Geochim. Cosmochim. Acta* **52**, 309.

Niemeyer, S. (1988b). *Isotopic Diversity in Nebular Dust: The Distribution of Ti Isotopic Anomalies in Carbonaceous Chondrites*, Lawrence Livermore National Laboratory, Preprint UCRL-98659; to be published in *Geochim. Cosmochim. Acta.*

Lindner, M., D. A. Leich, G. P. Russ, J. M. Bazan, and R. J. Borg (1988). *Direct Determination of the Half-Life of ^{187}Re*, Lawrence Livermore National Laboratory, Preprint UCRL-99534; submitted to *Geochim. Cosmochim. Acta.*

Ultrasensitive Laser Spectroscopy

Principal Investigator: R. J. Silva
Co-Investigator: R. E. Russo

We have developed and tested ultrasensitive photothermal deflection spectroscopy (PDS) and thermal lensing spectroscopy (TLS) for use in measuring optical absorption spectra in aqueous rare-earth and actinide solutions.

We have investigated three ultrasensitive photothermal laser spectroscopy techniques—PAS, PDS, and TLS—for identifying and quantifying submicromolar concentrations of actinide species in aqueous solutions. For each system (Figure 1), an excitation laser is used to induce optical absorption by the solution species; the resulting nonradiative relaxation processes induce a pressure pulse and thermal gradients in the solution. In PAS, the amplitude of the pressure pulse, measured with piezoelectric sensors, is directly proportional to the absorption coefficient. For PDS and TLS, a helium-neon laser probes the induced refractive index gradients. For PDS, the deflection of the probe beam is measured; for TLS, the defocusing of the probe beam is measured.

This year, we developed a differential PDS system with a single position sensor (Spear *et al.*, 1988). This system demonstrated enhanced sensitivity over the original PDS system assembled last year. Using aqueous solutions of Nd^{3+}, which are good stand-ins for the trivalent actinides, we estimated a detection limit (signal/noise = 3) of 1.4×10^{-7} *M* from Beer's Law plots.

We also developed a TLS system and tested its sensitivity with solutions of Nd^{3+}. Preliminary results showed that we can easily detect a concentration of 1×10^{-5} *M*, but the spectrum is strongly influenced by the beam of the excitation laser itself (in TLS, the excitation and probe beams are colinear). A narrow bandpass filter is used to block the excitation laser and to transmit the probe beam to the detector. However, a small amount of excitation beam leaks through the filter and reaches the detector, and this small background distorts the Nd^{3+} spectra at low solution concentrations. The preliminary TLS data suggest a sensitivity equivalent to that of PDS.

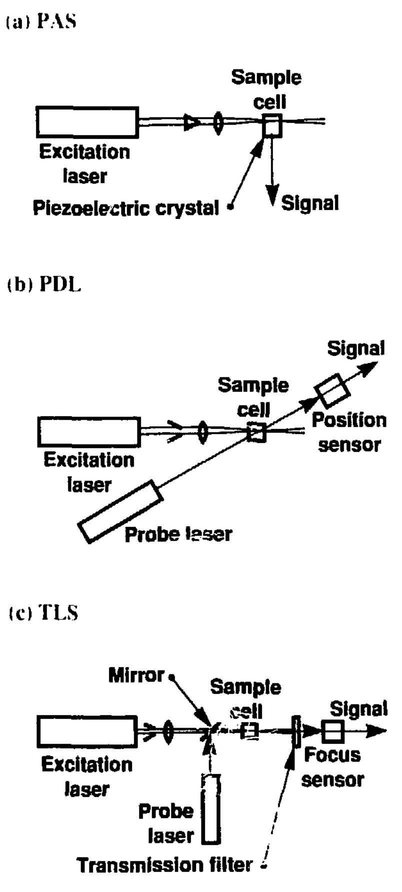

Figure 1. Experimental setups for (a) photoacoustic spectroscopy (PAS), (b) photothermal deflection spectroscopy (PDS), and (c) thermal lensing spectroscopy (TLS). PDS and TLS exhibit nearly the same sensitivity, which is about five times higher than that of our PAS system.

Both PDS and TLS are about five times more sensitive than PAS. However, PDS and TLS require precise alignment of the excitation and probe beams and thus are more difficult to set up and operate. In addition, for best results, PDS and LTS require a tightly focused excitation beam. Because of this tight focus, beam intensities of >0.75 mJ/pulse cause ablation of the sample cell's windows. A more diffuse beam can be used for PAS, and intensities of 3 mJ/pulse have been used in our PAS measurements.

In practice, the three systems exhibit about the same detection limits—that is, about 1×10^{-6} absorbance unit for signal/noise = 3. PAS is easier to set up and operate but requires sample volumes of 1 ml or greater. PDS and TLS can operate with much smaller sample volumes if necessary (e.g., 0.1 ml or perhaps less). Thus, PAS appears to be the method of choice unless only very small sample volumes are available.

Reference

Spear, J. D., R. E. Russo, and R. J. Silva (1988). "Differential Photothermal Deflection Spectroscopy Using a Single Position Sensor," *Appl. Spectrosc.* **42**, 1103.

FY88 $349,000

Measuring the Beta-Decay End Point of Atomic Tritium

Principal Investigators: W. Stoffl, D. Decman, and J. Engelage

We plan to determine the electron antineutrino mass with a precision of a few electron volts by measuring the shape of the tritium beta-decay spectrum near the end point. Our measurements will be sensitive to an electron antineutrino mass greater than 5 eV. We have completed the assembly of the gaseous atomic tritium source and the high-resolution magnetic spectrometer, and we have begun to test the experimental system.

The mass of the neutrino is an important parameter in many areas of physics. For example, a mass of even a few electron volts would have a profound effect on cosmology because of the vast number of neutrinos in the universe; the discovery of such a mass would support modern theories of particle physics and set values for some of the parameters.

The mass of the electron antineutrino, in theory, can be determined by careful measurement of the beta decay of tritium. A nonzero neutrino mass alters the shape of the electron spectrum near the end-point energy of the beta-decay process. Researchers in Moscow (Boris *et al.*, 1985) reported the results of such a tritium beta-decay measurement and claimed evidence for an electron antineutrino mass between 18 and 45 eV. The range comes from uncertainties in the final-state distribution of their source material. In contrast, groups in Switzerland (Frischi *et al.*, 1986) and Tokyo (Kawakami *et al.*, 1987) found no evidence for a neutrino mass with upper limits of 18 and 27 eV, respectively. These experiments used sources with the tritium embedded in a solid, a technique that introduces numerous systematic errors.

Our experiment has been designed to eliminate these systematic errors. Electrons from tritium atoms that decay in our cryogenic, gaseous, atomic tritium source are guided into a large, toroidal, magnetic-field spectrometer by a system of five solenoidal superconducting magnets. Only electrons emitted from the gaseous atomic tritium will successfully pass through the high-resolution spectrometer and be detected.

During FY88, we completed the hardware for our experiment. This was often a very complicated undertaking because most of the components involved some combination of high-vacuum surfaces, nonmagnetic materials, parts operating at cryogenic temperatures, and high voltage.

We completed the gas-handling system that introduces tritium into the gaseous tritium source and assembled the source. Figure 1 shows the flow of tritium and beta-decay electrons through the source assembly. Although not shown in this simplified diagram, the source tube is encased in a liquid-nitrogen-cooled radiation shield, which is further enclosed in a larger tube that is kept at high vacuum by its own pumping system. This multitube source assembly is positioned inside the bore of five superconducting magnets. Also not shown is the section of the source tube that is lined with charcoal that can be cooled to cryogenic temperatures. The absorption of tritium onto the cold charcoal further inhibits tritium gas from entering our spectrometer tank.

We run the source assembly, including its support table, at 5 kV; therefore all the power for the source equipment must be obtained through isolation transformers. We use optical-fiber lines for computer control of the source parameters. The source was tested at a 30-kV potential and found to be stable.

The magnetic spectrometer (Figure 2) is housed in a large (30,000 l) vacuum tank fabricated from nonmagnetic stainless steel. Using two turbopumps and two cryopumps, we achieved a vacuum of less than 5×10^{-9} Torr.

The spectrometer focuses the electrons onto a cylindrical silicon detector that is segmented into 16 independent ring elements. Each element has its own amplifier system. Because the silicon detector has good energy resolution, we can distinguish between good events and background from radioactive decays and secondary cosmic-ray interactions. To avoid thermal stress, the spectrometer will be operated at a constant field and current setting. We will obtain the energy spectrum of the electrons emitted in the source by applying a variable electric potential that accelerates the electrons to the energy that corresponds to the spectrometer's field setting.

We produce the toroidal magnetic field in the spectrometer with a 72-loop system that has a total resistance of about 0.5 Ω and involves more than 700 connections. This low resistance is necessary because each loop must carry 50 A. The outer portions of these loops are 0.5-in.-diam aluminum rods; for the inner part, we use 1-in.-wide, 0.055-in.-thick copper bands. We incorporated ways to ensure that the copper bands inside the loops are straight; this is crucial to the resolution of the spectrometer because the electrons pass close to these bands as they are focused. To make them straight, we stretched each 12-ft band section 1.5 in. with 3000 lb of force. The bands are held straight in the spectrometer by stainless-steel springs, each of which applies a 60-lb force.

Among our concerns were compensating for the earth's magnetic field, minimizing the effect of the electric field produced by the conductors, ensuring a stable temperature, and determining the spectrometer's resolution function. The magnetic spectrometer cannot focus the electrons properly unless we cancel the earth's magnetic field. To reduce the field to less than 5 mG, we surrounded the tank with a shield consisting of 30 coils containing approximately 20,000 ft of wire and energized with 17 computer-controlled power supplies.

We also considered the problem of the electric field produced by the conductors. Because the voltage is dropping along the current path of the spectrometer, this electric field varies with position. To minimize the deflection of the electrons by these electric fields, we strung shield wires at ground potential 0.25 in. on either side of the inner conductors. Similarly, we positioned a grounded wire mesh between the outer conductors and the electron paths.

We took several measures that should help keep the temperature of

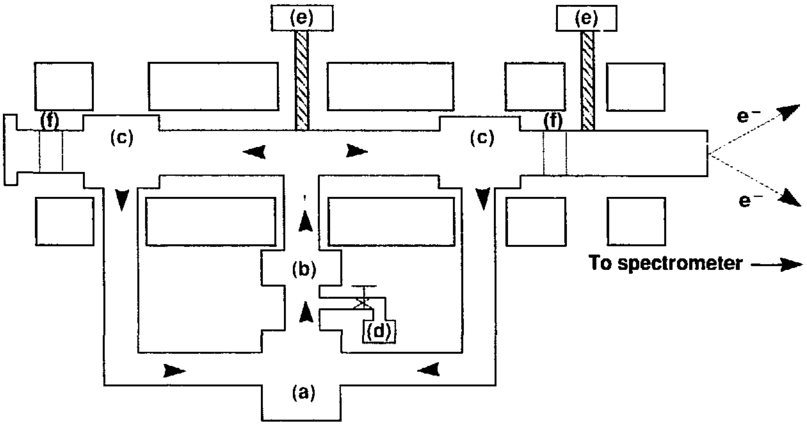

Figure 1. Cross-sectional view of the gaseous tritium source assembly. Tritium flows out of the liquid-nitrogen-cooled cleanup trap (a) and is made atomic in the radiofrequency dissociator (b). The source gas circulates through a 16.4-ft-long, 1.25-in.-diameter aluminum source tube until being pumped out by turbomolecular pumps, four at each point (c). These pumps decrease the tritium gas pressure from about 10^{-3} Torr at the center of the source tube to 10^{-7} Torr at its two ends. Tritium gas can be added to the system from a gas bottle (d). The source tube is kept at cryogenic temperatures as low as 10 K by having it in contact with the cold heads of a closed-loop refrigeration unit (e). Electrons from beta decay in the source tube are guided to the spectrometer by the magnetic field of the superconducting magnets (shaded areas). A potential of 5 kV across the acceleration gaps (f) "tags" the electrons from the source with this extra energy for a total of about 23 keV; electrons from tritium that has leaked into the tank have no more than 18.6 keV. The tritium exhausted from the turbopumps is sent back through the trap (a) and reinjected into the source tube.

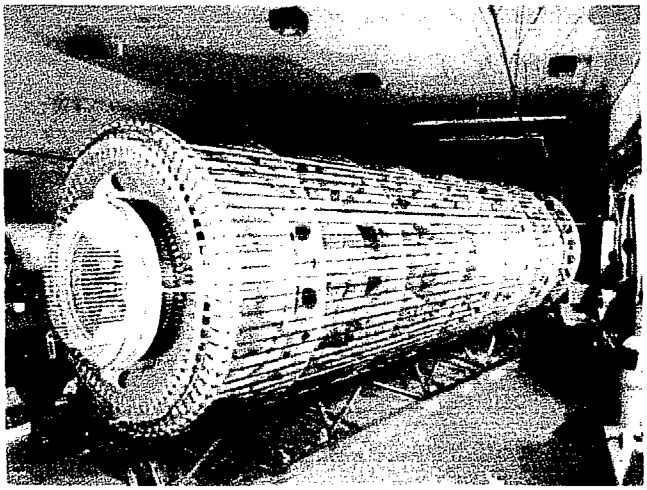

Figure 2. The 26-ft-long toroidal-field electron spectrometer that will be used to measure the tritium beta-decay spectrum near the end point. The large rings that support the 72 current loops are 6.5 ft in diameter.

the spectrometer stable to better than 1°C:

- We monitor the temperature of the conductors and the space frame using temperature-sensitive integrated circuits.
- We chemically blackened the conductors so that they can better radiate away the 1.2 kW of heat generated by the current they carry.
- We installed copper lines for cooling water on the space frame to stabilize the temperature inside the vacuum vessel.

We also built in several computer-controlled diagnostic and correction elements that help us achieve the necessary energy resolution. For example, 128 electrostatic deflector plates allow us to tune the spectrometer in 16 different sections. We can isolate the effects of each set of deflector plates by positioning a movable cup over the detector. The cup contains a slit that allows only a narrow range of electron trajectories to impinge on the detector. Similarly, a movable slit installed at the first focus of the spectrometer allows us to study the resolution of the spectrometer as a function of the trajectories accepted from the source. Because the stepping motors for both the detector diagnostic cup and the movable slit are computer-controlled, we can do a very thorough optimization.

An important apsect of our measurement is knowledge of the system's resolution function. The finite resolution of the spectrometer, as well as any energy loss in the source, will smear the shape of the beta-decay spectrum. Therefore, the resolution function must be unfolded from the data in order to extract the value of the neutrino mass. We will measure our resolution function by using the isomeric decay of the 17.8-keV conversion electron line of ^{83}Kr. This isomer, which has a half-life ($t_{1/2}$) of 1.8 hours, is produced by the decay of ^{83}Rb ($t_{1/2}$ = 86 days). Because the isomer is a gas, it mimics exactly the behavior of the tritium in our source, and it gives us a monochromatic line that enables us to measure and tune the resolution of our system. In addition, we can measure the ^{83}Kr line with admixtures of hydrogen, deuterium, or tritium gas at various pressures (the nominal operating pressure is about 10^{-3} Torr in the source tube) to measure the energy loss in the source gas.

To ensure that this complicated set of hardware is operating correctly, we developed a sophisticated, computerized, data acquisition and control system for our experiment. The system uses a dedicated VAX 11/750 computer and a commercially available branch driver to interface the computer to several computer-automated measurement and control (CAMAC) crates. To monitor and regulate more than 500 parameters, we developed software that can communicate with a wide range of devices, including digital voltmeters, output registers, valves, pumps, temperature sensors, magnetometers, stepping motors, and high-voltage power supplies. This system has been most useful during the developmental phase of the spectrometer; we expect to use it extensively to optimize the resolution of the spectrometer and to monitor the stability of the system in the final experiments.

In early FY89, we will continue to test and optimize the electron spectrometer by using an electron gun positioned at the entrance of the tank. Later, we will test the entire system using ^{83}Kr in the gaseous source. After these tests are complete, we will begin our first tritium measurements.

So far, we have found nothing that could keep our experiment from reaching the goal of being sensitive to a neutrino mass of 5 eV.

References

Boris, S., A. Golutvin, L. Laptin, V. Lubimov, V. Nagovizin, E. Novikov, V. Nozik, V. Soloshenko, I. Tigomirov, and E. Tretjakov (1985), "The Neutrino Mass from the Tritium Beta Spectrum in Valine," *Phys. Lett. B* **159**, 217.

Fritschi, M., E. Holzschuh, W. Kundig, J. W. Petersen, R. E. Pixley, and H. Stussi (1986), "An Upper Limit for the Mass of the Electron Anti-Neutrino from Tritium Beta Decay," *Phys. Lett. B* **173**, 485.

Kawakami, H., K. Nisimura, T. Ohshima, S. Shibata, Y. Shoji, I. Sugai, K. Ukai, T. Yasuda, N. Morikawa, N. Nogawa, T. Nagafuchi, F. Naito, T. Suzuki, H. Taketani, M. Iwahashi, K. Hisatake, M. Fujioka, Y. Fukushima, T. Matsuda, and T. Taniguchi (1987), "An Upper Limit for the Mass of the Electron Anti-Neutrino from the INS Experiment," *Phys. Lett. B* **187** 198.

Measuring the Thermodynamic Properties of Actinide Elements

We have developed two instruments for measuring the thermodynamic properties of actinide elements in aqueous solution: a variable-temperature calorimeter for gathering data at temperatures up to 125°C, and a laser-based photoacoustic spectrometer for investigating solution species at submicromolar concentrations.

Principal Investigators: P. A. Baisden and R. J. Silva
Co-Investigators: P. M. Grant, R. A. Torres, and C. E. A. Palmer

New technologies and instrumentation are essential to the development and application of improved methods for chemically isolating actinides from nuclear waste or nuclear test debris, for detecting and characterizing actinides at trace levels in the environment, and for predicting their chemical behavior in natural systems. We are investigating the chemical properties of actinide species in aqueous solutions by measuring their free energies of formation and their reaction enthalpies and entropies as a function of temperature, ionic strength, and oxidation/reduction conditions in solution. This information can be used to understand and predict the chemical behavior of these elements under a variety of conditions.

Most available thermodynamic data on actinides come from measurements made at or near room temperature. To obtain data for predicting the effect of temperature on actinide behavior, we are preparing to measure reaction enthalpies and entropies as a function of temperature. For these measurements, we have designed and constructed a variable-temperature titration calorimeter (Figure 1). This new calorimeter is similar to our

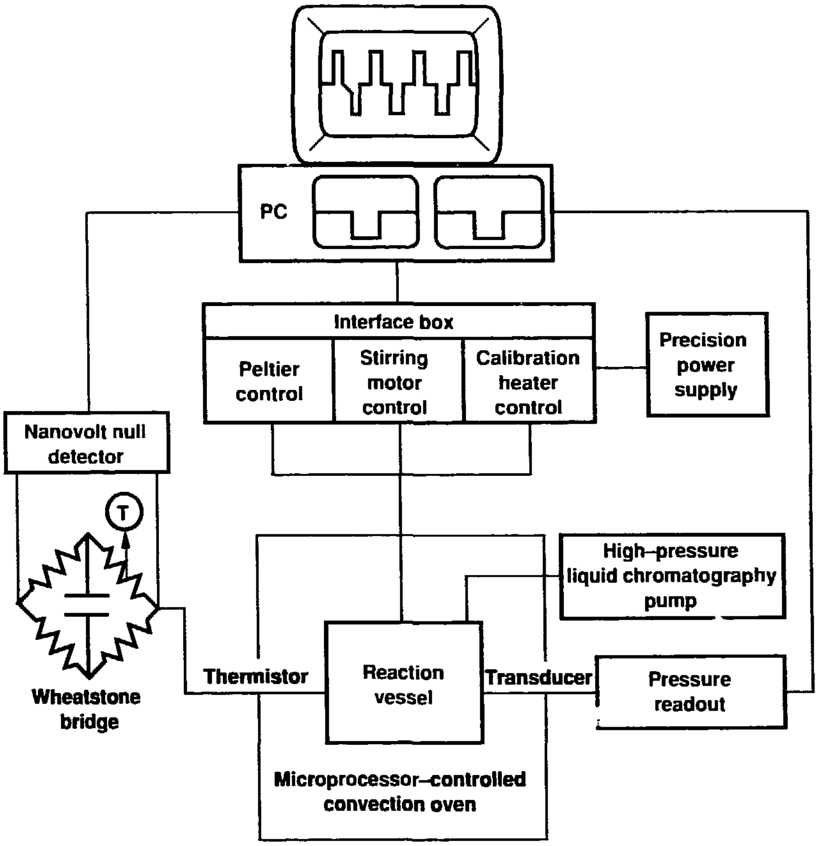

Figure 1. The variable-temperature calorimeter and associated equipment. The system is controlled by an IBM PC, which gives us an on-line graphics display of the experiment in process.

high-sensitivity 25°C calorimeter (Baisden *et al.*, 1987), except that a microprocessor-controlled convection oven rather than a water bath is used to maintain the working-point temperature of the vessel. Also, to prevent sample loss due to evaporation that accompanies working with aqueous solutions at high temperature, we have incorporated the capability of pressurizing the calorimeter's reaction vessel. This instrument is being tested and calibrated, and we expect to begin measurements in the next few months.

Since millimolar concentrations of the actinides are needed to provide measurable temperature changes upon reaction with most complexing agents ($\Delta T > 100$ μ°C per incremental addition of complexing agent), our initial studies will focus on the solution thermodynamics of reactions with uranium and thorium.

We are also interested in obtaining information about the behavior of actinides in near-neutral solutions, such as in natural water systems. However, under these conditions, hydrolysis severely limits the solubility of these elements and thus concentrations in the submicromolar range are typical. Since this concentration regime is inaccessible by conventional optical methods, we have developed a laser-based photoacoustic spectrometer (PAS) system. This gives us a sensitive means of measuring free energies of formation and thus of determining the speciation of aqueous actinide complexes at ultralow concentrations.

Initial testing of our laser-based PAS has been completed. A data-acquisition program running on an IBM PC steps the monochrometer through the desired wavelength range and collects the raw data by linearly averaging a predetermined number of analog-to-digital conversions per laser pulse for the required number of laser pulses per wavelength. With this program, we can acquire data simultaneously from the sample and from a reference cell and photodiode. The photodiode signal is used to correct the absorption spectra for the pulse-to-pulse variations in the intensity of the laser beam.

We found that precise repositioning of the cell between measurements is crucial for minimizing the errors in replicate sampling and in the off-line background subtraction of the sample's reference spectra. Therefore, we developed a cell holder in which we have rigidly bonded the quartz cuvette, the quartz coupling rod, and the piezoelectric transducer. The holder can be easily removed from the spectrometer, refilled, and then accurately replaced.

Using our new cell holder, we are determining the sensitivity of the system and the operating parameters of the laser for the detection of submicromolar quantities of $U^{4+,6+}$, $Np^{4+,5+,6+}$, $Pu^{4+,5+,6+}$, and Am^{3+}. Photoacoustic spectra of Am^{3+}, Pu^{4+}, Nd^{3+}, and Pr^{3+} have been obtained as a function of concentration in the micromolar range, and absorbances were found to be linear with concentration. A practical minimum absorbance limit (signal/noise = 10) of 5×10^{-6} absorbance units was determined; this value is about 1000 times lower than what can be achieved with conventional transmission spectrometers. Using this lower limit, we estimated the concentration sensitivities for the other actinide ions from their known molar absorptivities (see Table 1).

To obtain information about the speciation of aqueous actinide complexes from their photoacoustic spectra, we are developing analysis codes for extracting the free energies of formation for multiple species from the absorption spectra and from the known analytical concentrations of the actinide ions and the complexing agents.

Table 1. **Sensitivity limits for the detection of actinide ions by PAS.**

Ion	Excitation wavelength, nm	Molar absorptivity, 1/mol cm	Sensitivity, ppb
Am^{3+}	503	380	3
Pu^{3+}	600	38	30
Pu^{4+}	470	55	20
PuO_2^{+}	568	19	60
PuO_2^{2+}	830	550	2
Np^{4+}	723	127	9
NpO_2^{+}	980	395	3
NpO_2^{2+}	1223	45	30
U^{4+}	520	58	20
UO_2^{2+}	415	8	150

Reference

Baisden, P. A., P. M. Grant, and W. F. Kinard (1987), "Development of a High-Sensitivity Computer Controlled Titration Calorimeter," *Rev. Sci. Instrum.* 58, 1937.

Physics

B. Tarter

The Physics Department's IR&D work emphasizes innovative research that could have a significant impact on LLNL's energy and defense programs. We also support disciplinary efforts that either provide substantial new long-term capabilities or have the potential to produce major scientific results.

Our projects reflect three methods for seeding new programs: (1) the creation and development of new capabilities, (2) the exploitation of technological advances for application to other fields, and (3) a critical evaluation of the implications of major discoveries in the general physics community. Much of our work is interdisciplinary and multidepartmental in character. Our FY88 projects included collaborations with magnetic fusion, earth sciences, lasers, nuclear chemistry, and biomedical sciences, and next year's new proposals also include participation by chemistry and materials science and engineering.

Nearly half of our projects reached their final stage under FY88 IR&D sponsorship. Our multiyear effort to develop a comprehensive magnetic-fusion modeling code was limited by changes in the direction of the research program, but the BASIS code system we developed is finding significant applications in many other Laboratory computer projects. The experiment aimed at producing insulator-to-metal transitions in a diamond anvil cell set a new record with the 2-Mbar transitions observed in xenon, the highest pressure attained in noble gases. Fabrication of our new two-stage, light-gas gun is complete, and it is nearly operational. The high-pressure cell designed for benchmark measurements of the muon-catalysis fusion rate is nearly ready for use in accelerator experiments in Switzerland. The quark search project should soon yield the world's best upper limit on the number of free quarks in ordinary matter. Our accelerator mass spectrometry work identified such an extraordinary array of possible applications in archeology, biomedical and environmental science, and applied physics that it has expanded to a separately funded program.

Among our continuing research efforts is support of design studies of a laboratory x-ray laser. During the past year, we made significant progress on lasing at shorter wavelengths, and it was also shown that holography experiments are best carried out just short of the "water window." A cryogenic source that is the crucial element in our neutrino mass experiment is nearly complete, and we expect to be taking data in the coming year. Our gamma-ray laser work identified a number of nuclear shape isomars that are potential candidates for laser storage states. We have also made significant advances in understanding the mechanisms that could trigger the lasing action.

Our program to explore the physics of materials with short-pulse, high-intensity lasers saw both theoretical and experimental successes. In particular, we carried out a sequence of detailed multiphoton ionization measurements on xenon and modeled the results very accurately. The short-pulse experiments successfully demonstrated the technique of creating warm plasma under essentially hydrostatic conditions for material properties measurements.

Finally, our global-scale climate modeling efforts continue to provide important scientific developments. A highlight this year was the initial coupling of oceanic circulation models to the atmospheric circulation codes.

The Physics Department received $2,010,000 in IR&D funds in FY88.

FY88, $99,000

Magnetic Fusion Modeling

Principal Investigator: A. Friedman

We have investigated the computational modeling needs of the Laboratory's Magnetic Fusion Energy tokamak research program, examined computer codes used by other laboratories, and adapted critical codes to our needs.

This project was a joint effort of the Physics Department and the Magnetic Fusion Energy (MFE) Program to develop a comprehensive numerical modeling capability for near-term tokamak experiments and advanced reactor-scale systems. Our intent is to build on past efforts, both at LLNL and elsewhere. These include BASIS, an advanced general-purpose, code-development system and scientific computing environment, and MERTH, a tandem-mirror simulation code built by us using the BASIS system and incorporating physics relevant to the tokamak configuration, as well as a wide variety of computer codes developed elsewhere.

Our initial work was aimed at understanding the current state of the art in tokamak modeling. We acquired the tokamak transport code ONETWO, developed at General Atomics in San Diego. This code has been used extensively to model the DIII-D tokamak and its predecessors at General Atomics. It can be used in either a predictive (simulation) mode or an interpretive (analysis) mode, in which transport properties are inferred from experimental data.

If a tokamak machine is to sustain a stable equilibrium, a large plasma current must flow around the torus. In present-day machines, this current (and most of the plasma heating) is provided by induction drive: the plasma acts as the secondary of a transformer. The process is inherently pulsed, a major limitation as the primary current cannot be ramped up indefinitely. Any steady-state tokamak reactor thus will require alternative heating and current-drive mechanisms; a major thrust of our research program is to apply intense microwave radiation to these ends.

LLNL researchers visited the Kurchatov Institute in the Soviet Union, where the T-10 tokamak employs intense electron-cyclotron heating (ECH). We have run the ONETWO code using data acquired during this visit. To match the experimental observations, we had to improve the transport models in the code. We then used the enhanced ONETWO model to predict the range of behavior of the Laboratory's forthcoming Microwave Tokamak Experiment. In this experiment, we will use a modified version of the Laboratory's free-electron laser to provide pulsed ECH power for heating and current-drive experiments.

In designing and analyzing tokamaks with a noncircular cross section, we must understand the plasma shape that arises from a given combination of external-coil currents and plasma parameters. To this end, we are using the magnetohydrodynamic equilibrium codes GAEQ and EFIT from General Atomics and the NEQ code from the Oak Ridge National Laboratory. We have constructed equilibria for LLNL's conceptual reactor designs TIBER-II and ITER; these have been used for stability and ray-tracing studies here and at the Princeton Plasma Physics Laboratory.

We have learned to use the Princeton TSC code, a time-dependent magnetohydrodynamic program that embodies a wide variety of tokamak physics. The code models an entire tokamak discharge on a resistive time scale. We have employed it to determine a ramp-up sequence for external coil currents in an ITER start-up scenario. When the processes governing transport are better understood, the TSC code will provide a strong simulation framework.

The involvement of the Physics Department in this project has ended; ongoing efforts by MFE Program personnel are building on what has been accomplished during the IR&D phase of the project.

References

Dubois, P. F., Z. C. Motteler, and P. A. Willmann (1987). *The BASIS System*, Lawrence Livermore National Laboratory, Report M-189 (to be superceded by Report M-225).

Friedman, A., M. E. Rensink, and W. M. Nevins (1988), in *TMX-U Final Report*, G. D. Porter, Ed., Lawrence Livermore National Laboratory, Report UCID-20981.

Hooper, E. B., and A. Friedman (1987), "Energy and Particle Transport Modeling for ECRH Plasmas in the T-10 Tokamak: Implications for MTX," *Bull. Amer. Phys. Soc.* **32**, 1813.

Insulator-to-Metal Transition in Xenon

Principal Investigators: M. Ross, R. Reichlin, A. K. McMahan, and S. Martin

The equation of state and optical absorption of condensed xenon have been measured in a diamond anvil cell up to 172 GPa. At 150 GPa, we observed sudden changes in the absorption spectra of xenon that we attribute to the onset of metallization. Xenon is the first inert gas solid to be metallized.

Calculations of electron band structure indicate that in solid xenon the band gap between the empty 5*d*-like conduction band and the full 5*p*-like valence band is decreasing with increasing density and that a transition to the metallic state would occur when these bands cross at sufficiently high pressure, predicted to be in the range of 130 to 200 GPa. Structural studies of xenon using x-ray techniques have shown that xenon freezes in a face-centered cubic (fcc) structure. Recently, Jephcoat *et al.* (1987) reported phase transitions in xenon at 14 GPa from fcc to an intermediate, close-packed phase and at 75 GPa to a hexagonal close-packed (hcp) structure that remained stable to 137 GPa.

In our study, xenon samples were loaded in the diamond anvil cell by condensing gas on the tip of the diamond anvils and remotely closing the cell to trap the liquid (observed visually) in the sample chamber. Once a sample was sealed in a cell, it was warmed to room temperature. Absorption and reflection spectra were measured at Livermore, and energy-dispersive x-ray diffraction techniques were used to collect x-ray data at the Cornell High Energy Synchrotron Source (CHESS). Diffraction data were used to obtain the lattice constant of xenon to 172 GPa; pressures were determined from the equation of state of the rhenium gasket.

Optical absorption measurements, made at pressures up to 172 GPa (Figure 1), show two important features. First, above 150 GPa, a significant increase in absorption takes place at the lowest photon energies studied (1.3 eV). Second, near 150 GPa, a new pressure-insensitive absorption peak appears at 2.0 eV and increases in prominence with increasing pressure. Although the structure remains hcp, the sudden appearance of this peak over a narrow pressure range suggests the onset of a transition whose origin was mystifying until we calculated the electron band structure.

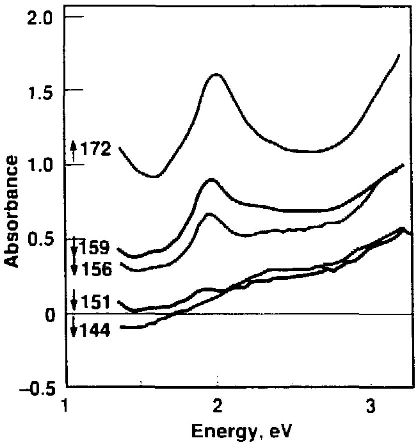

Figure 1. Absorbance of solid xenon plotted against energy at indicated pressures (arrows, in GPa). Note the increased absorption above 150 GPa at lower photon energies and the new, pressure-insensitive absorption peak around 150 GPa at 2.0 eV.

In hcp, unlike fcc, xenon the top of the 5*p* valence band is split into two subbands, separated by about 2 eV. We identify the absorption peak with this 2-eV splitting. Metallization occurs via the indirect gap when the bottom of the conduction band moves below the Fermi surface. This drops the Fermi level below the top of the valence band, providing empty states in the valence band that we believe are responsible for the 2-eV absorption peak. We made band structure calculations at several densities to verify the pressure independence of this transition. An inspection of the band structure fails to show any other transition that can lead to a relatively pressure-insensitive 2-eV absorption and can also account for the abrupt appearance of this feature.

The metallic character of the state is further supported by infrared reflectivity measurements we collected at the xenon-diamond interface at 160 GPa. Thus, the 2-eV optical transition provides a unique signature for the insulator-to-metal transition in hcp xenon.

References

Ross, M. (1968), "Shock Compression of Xenon to a Metallic-Like State," *Phys. Rev.* **171**, 777.

Ross, M., and A. K. McMahan (1980), "Condensed Xenon at High Pressure," *Phys. Rev.* **B21**, 1658.

Jephcoat, A. P., H. K. Mao, L. W. Finger, D. E. Cox, R. J. Hemley, and C. S. Zha (1987), "Pressure-Induced Structural Phase Transitions in Solid Xenon," *Phys. Rev. Lett.* **59**, 2670.

FY88 $150,000

Advanced High-Velocity Two-Stage Light-Gas Gun

Principal Investigator: W. J. Nellis

We are developing an advanced two-stage light-gas gun facility to increase the number of high-pressure shock-wave experiments and to achieve higher launch velocities, shock pressures, and shock temperatures in those experiments. The older two-stage gun will be modified to increase its launch velocity, thereby producing higher shock pressures and shock temperatures.

The two-stage light-gas gun (Figure 1) is used to study the properties of materials at high shock pressures and temperatures, to develop shock diagnostics for use at the Nevada Test Site, and to synthesize new materials. The wide variety of applications for the gun has created a high demand for gun time by various Laboratory researchers and UC collaborators. To meet this demand, we needed a second two-stage gun. To minimize equipment and operating costs, we designed a gun one-third the size of the original one, which is 19 m long. Because of advances in diagnostic resolution, many of the experiments performed with the original gun can also be performed with the smaller one.

Higher projectile velocities are also needed to achieve higher pressures and temperatures of relevance to Laboratory programs and to induce interesting physics phenomena. Computer calculations have shown that the way to achieve higher velocities is to use the original full-scale two-stage gun with a smaller-diameter lighter projectile, a shorter launch tube, and a reduced gas loading.

Our future plans are to move the new one-third-scale gun to a room adjacent to the full-scale gun and to procure hardware for the high-velocity version of the original gun. Funding for this work will be provided by Weapons Supporting Research in FY89.

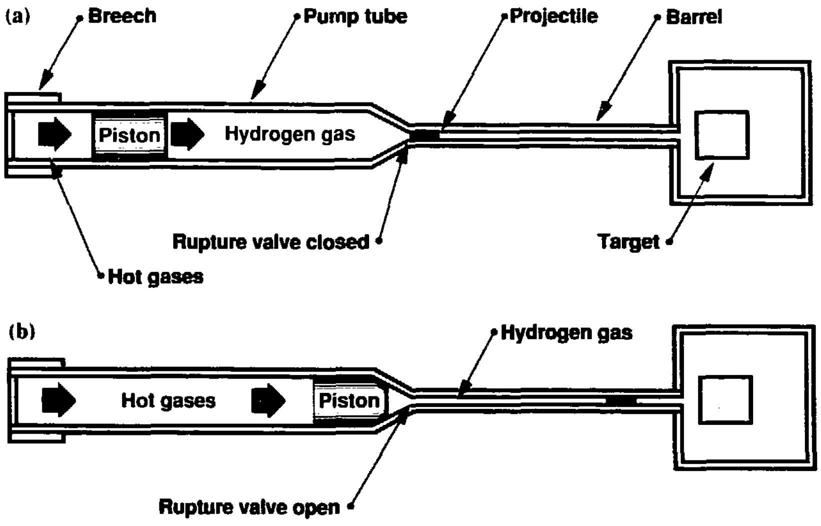

Figure 1. Diagram of the two-stage light-gas gun. (a) The hot burning gases from gunpowder in the breech drive a heavy piston that compresses hydrogen gas in the pump tube. The high-pressure hydrogen gas breaks open the rupture valve and accelerates the projectile down the barrel. (b) At the end of the barrel, the projectile has reached its highest velocity and impacts the target.

Muon-Catalyzed Fusion

Principal Investigators: **B. J. Alder and W. Durham**

Our work on muon-catalyzed fusion has focused on the design and assembly of a high-pressure cell in which to carry out key experiments at a Swiss accelerator. Our cell has successfully reached the maximum temperature and pressure required and is being tested for hydrogen permeability and the number of times it can be recycled. After safety tests, it will be shipped to Switzerland. Theoretical understanding of the stripping processes, which could lead to a scheme for enhanced catalysis, is progressing well.

It has been known for 30 years that a negative muon (μ) will induce a spontaneous fusion reaction in a cold (room-temperature) molecule of deuterium-tritium (DT) according to the reaction:

$$DT\mu \rightarrow \alpha + n + \mu + 17.6\ \text{MeV} .$$

In this reaction, the muon acts as an agent that brings the deuterium and tritium nuclei close enough together so that fusion occurs by quantum-mechanical tunneling. In principle, such a reaction could be used for large-scale production of usable energy. However, early erroneous calculations of muon capture cross sections discouraged further research. When, more than a decade ago, Soviet scientists found the mechanism that produces a larger cross section, interest revived in this alternative fusion technology.

Our muon-catalysis research has been directed at determining how many fusion reactions could be catalyzed by a single muon. Specifically, we are preparing an experiment in the high-pressure, high-temperature range where (controversial) extrapolation suggests a high fusion rate. We are also exploring theoretically the muon stripping rate to see whether there are ways to enhance the predicted catalysis efficiency. (The muon stripping rate is the probability of a muon captured by an alpha particle being freed to catalyze more fusion reactions, which in turn means lowering the crucial sticking parameter.)

Both our experimental and our theoretical programs have made good progress and will conclude by the end of FY89. The experimental apparatus has held pressure at 200 MPa and temperature at 2000 K, and is now in the final assembly stage (Figure 1). We have incorporated the pressure-producing part of the apparatus (a simple liquid-to-gas expansion device) and all electronic diagnostic controls. The chief remaining issues are how many times the pressure and temperature conditions can be recycled and the permeability of the metal container to hydrogen. We are still experimenting with the vessel liners and their surrounding ceramic (currently TZM) to find the best materials for them. We are testing ceramics from two commercial sources and vessel liners made of rhenium and a tungsten-rhenium alloy. We are also exploring the possibility of fabricating such a container on site.

We are currently in the final stages of testing the experimental apparatus. Using an inert gas, we have reached maximum design temperature and pressure. Preliminary indications from hydrogen testing show encouragingly low levels of hydrogen permeation throughout the liner. The tests with hydrogen should be completed in FY89. The apparatus will be shipped to Switzerland after the safety test has been satisfactorily completed in the presence of both Los Alamos and Swiss experts.

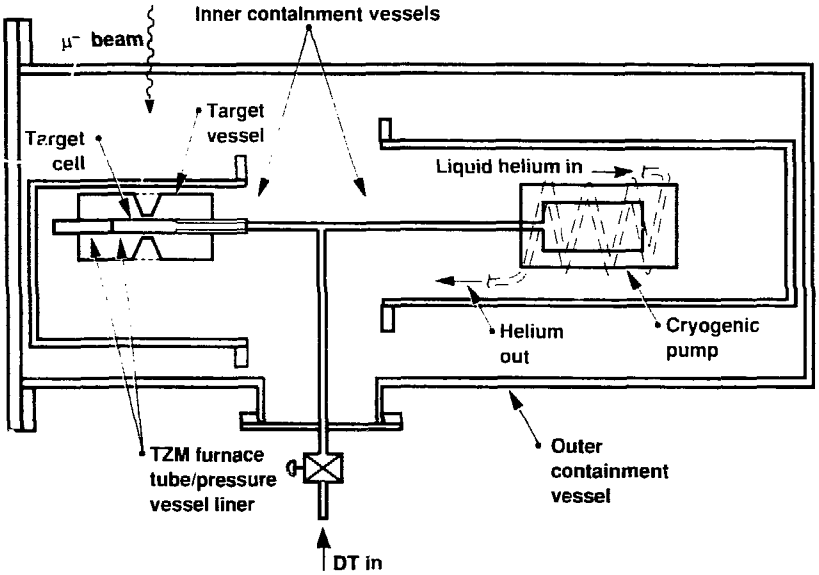

Figure 1. Schematic cross section of the experimental apparatus. The target cell, containing about 2 cm^3 of DT gas at high pressure and temperature, sits within an inner containment vessel. The cryogenic pump that injects the DT gas into the target cell sits in another vessel. A beam of negative muons (μ^-) enters from the outside, causing DT fusion in the target cell.

Our theoretical calculations of muon stripping evaluate part of the stripping process. We are in the process of checking out the computer program for calculating the remaining part. When completed in a few months, these calculations should predict the net stripping we can expect in the experiments. We will conclude our theoretical effort with calculations of the Stark mixing factor, the Auger decay rates, the nuclear fusion rates for excited states, and a multiphoton process that could lead to enhanced fusion in excited states (owing to considerably less sticking).

FY88 $158,000

Quark Search

Principal Investigator: C. Hendricks

During the past year, we significantly improved nearly every major feature of our experimental system: the drop generator, the rotating-disk chopper system, the data-acquisition system, the pressure controls on the gas system, and the overall electronic timing of the system. With this qualitatively improved experiment, we can now obtain an upper limit on the number of free quarks per gram in diffusion pump oil.

Although quarks are believed to be the elementary constituents of hadronic matter (protons and neutrons), a free, stable quark has yet to be detected. Experimental efforts to detect such a particle depend on the fractional electric charge that theory says it should carry: ±1/3 or ±2/3 the charge on a single electron. A fragment of matter that contains a single free quark thus should have a net charge equal to some whole number of electron charges plus a fractional charge contributed by the quark. Clearly, the experimental measurement of such fractional charges would be of fundamental importance to our understanding of the structure of matter.

The goal of our project is to search for free, long-lived quarks. We have designed and constructed an experiment that can measure the charge on small quantities of matter to an accuracy of about 5% of the charge on an electron. Our experimental approach provides a material throughput many orders of magnitude higher than that of competing schemes and can test a wide variety of materials. Particles (or droplets) of the material to be studied are generated and passed through an electric-field deflection system. The resulting particle trajectories depend on the ratio of each particle's net charge to its mass, the intensity of the electric field, and the time a particle spends in the field. The deflecting field is produced by creating an electric potential between two vertical, carefully aligned, parallel plates. Since the particles are generated with a uniform mass and velocity, the trajectory of an individual particle between the plates then depends only on its net electric charge.

During the past year, we completed the assembly of a new, very stable droplet generator (Figure 1) and a rotating-disk chopper system, and mounted them atop our 5-m drop tower. The droplet generator, operated with a 10-µm-diameter orifice, has produced droplets of diffusion pump oil continuously for more than 48 hours without any apparent change in their characteristics or direction of travel. The rotating-disk chopper removes the required number of droplets from a stream of 25-µm-diameter drops.

Drops are generated sequentially, about three drop diameters apart, from a cylindrical liquid jet at a high rate (up to 100,000 drops per second). To avoid interactions between the drops via induced dipole fields, the drops must be separated by about 60 drop diameters. This is accomplished by removing 19 out of every 20 drops in the stream using the chopper (a rotating slotted disk); the rotor frequency is synchronized with the drop-generation frequency. This attenuated stream of droplets is then passed through the electric-field deflection system where each particle's trajectory is observed and its net electric charge is determined.

After bench-testing the chopper, we mounted it on the drop tower and tested it again for proper operation. As in the bench test, drops generated at rates up to 100,000 per second were directed to the appropriate spot on the rotating disk. The chopper successfully removed 19 of every 20 drops, allowing the 20th drop to continue undeviated along its trajectory, producing an attenuated stream of 5000 drops per second. The drop stream and individual drops were observed optically above the chopper disk, and the attenuated stream and individual drops were observed below the chopper disk. Drop streams, both chopped and unchopped, have been observed at the bottom of the tower during the alignment process.

We have also implemented a much-improved data-acquisition

Figure 1. The 5-m drop tower used in our quark detection experiments. Small particles (or droplets) falling between the charged plates are deflected by an amount that depends on their net electric charge. Sensitive detectors and a data-analysis system can determine the charge on a particle to within 5% of the charge on an electron.

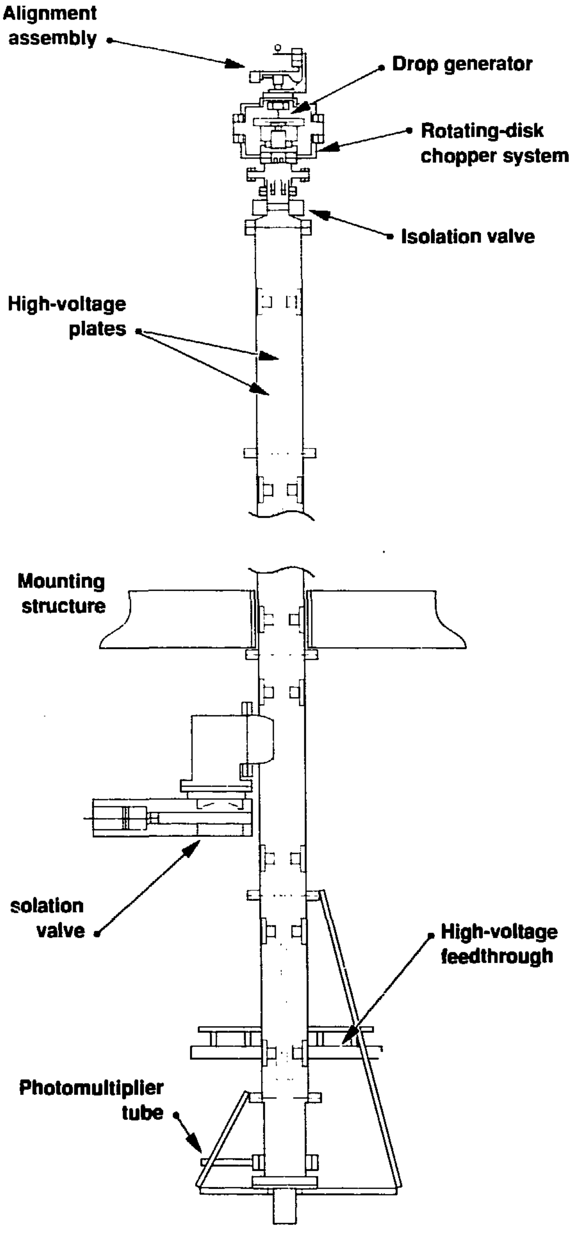

system. It consists of a moving light source with a better-focused CRT (cathode-ray-tube) spot that has a shorter decay time (now about 16 ns) than the earlier one, a better photomultiplier tube, and vastly improved computer hardware, software, data storage, and output systems. The data-acquisition system and the improved photomultiplier are currently being tested together on the drop tower.

In addition, we have improved the regulation of the gas system used to pressurize the droplet liquid to provide control of the pressure to about one part per million at a pressure of a few pounds per square inch to more than 200 psi (1.4 MPa). This ensures that the initial vertical velocity will be virtually constant from drop to drop.

The function generators used to drive the drop generator, the strobes, the chopper motor, and the CRT sweep are all locked to a stable oscillator that has both a long- and a short-time frequency stability of about one part in 10^{10}. This is an improvement over previous systems of about five orders of magnitude.

With all these improvements and changes, accomplished during the past year, we now have an operational experiment. Next year, we plan to do our first quark search on drops of diffusion pump oil and to publish the results. Simultaneously, we will develop a proposal for outside funding to produce and sample a variety of different candidate quark materials.

FY88 $153,000

Biomedical and Environmental Applications of Accelerator Mass Spectrometry

Principal Investigators: J. Davis and I. Proctor
Co-Investigators: C. Poppe, B. Gledhill, and E. Nelson*

*Simon Fraser University, Vancouver, British Columbia, Canada.

We are extending the use of accelerator mass spectrometry (AMS) to new areas in biomedical and environmental research. The gain of six to nine orders of sensitivity that AMS offers for detecting isotopic tags will make possible great reductions in dose in present clinical and research procedures and will allow the development of new ones.

New applications for other Laboratory programs have been identified as well.

Accelerator mass spectrometry (AMS) was developed to improve the sensitivity for counting small quantities of long-lived isotopes (e.g., ^{10}Be, ^{14}C, ^{36}Cl), primarily for archeological and geoscience applications. We are investigating new uses of the ultrasensitive AMS technique in biomedical and environmental research and in other energy-related Laboratory programs. Many of the isotopes for which AMS has been developed are also commonly used as tags in biomedical and environmental research. In addition to the search for new scientific applications, we are pursuing the technological advances necessary to increase greatly the throughput of AMS measurements, thus making the economics of the technique more attractive.

With the IR&D support available in FY88, we have accomplished the following:

- Convened at LLNL two workshops that have identified more than 20 experiments with potential for either dramatic scientific results or major clinical importance. Most important among these are adduct tagging experiments using ^{14}C and body calcium investigations using both ^{41}Ca and ^{45}Ca (the latter to be done with staff from UC San Francisco).
- Participated in a workshop with collaborators at Simon Fraser University that set the design for the ion sources and accelerators required for the next generation of AMS

Figure 1. Beamline and magnet of the UC-LLNL accelerator mass spectrometer; the accelerator vessel is at the upper left.

facilities. As a result of this meeting, we acquired a tandem accelerator to donate to a future dedicated AMS facility.

- Completed the initial beam-calibration runs of the UC-LLNL AMS in the Laboratory's new tandem accelerator laboratory (Figure 1).
- Supported the fabrication and programming of the electronics for the initial detector system on the UC-LLNL spectrometer. This system will be used for the initial measurements with light isotopes.
- Supported the construction of equipment for preparing graphite samples by the Environmental Sciences Division.

In FY89, we will bring the spectrometer into routine operation for light isotopes (i.e., atomic mass < 40), perform the experiments that use ^{14}C as a tag, and develop a detector system to make measurements with calcium isotopes. The beam diagnostics and computer systems required for automated operation of the tandem accelerator will be developed and tested. New applications of AMS in acquiring field data for climatology research will be assessed. Finally, we will explore the possibility of developing an AMS diagnostic for laser-driven inertial-confinement fusion experiments.

Reference

Davis, J. C., and Proctor, I. D. (1987). "Multidisciplinary Tandem Accelerator Laboratory," in *Energy and Technology Review*, Lawrence Livermore National Laboratory, Report UCRL-52000-87-6, pp. 14-20

FY88 $200,000

Laboratory X-Ray Lasers

Principal Investigators: M. D. Rosen
Co-Investigators: M. S. Maxon,
D. C. Eder, and R. A. London

We are providing the theoretical leadership for a joint effort to develop the physics and technology of laboratory x-ray lasers, with special emphasis on biological applications. This work is sponsored by the Physics Department and involves Lasers, Defense Systems, Biomedical Sciences, and Electronics Engineering. Analysis of experimental results continues in preparation for attempts at lasing in the 4.5-nm regime needed to image biological structures.

The Laboratory produced the first successful demonstration of lasing at x-ray wavelengths in FY84 using the Novette laser. Since that time, our work has focused on understanding the data to improve new designs for more coherent lasing at shorter wavelengths, with a view toward biological applications. Our specific FY88 goals were to understand the previous nickel-like x-ray laser (XRL) results and the 100-ps recombination XRL results, to design neodymium-like schemes, and to assess photopumped schemes.

In FY87, we designed targets that achieved gain at 7 and 5 nm with nickel-like $4d$–$4p$ systems. Two major mysteries—our failure to achieve predicted $J = 2$ gain (in europium and ytterbium) and the low $J = 0$ gain observed (in ytterbium)—have been largely solved this year. Analysis of a density profile from KMS Fusion, Inc. (Ann Arbor, MI) led us to change our hydrodynamics model to produce cooler, denser foils. The ensuing kinetics do a far better job now of explaining the large nickel-like database. This will enable us to design the tungsten experiment (4.3 nm) with more confidence. We are also serving as an international clearing house for the analysis of nickel-like data from lasers and tokamaks.

In collaboration with the Massachusetts Institute of Technology and Lockheed Corporation, we have designed neodymium-like ($5f$–$5d$) schemes that may be suited to short-wavelength, table-top lasers (6.5 nm with uranium); alternatively, with a large laser system, these neodymium-like schemes may serve as a test bed for saturation and laser-architecture studies.

We are preparing for hydrogen-like aluminum (3.9-nm) recombination experiments in the spring of 1989, when a required 20-ps oscillator comes on line on the Nova laser. We have been analyzing 100-ps data on aluminum from Nova and from the laser at Limeil, France, and on fluorine and magnesium from experiments conducted in the U.K. and Japan. Although some of the data agree with predictions, some do not; we are collaborating with modelers in the U.K. to study the problems. The situation is similar with regard to lithium-like schemes. In addition, since the Nova laser has more energy at 1.06 µm, we have designed a hydrogen-like aluminum scheme driven by hot electrons at that wavelength.

Our planning and design of a neon-like series at Limeil has yielded a rich harvest of optimization and Z-scaling data (Figure 1). We have begun to assess (in collaboration with J. Nilsen) the possibilities of enhancing gain with photopumped systems, particularly photoresonances that can enhance neon-like or nickel-like gain. We have also done hydrodynamic modeling of a hot-electron-boosted neon-like silver experiment carried out by a joint team from the Naval Research Laboratory and the University of Rochester Laboratory for Laser Energetics.

In FY89, we will seek to understand the physics behind our new *ad hoc* cooler hydrodynamics model for the nickel-like scheme. More data on density from KMS and on density and temperature from the National Research Center, Ottawa, will be available soon. Refined designs for tungsten will be carried out, as well as special pulse-shaped designs that enhance gain and shorten the XRL pulse.

In the recombination schemes, we hope to resolve some of the 100-ps discrepancies, either with different hydrodynamics models or with better atomic data files from the

Laboratory's high-temperature physics division. We have just received useful 20-ps (non-XRL) aluminum data from the U.K. and from Australia that will be compared to our modeling results; we expect to receive more 20-ps data from KMS and the Nuclear Regulatory Commission (NRC).

When the Limeil neon-like data are digitized, they will be analyzed, as will NRC data on temperature and density. More photon-driven schemes will be assessed, particularly inner-shell photoionizers. This approach can provide flexibility in drivers (for example, use of a compact torus) and will also involve us in the growing worldwide efforts in ultrashort pulses. Together with a consultant, we will address issues of coherence and possible explanations of weaker-than-expected lasing from the $3p$–$2s$, $J = 0$–1 line in neon-like selenium based on the idea that superfluorescence reduces the upper-level population before amplified spontaneous emission has a chance to occur.

References

Charatis, G., B. K. F. Young, G. E. Busch, C. J. Cerjan, W. H. Goldstein, A. L. Osterheld, T. W. Phillips, M. D. Rosen, R. E. Stewart, and R. S. Walling (1988), "Simultaneously Time- and Space-Resolved Spectroscopic Characterization of Laser-Produced Plasmas," in *Proc. Optoelectronics and Laser Applications in Science and Engineering (SPIE)*, January 10–15, Los Angeles, CA; also available as Lawrence Livermore National Laboratory, Preprint UCRL-98386.

Eder, D. C., M. D. Rosen, R. W. Lee, J. E. Trebes, N. M. Ceglio, M. J. Eckkart, B. J. MacGowan, R. L. Kauffman, and D. L. Matthews (1987), "Effect of Spontaneous Emission in Hydrogen-Like Magnesium and Aluminum X Ray Laser Schemes," *J. Opt. Soc. Amer. B* **4**, 1949.

Hunter, J. A., and R. A. London (1988), "Multi Dimensional Similarity Models for Exploding Foils," *Phys. Fluids* **31**, 3102.

London, R. A. (1988), "Beam Optics of Exploding Foil Plasma X-Ray Lasers," *Phys. Fluids* **31**, 184.

MacGowan, B. J., S. Maxon, P. L. Hagelstein, C. J. Keane, R. A. London, D. L. Matthews, M. D. Rosen, J. H. Scofield, and D. A. Whelan (1987), "Demonstration of Soft X-Ray Amplification in Nickel-Like Ions," *Phys. Rev. Lett.* **59**, 2157.

Maxon, S., B. MacGowan, R. London, J. Scofield, M. Rosen, M. Chen, and P. Hagelstein (1988), "Calculation and Design of a Ni-Like Eu Soft X-Ray Laser," *Phys. Rev. A* **37**, 2227.

Rosen, M. D., P. L. Hagelstein, and R. A. London (1988), "On the Scaling of Ne-Like Schemes for XRLs to Short Wavelength," *Phys. Fluids* **31**, 666.

Rosen, M. D., R. A. London, P. L. Hagelstein, M. S. Maxon, D. C. Eder, B. L. Whitten, M. H. Chen, J. K. Nash, J. H. Scofield, A. U. Hazi, R. Minner, D. A. Whelan, R. E. Stewart, T. W. Phillips, H. E. Dalhed, B. J. MacGowan, J. E. Trebes, C. J. Keane, and D. L. Matthews (1988), "No Pain—No Gain: The Complex Art of Soft X-Ray Laser Target Design and Analysis," *Conf. Atomic Processes in Plasma*, Santa Fe, NM, October 1987 (invited paper), A. Hauer and A. Merts, Eds. (American Institute of Physics, NY), p. 102.

Rosen, M. D., J. E. Trebes, B. J. MacGowan, P. L. Hagelstein, R. A. London, D. L. Matthews, D. G. Nilsen, T. M. Phillips, D. Whelan, and V. L. Jacobs (1987), "On the Dynamics of Collisional Excitation XRLs," *Phys. Rev. Lett.* **59**, 2283.

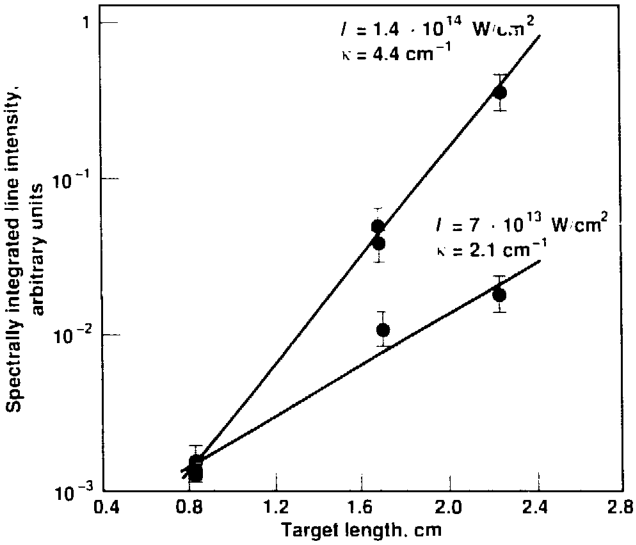

Figure 1. Example of Z-scaling and optimization data obtained at Limeil, France. The plots show how the λ = 16.41-nm line intensity of a strontium target (an element not previously studied at LLNL) varies with target length for two incident irradiances. The gain coefficient κ is derived.

Neutrino Mass Experiment Using a Frozen Tritium Source

Principal Investigators: O. Fackler and M. Mugge

We are attempting to determine the mass of the electron neutrino with a precision of a few electron volts by measuring the tritium beta-decay energy spectrum near the maximum beta energy. Unique features of our experiment are an extremely high-resolution electrostatic spectrometer and a frozen tritium source. Last year, we demonstrated successful operation of the spectrometer. This year's work focused on designing and fabricating the cryogenic tritium source and on upgrading the spectrometer.

A finding that the electron neutrino has a finite mass would have significant consequences for both elementary-particle physics and astrophysics. Since the neutrino is one of the elementary building blocks of all matter, its properties and the forces that govern its interactions are of great interest. Furthermore, since more neutrinos were created in the Big Bang than any other elementary particle, even a very small neutrino mass—on the order of a few electron volts—would be sufficient eventually to halt the expansion of the universe. The physical importance of the neutrino mass is evidenced by the fact that more than a dozen groups throughout the world are attempting to measure it.

Our goal is to determine the mass of the electron neutrino to within a few electron volts. Our experimental approach is to measure the shape of the beta-decay spectrum of tritium near the maximum beta energy. The measured energy distribution is sensitive to the mass of the neutrino that accompanies beta decay. The use of a frozen, pure tritium source, a feature unique to our experiment, allows calculation of molecular final-state and solid-state effects to an accuracy of better than 0.5 eV. A pure source also permits very high data rates. These features, together with the high resolution of our spectrometer, should enable us to determine the neutrino mass to within a few electron volts, the best accuracy currently obtainable.

Progress this year has centered on completing the cryogenic source and on improving the spectrometer. In addition, we have worked on a new low-noise detector system and on a new data-logging and acquisition system. Spectrometer upgrades to ready it for the source are also being completed.

The ultrahigh-vacuum, cryogenic, high-voltage, and mechanical tolerance requirements associated with freezing tritium and installing the source in the apparatus posed difficult engineering challenges. To meet these, we:

- Developed a source substrate with a smoothness of better than 1 nm.
- Designed a liquid helium feedthrough that is nonmagnetic and electrically insulating.
- Designed low-gas-leakage and thermal seals between the 2-K source substrate and the tritium deposition chamber.
- Developed a specially shaped tritium deposition chamber to obtain a tritium source of uniform thickness.

The partially assembled source is shown in Figure 1a. The 2-m-long source arm enters the tritium deposition chamber's heat shield at the left. The shorter arm at the right holds the deposition chamber, which mates with the source during tritium deposition. After tritium is frozen on the substrate, the source is passed through a vacuum valve into the spectrometer vacuum vessel. Figure 1b is a closer view of the source entering the heat shield; the extremely smooth source substrate is clearly visible. Development and assembly of the source and component testing are both nearing completion.

We have developed a new detector that counts low-energy electrons. Its important feature is that it discriminates against most backgrounds. Final background rates will be less than one count per 20 seconds, with the possibility of achieving one count per 400 seconds. This low background rate will provide a statistical sensitivity to neutrino mass of better than 4 eV. We expect the detector to be completed shortly after source installation.

We have also nearly completed development of a new data-acquisition system to replace the aging equipment used in prior data taking. The new system will be substantially faster, more reliable, and more flexible.

Our experimental apparatus has been improved and upgraded in several ways to accommodate the cryogenic source and to correct background problems found in earlier data. Modified components include the spectrometer, the collimator, and the reflector. The spectrometer has been modified to increase its acceptance and resolution. The collimator has been adjusted to produce an experimental resolution of 3 eV. We have designed a new reflector with higher acceptance that eliminates backgrounds discovered in the early phase of this work.

Our spectrometer, which contains a number of significant improvements, will soon be mated with the newly fabricated, cryogenic tritium source. All work this year has proceeded successfully on a schedule that will permit us to conduct experiments with frozen tritium in FY89. This should make us the first group among the competing Russian, Japanese, German, Swiss, and U.S. groups able to detect neutrino masses of less than 15 eV. We plan to probe for masses down to 5 eV in FY90.

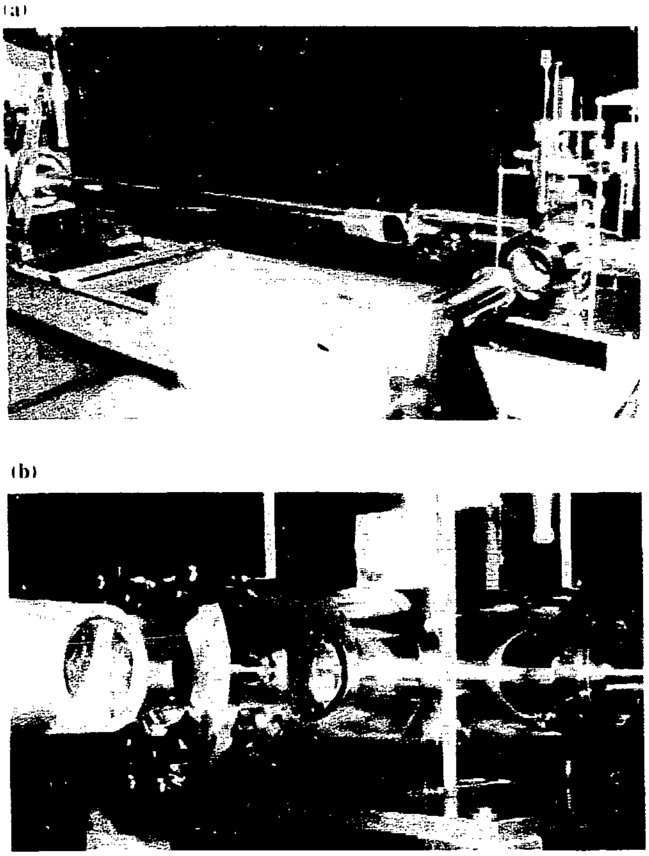

Figure 1. (a) Source assembly during construction. The 2-m-long source arm is shown entering the deposition chamber's three-armed heat shield (right). The shorter arm, at right, contains the tritium deposition chamber itself, which mates with the source during tritium deposition. (b) Closer view of the source entering the heat shield.

FY88: $103,000

Nuclear Shape Isomers as Candidates for a Gamma-Ray Laser

Principal Investigator: M. Weiss

We have used the most modern techniques of nuclear theory to predict a new class of nuclear isomers efficacious for the design of a gamma-ray laser. We have identified several species for experimental verification. Advances in many-body theory, in progress, will refine these predictions by adding nuclear dynamics and will permit calculation of branching ratios and lifetimes.

The overall goal of this project is to explore the possibility of making a gamma-ray laser based on nuclear storage states. Last year, we identified shape isomers as the most promising nuclei. This year, our main objective was to complete static Hartree-Fock calculations of osmium and mercury nuclei to delineate those species with secondary minima in their potential energy surfaces and to identify those most likely to yield experimentally verifiable shape isomers. A second aim was to begin work on incorporating nuclear dynamics into these static calculations. A third goal was to complete our semiclassical calculations of laser-induced nuclear transitions and to begin to look for quantum-mechanical corrections.

Toward our main objective, we have completed three-dimensional potential-energy maps for 12 even-numbered osmium isotopes with the Skyrme III nuclear potential and for 16 mercury isotopes with both the Skyrme III and the more modern SKM* potential (Weiss, 1988). From these we have selected mercury-194 (Figure 1) as the most accessible for experimental verification, and several experiments are being designed.

Toward the second goal, we have begun configuration-mixing nuclear Hartree-Fock calculations that will provide dynamic corrections to our static results. The algebra has been completed, and computer codes are being tested.

Toward the third goal, we have formulated a solvable quantum-mechanical model that yields an analytic solution to the Schrödinger equation for an atomic electron in an intense laser field. We have derived expressions for the nuclear transition rates from coupling to the atomic electron. Numerical evaluation of the analytic formulas is in progress for comparison with our semiclassical calculation (Berger, 1987) of the nuclear transition rate and inversion density.

For future work, our primary objective is to test and implement the

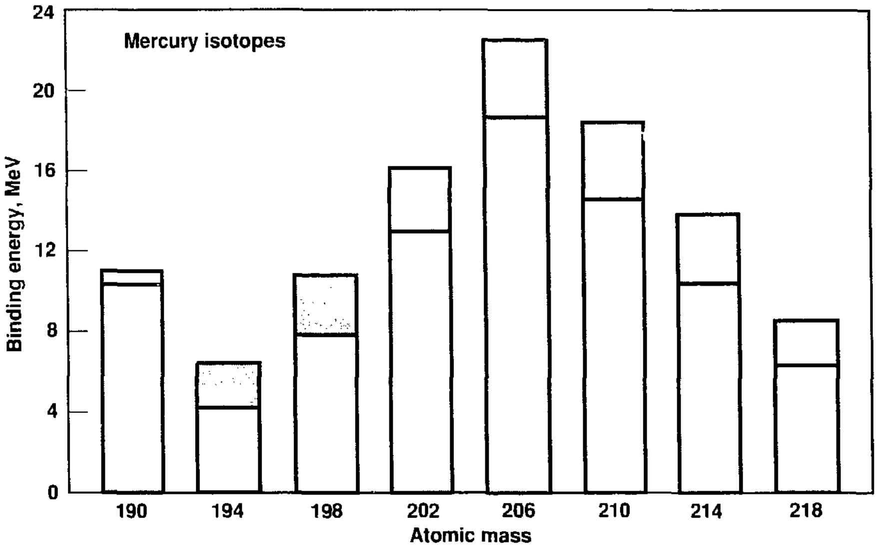

Figure 1. Excitation energy (dark gray) and well depth (light gray) predicted for shape isomers in mercury isotopes. Mercury-194 provides the best ratio of excitation energy to well depth and has neighboring stable nuclei that can also be used as targets.

configuration-mixing nuclear Hartree-Fock theory, to apply it to dynamic corrections to our static predictions, and to extract lifetimes and branching ratios. We hope also to be able to test the physics on actinide nuclei for which fissioning shape isomers have been measured. On the basis of these results, we may look into other regions of the periodic table for nuclei that may have more interesting properties as laser storage states. In addition, we will finish and evaluate our solvable model of laser-atomic electron-nucleus interaction and will compare it with our semiclassical calculation.

A spin-off of this work that is far less demanding technically is the possibility of generating multi-keV per atom explosives by triggering an isomer to decay. It will do so by emitting a cascade of gamma rays, and, if the ground state is stable, there will be no radioactivity. Speculations along these lines using the far-less-efficient spin isomers have been reported in Soviet journals (Arutyunyam, 1987; Avramenko, 1986). We will carry out some preliminary estimates along these lines in the coming year.

References

Arutyunyam, R.V., *et al.* (1987). *Pis'ma Zh Eksp. Teor. Fiz.* **46**, 345.

Avramenko, S.A., *et al.* (1986). *Zh. Eksp. Teor. Fiz.* **91**, 353.

Berger, J. F., D. Gogny, and M. S. Weiss (1987). Lawrence Livermore National Laboratory, Preprint UCRL-96 59; also published in *J. Quant. Spectrosc. Radiat. Transfer* (December 1988).

Weiss, M. S. (1988). "Shape Isomers as Candidates for the Gamma-Ray Laser Storage State," in *Short and Ultrashort Wavelength Lasers*, C. R. Jones, Ed. (Proc. SPIE 875).

FY88 $180,000

The Femtosecond Laser Project

Principal Investigators: N. Landen, R. M. More, D. G. Stearns, and E. M. Campbell

The very short pulse of a subpicosecond laser allows us to heat solid targets to plasma temperatures (1–50 eV) before hydrodynamic expansion occurs, producing a thin layer of target material at solid-state density and plasma temperature. Studies of matter under these unique conditions will help resolve fundamental questions about atomic processes, previously inaccessible to direct experiment, that occur at high densities in stellar interiors, laser fusion targets, and nuclear weapon experiments.

During the past year, we completed the construction of a short-pulse laser that produces pulses with a 0.33-ps pulse width and exhibits excellent energy reproducibility. We characterized the laser output using pinhole-focus, autocorrelation, and spectral-analysis techniques, and verified that a transform-limited pulse is indeed produced (Figure 1). When focused to a several-times diffraction limited spot, this laser will be capable of producing intensities in excess of 10^{14} W/cm^2.

We also investigated the interaction of a high-intensity, picosecond laser probe beam with a preformed plasma. The plasma is produced first by focusing a pump picosecond laser beam onto a solid, planar target of gold, silicon, or carbon. X-ray yield is produced by a second probe beam. We monitored x-ray yield as a function of the intensity, polarization, and angle of incidence of the probe beam and of the relative time delay between pump and probe beams.

The measured x-ray yields, plotted as a function of beam polarization and angle of incidence, are characteristically produced by a combination of inverse bremsstrahlung and resonance absorption processes. Figure 2 shows resonance absorption for a gold target with a pulse delay time of 10 ps and a laser wavelength of 583 nm; a theoretical fit to these data yields a critical density scalelength of 75 nm.

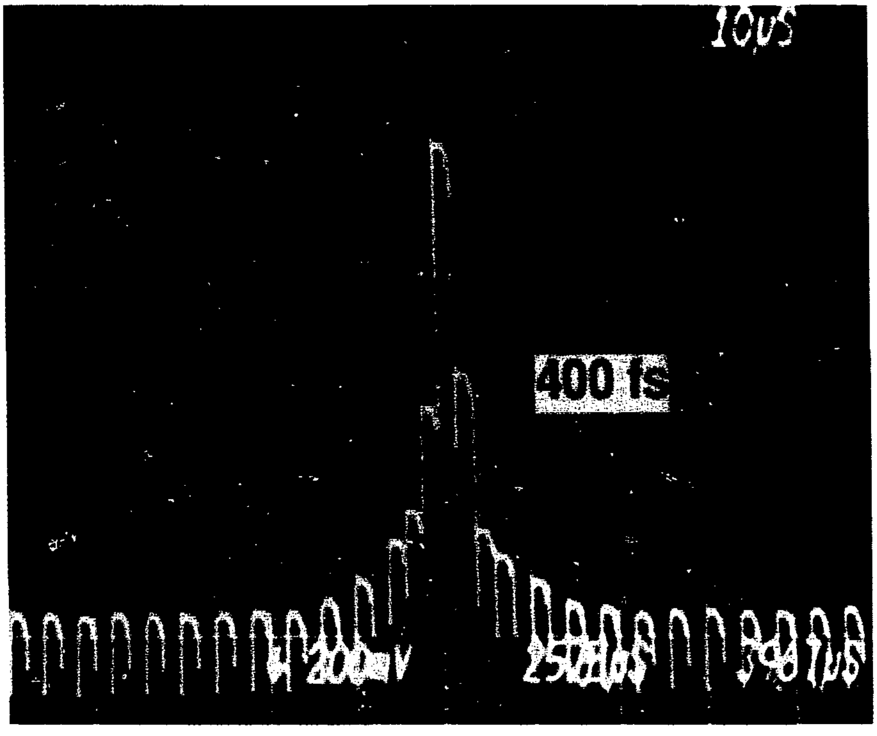

Figure 1. Autocorrelation curve of an amplified 583-nm laser beam showing a 400-fs (full width at half maximum) pulse.

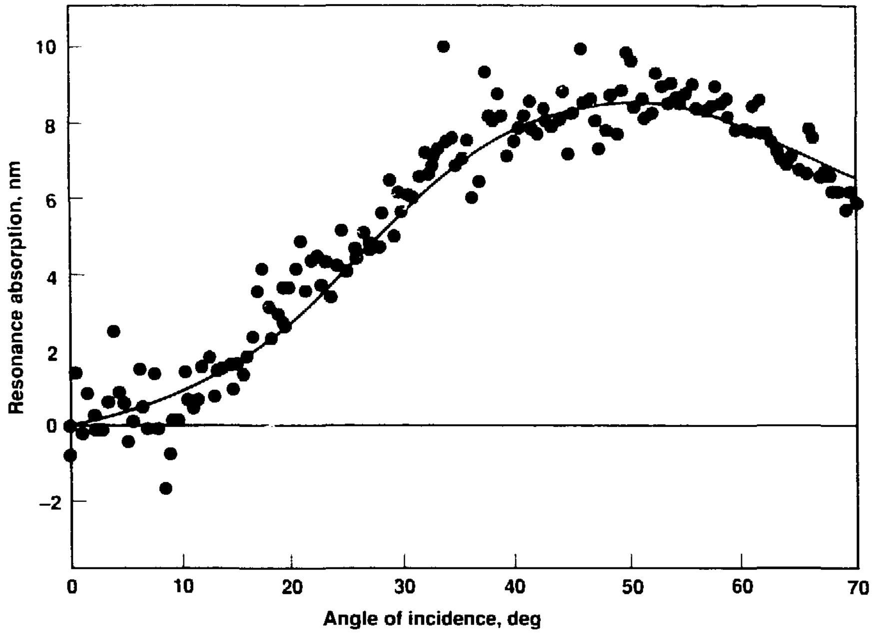

Figure 2. Measured resonance absorption vs angle of incidence of the laser probe beam. We used a gold target, a laser wavelength of 583 nm, a pump beam intensity of 10^{13} W/cm^2, a probe beam intensity of 10^{14} W/cm^2, and a 10-ps delay between pulses. The solid curve is a fit to theory that assumes a linear density gradient, yielding a critical density scalelength of 75 ± 10 nm.

By measuring scalelengths for various time delays, we infer plasma blow-off velocities on a picosecond time scale. The shortest scalelength measured to date is 20 nm and represents an improvement in spatial resolution of almost two orders of magnitude over more conventional interferometric techniques.

Our theoretical work centered on interpretation of aluminum reflectivity data taken by our collaborators at A.T.&T. Bell Laboratories. These experiments show a minimum reflectivity of 35% (*p*-polarization), which closely mirrors the theoretical minimum electrical conductivity occurring at target temperatures of 10–20 eV.

Next year, we plan to refine the two-pulse experiments to provide a direct measure of the target's surface expansion velocity for various materials in the preheat temperature range (1–50 eV). We will also consider a second method of measuring expansion velocity based on Doppler shift of the incident laser radiation; measurements by this method have been performed at Bell Laboratories, and we will analyze those data. In addition, we will make a number of improvements to the SPRINT computer code used to calculate short-pulse laser-target interaction. In particular, we will extend the code to treat interband transitions in more complicated metallic target materials and to allow for a limited degree of hydrodynamic expansion during the laser pulse.

Multiphoton Interaction of Intense Lasers with Atoms

Principal Investigators: A. Szoke, J. N. Bardsley, N. Landen, and M. D. Perry

Our laser facility, designed to carry out a variety of physics experiments, is now in full operation. We are investigating the process of multiphoton ionization and the properties of materials in the warm (few-electron-volt) solid-density phase. We are also assessing the physical phenomena that may be accessible with future, more powerful lasers.

Intense laser fields (10^{13} to 10^{17} W/cm^2) distort the electronic structure of atoms and ionize them when electrons absorb many photons. The objective of our experimental and theoretical research is to demonstrate clearly the role of intermediate excited states in multiphoton ionization. We used our time-dependent Hartree-Fock, split-operator, and quantum-defect codes to simulate data from experiments performed at LLNL, Bell Laboratories (Murray Hill, NJ), and Saclay (France). This work has dispelled much but not all of the controversy regarding the ionization process and the associated production of high-order harmonics. Figure 1 shows that our model calculations are in very good agreement with experimental results. Our work, both experimental and theoretical, has been extensively published.

We plan a second year of experiments, designed primarily to explore the effects of electron correlation. An improved electron spectrometer will be built to enable us to take full advantage of the current lasers and to ensure a continued flow of new data while more powerful lasers are being designed and constructed.

In our theoretical efforts for next year, we will continue to perform calculations on multiphoton ionization and harmonic generation to complement current experiments. We will apply the insights gained this year to computer simulations of the interaction of very intense lasers (10^{19} to 10^{21} W/cm^2) with dense gases and solids; this will help us to identify future applications of short-pulse, high-intensity lasers. Initially, we will concentrate on analyzing

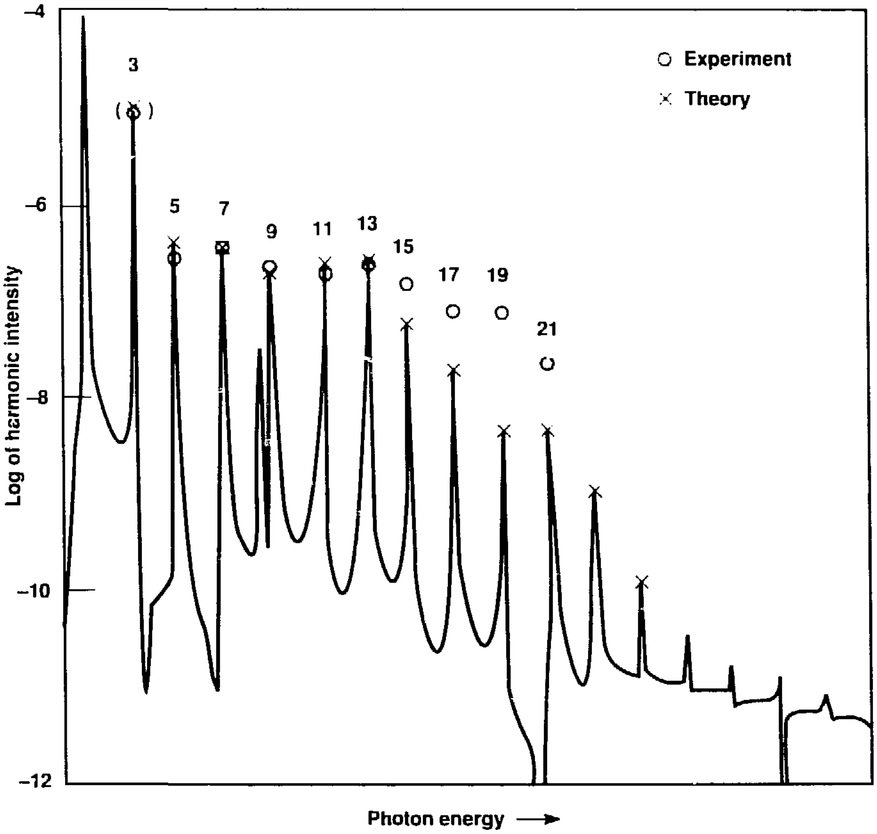

Figure 1. Predicted (×) and measured (o) harmonic intensities demonstrate intermediate states in xenon gas excited by 1.06-μm laser light. The numbers above the lines identify the harmonics of the laser frequency. Computer results are scaled to agree with the measured seventh harmonic intensity.

laser-induced fission and pair production; then we will shift our emphasis to characterizing the production of cold, strongly ionized plasmas suitable for recombination extreme-ultraviolet lasers. This latter study will be performed in conjunction with an analysis of similar electron-beam-pumped lasers initiated at the request of the 1988 Jason Study Group.

References

Appling, J. R., M. G. White, R. B. Dubs, S. N. Dixit, and B. V. McKoy (1987), "Circular Dichroism in Photoelectron Angular Distributions from Two-Color (1+1) REMPI of NO," *J. Chem. Phys.* **87**, 6927.

Cerjan, C., and R. Kosloff (1987), "Non-Perturbative Treatment of Particle Dynamics in a Semi-Classical Photon Field," *J. Phys. B* **20**, 441.

Dixit, S. N., D. A. Levin, and B. V. McKoy (1988), "Resonant Enhanced Multiphoton Ionization Studies in Atomic Oxygen," *Phys. Rev. A* **37**, 4220.

Kulander, K. C. (1987), "Time-Dependent Hartree-Fock Theory of Multiphoton Ionization: Helium," *Phys. Rev. A* **36**, 2726.

Kulander, K. C. (1988), "Time-Dependent Theory of Multiphoton Ionization of Xenon," *Phys. Rev. A* **38** (in press).

Landen, O. L., M. D. Perry, and E. M. Campbell (1987), "Resonant Multiphoton Ionization of Krypton by Intense UV Laser Radiation," *Phys. Rev. Lett.* **59**, 13.

Perry, M. D., and O. L. Landen (1988), "Resonantly Enhanced Multiphoton Ionization of Krypton and Xenon with Intense Ultraviolet Laser Radiation," *Phys. Rev. A* **38** (in press).

Perry, M. D., O. L. Landen, A. Szoke, and E. M. Campbell (1988), "Multiphoton Ionization of the Noble Gases by an Intense 10^{13} W/cm^2 Dye Laser," *Phys. Rev. A* **37**, 747.

Perry, M. D., A. Szoke, O. L. Landen, and E. M. Campbell (1988), "Nonresonant Multiphoton Ionization of Noble Gases: Theory and Experiment," *Phys. Rev. Lett.* **60**, 13.

Perry, M. D. (1987), *High Order Multiphoton Ionization of the Noble Gases*, Ph.D. thesis, University of California, Berkeley.

Rudolph, H., S. N. Dixit, B. V. McKoy, and W. M. Huo (1988), "Ionic Rotational Branching Ratios for REMPI of NO via the A $^2\Sigma^+(3s\sigma)$ and D $^2\Sigma^+(3p\sigma)$ States," *J. Chem. Phys.* **88**, 637.

Szoke, A. (1988a), "Note on Resonant and Non-Resonant Multiphoton Ionization," *J. Phys. B* **21**, L125.

Szoke, A. (1988b), "Theory of Multiphoton Ionization," in *Atomic Processes with Short Intense Laser Pulses*, A. D. Bandrauk, Ed. (*NATO ASI Series B: Physics*, Plenum Press), Vol. 171.

Szoke, A. (1987), *Theory of Atoms in Strong Pulsed Electromagnetic Fields*, Lawrence Livermore National Laboratory, Preprint UCRL-95294.

Szoke, A., and J. Garrison (1987), *Theory of Atoms in Strong Pulsed Electromagnetic Fields II*, Lawrence Livermore National Laboratory, Report UCID-21103.

Modeling Trace Gases and Atmospheric Chemistry

Principal Investigators: D. Wuebbles, J. Penner, and M. MacCracken

Our atmospheric models have played key roles in national and international analyses of the possible effects of trace gases on atmospheric ozone. We are now extending them to address the impact of trace gases on climate and on global atmospheric chemistry in the troposphere and stratosphere.

During FY88, we continued development of a new two-dimensional (zonally averaged) chemical-radiative-transport model of the global troposphere and stratosphere. This model is now operational and is being used to study the potential impact of chlorofluorocarbons and other trace gases on chemistry and climate. There is a pressing need for such research. NASA is even now sponsoring several conceptual designs for high-flying, hypersonic transport aircraft, although studies done in the 1970s, before sophisticated models were available, found a high sensitivity of stratospheric ozone (O_3) to nitrogen oxide (NO_x) emissions from possible future fleets of high-flying aircraft.

Comprehensive studies of trace-gas effects will require further development of our model. We must include additional feedback of atmospheric chemical and radiative processes with advective and eddy transport processes, and eventually climatic feedback processes and interactions with the oceans and the biosphere. To make the model more representative, we must find ways to treat the effects of wave interactions on eddy transport and to handle chemistry-wave interactions. We also need to make the model more efficient computationally to permit greater resolution and longer simulations. In addition, we plan to develop a special version of this two-dimensional model for detailed studies of global tropospheric chemistry; we will investigate the possibility of coupling this model with a two-dimensional ocean model for studies of air-sea chemical interactions.

We are also working to develop a global, three-dimensional tropospheric transport, transformation, and deposition model for investigating subcontinental, hemispheric, and global-scale perturbations of the reactive chemistry of the troposphere. Such a model is needed to study the international impacts of various energy policies and complicated climate-chemistry interactions. Within the past year, several attempts to simulate the tropospheric distribution of several long-lived species (whose chemistry can essentially be ignored) have been published, both by our group and by others.

We are developing a tropospheric reactive-chemistry model, using the Lagrangian approach embodied in our GRANTOUR model, that should accurately portray the gradients and spatial heterogeneity present in the tropospheric distributions of reactive species whose sources are primarily continental. With this model, we will initially treat species that react primarily with the hydroxyl (OH) radical: NO_x, CH_4, CO, and nonmethane hydrocarbons (NMHCs). The straightforward chemistry of these species will allow us to study their cycles as we develop and refine the model. The next step will be to parameterize O_3 production and loss for the concentration of these species. The concentration of OH will also become a parameterized function of the concentrations of the other species. During FY89, we expect to complete our studies of the NO_x and CH_4 cycles. Studies of CO and NMHCs, as well as the development of a parameterized chemistry model for O_3 and OH will be carried out in FY90.

References

Kinnison, D., H. Johnson, and D. Wuebbles (1988). "Sensitivity Study of Global Ozone to NO_x Emissions from Aircraft," *Proc. Quadrennial Ozone Symp.* (Gottingen, Federal Republic of Germany).

Walton, J., J. Penner, and S. Hameed (1988). *A Comment on "Seasonal and Diurnal Variability of Nitric Acid Vapor and Ionic Aerosol Species in the Remote Free Troposphere in Mauna Loa, Hawaii," by J. E. Galasyn, K. L. Tschudy, and B. J. Huebert, and on the Comment of E. Robinson and J. Harris*, Lawrence Livermore National Laboratory, Preprint UCRL-99535; submitted to *J. Geophys. Res.*

FY88 $90,000

Global-Scale Climate-Chemistry Modeling

Principal Investigators: C. Covey, D. Wuebbles, J. Penner, and M. MacCracken

To meet DOE programmatic requirements for addressing potential global-scale environmental perturbations arising from energy and national-security activities, we are developing three-dimensional interactive models of the climate and chemistry of the coupled atmosphere-ocean-land surface system in both prognostic (predictive) and diagnostic modes. The models will eventually cover scales from regional to global and domains from the deep ocean to the stratosphere. As interim steps toward this five-year objective, we are developing, testing, and applying a suite of models incorporating various dimensions, domains, and physical-chemical processes.

Over the past several years, interest has increased in the potential global-scale effects of human activities. Emissions of carbon dioxide, methane, nitrous oxide, carbon monoxide, reactive hydrocarbons, and other species pose the potential for significant chemical and climatic change. In addition, potential effects of global-scale nuclear war include significant chemical and climatic interactions among atmosphere, ocean, and land domains. Only models, carefully tested against observations, can address these issues.

Recent evidence of global climatic warming due to industrial activities (the greenhouse effect) has stimulated attempts at realistic ocean-atmosphere modeling. Accordingly, last year we focused our global climate modeling (GCM) efforts on assessing the effects of oceanic heat transport on present-day climate and on simulating possible climatic changes. Results from the first of these efforts support our hypothesis that changes in oceanic heat transport can be counteracted by compensating changes in atmospheric heat transport (Covey, 1988). In the second effort, we examined the sensitivity of climate to changes in ocean surface temperature and atmospheric aerosols. We postulated massive dust loading following impact of an asteroid or comet with the earth at the time of the Cretaceous-Tertiary boundary and at other times in the distant past. Surface temperature reductions resulting from blockage of sunlight by dust resemble but are more severe than "nuclear winter" (Figure 1).

We plan to extend our atmospheric GCM studies to model versions that include the cycle of the seasons and more realistic treatment of turbulence and surface processes. We also propose to test an intermediate-stage atmosphere-ocean model in which the atmosphere is represented by our GCM but the ocean is represented by a simple model of the upper mixed layer only. The foregoing steps, in addition to being necessary preconditions for developing a complete coupled ocean-atmosphere model, will continue to produce useful results concerning climate processes and sensitivity.

Reference

Covey, C. (1988). "Atmospheric and Oceanic Heat Transport: Simulations versus Observations," *Climatic Change* **13**, 149–159.

(a) Day 0

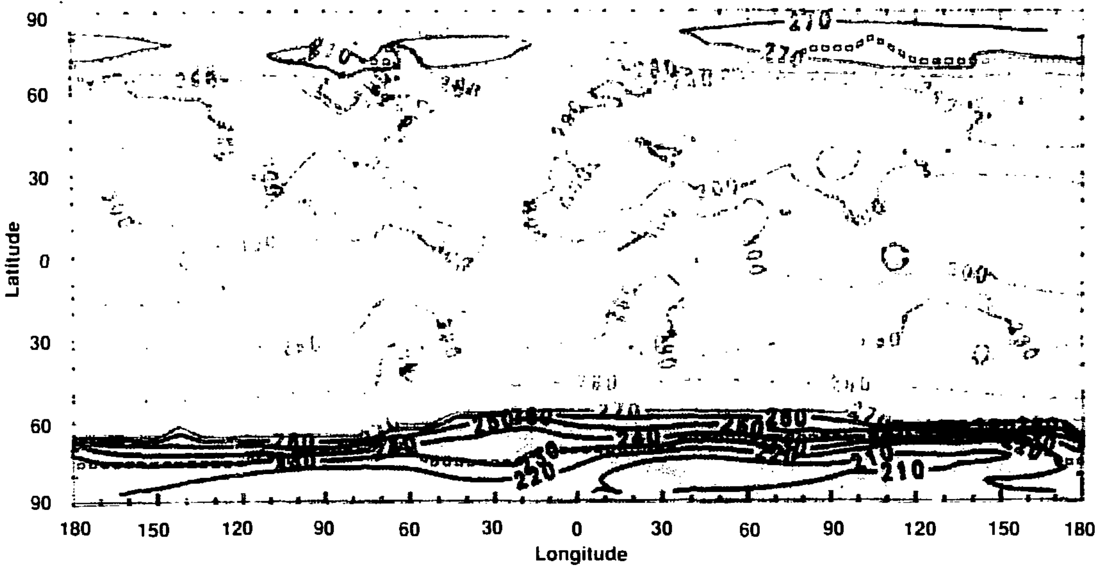

(b) Days 10–20

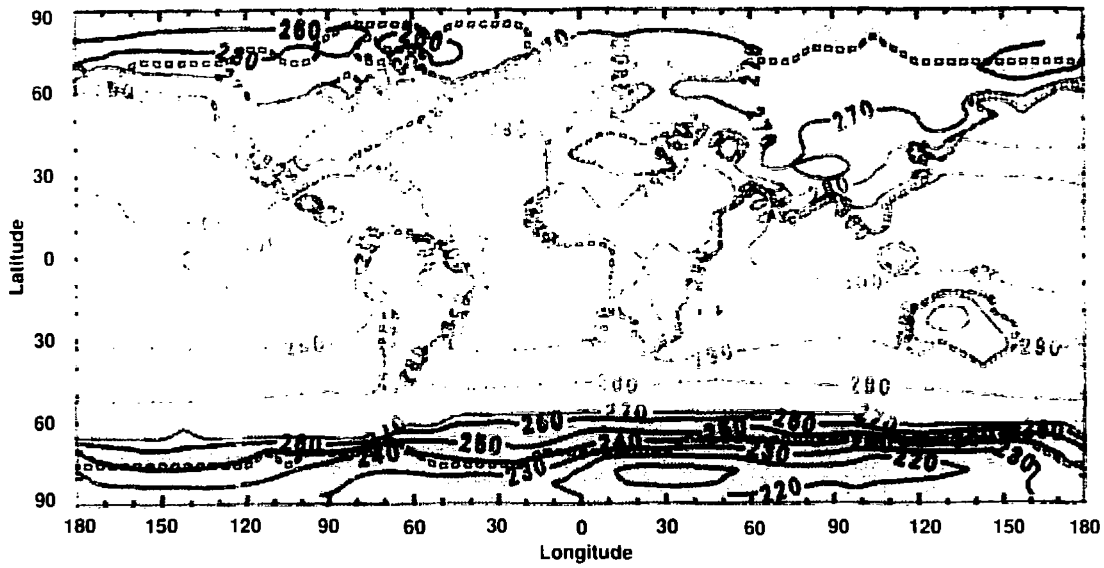

Figure 1. Isotherms show temperature response (in kelvins) of our global climate model to stratospheric dust aerosols generated by hypothetical impact with earth of a large asteroid or comet at the end of the Cretaceous era, about 70 million years ago. Extensive terrestrial and marine extinctions at that time included the disappearance of the dinosaurs. The amount of dust assumed saturates absorption of both visible and infrared radiation; virtually all sunlight is absorbed at the top of the model's atmosphere, and the dust acts as a blackbody in the infrared. Surface temperature reductions are qualitatively similar to, but more extreme than, those obtained in "nuclear winter" simulations; the global average of land surface temperature drops by about 15 K between Day 0, in mid-July (a), and Days 10–20 (b), nearly reaching the freezing point. Cooling is concentrated in the eastern (downwind) portions of the large Eurasian continent, however, with temperatures generally above freezing (>270 K) elsewhere.

I • R • & • D

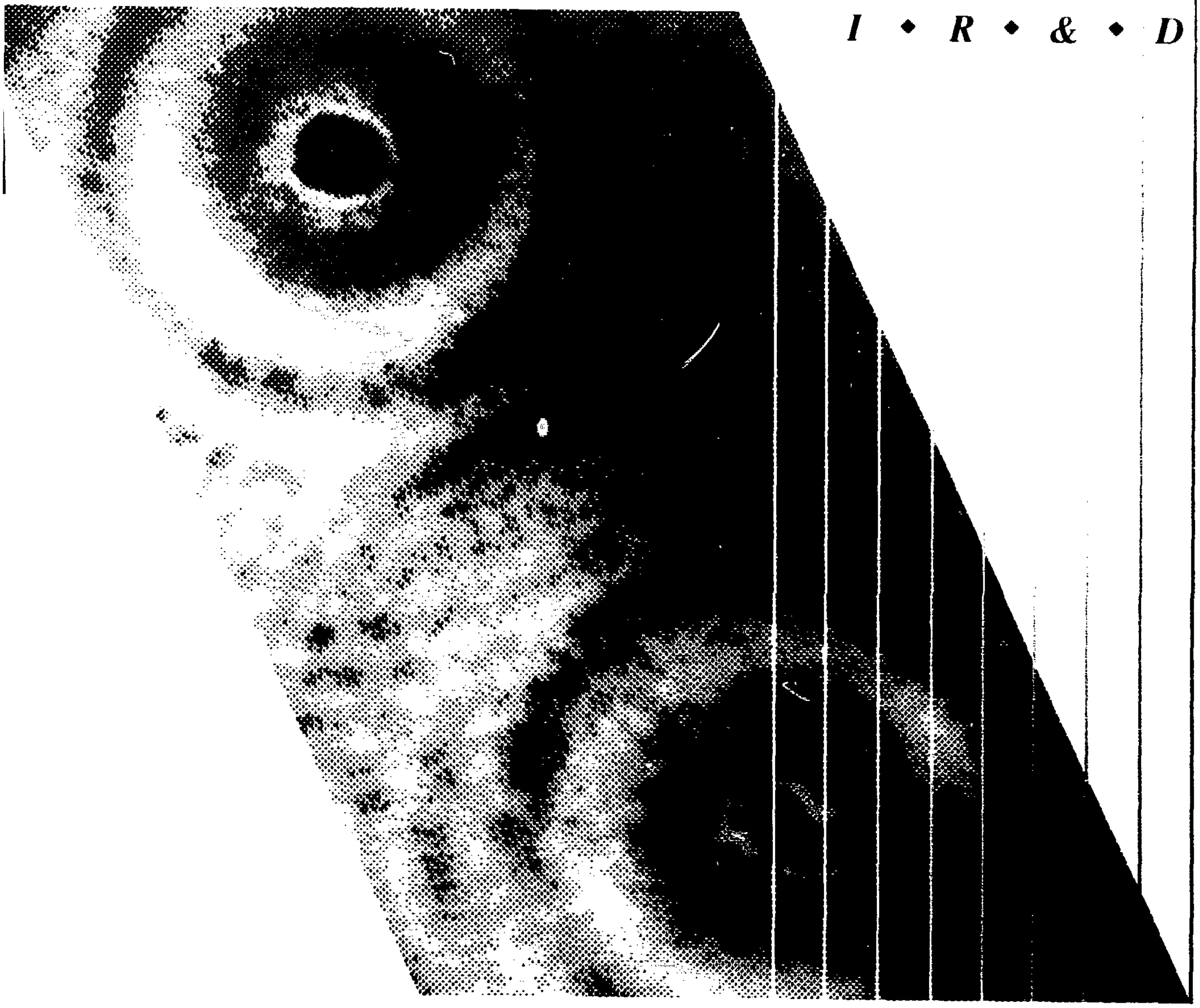

Director's Initiatives

Lawrence Livermore National Laboratory

Director's Initiatives

G. L. Struble

The Director's Initiatives are a select group of larger projects chosen by the LLNL Director for their technical merit and their potential to develop into large, independent, multiyear programs. Proposals are submitted by the appropriate Associate Director, who agrees to field a team of expert scientists and engineers and to manage the project. The proposals are carefully reviewed by the IR&D Review Committee and by invited specialists from inside and outside LLNL. Their recommendations are submitted to the Director for his approval. A typical Director's Initiative is funded for no more than three years at $0.5 to $1.5 million per year. Each project is reviewed by the IR&D Review Committee at least twice a year. In FY88, 14 Director's Initiatives were supported, for a total of $6.5 million.

The Director's Initiatives for biotechnology addressed three topics with broad impact: the ecological effects of low temperature and low light that are projected to follow nuclear war, the application of monoclonal antibodies as immunochemical sensors for monitoring environmental pollutants, and the use of recombinant DNA techniques to address environmental, energy production, and resource recovery issues. IR&D funds are also being used to track the national energy supply and demand; this helps us anticipate future energy trends and adjust Laboratory research efforts accordingly.

Beam research scientists are developing relativistic klystrons as a power source for high-gradient accelerators. Such klystrons could be used for large, linear electron-positron colliders, compact accelerators, and free-electron laser sources. Two relativistic klystrons have been built and tested so far.

Laboratory expertise in lasers is being extended in three Initiatives. In the first, new processes are being developed for growing the large, optically homogeneous crystals required for high-power lasers. Problems in optical homogeneity plague existing crystal-growth methods, and new process development is crucial to the future of solid-state lasers. The removal of waste heat is a serious problem in diode-array lasers; a second project is adapting silicon microchannel coolers, originally invented for wafer-scale integrated circuits, to cool laser diode arrays. In the third project, researchers are developing the technology to create three-dimensional, high-resolution x-ray holograms of biological structures *in vitro*, a long-sought goal of both x-ray-laser and biological research. The IR&D also sponsors a project to develop nonstandard high-resolution imaging techniques to overcome the atmospheric distortions that currently limit ground-based observations of objects in space.

One of the Laboratory's long-standing missions is the development of low-cost fusion energy. The goal of the Compact Torus project is to demonstrate the proof of principle of accelerating and focusing plasma rings magnetically confined by the fields of a compact torus. If successful, this work will provide the basis for an accelerator that could serve as an efficient, low-cost, inertial fusion driver, as a fast-opening switch, as an injector for magnetic fusion machines, and as an x-ray generator for simulating nuclear weapon effects.

Finally, the Director's Initiatives are supporting two projects to develop the tools and techniques needed to design, manufacture, and test the complex digital processors of the 1990s and the 21st century. These will be very highly integrated, with electronic assemblies containing millions of components on a single 10- to 15-cm-diameter silicon wafer. The goal of one project is to develop the computer-aided design tools for optimizing the layout of these complex circuits; the goal of the other is to devise the new fabrication techniques that will be needed.

FY88 $227,000

Biological and Ecological Effects of Nuclear War

Principal Investigators: J. R. Kercher and L. R. Anspaugh

We are developing our capability to assess the effects of climate change caused by nuclear war on both agricultural and natural ecosystems. We found that in two of the three tested crops, existing crop models do not predict the results of experimental treatments of lowered light and temperature. In addition, our regional model of forest recovery indicates that reforestation of dominant species occurs in a regular pattern, whereas reforestation of subordinate species is irregular and stochastic.

Our goal is to determine the biological and ecological effects that would be caused by a period of reduced light and temperature that has been projected to follow a nuclear exchange. We first convened a workshop to develop an agenda for such research (Kercher and Mooney, 1985). The workshop recommended an approach that distinguished between agricultural systems and natural, unmanaged ecosystems. It also recommended research at the organism, community, and regional levels of resolution for both agricultural and natural ecosystems. The report from the workshop stressed that the physiological responses of interest would arise from a climate regime outside our current research experience, and new phenomena might well be observed.

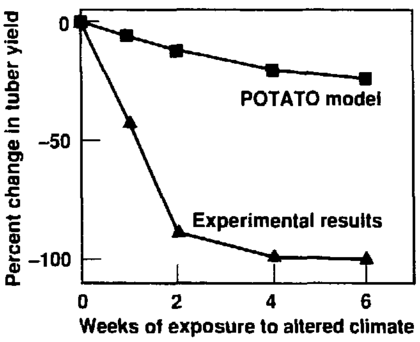

Figure 1. Comparison of calculations on tuber yield from the POTATO model versus experimental data on potatoes from the University of Wisconsin Biotron. The large disagreement at extended exposures to altered climate conditions is due to the inability of the POTATO model to simulate the mortality of tops of potato plants observed during recovery from altered climate.

We are implementing these recommendations by carrying out two types of studies. The first includes coordinated experimental and modeling studies on individual crops to provide the capability for an agricultural assessment. The second includes modeling studies on natural systems at the regional scale to assess the recovery potential of unmanaged systems. We identified integrated modeling and experimental studies at the plant level as necessary precursors for crop assessments (Detling *et al.*, 1988). We studied the three crops—wheat, potatoes, and soybeans—that rank first, third, and eighth, respectively, in global production. In natural systems, we are continuing our modeling of forest recovery at the regional scale. The unique computational capabilities at LLNL lend themselves to research in this area: regional studies constitute a new field in ecology, and exploratory work should yield large returns.

In FY88, we compared the output of existing models for wheat, potatoes, and soybeans to the experimental response to reduced light and temperature obtained in prior years (Cowles *et al.*, 1988). As described below, we found that existing models for wheat and potatoes do not exhibit the phenomena actually observed in experiments. In soybeans, on the other hand, an existing model does yield an adequate description of experimental responses (Kercher *et al.*, 1988a).

In research funded by LLNL and conducted at the University of Wisconsin Biotron (Rose *et al.*, 1986 and 1987), potatoes, wheat, and loblolly pine were exposed to a 99% light reduction and a 15°C temperature reduction for 1, 2, 4, and 6 weeks (soybeans were exposed for 1 and 2 weeks only). Potato yield was reduced by 42, 89, 99, and 99% for the 1-, 2-, 4-, and 6-week treatments, respectively. No potato plant tops survived the 4- and 6-week treatments, and most plant tops for the 2-week treatment died as well. In contrast, the POTATO model of Ng and Loomis (1984) predicts yield reductions of only 10, 23, 48, and 72%, respectively. In this model, reduced yields result from reduced top growth during the treatment period and natural leaf senescence resulting in reduced levels of net production recovery for tuber growth. Figure 1 compares the POTATO model for tuber yield with the Wisconsin data. The model did not predict the plant-top mortality observed in experiments.

In wheat, Rose *et al.* (1986) found that yield was reduced over the same four treatment periods by 0, 71, 86, and 81%, whereas the CERES wheat model (Otter and Ritchie, 1985), predicted a yield change of +24, +3, −26, and −38%, respectively. Although a dramatic decrease in tiller and spike production occurred between the 1- and 2-week experimental treatments, the model predicted no such reduction. The yield loss computed for long treatments can be attributed to reduced top growth and natural senescence in the model simulations.

Experimental yield reductions for soybeans were not significant for the 1- and 2-week treatments (Rose *et al.*, 1986). The SOYGRO model (Jones *et al.*, 1987) predicted a yield reduction of 4 and 8%, respectively; the GLYCIM model (Acock *et al.*, 1983) predicted no yield change for both treatments. Rose *et al.* (1987) have suggested that compensatory growth occurs in pine and soybeans after the treatment period, but no such growth occurs in wheat and potatoes.

The conditions we have studied lie outside the range of experimental experience on which most crop models are based. We conclude that existing models do not simulate the phenomena that occur in wheat and potatoes under such unusual conditions.

We have continued to develop our regional-scale model of forest recovery, VISTA (Kercher *et al.*, 1988b), which is constructed as a grid of community models spread over a landscape. At each grid square, the community model SILVA simulates tree growth and succession of species in that grid square. Fire and seeds can spread from one grid square to another. During FY88, we completed modifications to VISTA to allow empirical functions of seed spread, and we installed seed spread functions extracted from the ecological literature. We also performed preliminary tests of model performance and examined the reforestation response of a mixed-conifer forest to a massive disturbance. Our simulations indicate that reforestation is regular and deterministic for the dominant species and irregular and stochastic for subordinate species.

Figure 2 shows a simulation of reforestation from seeds of a mixed-conifer forest deposited in one corner of a 200- by 200-m area. Figure 2a shows the ponderosa pine basal area 50 years after seed deposition, just before maturation and seed production. The term "basal area" refers to the total cross-sectional area of a species in the stand; the basal area in the figure is in square meters per hectare. Figure 2b shows the basal area 100 years after seed deposition from mature trees. A monotonic decrease in seed dispersal from the source results in larger values of basal area near the source. At 200 years, available seed no longer limits basal area growth. Other species of the mixed-conifer type persisted near the original corner but were not as successful as pine in dispersing throughout the area.

We plan to study the biological assumptions embedded in the crop models that produce the discrepancies between predictions and observation. We will examine the possible modifications of the models' treatments of aging, wilting, and phenology (timing of life stages) that might improve predictions for conditions of reduced light and temperature. We also plan to continue developing and testing the spatial forest community model. We expect to improve the submodel concerning water relations for increased accuracy for California topology, to include other California conifers, and to make comparisons of model results to selected data from California forests.

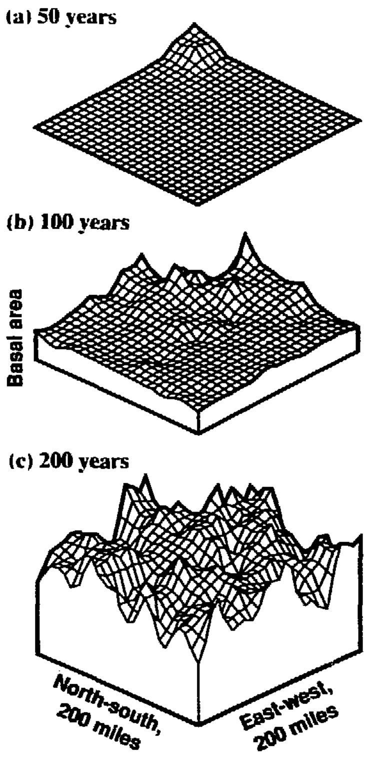

Figure 2. Simulation of reforestation at three times following a massive disturbance. (a) Basal area of ponderosa pine 50 years after deposition of a mix of seeds of the mixed-conifer forest type in one corner of a 200- by 200-mile area. The onset of maturity occurred approximately 46 to 48 years after seed deposition. (b) Basal area of ponderosa pine 100 years after deposition. (c) Basal area of ponderosa pine 200 years after deposition.

References

Acock, F., V. R. Reddy, F. D. Whisler, D. N. Baker, J. M. McKinion, H. F. Hodges, and K. J. Boote (1983). *Response of Vegetation to Carbon Dioxide. The Soybean Crop Simulator GLYCIM Model Documentation 1982*. Department of Agronomy, Mississippi Agriculture and Forestry Experimental Station, Mississippi State University, Mississippi State, MS.

Cowles, S., J. R. Kercher, and P. J. Tate (1988). "Investigation of Crop Response to Climate Alterations Induced by Nuclear Exchange," *Bull. Eco. Soc. Amer.* **69** (abstract, in press).

Detling, J. K., J. R. Kercher, W. M. Post, S. W. Cowles, and M. A. Harwell (1988). "Priorities for Modeling Biological Processes in Climates Altered by Nuclear War," in *Proc. Workshop on Ecological Effects of Nuclear War*, Technology Application Center Report 88-2, University of New Mexico, Albuquerque, NM.

Jones, J. W., K. J. Boote, S. S. Jagtap, G. Hoogenboom, and G. G. Wilkerson (1987). *SOYGRO V5.4 Soybean Crop Growth Simulation Model User's Guide*. Agricultural Engineering Department and Agronomy Department, University of Florida, Gainesville, FL, and IBSNAT Project, Department of Agronomy and Soil Science, University of Hawaii, Honolulu, HI; Florida Agricultural Experimental Station, Journal No. 8304.

Kercher, J. R., S. Cowles, P. Tate, and L. R. Anspaugh (1988a). "Ecological Effects of Climate Changes Caused by Nuclear War," in *Proc. Global Effects Program Technical Meeting* (Defense Nuclear Agency, Washington, D.C.).

Kercher, J. R., S. M. Umschied, and D. Fledderman (1988b) "Modeling Dynamics of Spatial Heterogeneity in a Mixed-Conifer Landscape," *Bull. Eco. Soc. Amer.* **69** (abstract, in press).

Kercher, J. R. and H. A. Mooney, Eds. (1985). *Research Agenda for Ecological Effects of Nuclear Winter*, Lawrence Livermore National Laboratory, Report UCRL-53588.

Ng, N., and R. S. Loomis (1984). "Simulation of Growth and Yield of the Potato Crop," *Simulation Monographs* (PUDOC, Wageningen, The Netherlands).

Otter, S. and J. T. Ritchie (1985). "Validation of the CERES Wheat Model in Diverse Environments," in *Wheat and Growth Modeling*, W. Day and R. K. Atkin, Eds. (NATO Advanced Science Institutes Series A: Life Sciences, Plenum Press, NY), Vol. 86, pp. 307–310.

Rose, E., J. Palta, B. McCown, T. Tibbitts, and M. Vinotti (1986). "Productivity of Winter Wheat and Potatoes during a Nuclear Winter Scenario," *Agronomy Abstracts* (American Society of Agronomy), p. 19.

Rose, E., J. Palta, B. McCown, T. Tibbitts, and M. Vinotti (1987). "Productivity of Loblolly Pines and Soybeans Under a Nuclear Winter Scenario," *Plant Physiol.* **83**, 71.

Monoclonal Antibody Research and Instrumentation

Principal Investigator: M. Vanderlaan

We are building two biosensors that combine the specificity of antigen-antibody reactions with microelectronic sensors using our antibodies to dioxin and pesticides. One sensor is based on changing the vibrational frequency of a piezoelectric silicone membrane; the other is based on an optical-fiber fluorescence detector.

Our long-range goal is to fabricate real-time, portable assay systems for detecting environmental pollutants. In past years, we have developed a set of monoclonal antibodies to dioxin and various pesticides. Methods have also been refined for extracting these pollutants from food, soil, and chemical wastes. We have shown that immunochemical methods are comparable in sensitivity to techniques of conventional analytical chemistry for environmental monitoring while offering considerably faster sample analyses. This year, we have been integrating our antibodies into two new sensing devices. The devices differ from conventional antigen-antibody immunochemical assays in that they provide an electronic output, are suitable for microfabrication, and can potentially offer on-line immunochemical detection.

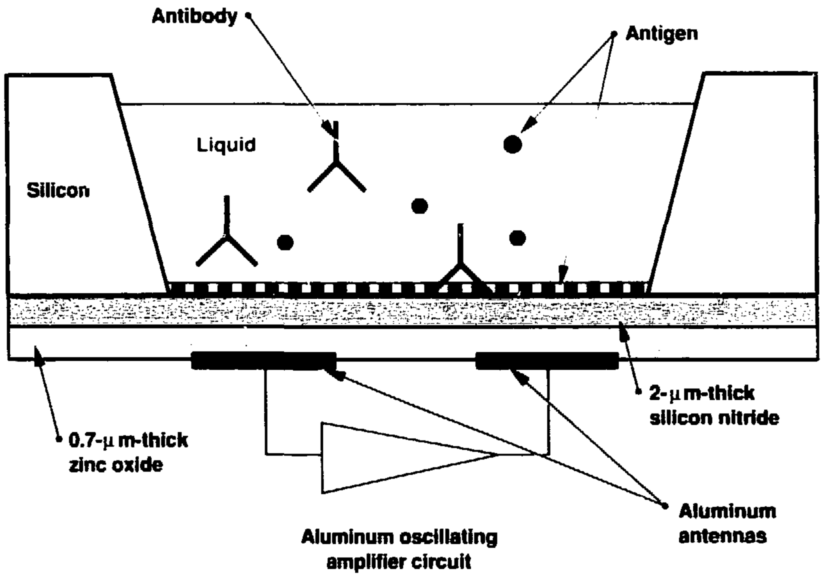

Figure 1. Surface-acoustic-wave immunosensor. A silicon wafer is coated with a layer of silicon nitride and a piezoelectric layer of zinc oxide. Next, a well about 1 mm wide is chemically etched in the silicon, leaving a thin membrane. After an aluminum oscillating amplifier circuit is printed on the bottom of the membrane, a wave launched from one antenna is received by the other. When antibody and free antigen are added to the well, the amount of antibody bound to the membrane causes a shift in frequency to the acoustic wave. We can enhance antibody detection by increasing antibody mass through conjugation to colloidal gold.

In collaboration with the Sensor and Actuator Center at UC Berkeley, we have designed and fabricated surface-acoustic-wave immunosensors. Acoustic waves propagate in piezoelectric crystals and are influenced by changes in the crystal surface. The detector shown in Figure 1 consists of a silicon wafer coated on one side with silicon nitride and with zinc oxide (a piezoelectric material). The silicon is etched away completely, leaving a rectangular well about 1 cm^2 in area, where the immunochemical reaction occurs. The remaining membrane of silicon nitride and zinc oxide is induced to oscillate by launching a wave from one interdigitated aluminum transducer. The wave propagates across the membrane and is detected with the second antenna. Because the wavelength of the oscillation is longer than the thickness of the membrane, wave propagation is influenced by factors on both surfaces of the membrane. With this device, we can measure shifts in wave frequency as small as one part per million. The long wavelength also minimizes loss of energy into the liquid in the well

We have now fabricated several sensors that show exquisite sensitivity to changes in temperature, pressure, fluid density, fluid viscosity, and surface loading. The wells on these wafers can be coated with antigen, and the antibody in solution can be conjugated to colloidal gold. The mass of gold binding to the surface of the sensor should produce a readily detectable shift in the Lamb-wave frequency and thus enhance antibody detection.

We are developing another sensor using optical-fiber probes previously developed at LLNL. Our goal here has been to fabricate immunosensors that can be plugged into available optical hardware for measurements of environmental pollution. In this work, antigen is coated on an optical fiber, and the binding of fluorescein-conjugated antibodies is measured using the evanescent wave.

Figure 2 shows the equilibrium fluorescence intensity observed when antigen-coated fibers are incubated in solutions of various concentrations of fluorescein-conjugated antibodies. Figure 2a shows how fluorescence intensity saturates in antibody solutions greater than 0.1 mg/ml, reflecting a saturation of available binding sites on the fiber. Figure 2b shows that at low concentrations of antibody (<0.01 mg/ml), fluorescence intensity is proportional to antibody concentration. These relative values of equilibrium fluorescence intensity are reached within 10 min of reaction time. In addition to studies on the equilibrium fluorescence intensity, optical-fiber immunoassays can be used to independently measure the on and off rates for antigen-antibody binding.

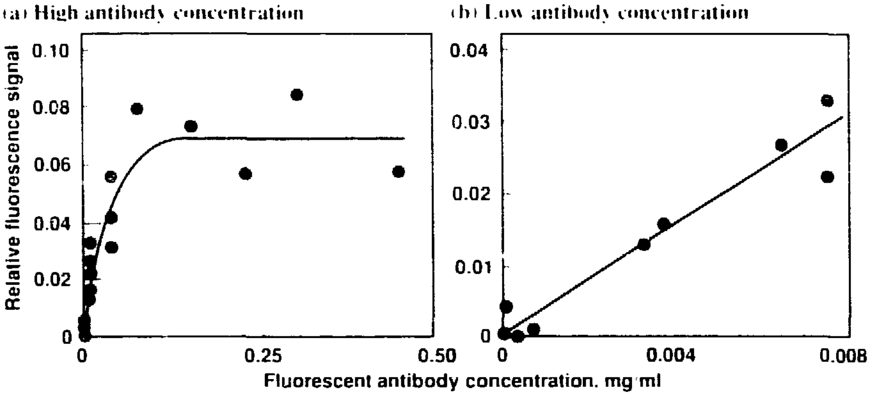
(a) High antibody concentration

(b) Low antibody concentration

Figure 2. Fluorescence signals recorded by our optical-fiber probe. Fibers were coated with albumin-phenoxybenzoic acid and incubated with the PY-1 monoclonal antibody. This antibody recognizes both phenoxybenzoic acid and permethrin, a widely used insecticide. The PY-1 antibody was conjugated to fluorescein to provide a fluorescence tag for detection. (a) Fluorescence saturates in antibody solutions >0.1 mg/ml. Equilibrium fluorescence was reached 10 min after placing the fiber in solution. (b) At low concentrations of antibody, fluorescence is proportional to antibody concentration.

References

Vanderlaan, M., L. H. Stanker, B. E. Watkins, P. Petrovic, and S. Gorbach (1988). "Improvements and Application of an Immunoassay for Dioxin Environmental Toxicology and Chemistry," *Environmental Toxicol. Chem.* 7, 859–870.

Vanderlaan, M., B. Watkins, and L. Stanker (1988). "Environmental Monitoring by Immunoassay," *Environmental Sci. Technol.* **22**, 247–254.

Microbial Genetic Engineering Biotechnology

Principal Investigator: E. Garcia
Co-Investigator: L. J. Fry

We are continuing to develop technologies for the genetic engineering of bacterial species with metal-detoxification and resource-recovery properties. Our effort is focused on two microorganisms:* Thiobacillus ferrooxidans *will be used as a biological agent for removing pyritic sulfur from high-sulfur coal and for recovering valuable metals from fly ash, and* Clostridium pasteurianum *will be used in a bioreductive process that may be useful in the detoxification of oxyanions from agricultural and mining drainage waters. We have also started a collaborative project to study the properties and potential applications of newly discovered, extremely thermophilic bacteria found in geothermal fluids.

Using the technique of recombinant DNA, we plan to enhance bioconversions carried out by microorganisms as viable alternatives for the reclamation of resources and the detoxification of energy-related wastes. Some of the possibilities for this biotechnology include the recovery of strategic metals from fly ash, the removal of pyritic sulfur from coal, and the removal of toxic selenate from waste water.

Most conventional chemical or physical techniques for removing waste products and for recovering metals involve technologies that are energy-intensive, detrimental to the environment, and expensive. Microbial activities that can be substituted for the more conventional techniques have distinct advantages in that they are simple, environmentally safe, and inexpensive. Although natural activities carried out by microorganisms often coincide with those activities that are desirable in terms of biotechnological applications, the reactions involved are, for the most part, slow, low in yield, and limited by factors not well understood. To address some of these shortcomings, we are developing genetic engineering techniques to be used in two suitable bacterial species. Development of these techniques should allow for the elucidation and manipulation of pathways in the bacteria of interest that are crucial to metal detoxification and recovery.

We have made important advances this year in developing genetic techniques for studying *Thiobacillus ferrooxidans* and *Clostridium pasteurianum*, two bacterial species that exhibit unique reductive and oxidative properties, respectively, towards metals. In the area of metal reduction, we have

Table 1. Removal of selenate ions from solution by genetically engineered *E. coli*.

Original concentration, ppm	***E. coli* with pSelr2**		***E. coli* with pUC18**		***E. coli* with pSelr3**	
	Concentration,* ppm	**Percent removal**	**Concentration,* ppm**	**Percent removal**	**Concentration,* ppm**	**Percent removal**
0	–	–	0	–	0	–
25	15.3	39	18.1	27	18.3	27
50	31.0	38	34.3	31	34.2	31
100	60.9	39	80.0	20	92.0	8

*Data are expressed as parts per million (ppm) selenate remaining in solution after incubating samples with a fixed number of cells for 24 hours at 30°C. Limits of detection for the assay are 1 ppm; limits of precision are ±0.5 ppm.

cloned for the first time a gene encoding an enzymatic activity involved in the reduction of the toxic oxyanion selenate to the nontoxic element selenium. The gene responsible for the reductive step has been thoroughly characterized and shown to confer on *Escherichia coli* cells (cells normally incapable of reducing selenate) the ability to intracellularly reduce the toxic compound. We performed a preliminary chemical analysis of samples treated with the genetically engineered *E. coli* strain to determine the amounts of selenate remaining in solution after incubating the cells for 24 hours. Table 1 shows the percent removal of selenate by *E. coli* cells carrying the plasmid pSelr2. (The term "plasmid" refers to an autonomously replicating, circular DNA molecule that can be used to move genes into and out of bacteria; the name "pSelr" arises from the selenate-reducing properties of this plasmid.) The cells carrying pSelr2 removed significantly larger amounts of selenate originally present in the solution than control cells (cells containing the parent cloning vector plasmid pUC18, without a *Clostridium* gene insert) or than cells with the plasmid pSelr3 (in which part of the Selr gene has been deleted). We expect that reintroduction of multiple copies of this selenate-reducing (Selr) gene will improve the ability of *C. pasteurianum* cells to reduce selenate. We are currently developing the methodology for reintroducing this gene into *C. pasteurianum*.

The useful properties of *T. ferrooxidans* in the recovery and exploitation of mineral ore and waste detoxification depend on the organism's ability to oxidize ferrous ions and/or sulfur compounds, with the production of sulfuric acid from the latter. To better understand the overall scheme in the sulfur metabolism of this bacterium, we have isolated the gene encoding the ATP sulfurylase enzyme, which is the first enzyme in the sulfur assimilatory pathway. Studies of the enzymatic activity obtained in cells carrying the cloned gene showed that an active product is obtained and that the gene appears to be under a type of regulation distinct from that of the *E. coli* host.

We have also isolated a new plasmid from a *T. ferrooxidans* strain

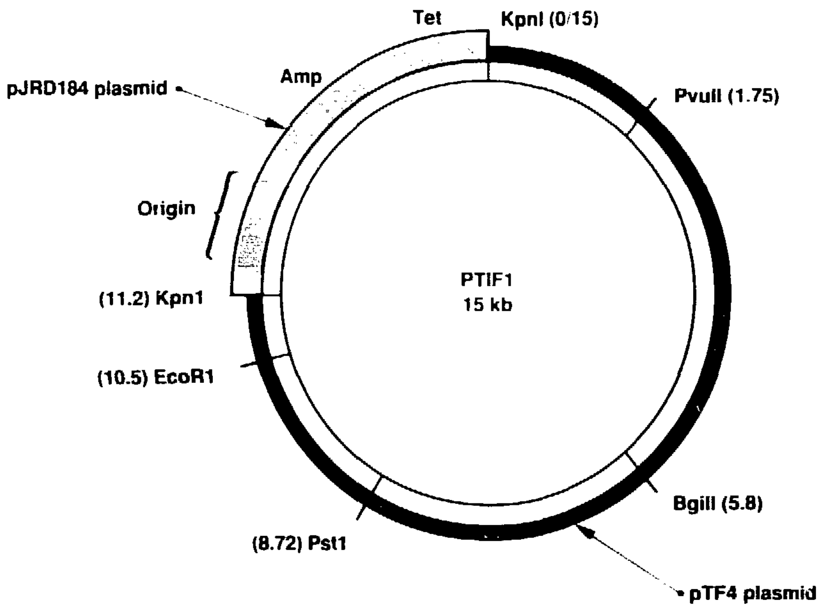

Figure 1. *Thiobacillus ferrooxidans–Escherichia coli* hybrid plasmid. This hybrid plasmid was constructed by ligating DNA segments from an *E. coli* plasmid (pJRD184) and a newly discovered plasmid from *T. ferrooxidans* (pTF4). Plasmid pJRD184 contributes genetic information that allows replication of this hybrid plasmid in *E. coli* cells and genes for ampicillin and tetracycline resistance useful for selection and maintenance of the plasmid. Plasmid pTF4 contributes appropriate genetic information for replication and maintenance of the hybrid plasmid when resident in *Thiobacillus* host cells. The term kb refers to the size of the plasmid in kilobases or 1000 bases (such bases are the building blocks of DNA). Numbers in parentheses are the distance in bases from an arbitrary beginning to a given point in the plasmid. Designations such as KpnI and PvuII refer to sites in the plasmid at which specific DNA-cutting enzymes can act. The origin of replication is the part of the plasmid involved in making new copies at the time of cell division. The total size of this hybrid plasmid is 15 kb.

Using this plasmid, we have recently constructed a hybrid genetic vector that possesses all the functions required for its appropriate expression in *T. ferrooxidans* (see Figure 1). We plan to test this vector for its ability to reintroduce genes back into *T. ferrooxidans*.

As a direct result of our research under this program, we have established a four-person collaboration with researchers in the Laboratory's Earth Sciences Department to study microorganisms living under extreme temperatures and pressures. We have analyzed geothermal fluids from three wells in Nevada and California for the presence of viable microorganisms. Bacteria with morphologies that are characteristic of extreme thermophiles (heat lovers) have been observed repeatedly by phase-contrast microscopy in each of the water samples obtained thus far. Our preliminary studies indicated that some of the organisms could grow in the laboratory at temperatures as high as 105°C. We have recently cultured in large numbers one class of organism that grows at 100°C. We have obtained for the first time scanning electron micrographs of one of the new thermophilic bacteria (see Figure 2). Eventually we hope to identify thermophilic bacteria from which we can develop biotechnologies for use in subsurface processing of mineral, organic, and geothermal wastes. Novel, heat-resistant biocatalysts and biopolymers obtained from such bacteria would provide for unique enzymatic reactions at high temperatures and the production of unparalleled biodegradable, heat-resistant plastics.

Next year, we will attempt to capitalize on some of our recent findings in the area of bacterial reduction. The availability of the selenate-reducing gene(s) will enable us to select environmentally occurring bacteria from selenium-contaminated waters or soils. Such bacteria possess selenate-reducing ability and are even more efficient than the presently available laboratory strains. Construction of genetic vectors capable of introducing new genetic material into *T. ferrooxidans* and *C. pasteurianum* will be a high priority. We will use the recently discovered plasmid(s) from *T. ferrooxidans* coupled to appropriate antibiotic and metal-resistant genes for the construction of vectors capable of replicating and transferring genes into and out of this strain. For *C. pasteurianum*, we will develop a similar shuttle vector by adapting a plasmid from a related bacterium.

In the area of DNA uptake and transfer, we will continue our work on protoplast generation and regeneration established for *C. pasteurianum*. We will use the newly developed method of electroporation, which makes use of an electric field to effect DNA uptake by bacterial cells.

(a) Visible-light micrograph

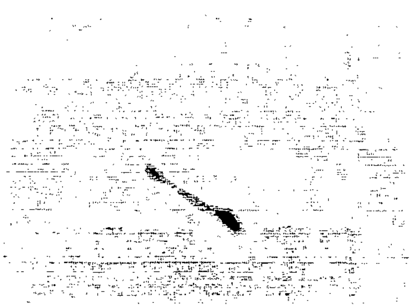

(b) Electron micrograph

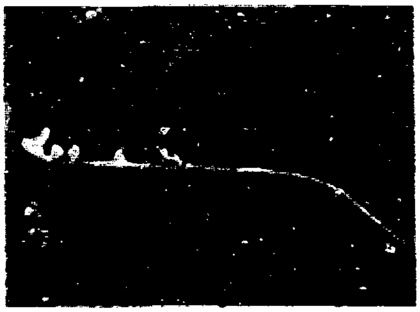

Figure 2. (a) Visible-light micrograph (3500×) of a recently isolated thermophilic bacterium. The cell is approximately 3 µm in length, with an enlarged structure at one of its ends. (b) Electron micrograph of the same bacterium as that shown in (a). The magnification is 9940×. We obtained this organism by culturing fluid samples from the Steamboat Hill Geothermal plant near Reno, Nevada. The incubation temperature was 100°C.

References

Fry, I. J., M. L. Hanna, R. T. Taylor, G. E. Bush, and E. Garcia (1988), "Cloning of ATP Sulfurylase Activity from *Thiobacillus ferrooxidans* and its Expression in *Escherichia coli*," *Ann. Mtg. Amer. Soc. Microbiol.* **88**, 167.

Taylor, R. T., M. L. Hanna, G. E. Bush, and E. Garcia (1988), "Bacterial Reduction of Selenium Oxyanions," *Ann. Mtg. Amer. Soc. Microbiol.* **88**, 250.

Methane-Conversion Enzymes

Principal Investigators: R. T. Taylor and M. W. Droege
Co-Investigators: S. S. Park and M. L. Carman

We are attempting to develop technologies that convert methane to a useful liquid fuel by duplicating the characteristics of the reaction catalyzed by methane monooxygenases, naturally occurring bacterial enzymes that transform methane into methanol.

It is well known that certain microorganisms can efficiently and selectively utilize methane gas (CH_4) as the sole source of carbon for energy and cellular growth. The first reaction in this metabolic pathway is the conversion of methane to methanol, catalyzed by the methane monooxygenase enzymes:

$$CH_4 + O_2 + NADH + H^+ \xrightarrow{25\text{–}50^\circ C} CH_3OH + H_2O + NAD^+ \ .$$

A thorough understanding of this biocatalytic system may lead to the development of a process that uses stabilized protein components for the conversion of methane to methanol and perhaps even to the design of new lower-temperature, nonenzymatic chemical catalysts that mimic the enzymatic action that occurs in the initial bioconversion of methane.

Our research is being conducted in three stages: (1) growing select organisms that contain methane monooxygenase, (2) isolating and purifying the active enzyme protein, and (3) identifying the active catalytic site and elucidating the mechanism of the enzymatic reaction. In FY88, we concentrated our efforts on the first phase—studying the growth of the organisms.

We are studying two types of bacteria, *Methylobacterium organophilum* (CRL-26) and *Methylosinus tricosporium* (OB-3b). We cultured these organisms in sterile nutrient media using methane gas as the substrate. We transferred the growing organisms to agar nutrient culture plates and stored them under methane gas, allowing the growth of individual bacterial colonies. Individual colonies were then cultured and plated to produce single-clone subcultures of the bacteria. These subcultures have been frozen and will serve as seed cultures for future experiments.

Preliminary kinetic studies are under way to determine the growth curves of these two organisms in order to maximize bacterial growth rates in the presence of methane and to maximize intracellular enzyme production. In FY89, we will continue to examine the influence of cell-culture parameters on the intracellular levels and stability of the methane monooxygenase enzyme. This work will lead directly to large-scale production of the bacteria (using a fermentation reactor) and subsequently to isolation of the enzyme protein from broken cell extracts for nonaqueous-solvent catalytic studies and for experiments directed at describing the properties of the metal-binding active site within the biocatalyst.

Culturing Thermophilic Microorganisms from Geothermal Fluids

Principal Investigators: J. Tang, E. Garcia, and J. J. Sweeney

Strains of extreme thermophilic bacteria have been identified in and isolated from geothermal fluids taken from several locations in western Nevada. We are attempting to develop the techniques and apparatus needed to culture these bacteria in the laboratory.

In FY87, we used direct microscopic examination and scanning electron microscopy to analyze samples of geothermal fluids for the presence of viable microorganisms. A number of interesting cell morphologies were identified that are consistent with the characteristics of extreme thermophiles, the bacteria that thrive in conditions of extreme heat and pressure.

This year, with funding from both the Energy Program and Earth Sciences, we have investigated several techniques for determining the optimal media and conditions for culturing the thermophilic bacteria from our samples. Success in characterizing the physiology and metabolic activity of these bacteria would open up possibilities for identifying and developing strains of thermophiles that can be used for enhancing oil recovery, for *in-situ* processing of mineral, organic, or geothermal wastes at temperatures fatal to ordinary bacteria, and for other biotechnological applications that exploit the thermal stabilities of the protein catalysts (enzymes) present in these bacteria. It is likely that this work can also improve our understanding of how microorganisms may contribute to underground metal corrosion and the subsurface geocycling of metals.

Critical to this investigation is the ability to obtain the observed organisms in pure form. To this end, we have designed specialized solid media and have recently isolated pure cultures of three types of thermophilic bacteria taken from samples obtained from a discharge pond at a geothermal food-processing plant in Nevada. The temperature of the fluid in the pond is 93°C. All three isolates are gram-negative (possessing a characteristic type of cell wall), rod-shaped bacteria, and all three are facultative anaerobes (capable of growing in the presence or absence of oxygen). However,

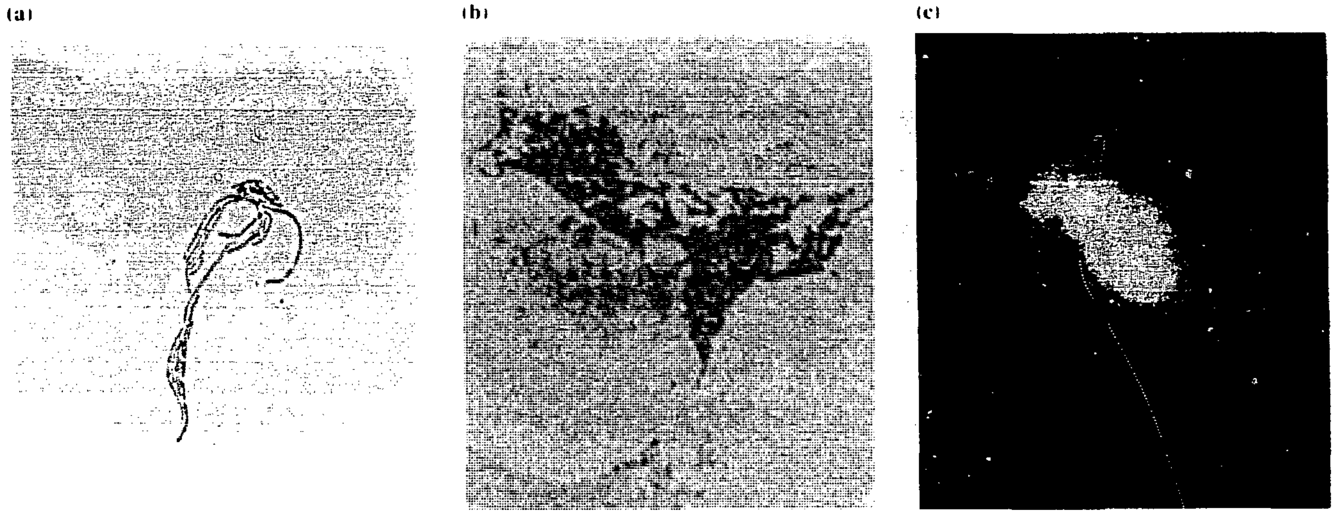

Figure 1. Phase-contrast micrographs (2500×) showing the morphologies of the three isolated thermophiles: (a) *filamentous rods that can form chains up to 20 μm long,* (b) *short rods occurring in pairs,* and (c) *rods that have specialized endospore structures.*

they differ from each other in morphology. Bacteria from one of the strains are 3–5 µm long and usually occur singly, although they tend to form chains up to 20 µm long (Figure 1a) as the culture grows old. Bacteria from the second strain have a length of 1–2 µm and usually occur in pairs (Figure 1b). These two types of organisms can grow at temperatures up to 80°C. The third type of bacteria is endospores, belonging to the group of organisms capable of forming specialized heat and desiccation-resistant structures; they are 3–5 µm long and do not form chains or pairs (Figure 1c).

We have also been able to obtain a type of bacteria that can grow at 100°C in liquid medium. This rod has a semitransparent sheath that surrounds the cell. We are currently attempting to further characterize this organism.

We have recently tried growing cultures in an apparatus designed by D. S. Clark of UC Berkeley. This apparatus allows cultures to grow at pressures up to 3000 psi and temperatures above 100°C, simulating the subsurface conditions at which the thermophiles may be expected to exist. We are now working to optimize growth media and environmental conditions in order to achieve large cultures of the bacteria. We have also recently obtained an anaerobic chamber for proper handling and culturing of strict anaerobes (which grow only in the absence of oxygen) to be taken from a new set of geothermal samples. We will use this chamber in conjunction with a pressure vessel we have begun to build at LLNL, based on Clark's design, that will enable us to grow cultures anaerobically at temperatures above 100°C and pressures above 3000 psi. In preparation for the chemical and physiological characterization of thermophiles from the new samples, we have started a collaboration with D. White of the Institute for Applied Microbiology at the University of Tennessee. We intend to use his technique of coupling an ultramicro method of lipid analysis to a mass spectrometer for studying the presence of ether or ester links in the fatty acids of the cells. With this kind of analysis, we can tell whether the bacteria are *Archaebacteria*, the group to which most extreme thermophiles belong.

In the future, we expect to undertake further physiological characterization and to learn more about which metabolic activities of thermophilic microorganisms might be useful for biotechnology.

U.S. Energy Supply and Demand

Principal Investigator: I. Borg

We have analyzed the U.S. energy situation for 1987 as part of our mission to identify critical research needs. Improving the efficiency of processes that convert fossil fuels to useful energy poses important technical challenges, especially to the transportation industry.

Our analysis of energy demand in the U.S. revealed that energy use increased by 3% in 1987. Energy flow diagrams like Figure 1 indicate several areas of concern.

Energy use for transportation increased for the fifth consecutive year, despite improved average mileage of the automotive fleet. Most of the petroleum consumed is used in the transportation sector, which is highly dependent on imported oil. Domestic crude oil production declined in 1987, while oil imports increased again in 1987; the value (in 1982 dollars) of gross imports of crude oil and petroleum products comprised 14% of total U.S. imports of durable and nondurable goods in both 1986 and 1987. Increasing the efficiency of this sector or decreasing use through conservation, or both, would reduce our dependence on oil imports.

Electrical sales rose by 3.3%, exceeding the projections of almost all forecasters. As a result of the rapid growth of the electrical energy sector, increasing amounts of the nation's large coal resources are being used to generate electrical energy. This promises to exacerbate the environmental problems associated with the use of coal.

Non-utility generation of power, some of which is sold to the utilities by cogenerators, contributed about 4% of the whole. The amount of electricity generated by independent power producers is incompletely assessed, however, since some or all of the power is used by the self-generators themselves and is not reported. Regulatory changes under discussion, anticipated regional shortages of electricity, and the inability of many utilities to finance large base-load plants promise to encourage the growth of non-utility power generation in the next decade.

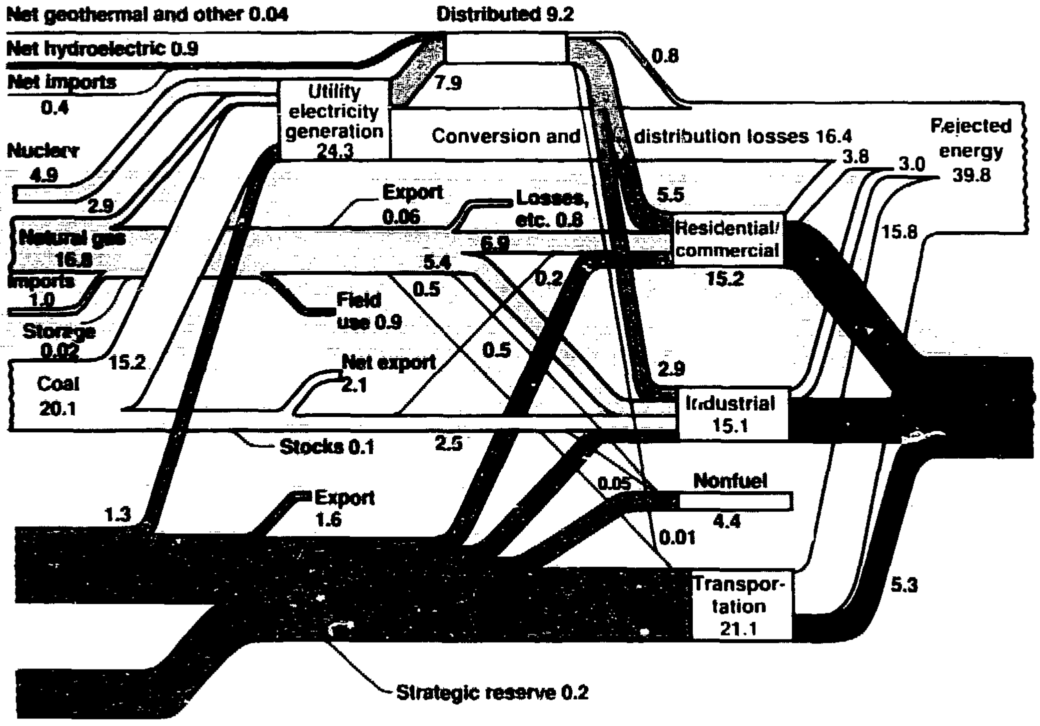

Figure 1. Energy flow diagram showing a net primary resource consumption in the U.S. in 1987 of 76 quads (1 quad equals 10^{15} Btu).

FY88 $773,000

Relativistic Klystron Research for High-Gradient Accelerators

Principal Investigators: S. S. Yu and G. A. Westenskow*

We are developing relativistic klystrons as a power source for high-gradient accelerator applications that include large linear electron-positron colliders, compact accelerators, and free-electron laser sources. Our near-term goal is a high-power (500-MW), short-wavelength (2.6-cm) relativistic klystron. We have attained 200 MW peak power at 11.4 GHz from a relativistic klystron and 140-MV/m longitudinal gradient in a short, 11.4-GHz accelerator section.

Large linear electron-positron colliders, compact accelerators, and free-electron laser sources require a new generation of high-gradient accelerators. For example, conceptual designs of linear electron colliders for research at the frontier of particle physics call for center-of-mass energies of 1 to 2 TeV and luminosities of 10^{33} to 10^{34} cm^{-2}s^{-1}. Accelerating gradients of 150–200 MV/m are desired to minimize accelerator length, and frequencies of 11–17 GHz are desired to keep peak-power requirements and beam loading reasonably small. The peak power necessary to drive a traveling-wave structure in this frequency range with the desired gradient is ~1 GW/m, with a pulse length of 50–100 ns.

Pulsed electron beams of such high peak power can be obtained using the technologies of magnetic pulse compression and induction acceleration (Reginato and Birx, 1988). Beam pulses of 1-kA current and 50–100-ns duration are routinely accelerated to several MeV at LLNL. These beams contain several gigawatts of peak power.

The first demonstration of radiofrequency (rf) power extraction from such a beam yielded more than 1 GW at 35 GHz, using a free electron laser (Orzechowski *et al.*, 1985). A. M. Sessler and S. S. Yu, following a suggestion by W. K. H. Panofsky, proposed a more direct method to extract energy by bunching a relativistic beam and passing it through extraction cavities. Sessler and Yu suggested that if only part of the beam energy were extracted, the beam could be reaccelerated and energy again extracted. The concept of repeated reacceleration and extraction was called a "relativistic klystron two-beam accelerator" (Sessler and Yu, 1987). Relativistic klystrons can be imagined that span the range from a 1-GW device powering 1 m of accelerator, to a 10-GW device powering 10 m, to a two-beam device extending several kilometers.

These ideas led to collaboration between the Stanford Linear Accelerator Center, Lawrence Berkeley Laboratory, and LLNL to study how to combine the klystron concept with induction accelerator and magnetic pulse-compression technology (Allen *et al.*, 1988). The first experiments have been done at the Accelerator Research Center (ARC) at LLNL, using as a gun (or injector) an induction accelerator designed to produce 1-kA currents with 1.2-MeV kinetic energy for up to 75 ns. Three klystrons have been tested with this injector:

- SL3, a multicavity klystron with a conventional gun, designed to operate at 8.6 GHz.
- SHARK, a subharmonic-drive relativistic klystron with relatively low gain.
- SL4, a high-gain relativistic klystron designed for a high-power pulsed beam.

Below, we summarize the design of these klystrons, our FY88 experiments with them, and our future plans.

Klystron Scaling. In a klystron, the beam is velocity modulated by an rf drive cavity and allowed to drift until velocity modulation bunches the beam. The bunched beam is then passed through another cavity that may be used to extract rf power. In practice, such a two-cavity klystron has low gain; most klystrons have several intermediate "idler" cavities. The first cavity bunches the beam. The bunched beam drives the second cavity to an rf voltage an order of magnitude greater than the first, which in turn bunches the beam more strongly. This process continues until the final idler cavity of the klystron's linear-gain region.

---

*Reporting on joint research by Lawrence Livermore National Laboratory, Stanford Linear Accelerator Center, and Lawrence Berkeley Laboratory

Bunching is determined primarily by the voltage on the final idler cavity. After this cavity, the bunches are allowed to drift until the rf current is at a maximum. At this point, the beam is passed through two more cavities: a highly detuned penultimate cavity that sweeps still-unbunched electrons into the bunch, and an output cavity that extracts energy by decelerating the beam. The output cavity could be replaced by a series of cavities or by a traveling-wave structure.

An important parameter in klystron scaling is the beam plasma wavelength. Velocity modulation bunches a dc beam. However, space-charge repulsion (modified by the drift tube) causes the beam to debunch. In the linear region, this process produces oscillations. The distances between cavities in a klystron are chosen to be approximately one-quarter of a plasma wavelength for optimal bunching. For a long relativistic beam of current I and radius a in a narrow tube of radius b, the plasma wavelength on axis is

$$\lambda_p \approx \lambda_{rf} \sqrt{\frac{17\,\mathrm{kA}}{I} \frac{(\beta\gamma)^3}{1+2\ln(b/a)}}\ ,$$

where $\beta = v/c$ and $\gamma = 1/(1-\beta^2)^{1/2}$. Increasing the beam energy ameliorates longitudinal space-charge effects but increases the bunching distance. Increasing the frequency reduces the bunching distance.

Our choice of a 2.6-cm rf wavelength makes possible a multicavity klystron that can efficiently bunch a 1-MV, 1-kA beam and extract power from it in a total distance of 1 m. For more energetic beams, bending magnets can be used to create differences in path lengths for particles of different energies. This permits bunching of such beams even though their velocity is nearly independent of energy.

Another important parameter in klystron scaling is the magnetic field necessary to focus the beam. For a space-charge-dominated beam of uniform cross section, the solenoid field B necessary to confine the beam current I to radius a is

$$B = \frac{2m_e c^2}{ea} \sqrt{\frac{2I}{17\,\mathrm{kA}} \frac{1}{\beta\gamma}}$$

$$= \frac{3.4\,\mathrm{kG}\,\mathrm{cm}}{a}\ .$$

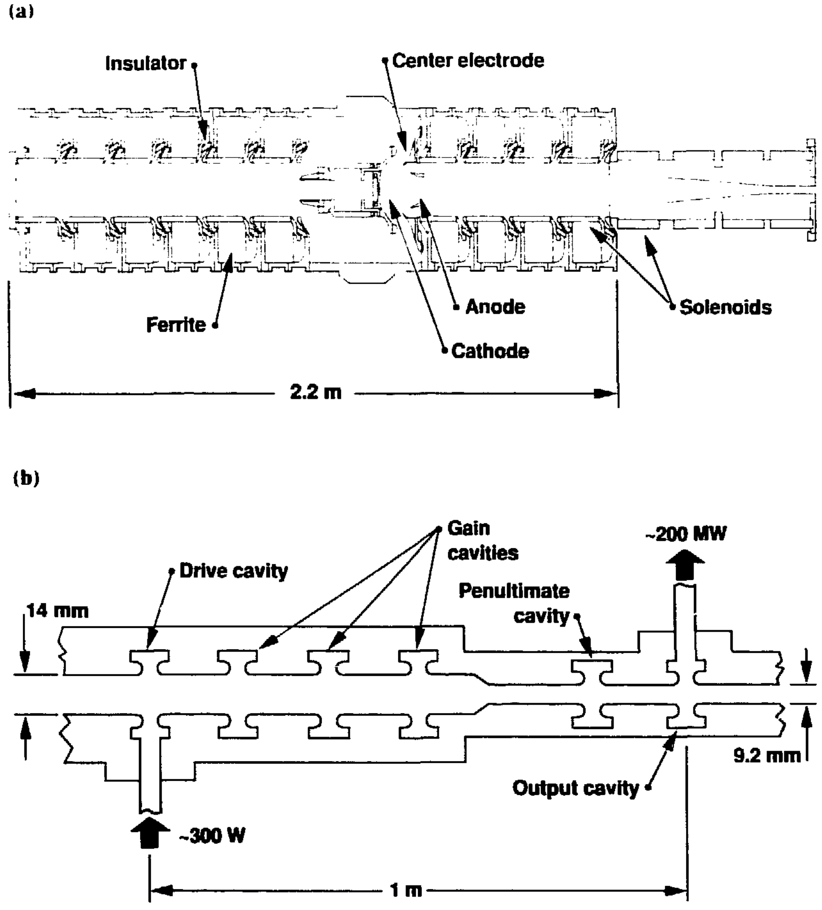

Figure 1. Schematic of (a) the SNOWTRON injector and (b) the SL4 klystron experiment.

In the relativistic klystrons discussed here, both γ and I are greater than in conventional klystrons. At shorter wavelengths, higher magnetic fields are needed to focus the beam since the radius of the drift tube scales with wavelength. An estimate of the required field must include the effects of beam bunching. The peak current in the bunched beam typically is about four times the initial dc current. Thus the magnetic field required is typically twice that calculated for focusing a dc beam.

FY88 Experiments. Most of our experimental studies were performed using the SNOWTRON injector at the ARC facility. SNOWTRON is a linear induction injector composed of ten 150-kV induction cells driven by pulsed magnetics (Reginato and Birx, 1988). For klystron experiments, a triode-electrode configuration was used with a cathode of 12.5-cm diameter and 35-cm spherical radius. The inner diameter of the anode drift tube was 8.8 cm. The cathode was placed 35 cm from the downstream end of the injector (see Figure 1). Accelerating voltages up to 1.2 MV, beam currents up to 1.4 kA, and pulse widths up to 75 ns have been obtained. The greatest stress on the injector is 260 kV/cm on the cathode shroud at peak voltage. The DPC computer code, which was used to design SNOWTRON, predicts peak currents of 2.3 kA at 1.2 MV (Boyd, 1987). However, the operating pressure of the injector led to cathode contamination, which precluded uniform space-charge-limited emission.

The distance from cathode to klystron was 4 m for the SL3 test and 1.6 m for the SHARK and SL4 tests. Just downstream from the injector is a 30-cm taper, where the beam pipe narrows from an 8.8- to a 1.9-cm diameter. The pipe narrows further to 9.2 mm in the SHARK and SL4 klystrons (see Figure 1). Nine 2.5-kG solenoid coils powered by five separate power supplies focus the beam between the cathode and the klystron. Three independently controlled, 5-kG solenoids focus the beam in the relativistic klystron. Four sets of dipole magnets for horizontal and vertical steering are used to correct for beamline misalignments. Additional klystron parameters are listed in Table 1.

Table 1. Parameters of relativistic klystrons tested.

	SL3	SHARK	SL4
Output frequency, GHz	8.57	11.4	11.4
Drive frequency, GHz	8.57	5.7	11.4
Output power, MW			
Peak (maximum)	75	82	200
Wide pulse (maximum)	75	47	68
Design gain, dB	54	20	65
Efficiency, %			
Design	60	20	40
Operation (maximum)	55	25	50
Beam voltage, kV			
Design	330	1200	1200
Operation	1000	1200	1000
Beam current, A			
Design	300	1000	1000
Operation (maximum)	350	750	750
Number of cavities	5	2	6
Total length, cm	31	25	98
Drift tube diameter, mm	11	19–9.2	14–9.2
Beam-off loaded Q			
Input cavity	250	725	280
Idler cavities	4000	—	120
Penultimate cavity	4000	—	3800
Output cavity	44	40	20

Beam transport calculations made with the ST code have been used to estimate the required strengths of the focusing fields for 100% current transmission through the klystron (Boyd, 1987). The result of one such calculation is shown in Figure 2.

SL3 is a conventional high-gain klystron designed to operate at 8.6 GHz with a conventional gun or injector. With this gun replaced by an induction accelerator, it served as an expedient first demonstration of a relativistic klystron. It was driven by a 1-kW, X-band, traveling-wave tube (TWT) amplifier.

SHARK is a two-cavity, subharmonic-drive relativistic klystron. The input cavity is driven by a 5-MW, 5.7-GHz rf klystron that modulates the beam velocity. After drifting, the beam current has large Fourier components at 5.7, 11.4, and 17.2 GHz. Resonant cavities tuned to the higher harmonics can be used to extract power and measure breakdown fields at the higher frequencies. The 11.4-GHz output cavity is positioned after a 25-cm drift pipe for optimal bunching at that harmonic. With only two high-Q resonant structures in this klystron, problems with beam breakup instabilities are minimized. However, the gain of a two-cavity tube is low. Therefore, to achieve a beam-to-rf power conversion comparable to that in multicavity tubes, a conventional klystron is used to drive SHARK. The rf fields in the input and output cavities are comparable for 2 MW of drive and 50 MW of output because of the different *Q*s.

SHARK was designed as a test bed for cavity designs. It allows us to study a wide range of beam parameters and minimizes difficulties with beam propagation. The drift pipe and output cavity are easy to replace, making it possible to use SHARK to study different output cavities at several frequencies.

SL4 is a six-cavity relativistic klystron that operates at 11.4 GHz and was designed specifically for the 50-ns, pulsed SNOWTRON beam. Therefore, unlike most klystrons, it was designed without an integral gun assembly. To make the rf filling time of the SL4 cavities much shorter than the 50-ns beam pulses, three of the gain cavities are coupled by irises and waveguides to absorptive ceramic wedges. This results in loaded *Q*s of 120 and filling times of 2 to 3 ns for these cavities.

To reduce the difficulty of maintaining a well-focused electron beam over a 1-m drift length, we tapered the SL4 drift tube. Its 14-mm diameter in the first four cavities tapers to 9.2 mm just upstream of the penultimate cavity. Tapering permits the use of solenoid magnets with axial fields of 2.7 kG for most of the klystron's length. A 5-kG solenoid surrounds the penultimate and output cavities.

The design gain (65 dB) and efficiency (40%) for SL4 were obtained with the MASK computer code (Eppley, 1988). MASK simulations optimize the SL4 design parameters and predicted the efficiency and gain at several different beam currents and voltages. Some simulation results are shown in Figure 3. The saturation rf drive power is approximately 200 W, which is supplied by a 1-kW, X-band TWT amplifier.

Because of the high peak electric fields in the SL4 penultimate and output cavities, good vacuum is necessary to prevent cavity breakdown. A 500-liter/s cryopump evacuates the klystron collector section, and two 8-liter/s vacuum ion pumps evacuate the output waveguide. In this configuration, waveguide and collector pressures can be maintained at 10^{-8} Torr.

To complement the SL4 experiment, a 26-cm-long, 11.4-GHz accelerator structure operating in the $2\pi/3$ traveling-wave mode was built. This constant-impedance structure consists of 30 cells and has r/Q = 14.2 kW/m. The attenuation parameter is 0.136 Np. The group velocity is $0.031c$, giving a filling time of 28.4 ns. The iris diameter was chosen to be 7.5 mm. Parameters were calculated by the SUPERFISH code and confirmed by cold-test measurements. Coupler dimensions were approximated by extrapolation from S-band data and finalized by cold test. The accelerator was fabricated from machined "cups" that were stacked and brazed. A special tool permits each cavity to be tuned up or down in frequency to obtain the correct phase advance per cell.

Experimental Results. Our design goal of 100% beam transmission through the klystrons has not been achieved experimentally, even after focusing adjustments were made. The maximum current transported through SHARK is 750 A, only 65% of the current entering the klystron. Up to 80% transmission has been achieved at 400 A. Transmission achieved through SL4 (which is four times longer than SHARK) is 55% at 800 A and 65% at 500 A. Transmission is independent of rf drive for SHARK. For SL4, a slight decrease in transmission was noted at high rf output levels. (There was no downstream current monitor in the SL3 tests; transmission through SL3 was not measured.)

The SL3 test was designed to demonstrate of the effects of putting a conventional klystron tube (stripped of its gun) in a high-power pulsed beam. No unusual or unexpected phenomena were observed. No

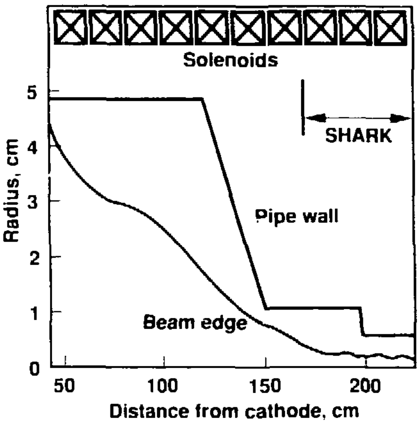

Figure 2. Beam size calculated through SHARK.

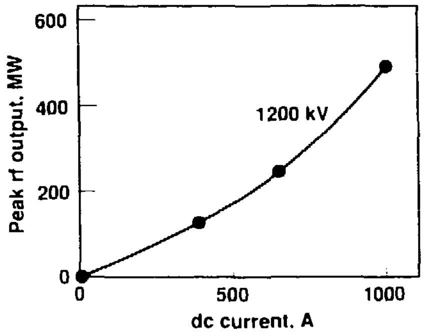

Figure 3. MASK simulations of SL4 output power.

evidence of multipactor, rf breakdown, parasitic oscillations, or other instabilities was observed. The rf-pulse risetimes were 5 to 10 ns. These pulses reproduced the shape of the beam current pulses quite well. Peak power of 75 MW was attained with an 800-kV, ~250-A beam. Output power agreed well with the predictions of the MASK simulation code.

Peak output power of 200 MW at 11.4 GHz was attained with the SL4 klystron using a 930-kV, 420-A beam. SL4 has not yet operated at its 1000-A design current. However, agreement is excellent between output power measured at lower currents and MASK predictions (Figure 3) for operation at these currents. The 200-MW peak power delivered by SL4 to the 11.4-GHz accelerator corresponds to a longitudinal accelerating gradient of 140 MV/m. Early indications are that there is appreciable dark current in the accelerator when the accelerating gradient exceeds 90 MV/m.

In our tests of both SHARK and SL4, we observed that as the beam current through the klystron is increased up to a certain level (~250 A), the output-power pulses remain relatively flat. However, when the beam current is increased beyond this level, the trailing edges of the output-power pulses diminish in amplitude, while the leading edges continue to grow. This behavior in SHARK tests is illustrated in Figure 4.

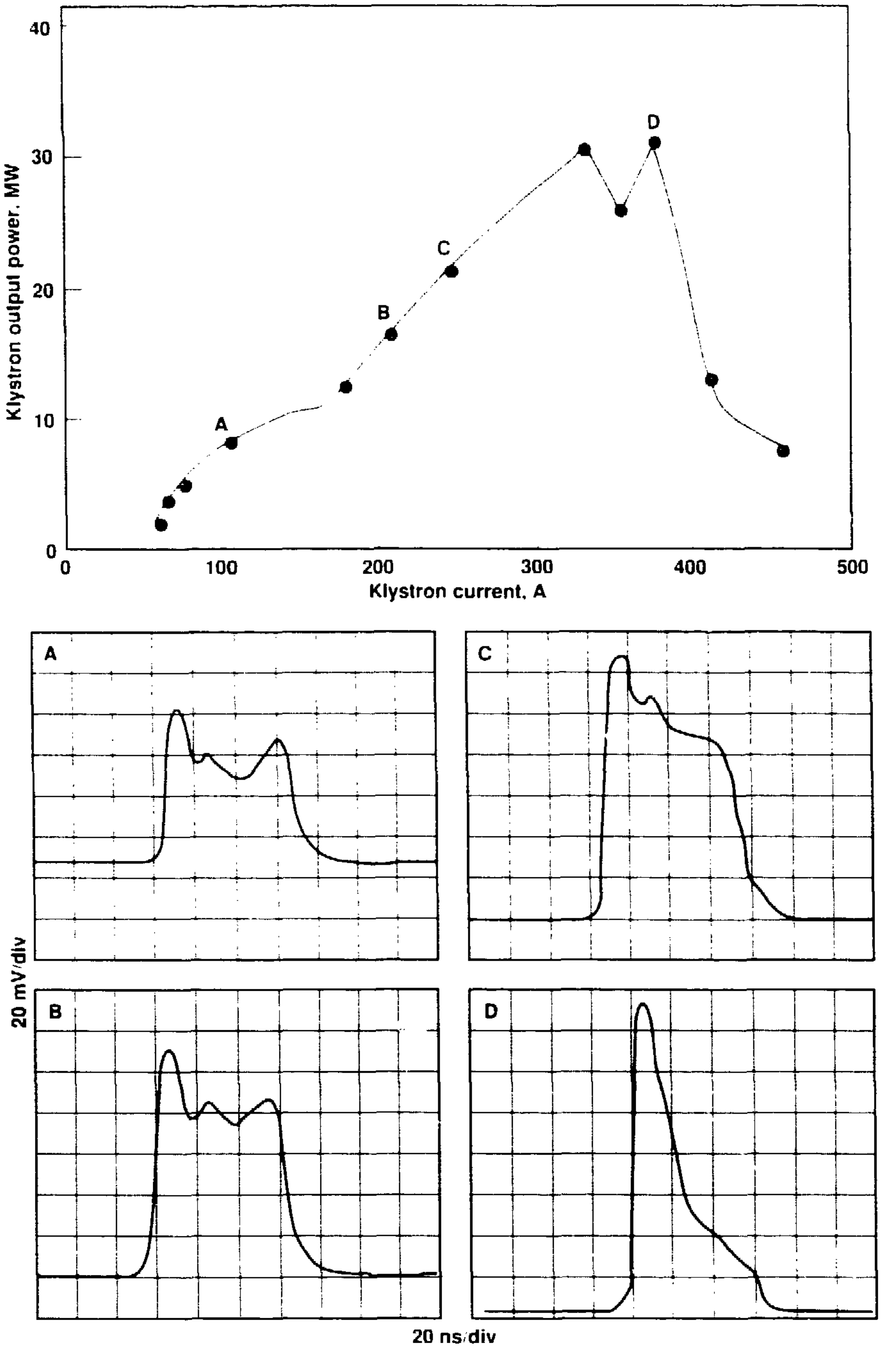

Figure 4. Radiofrequency pulse shortening observed in SHARK tests. Beam voltage is 950 kV; drive power is ~1.4 MW.

Our ability to obtain flat output-power pulses is affected by beam current, rf-drive level, and focusing magnetic-field strength. The practical importance of these observations is that even though 200 MW of rf power was produced with SL4, the maximum, reasonably flat rf pulse achieved was only

60 MW. Low (wide) and high peak power pulses for SL-4 are shown in Figure 5. This pulse-shortening phenomenon is a serious impediment to making flat, high-power rf pulses. It is not due to beam breakup because the transmitted dc beam current pulse does not shorten with the rf pulse. Two possible explanations are anomalous beam loading and transient effects.

While the beam is on, secondary electrons produced by x rays are emitted from the high electric field regions around the cavity. When the cavity field is low, these secondaries oscillate in trajectories close to the cavity walls with no net energy absorption. At higher field gradients, these electrons have longer path lengths. Above a critical field value (~200 MV/m), their path lengths are long enough for the secondaries to hit the opposite nose cone and deposit their kinetic energy in the walls, which constitutes a loading phenomenon. The secondary electrons in this anomalous beam loading may be caused by x rays from the beam. Hence, they turn on and off with the beam. Preliminary calculations indicate that the x rays produced are consistent with the secondary-electron currents required to account for the additional loading (5–10 A).

We recently installed a new drive cavity for SHARK with an iron ring that shunts the magnetic field from the drive cavity, creating a magnetic hole near the cavity's center. This experimentally increased the onset of the pulse-shortening phenomenon to above operating conditions. However, the shape of the magnetic field increased the radial flutter of the beam after the cavity. Cavities that operate with lower electric field levels have been built and are ready for testing.

In addition to anomalous beam loading, transient effects due to normal resistive loading and reactive detuning of cavities by a high power pulsed beam may influence the shape of the output-power pulses. The pulse shapes we have calculated look strikingly similar to some of the pulses we have observed. They may be described qualitatively as having a transient precursor followed by a flat pulse. The precursor is due primarily to the transient detuning that results from reactive beam loading and, in some cases, may be of much larger amplitude than the trailing flat part of the pulse. High-power, flat top rf pulses have emerged in our calculations with a driving-frequency bandwidth narrower than and shifted upward from the bandwidth of the large precursor. However, we have not yet observed these rectangular pulses from SL-4 at any frequency, presumably because of anomalous beam loading.

Other experimental problems encountered were breakdowns in the SHARK and multipactoring in the SL-4 input cavities. When first installed, the SHARK cavity operated at drive levels as high as 2 MW without arcing. As testing progressed, the arcing threshold gradually decreased to about 1 MW. Arcing was evidenced by the input cavity's reflection coefficient suddenly jumping to unity and staying there until the end of the rf drive pulse. At threshold, the arcs were initiated apparently at random times during the pulse. At drive levels well above threshold, the arcs occurred on every pulse and started early in the drive pulse. We could raise the threshold from 1 to about 1.5 MW by rf processing at 15–20 pps with the beam off. The cavity was processed in this way for 1–2 hours. However, when the repetition rate was reduced to 1 pps and the beam was turned on (inadequate radiation shielding limited the repetition rate to 1 pps with the beam on), the threshold quickly decreased again to about 1 MW and limited the maximum output power that could be obtained.

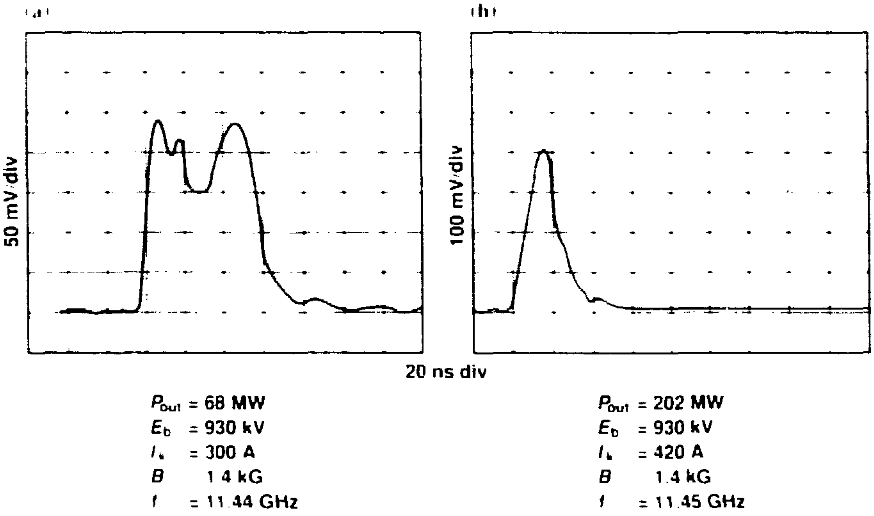

Figure 5. Peak power in SL-4 tests: (a) low (wide) and (b) high (narrow) pulses. Pulse shortening at high peak power is the most serious problem encountered in our relativistic klystron experiments.

The reflection coefficient of the SL-4 input cavity is a function of drive power even when the beam is off. At low drive levels (< 40 W), the coefficient is constant and equal to that measured during cold testing. Above a 40-W drive, it drops rather abruptly. Since the cavity is heavily overcoupled (9.5 standing wave ratio), this lower coefficient means that something is absorbing power from the cavity. The threshold for the onset is sensitive to the solenoid *B* field. We feel this is evidence of multipactor. Nevertheless, stable output power was achieved.

Future Plans. At present, SL-4 and the high-gradient accelerator section are experimental and tests are continuing. To further understand transient effects, we will continue to measure input-cavity beam loading and detuning on SL-4. Similar studies will be initiated on the high-field SHARK input cavity when it is reinstalled. We hope to study correlations between input-cavity beam loading and output pulse shapes as functions of beam energy, current, and focusing on both SL-4 and SHARK. Studies of high-gradient accelerator breakdown at high frequencies and measurement of accelerating gradients also are anticipated.

To reduce anomalous beam loading in SHARK, we plan to apply techniques that have reduced multipactoring in other rf systems. These include collimating the beam aperture upstream of the klystron, rf conditioning at higher repetition rates with better shielding, and slotting the noses of the drive cavity to reduce secondary-electron emission.

Several modifications to the current SHARK output cavity are planned. First, it will be replaced by the SL-4 penultimate and ouput cavities, which were designed as a modular section. The addition of a penultimate cavity to SHARK should improve bunching and increase output power. Second, a traveling wave output structure that has been fabricated will also be used to replace the SHARK output cavity. New output cavities at the 5.7- and 17-GHz harmonics may be built and tested.

We are also building a version of SL-4 that is better diagnosed to locate the cavity *in which the onset of the* pulse-shortening problem occurs. In the new SL-4 setup, the electric fields in all of the gain cavities will be monitored.

We would like to operate the relativistic klystron at beam energies higher than what is possible using velocity modulation (>3 MeV). A chopper scheme for current modulation at these higher energies has been worked out and is being prepared for testing. The scheme uses a transverse deflector cavity to sweep the beam past a collimator. After the collimator, the chopped beam is then passed through several transfer cavities. With a 3-MeV, 1-kA beam, we should be able to produce near 1 GW of rf power at 11.4 GHz. To reduce the deflection system's sensitivity to electron-beam entry angle, energy, and emittance, the system is fully confined within an axial magnetic field with a quarter-betatron-wavelength resonance between the drive cavity and the collimator. The system has a high energy acceptance and good phase stability with only a modest emittance growth.

To aid in understanding what is occurring in our experiments, we have been developing several time-dependent klystron codes. A one-dimensional particle code was developed early in our relativistic klystron program and has been used to determine proper distances between cavities. A two-dimensional beam dynamics code is now under way. Work on a klystron-cavity electromagnetics code that includes higher-order modes and deviations from axisymmetry is also under way.

References

Allen, M. A., *et al.* (1988), *Relativistic Klystron Research for High Gradient Accelerators*, Lawrence Livermore National Laboratory, Preprint UCRL-98843.

Boyd, J. K. (1987), *SNOWTRON Numerical Calculations*, Lawrence Livermore National Laboratory, Report LLNL-RM 87-48.

Eppley, K. (1988), *Algorithms for the Self Consistent Simulation of High Power Klystrons*, Stanford Linear Accelerator Center, Stanford, CA, Report SLAC-PUB-4622.

Orzechowski, T. J., *et al.* (1985), "High Efficiency Extraction of Microwave Radiation from a Tapered Wiggler Free Electron Laser," *Phys. Rev. Lett.* **54**, 889.

Reginato, L. L., and D. L. Birx (1988), *Pulsed High Power Beams*, Lawrence Livermore National Laboratory, Preprint UCRL-98553.

Sessler, A. M., and S. S. Yu (1987), "Relativistic Klystron Two Beam Accelerator," *Phys. Rev. Lett.* **58**, 2439.

Advanced Technologies for Growing Large Optical Crystals

Principal Investigators: J. F. Cooper and L. J. Atherton

We are developing a modified Bridgman process for growing large, optically homogeneous crystals for high-power laser applications. To test this crystal growth process, we have developed a new, inductively heated furnace and have modeled the temperature distribution within it. We have grown Nd:YAG crystals in an existing furnace of a related design to resolve critical diagnostic, control, and materials issues.

We are developing new technologies for growing optical crystals in the form of large slabs ($10 \times 20 \times 1$ cm^3) with the size, shape, and optical homogeneity required for high-power lasers. Currently, the favorable properties of known laser materials cannot be fully exploited because of limitations in scale-up and optical homogeneity encountered with existing crystal-growth technologies.

We are attacking this problem on several fronts. We have designed and have had built a classical Bridgman furnace for growing slab-shaped crystals. We are growing neodymium-doped yttrium-aluminum-garnet (Nd:YAG) crystals in a gradient-freeze furnace that is similar enough to the new furnace to allow us to address crystal-growth problems common to both furnaces. We are also improving the analytical techniques used to address critical diagnostic, control, chemistry, and materials issues and to develop better thermal diagnostics and more stable furnace-heating units. We expect that we will be able subsequently to apply the equipment and techniques developed in this project to other important laser crystals, such as gadolinium-scandium-aluminum-garnet (GSAG) and lithium-calcium-aluminum-fluoride (LiCAF).

New Furnace Development

A vertical Bridgman furnace has been designed and built to our specifications by Crystalox, Ltd., England; it will be delivered to LLNL in January 1989. This furnace will enable us to grow large, slab-shaped crystals of high optical quality. With it, we will test advanced furnace-control programs, different heating configurations, and new furnace and crystal-growth diagnostics.

In the classical Bridgman crystal-growth process, an ampoule containing a polycrystalline feed material (with the laser-active dopant) and a seed crystal is lowered through a two-zone furnace to progressively melt the feed material and grow the crystal (see Figure 1a). The top zone is held at a temperature above the melting point of the material, and the bottom zone is held at a lower temperature. An insulated ("adiabatic") zone between these two actively heated regions serves to flatten the melt/crystal interface. The temperature gradient at the interface is determined by the temperature difference between the upper "hot" zone and the lower "cold" zone.

In classical Bridgman growth of many materials, the laser-active dopant in the melt builds up at the melt/crystal interface because it is selectively rejected by the growing crystal. Its concentration increases monotonically along the length of the crystal, and this inhomogeneity can degrade laser performance. One of our primary motivations for developing a modified Bridgman process is to grow crystals with an axially level or homogeneous dopant concentration.

In our modified Bridgman process, a third thermal region is added to the furnace, above the hot zone, which is colder than the melting point of the crystal (see Figure 1b). This topmost zone serves as a preheater and permits the size of the middle hot zone to be reduced. This relatively small hot zone produces only a small region of melt in the ampoule; above the melt zone is the polycrystalline feed slab and below it is the newly grown crystal. Viewed from the ampoule's frame of reference, this small melt zone moves from one end to the other; we call this variation of classical Bridgman crystal growth the "moving melt zone" (MMZ) process. A steady state is reached in the MMZ process in which the rate at which material is added to the melt at the upper interface equals the rate at which it is "frozen" into the newly grown crystal at the lower interface. Laser-active dopants in the polycrystalline feed will therefore be uniformly distributed axially. In addition, the small melt volume stabilizes fluid flow, thereby producing a crystal with a high degree of optical homogeneity.

A process related to classical Bridgman crystal growth is called gradient freeze (Figure 1c). A temperature gradient is established in the furnace using tapered radiation shields, and the location of the melt/crystal interface is determined by the position of the melting point in the furnace. In the gradient freeze process, the ampoule and its contents are stationary in the furnace; steady reduction of power to the furnace causes the melt crystal interface to move upward. Thus, from the perspective of the growing crystal, the gradient freeze process is identical to the classical Bridgman process. The main limitation of the gradient freeze process is the difficulty of maintaining the thermal gradient required for growth over the full length of the ampoule. Important results obtained in crystal growth experiments in our gradient freeze furnace are described later in this article.

The Crystalox furnace is shown schematically in Figure 2. It will be delivered as a two-zone classical Bridgman furnace, and we will use it as such to grow large crystal slabs to test advanced control programs, furnace configurations, and diagnostics prior to addition of the third thermal zone. The Crystalox furnace core consists of two stacks of graphite cylinders (susceptors) that are inductively heated by two 40-kW, 25-kHz power supplies to provide a core temperature of 2100°C with exceptional power stability (0.03%). (The graphite cylinders are called susceptors because they couple with the electromagnetic field produced by the generator coils.) An axial, rectangular slot accommodates the rectangular ampoule, which is supported on a vertical shaft that can be moved in increments of 0.125 µm. The core is surrounded by fibrous graphite insulation to retard heat loss.

The temperature of the furnace must be extremely stable to grow an optically homogeneous crystal. Before we could specify the required temperature stability for the Crystalox furnace, we first had to clearly understand the relation between temperature fluctuations in the melt zone during crystal growth and local stress-induced birefringence (a key indicator of the degree of optical homogeneity) in the resulting crystal. Abrupt changes in temperature at the melt/crystal interface during growth will alter the rate of incorporation of dopant into the crystal structure, causing the expansion or contraction of adjacent layers and thus introducing shear stresses in the crystal. Since these layers contain varying concentrations of the dopant (e.g., neodymium), they therefore have varying refractive indexes and degrees of stress induced birefringence on an otherwise uniaxial material. Crystals grown under such conditions will contain striations, serious optical defects that are visible under polarized light.

We derived an equation that relates stress birefringence to fluctuations in dopant concentrations (Cooper, 1988), confirming the results of Hayakawa *et al.* (1985), based on photoelastic and elastic strain theory. Using theoretical and empirical thermodynamic data, we extended the model to account for the dependence of dopant concentration on temperature during crystal growth. When we evaluated this relation for Nd:YAG, we found that a low absolute birefringence of 3 nm/cm demanded a growth-temperature stability band of 0.1°C at the growth temperature of 1950°C (Cooper, 1988).

We modeled the induction heating and heat transfer of the Crystalox furnace through the graphite insulation and susceptor stack to determine the stability of the power supply needed to restrict

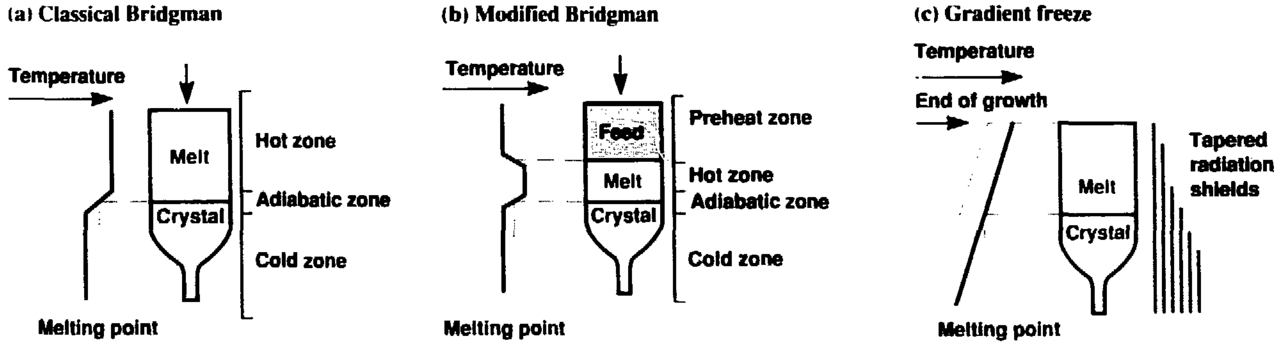

Figure 1. In the classical Bridgman process (a), an ampoule containing the polycrystalline feed slab (with laser-active dopant) and a seed crystal is lowered through a two-zone furnace: an upper hot zone is separated from a lower cold zone by an adiabatic region that flattens the melt crystal interface. In our modification of the classical Bridgman process (b), a preheat zone is added above the hot zone; this allows a reduction in the size of the melt zone and the volume of melt, producing conditions in which optically homogeneous crystals can be grown. The gradient freeze configuration (c) is closely related to the classical Bridgman process (from the growing crystal's point of view). The ampoule is stationary within the furnace and as power is progressively reduced to the furnace, the crystal grows as the melt crystal interface moves upward.

ampoule temperature changes to within the 0.1°C bandwidth. We found that temperature fluctuations at the susceptor surface were attenuated (muffled) in about 14 s by the thermal mass of the susceptor. Therefore, to provide the required 0.1°C ampoule temperature stability, power fluctuations must be limited to a 1–2-s period, which in turn requires a power stability of 0.05% (Atherton, 1988). The power stability of the Crystalox furnace has been measured to be 0.03%.

Gradient Freeze Technique. Concurrent with the development of the Crystalox furnace, we conducted crystal growth experiments at LLNL in a resistively heated furnace adapted for growth by the gradient freeze technique. Gradient freeze growth of Nd:YAG provides invaluable information for the development of the modified Bridgman process. Both of these techniques share several important features, including crucible-contained growth, vertical stratification of melt density, and analogous profiles of temperature and chemical activity. The gradient freeze experiments are enabling us to develop and test advanced thermal diagnostics, resolve materials issues concerning the growth and chemical stability of YAG in metal crucibles, and develop and test computer control programs for use in an MMZ furnace (Cooper *et al.*, 1988).

In a gradient freeze furnace, specially designed shielding (a series of concentric metal foil tubes) surrounds the ampoule and imposes a vertical thermal gradient of about 10°C/cm. As power is reduced to the furnace, crystal growth follows the continuous upward displacement of the melting point isotherm (see Figure 3).

Our gradient freeze furnace is controlled by a Hewlett Packard 9816 microcomputer. We developed a control program that provides for cascaded power-temperature control using feedback signals from power and temperature diagnostics within the furnace. (The principal diagnostics for measuring and monitoring temperature in the furnace and at the melt/crystal interface are briefly described in Table 1.) The program uses temperature-dependent PID coefficients to control furnace temperature to 1°C over a temperature range of 200 to 2200°C. Power levels, temperatures, and water and gas flow rates are recorded to permit quantitative postgrowth analysis.

Modeling the Susceptor Temperature Distribution. Prior to and concurrent with the development of the Crystalox furnace, we applied the induction-heating model developed by Gresho and Derby (1987) to determine the power deposition profile in the new furnace. We solved the time-harmonic version of Maxwell's equations within the furnace chamber using a sinusoidal current source term in the coils that surround the susceptor and insulation. This yields coupled elliptic equations that are solved for complex furnace geometries with FIDAP, a finite-element fluid dynamic code (Engleman, 1982), to obtain the power deposition profile. This profile is then used as the source term in the three-dimensional heat conduction equation to obtain the resulting temperature profile.

With these calculations (Atherton and Martin, 1988; Atherton *et al.*, 1988), we verified the fundamental induction heating approach for growing slab-shaped crystals before Crystalox began their work. We also

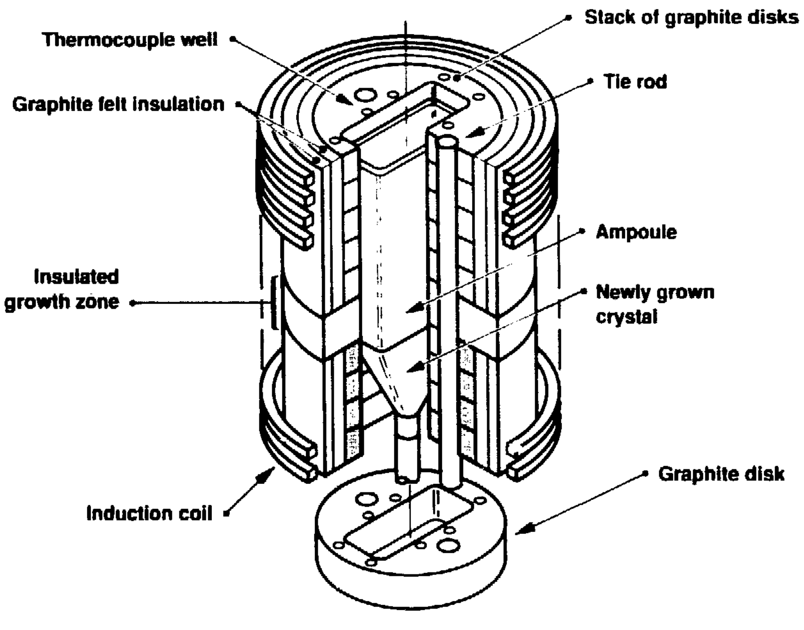

Figure 2. The Crystalox furnace consists of two stacks of graphite disks (susceptors) that inductively couple to the magnetic field of two independently controlled generator coils, surrounded by fibrous graphite insulation. The two stacks of disks are separated by insulation to flatten the melt crystal interface. A rectangular ampoule is slowly lowered through the axial slot in the graphite disks to grow the crystal.

used these calculations to study the effects of changes in susceptor geometry and identified two design changes that significantly improve the furnace temperature profile. One change was to extend the susceptor outside the adiabatic zone to flatten the melt/crystal interface. The other was to use an annular conductor within the susceptor to provide an azimuthally uniform heat source.

To validate these model predictions, we constructed a half-scale inductively heated furnace here at LLNL. In this furnace, the susceptor and insulation are the same diameter but only half as long as in the Crystalox furnace. The susceptor is heated by a single 40-kW, 25-kHz generator, identical to those developed for the Crystalox furnace but with relaxed power-stability requirements. The initial results from tests in this furnace support our model calculations, and further tests are under way.

Materials Studies. We are developing the new furnace and crystal growth process using Nd:YAG because it possesses growth problems typical of those encountered with many other laser materials. During process development, it is critically important to distinguish process-induced defects from defects inherent to the material or errors in its preparation. As noted above, the gradient freeze method and our modified Bridgman process of crystal growth share several very important features (e.g., crucible-contained growth, vertical stratification of melt density, and analogous profiles of temperature and chemical activity) that affect the inclusions, striations, and dopant density of the resulting crystal. We examined Nd:YAG crystals grown via gradient freeze to learn how best to control their growth and produce optically homogeneous crystals.

A few, rare inclusions of Al_2O_3 and $Y_3Al_{11}O_{21}$, resulting from errors in the composition of the starting materials, were identified by scanning electron microscopy and microprobe analysis. More common inclusions of metallic tungsten (~1 μm diameter, ~4 particles/mm^2 in cross section) were found in Nd:YAG grown in lidded but unsealed tungsten crucibles. These particles evidently result from the dissociative evaporation of alumina from the melt ($Al_2O_3 \rightarrow Al_2O + O_2$) followed by the reduction of dissolved tungsten oxides by the Al_2O. No inclusions were found with Nd:YAG samples grown in sealed molybdenum crucibles (procured from researchers in the People's Republic of China). Thus, careful choice of crucible material and/or strict retardation of evaporation should eliminate inclusions.

We also examined the occurrence of striations in Nd:YAG. As discussed above, striations are periodic variations of optical properties (such as birefringence or absorptivity) along the direction of crystal growth. In Nd:YAG, periodic stress-induced birefringence reflects local changes in the neodymium concentration of the crystal, and the concentration of neodymium absorbed is a strong function of growth temperature. We constructed a circularly polarized light polarimeter to measure the layered strain fields in samples of Nd:YAG. Initial results show fluctuations in birefringence of about 20–30 nm/cm, which is in good agreement with our model predictions for the measured temperature bandwidth of ~1°C in our unmuffled furnace. In the Crystalox furnace, the use of high-thermal-mass materials for furnace internal components together with the improved power stability will provide the required 0.1°C temperature stability and thus limit birefringence to the target level of 3 nm/cm.

Table 1. **Diagnostic techniques used to measure temperature distributions and fluctuations in crystal-growth furnaces operating above 2000°C.**

Diagnostic	Precision	Resolution	Accuracy	Description
Optical-fiber thermometry (OFT)	0.2°C	10^{-4}°C	—	Fast-response pyrometric technique; can detect very small fluctuations (10^{-5}°C at 1000°C); particularly useful for distinguishing between hydrodynamic instabilities in the melt and changes in furnace power.
W/W-0.26 Re thermocouples	10°C	0.1°C	10°C	Used to measure furnace temperature distribution; also being used to guide development of furnace hardware to provide high thermal gradients (10–20°C) required for crystal growth.
Rhodium melting point	—	—	3°C	Provides a physical reference point (1966 ± 3°C) that can be localized within the furnace for *in situ* sensor calibration.

In addition, we measured the distribution of the neodymium dopant in the YAG crystal using x-ray fluorescence and absorption spectroscopy. We found a nearly uniform axial (vertical) distribution of neodymium, despite the low segregation coefficient of neodymium in YAG. These results are contrary to the predictions of two transport models, one assuming a well-mixed fluid and the other assuming a stagnant fluid (see Figure 3) and may have important implications for our modified Bridgman process. When we examined the radial distribution of dopant in YAG, we found that it was essentially uniform except for a very high concentration of neodymium (roughly 30× enhancement) in a 50-µm-thick layer adjacent to the crucible wall, where the interface between crystal and melt curves sharply downwards to form a crevice. Such a crevice is predicted from heat-transfer analyses, given the differing thermal conductivities of melt, crystal, and metal, but we had not anticipated such a large concentration of neodymium at the wall. We conclude that the axial uniformity of dopant concentration results from a balance of the rate of rejection of neodymium from the growing interface, the flow of neodymium-rich melt into the crevice, and its spontaneous precipitation in the crevice. This effect has not been reported for growth of large cylinders of Nd:YAG by gradient freeze: the smaller surface-to-volume ratio for these larger crystals would reduce the impact of the relatively small layer of neodymium-enhanced polycrystal at the edge of the crystal on the overall crystal mass balance. However, in the growth of crystal slabs by the Bridgman process, the surface-to-volume ratio is similar to our small-scale cylindrical experiments in gradient freeze. Thus, we expect to see a similar behavior for the growth of Nd:YAG in the Crystalox furnace; if this is indeed the case, we may be able to produce axially homogeneous Nd:YAG without adding the third thermal zone to form a MMZ furnace.

Future Plans. In FY89, we will concentrate on growing slabs of Nd:YAG in the Crystalox furnace in both the classical and the modified Bridgman configuration. We will also refine our models of temperature distribution and stability to fully understand their effects on crystal growth and on dopant distribution. We will continue to develop appropriate crucible materials and furnace controls and diagnostics, and we will explore the extension of the technology thus developed to other materials.

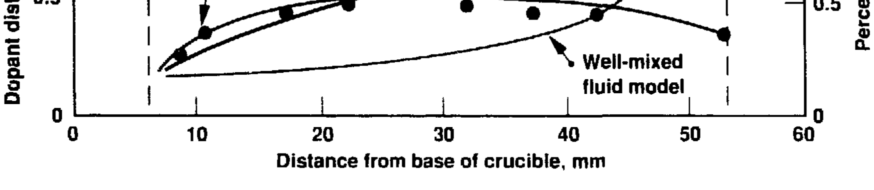

Figure 3. Axial distribution of neodymium in a YAG crystal grown in a gradient freeze furnace. The dopant distribution measured in this crystal was found to be nearly uniform, contrary to predictions by mass-transport models based on the limiting cases of well-mixed and stagnant fluids. This uniform composition evidently results from a combination of balanced rejection of neodymium from the axial interface and enhanced precipitation at the crucible wall. This discovery may provide a way to achieve uniform doping levels in slab-shaped crystals using the classical Bridgman process.

References

Atherton, L. J. (1988). *Analysis of Temperature Fluctuations in a Graphite Susceptor*. Lawrence Livermore National Laboratory, Technical Memorandum LRD-88-025 (February 23).

Atherton, L. J., and R. W. Martin (1988). *Modeling Induction Heating and 3-D Heat Transfer for Growth of Rectangular Crystals Using FIDAP*. Lawrence Livermore National Laboratory, Preprint UCRL-99629.

Atherton, L. J., R. W. Martin, D. H. Roberts, and J. F. Cooper (1988). *Induction Heating for Bridgman Crystal Growth: Model Predictions and Experimental Results*. Lawrence Livermore National Laboratory, Preprint UCRL-98875.

Cooper, J. F. (1988). *The Dependence of Stress Birefringence on Temperature Fluctuations at the Crystal Melt Interface*. Lawrence Livermore National Laboratory, Technical Memorandum OMG-88-19 (April 5).

Cooper, J. F., H. Lugg, M. Shinn, D. Roberts, and L. J. Atherton (1988). *Growth of Yttrium Aluminum Garnet by Gradient Freeze Technique*. Lawrence Livermore National Laboratory, Preprint UCRL-98877.

Engleman, M. S. (1982). "FIDAP—A Fluid Dynamics Analysis Package." *Adv. Eng. Software* **4**, 163.

Gresho, P. M., and J. J. Derby (1987). *Solution of the Time-Harmonic Semi-Maxwell Equations for Induction Heating Using FIDAP*. Lawrence Livermore National Laboratory, Preprint UCRL-97322.

Hayakawa, H., M. Umino, H. Mori, and Y. Fuji (1985). "Observation of Striations in Nd:YAG with Circularly Polarized Light." *Japanese J. Appl. Phys.* **24** (8), L-614.

Diode Array Development

Principal Investigator: R. W. Solarz
Co-Investigators: D. C. Mundinger, R. J. Beach, W. F. Krupke, and W. J. Benett

We are adapting the technology of silicon microchannel coolers to that of high-power semiconductor laser arrays. When integrated, these two technologies will make it possible for semiconductor lasers to operate at average powers in excess of 1 kW/cm² for very long lifetimes.

For high-average-power semiconductor lasers, waste heat removal is the primary limiting factor. This in turn affects both laser lifetime and laser system cost. Lifetime and efficiency decrease rapidly as the operating temperature rises above 40–50°C, and the cost per watt of average power scales inversely with the device duty factor. The heat-sink technology currently used to package diode arrays typically allows a device duty factor of only 1% or less, severely limiting the use of these arrays in many potential applications.

Our objective is to adapt silicon microchannel coolers (Mundinger *et al.*, 1988) to cool laser diode arrays, with the primary emphasis on developing incoherent pump sources for solid-state lasers. Microchannel coolers were originally invented for cooling wafer-scale integrated circuits and have proven to be very effective at removing large amounts of waste heat with only a small temperature rise. Using microchannel coolers for laser diode arrays should easily give a factor-of-ten improvement in average power over present diode packages and even larger improvements in lifetime. The packages, once developed, should allow pulsed and continuous-wave (cw) pumping of high-average-power solid-state lasers and will find ready application wherever low-cost, high-pulse-repetition lasers are required.

Our activities have been both analytical and experimental. We have developed a model that describes the heat flow between the active region of the semiconductor laser and the coolant, and have projected the performance for a range of cooler architectures and channel dimensions. We developed bonding procedures for achieving reliable, low-thermal resistivity bonds. We also developed a simple and reliable coolant manifold that provides high flow rates with a minimum of pump power. In addition, we fabricated and tested several integrated assemblies that demonstrate the essential features of this cooling approach using a one-dimensional diode array. The measured performance of these assemblies is in good agreement with our projections.

Figure 1 shows the design for a compact, high-power array of diode bars alternating with heat-conducting fins to form a two-dimensional stack (rack-and stack-architecture). This design uses the readily available, high-power, edge-emitting diode bars to achieve peak power densities of kilowatts per square centimeter. It also uses commercially available synthetic type-2a diamonds as chip carriers. These carriers have high thermal conductivity and thus reduce the thermal impedance between the lasing junction and the surface of the silicon microchannel plate to a value that is small compared to the overall thermal impedance of the diode package. This rack-and-stack approach could readily be realized

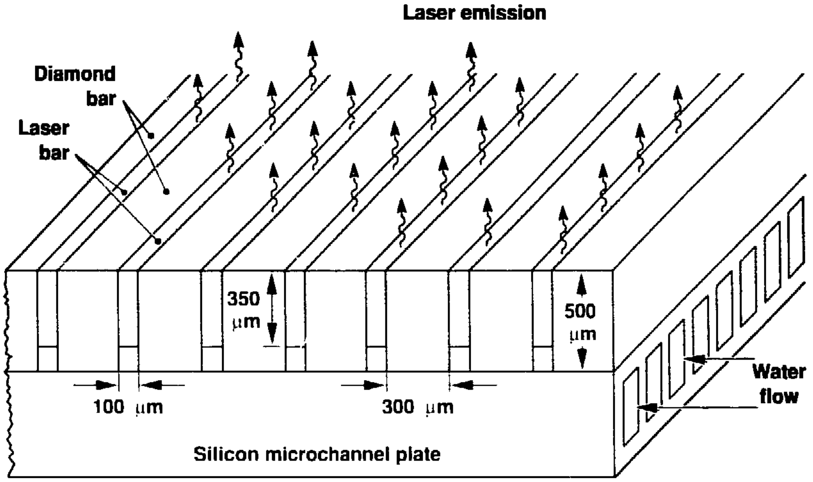

Figure 1. Design of a compact, high-average-power, laser-diode array. In this rack-and-stack architecture, diode bars alternate with heat-conducting fins to form a two-dimensional stack.

for near-term applications. in the longer term, similar results could also be realized using a monolithic or surface-emitting architecture in junction-down configurations.

The low thermal impedance of these microchannel structures is achieved in two ways. First, the coolant boundary layer is kept as thin as possible while still maintaining a sufficient flow rate to avoid coolant heating. Second, material with high thermal conductivity is used to maximize the effective area of the coolant boundary layer. The flow through the channels is laminar, which gives better cooling performance for reasonable pump power than turbulent flow. Figure 2 is a photograph of the microchannel structure.

Figure 3 shows the fabricated assembly, consisting of a silicon heat exchanger, a diamond-chip carrier, a copper *n*-side contact, and a 3-mm-thick laser diode bar. For this test, the microchannels were "sawn" in the silicon using a diamond wafer saw. After the channels were cut, the silicon wafer was attached to a borosilicate glass back-plate manifold by anodic bonding. The glass was etched with grooves to provide for water inlet and outlet in the microchannels. This composite wafer was then cut into four individual coolers, each with an area of 4 cm^2. Two electrically separate contact pads were created on the upper surface of the cooler by depositing a 5-mm layer of nickel. Silicon with high electrical resistivity (>30 W/cm) was used to ensure good electrical isolation between the two pads. The 3-mm-thick diode bar was a gain-guided device with 100-mm-wide emitting facets located on 150-mm centers. Typical optical output for these devices is 5 W per 3-mm bar or 250 mW per facet at three to four times the threshold current. Threshold current was typically 150 mA per stripe (or channel), and the slope efficiency was 60–70%.

Figure 4 plots the temperature response of one heat sink diode bar assembly as a function of thermal power under cw operation. This measurement was made with a 75-mm-diam chromel-alumel thermocouple mounted on an x-y-z stage with 10-mm resolution. Temperature was measured on the diamond chip near the emitting end of the diode array. By sweeping the thermocouple junction across this surface, we determined that the diode bar assembly was uniform in temperature to within our measuring accuracy of ±1 C.

From these data, with a heat-source footprint of 0.009 cm^2, we infer a thermal resistivity of 0.04 C/cm^2/W between the diode-diamond bar interface and the flowing coolant. For comparison, detailed calculations based on the formalism presented by Tuckerman (1984) predict a value of 0.09°C/cm^2/W for a close-packed, two-dimensional array. In our single-bar package, the silicon experienced some thermal spreading, which increased the effective size of the heat-source footprint at the coolant boundary layer. The degree of expected spreading is consistent with the measured thermal resistance of 0.04 C/cm^2/W.

Recently, we fabricated diode packages with 3-mm-diam apertures that can operate at higher average power. Under cw operation they achieved an optical power of 1 W, and under quasi-cw operation they reached a peak power of 14 W. We have also developed a silicon-etched manifold system that will allow us to achieve very short channel lengths (~500 mm), ensuring low thermal resistivity and very uniform cooling. These devices were recently measured to have a thermal resistivity of 0.013°C/cm^2/W.

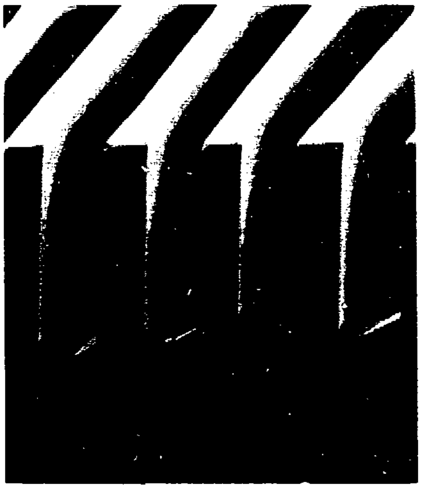

Figure 2. Typical silicon microchannel structure.

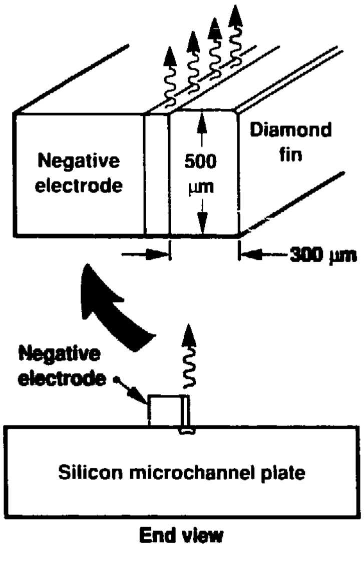

Figure 3. Diagram of the integrated laser-diode/microchannel cooler assembly used to demonstrate heat-sink performance.

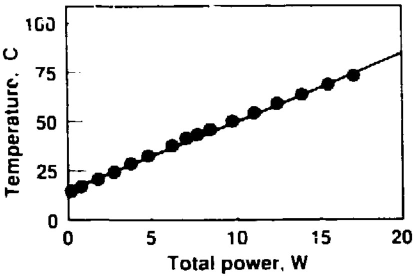

Figure 4. Temperature rise versus thermal power for one heat-sink diode-bar assembly (like the diagram in Figure 3). This assembly was determined to be uniform in temperature to within ±1 C (the accuracy limit of our measurements). For this assembly, we inferred a thermal resistivity of 0.04 C/cm^2/W.

During FY89, we expect to be able to demonstrate very high thermo-optical performance with diamond bar/microchannel cooler packages that deliver more than 15–20 W (cw) per centimeter of aperture, and with two-dimensional packages that generate more than 100 W/cm^2 (cw) of optical power. We will continue our evaluation of silicon-on-silicon bonding methods, and we will investigate various micro-optics fabrication concepts for efficiently transporting radiation from two-dimensional diode arrays to solid-state laser amplifiers.

References

Mundinger, D. C., R. J. Beach, W. J. Benett, R. W. Solarz, W. F. Krupke, P. R. Staver, and D. B. Tuckerman (1988), "Demonstration of High-Performance Silicon Microchannel Heat Exchangers for Laser Diode Array Cooling," *Appl. Phys. Lett.* **53** (12), 1030.

Tuckerman, D. B. (1984), *Heat Transfer Microstructures for Integrated Circuits*, Ph.D dissertation, Stanford University, Stanford, CA

Development of X-Ray Laser Holography

Principal Investigators: J. Trebes and D. Pinkel
Co-Investigators: J. Brase, G. Clark, J. Gray, R. London, D. Matthews, D. Peters, M. Rosen, P. Van Arsdall, and T. Yorkey

High-brightness x-ray lasers offer the possibility of creating three-dimensional, high-resolution, x-ray holographic images of biological microstructures* in vitro. *This new imaging technology will be a major advance over current imaging capabilities, with the potential to provide structural information about cellular components that cannot be obtained by any other method. We are developing this imaging technology and are assessing its ultimate limits and utility.

The development of x-ray lasers for high-resolution holographic imaging of biological structures has long been a goal of laser researchers worldwide. Although x-ray laser holography has been demonstrated (Trebes *et al.*, 1987), fundamental questions remain about its practicality and its ultimate limitations. We have been investigating these issues both experimentally and theoretically. Specifically, we are attempting to determine:

- The optimal x-ray wavelength, exposure, and exposure duration for coherent imaging.
- The ultimate three-dimensional spatial resolution.
- The effect of the target object's complexity on resolution.
- The effect of x-ray absorption by the object (and resultant damage) on resolution.

We have developed a simple model for x-ray scattering for biological materials in water based on Rayleigh-Gans scattering (London *et al.*, 1989). With this model, we have determined the optimal wavelength for maximum scattering and minimum absorption. It appears that an x-ray laser with a wavelength of 4.5 nm, a coherent output energy of 50 µJ, and a pulse duration of 50 ps should be sufficient for holographic imaging of biological materials with a 30-nm spatial resolution.

We have also been investigating the fundamental capabilities of x-ray holography using scaled visible-light analog experiments (Peters *et al.*, 1988). Familiar holography deals with the three-dimensional representation of the (two-dimensional) exterior surface of an object. Using an optical holography system, we can test our ability to obtain three-dimensional information from holograms, including features of the interior of complex objects. Clusters of transparent plastic spheres make suitable test objects for preliminary studies (see Figures 1–3); their size can be scaled so that the ratio of the sphere diameter to the optical wavelength is the same as that for the desired x-ray resolution to the x-ray wavelength. The true three-dimensional configuration is obtained by standard optical-microscopic sectioning. The holograms are reconstructed using numerical codes.

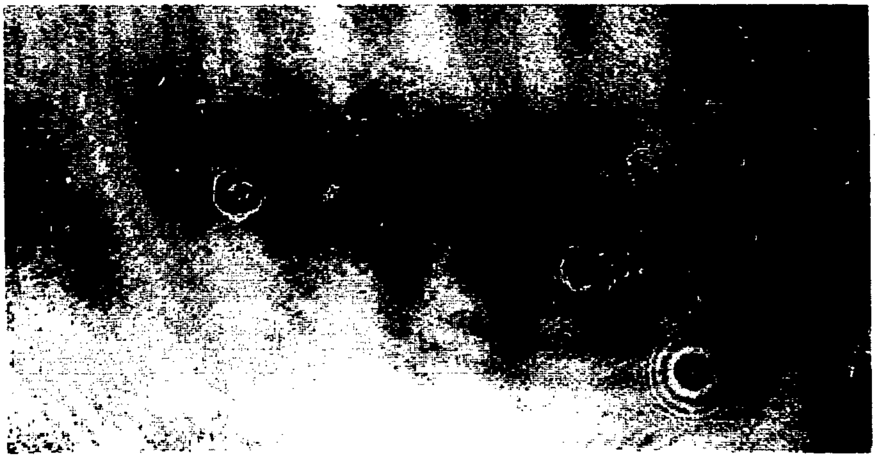

Figure 1. Photograph of two clusters of plastic spheres illuminated with laser light. The lens is placed so that a plane through the clusters is in focus. Spheres above and below the plane cause blurring. Some interference rings due to the coherence of the illumination light are visible.

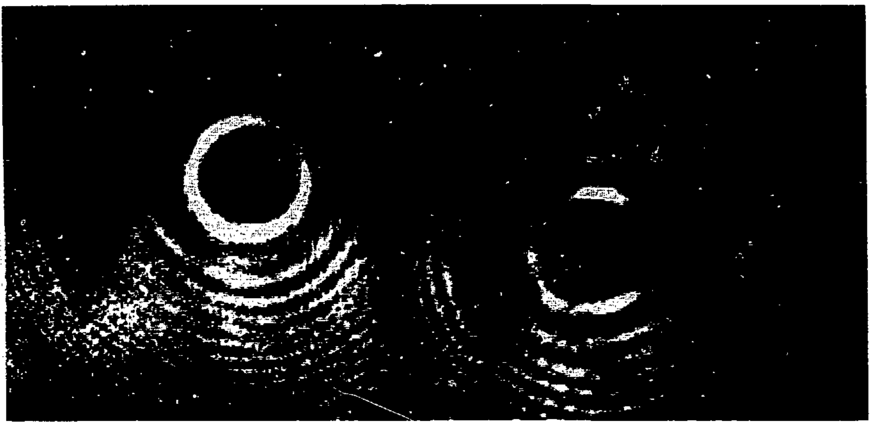

Figure 2. Hologram (in Gabor geometry) of the same clusters shown in Figure 1 using the same illumination source.

Figure 3. Digital reconstruction of the hologram shown in Figure 2. The depth of the plane of the reconstruction has been chosen to give the best correspondence to the image in Figure 1. Most of the features of the direct image are visible. The remaining interference rings are due primarily to the presence of the virtual image in the reconstruction. Improved reconstruction techniques and alternative holography geometries are being explored.

These codes also allow simulation and evaluation of a variety of holography geometries, and will be used next year in our efforts to design x-ray proof-of-principle holography experiments for laboratory x-ray lasers produced with the Nova laser.

References

Trebes, J., S. Brown, E. Campbell, D. Matthews, D. Nilson, G. Stone, and D. Whelan (1987). "Demonstration of X-Ray Holography with an X-Ray Laser." *Science* **233**, 517.

London, R., J. Trebes, and M. Rosen (1989). *X-Ray Holography: X-Ray Interactions and their Effects*. Lawrence Livermore National Laboratory, Preprint UCRL-98836.

Peters, D., J. Brase, G. Clark, J. Gray, D. Pinkel, J. Trebes, P. Van Arsdall, and T. Yorkey (1988). "A Comparison of Holography and Optical Sectioning for Three Dimensional Image Analysis." *Cytometry* Supp. 2, pg. 31.

FY88 $650,000

High-Resolution Imaging

Principal Investigators: J. I. Davis, N. A. Massie, and J. P. Fitch

We are pursuing advances in nonstandard imaging techniques for ground-based telescopes that will lead to angular resolutions limited solely by a telescope's diameter. We have completed important experimental demonstrations this year and have generated concepts for economical telescopes with effective apertures of 20 to 100 m.

The angular resolution of objects in space for ground-based telescopes using conventional imaging techniques is limited by the distortions of the atmosphere. This effect is caused by the same phenomena that cause stars to twinkle and is the result of minute temperature fluctuations in the atmosphere. As a consequence, even the 5-m telescope at Mount Palomar in southern California has an effective resolving power of a 10-cm telescope, despite its enormous light-collecting capability.

Obtaining diffraction-limited images would be of great value in terms of national security and for the discipline of astronomy. The Soviet Union, for example, launches over 100 satellites per year and is alleged to have the capability of launching four antisatellite weapons in a single day. Forty percent of the more than 7000 objects in orbit belong to the Soviet Union. The Soviets have clearly demonstrated their launch capacity and national resolve to provide for a tremendous presence in space. The mandate of national security requires that the U.S. determine the precise nature of that presence. Our project seeks to provide a low-cost technology for ground-based identification and assessment of objects in space.

Substantial scientific benefits will arise from diffraction-limited imaging as well. For example, at telescope diameters of about 10 m, features on the surfaces of supergiant stars can be resolved; at 100 m, active galactic nuclei can be resolved. Contributions of high-resolution imaging to date include measurement of the separations of double stars, determination of the diameter of supernova 1987A in the Large Magellanic cloud, and resolution of the controversy concerning the existence of superluminous stars. Properly designed large arrays could resolve planets around local stars.

Our technical approach, called speckle interferometry, is derived from a family of so-called "nonstandard" imaging techniques and is the optical analog of successful techniques used by radio astronomers. Astronomers have pioneered such techniques in imaging simple celestial objects, albeit with extremely long integration periods. The technological advances we seek would generate high-resolution images of the more complex satellites from data obtained during short observation periods. Furthermore, given the desire for 10-cm resolution, telescopes with effective apertures greater than 100 m will eventually be required. As a result, cost reduction becomes a major objective. Our near-term objectives are to provide a hundredfold increase in resolution together with a tenfold reduction in cost.

We faced three separate but related technical problems, each of which is discussed in more detail below:

- Signal-to-noise enhancement.
- Signal processing; that is, unscrambling the signal of interest.
- Large-effective-aperture, low-cost telescope design.

Our initial analysis of the first problem revealed that the signal-to-noise ratio would be substantially improved if we made our observations at the red end of the spectrum. This realization led us to consider using a charge-coupled device (CCD) imaging sensor. This concept is contrary to the prevailing wisdom, which asserts that imaging should be performed in the midvisible range with photon-counting sensors, primarily because the use of CCD sensors necessitates overcoming additive noise. We felt that to gain acceptance of CCD sensors and to validate imaging of complex, faint objects, an experimental validation would be beneficial. However, observing an actual satellite would be expensive, and detectors for optimal observations do not yet exist. Thus, as an economical and advantageous alternative, we designed an experiment in which imaging could be achieved through substantial turbulence along a horizontal path. The level and nature of the turbulence in our experiment was similar to that experienced by an observer looking upward. In addition we could perform parametric studies, varying the brightness, wavelength, and other factors.

To understand the problem posed by signal processing in the speckle-imaging process, consider observation by a large telescope of a point source, such as a star. Random distortions of the atmosphere, when averaged over seconds, create a circular blur of light at the focal plane. A perfect telescope of diameter D imaging an object through a vacuum would produce a spot of angular width λ/D, whereas looking through the atmosphere produces a spot of angular width of λ/r_0, where r_0 is the coherence length of the distortion, typically 10 cm. By using a narrowband filter to increase the coherence length of light, and by taking short exposures to freeze the distortions, we find that the image is actually composed of a random array of tiny spots, called speckles, of size λ/D. Information up to the diffraction limit of a telescope is present even though it is scrambled. The issue then becomes one of how to unscramble that information. Unscrambling the information to obtain the image is the signal-processing challenge.

The problem of recovering a diffraction-limited image from a sequence of speckle images is usually treated as the separate estimation of the magnitude and phase of the spatial frequency components of the image. Magnitude estimation is the same as power spectral estimation. Such estimations are accomplished by collecting a set of speckle images from the object of interest and a second set of speckle images from a point star. An estimate of the power spectrum for each set of data is calculated by averaging the power spectrum from each frame. The estimate for the point-star data represents the telescope-atmosphere system. If the power spectrum estimate from the object speckle sequence is divided by the power spectrum estimate from the point star, the effects of the telescope-atmosphere system are corrected out to the diffraction limit of the telescope, resulting in an estimate of the object's power spectrum. This technique for estimating the power spectrum (or Fourier magnitude) of an object from two sets of speckle images is called Labeyrie's technique. Except for certain special cases, however, an image cannot be obtained without knowledge of the Fourier phase.

Two techniques for recovering the Fourier phase of the object from speckle measurements have been implemented. One technique, known as Feinup's spectral iteration, uses the magnitude estimate from the Labeyrie algorithm together with finite support and positivity constraints of the spatial-domain object image to estimate the phase. This technique is computationally slow, stagnates, and can lead to artifacts in the image. The second technique, known as bispectral estimation, is similar to the power spectral estimation of Labeyrie's algorithm, but does not require a reference point star for phase estimation. An estimate of the object's bispectrum (Fourier transform of the object's triple correlation) is obtained by averaging the bispectra of each speckle frame. The Fourier phase estimate is then obtained by an appropriate integration of phases in the bispectral estimate. This estimate, together with the Labeyrie estimate, produces a reconstructed image.

To evaluate the basic imaging processes and the potential use of CCD detectors, we developed capabilities for both numerical and experimental simulation. Our computer-based atmospheric simulator allows input objects to be propagated through an isoplanatic atmosphere with arbitrary r_0. The objects are received by a telescope with a pupil function defined as the superposition of several circular apertures with different sizes and arbitrary obscurations. The simulator also includes noise sources resulting from Poisson photon statistics and nonideal photon detection. With respect to our "terrestrial" experiment, we obtained several gigabytes of data in FY88. We used a 0.5-m telescope to image small targets over a distance of 1.2 km. Because we control the target size, shape, and brightness, we can demonstrate imaging over a wide range of conditions.

Figure 1 shows images of a satellite target obtained from data taken during our experiment. This test image has a large dynamic range and contains a full range of feature sizes extending to outside of the diffraction limit of our telescope. This set of data is representative of the performance we anticipate for algorithms applied to imaging a satellite at a range of about 1000 km. Even though the reconstruction represents a significant enhancement compared to what can be seen in a single frame, we believe that future improvements in signal processing will provide images of even greater fidelity.

Our goal in terms of resolution for an initial system would be to resolve 10 cm at a range of 1000 km. This goal implies a telescope with an effective aperture of 12 m. To achieve such an aperture, we will use multiple telescopes arranged in a nonredundant pattern with outputs coherently combined at the sensor, as shown in Figure 2. The speckle-imaging process requires that paths be matched only to within the coherence length of filtered light, not to a fraction of a wavelength, as in conventional imaging. Thus, the requirement for path-length matching is nearly one hundred times lower. With this concept in mind, we can now contemplate the design problems for large, low-cost telescopes.

Consider that the Keck telescope, which is now under construction, is planned to cost $100 million and to have a single, contiguous, segmented aperture of 10 m. Telescope cost classically scales as the diameter cubed. Thus, a 40-m-diameter system should cost $1.5 billion. Obviously, we must seek concepts for radical cost reduction.

Our rationale for achieving large effective apertures at low cost is based on several important concepts. First, the use of an array of telescopes specifically designed for speckle imaging provides for substantial cost

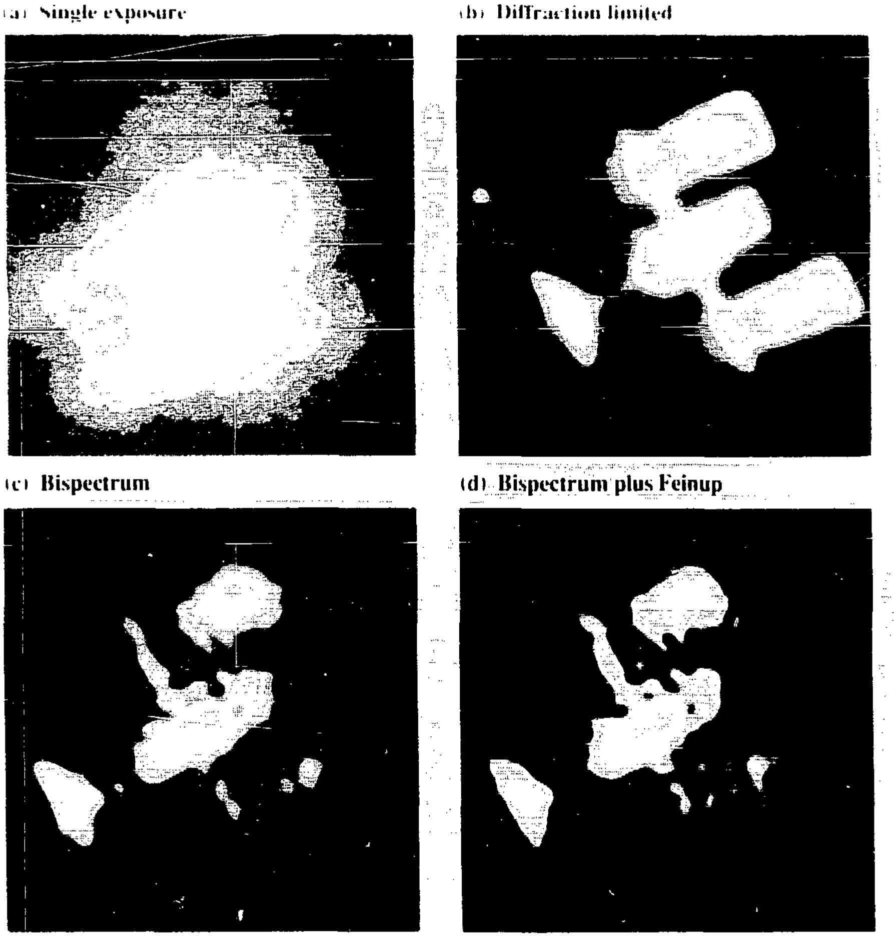

Figure 1. Experimental results from the terrestrial experiment. This experiment was conducted with a 0.5-m telescope, a wavelength of 0.7 mm, an optical bandwidth of 40 nm, an image exposure time of 5 ms, and a 3-cm-diameter satellite target (film transparency) at a range of about 1.2 km. These data are representative of imaging a satellite at 1000 km; 2000 speckle images were collected with D/r_0 = 17. (a) Single, short-exposure speckle image; (b) numerical calculation of the expected diffraction-limited image (no atmosphere, theoretical best case); (c) reconstructed image using bispectral estimation; and (d) reconstructed image after constraint (support and positivity) imposition on the bispectral estimate using 5000 iterations of the Feinup algorithm.

reduction. Second, from a review of design and cost reports for large telescopes, we recognized that the dome, site, and civil engineering represent a major fraction of ultimate cost. As a result, we elected to construct a telescope that would not require a classical dome but would be designed to operate in the wind. Our telescope would have an inexpensive, inflatable cover during the daytime and for protection during inclement weather. Third, our studies revealed that the high-altitude sites classically used by astronomers contribute substantially to cost. Such sites are unnecessary for our telescope; that is, we need not rise above atmospheric water vapor for 10-μm astronomy. Indeed, we have identified a site along the northern California coast that has superb "seeing" (large r_0 values) and that involves low cost in terms of construction. Fourth, the thickness of our telescope is controlled by its f ratio times the diameter of the smaller telescopes. As a result, our telescope array is almost two-dimensional. This design leads to tremendous savings in the mechanical structure and readily admits to resonances sufficiently high for protected operation without a dome.

The telescope mount currently favored by astronomers is known as

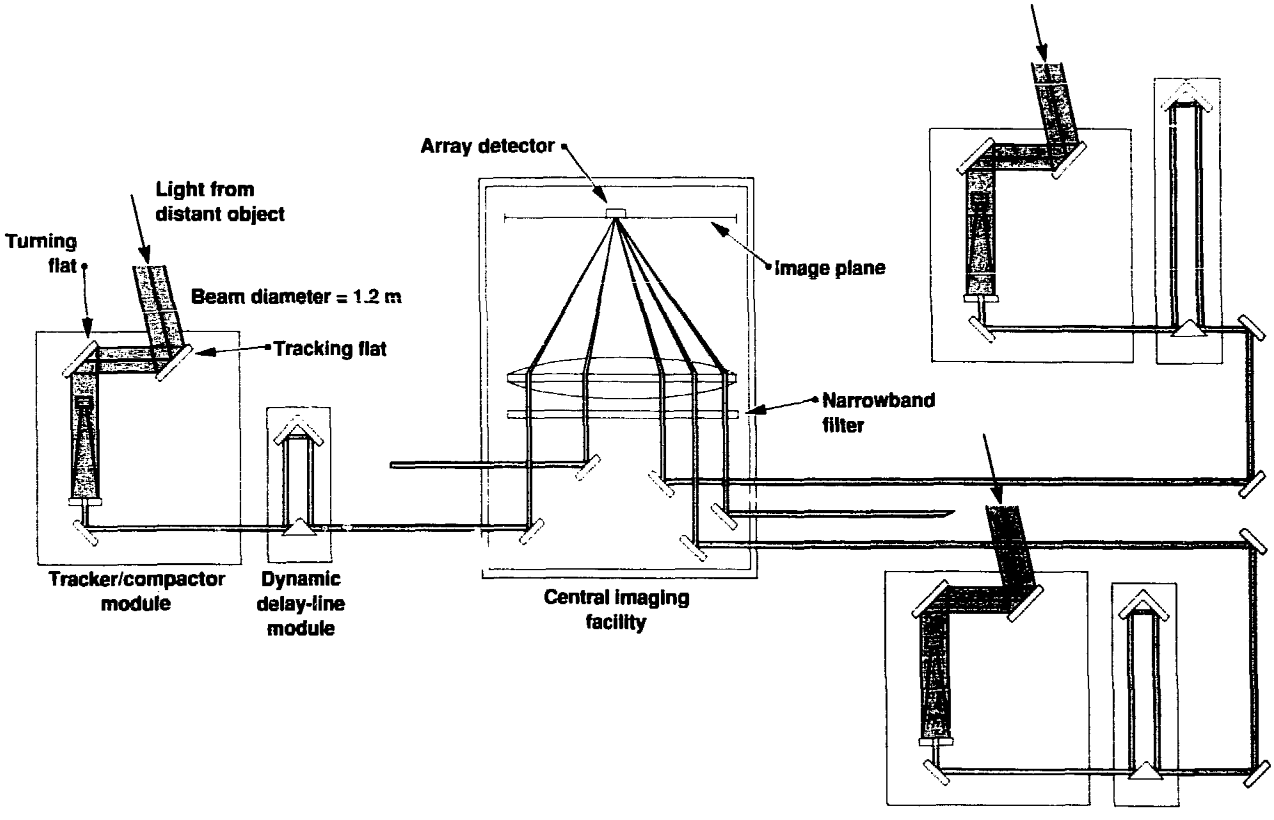

Figure 2. Optical layout of the high-resolution-imaging telescope. Outputs are coherently combined in this array. Requirements for path-length control are nominally 100 times lower for a speckle interferometry telescope compared to those requirements for conventional imaging.

the azimuth altitude mount. This mount consists of a large rotating turntable resting on the ground for the azimuth motion, with two posts mounted at the periphery of the turntable. Bearings for the altitude motion are at the top of the posts. The telescope is supported between these structures. Such a mount is quite large; the unsupported span is at least the diameter D of the telescope. When objects pass directly overhead in this design, they cannot be tracked due to the requirement for infinite acceleration in the azimuth axis, and such a failure represents a major drawback for satellite tracking.

In our concept, on the other hand, the telescope is centrally supported on a ball or gimbal, and the longest unsupported span is $D/2$. Because the lowest structural resonance scales as the cube of the unsupported length, the resonance is eight times higher, leading to greater freedom to operate in the wind. The mount is free to rotate in both angular directions, allowing for alt-alt tracking control, and cables are used as force actuators. Figure 3 shows a 20-m, 12-aperture embodiment of our design. In addition, we have also designed a 10-m version of the telescope. This size would perhaps represent an optimal compromise between utility and risk and is likely to become the demonstration system.

During FY89, we will continue to assess system performance. We plan extensive use of the numerical simulator and will conduct additional terrestrial experiments. We will also construct a detailed design of the 10-m system, with the objective of ascertaining a cost estimate accurate to within 20%.

(a) Plan view

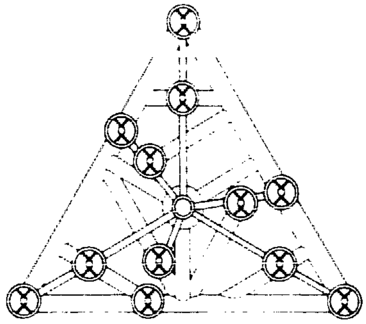

(b) Elevation view

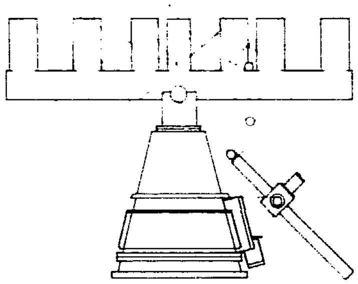

(c) Model

Figure 3. (a) Plan view, (b) elevation view, and (c) photograph of a model of the high-resolution-imaging telescope. Our unique design uses a mounting on a centrally located ball. A 12-element, nonredundant array is shown with 1.5-m telescopes for a total effective aperture of 20 m.

Compact Torus Accelerator

Principal Investigators: C. W. Hartman and J. H. Hammer

The Compact Torus Accelerator project reached a major milestone this year. Ring-trajectory determinations from magnetic field measurements, accelerator inductance, and code calculations using the measured ring mass are in good agreement and strongly support the predicted acceleration process. Qualitative agreement was also obtained between the ring's measured and predicted internal structure and between ring-focusing experiments and predicted magnetic field increases and ring reflection in the cone. In addition, we have shown that a compact torus accelerator could be an efficient soft-x-ray generator for simulating nuclear weapon effects.

The objective of the Compact Torus Accelerator project (also known as RACE) is to accelerate, compress, and focus plasma rings confined by compact-torus magnetic fields. In 1987, we successfully accelerated plasma rings in straight coaxial electrodes to 20 kJ kinetic energy with a trajectory-inferred mass of 20 μg (Hartman and Hammer, 1987). The measurements of ring acceleration made then, although incomplete, supported the predicted acceleration process based on magnetohydromagnetic (MHD) theory and simulations of a constant-mass ring. Measurements of the ring trajectory with probes, measured accelerator inductance, and calculations of ring trajectory using the RAC ring acceleration code could be brought into agreement by fitting the inferred ring mass.

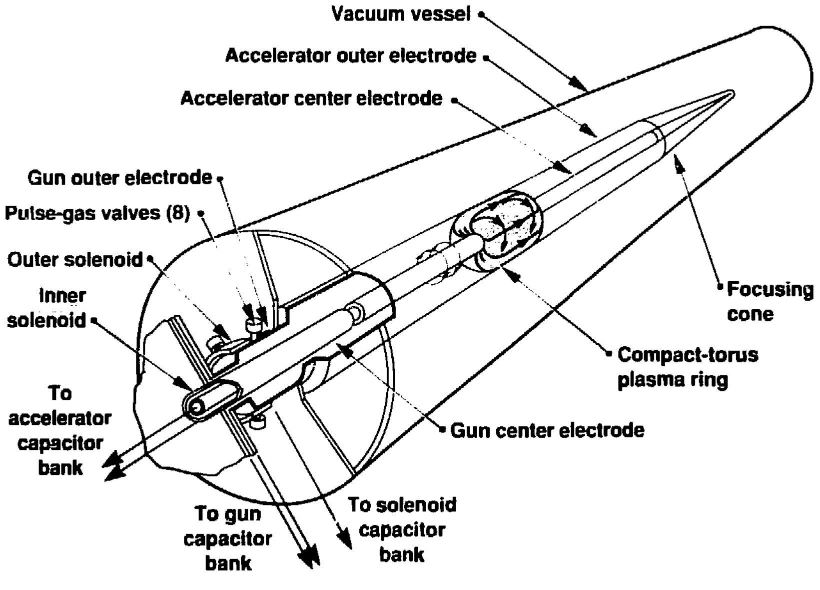

Figure 1. A compact torus undergoing acceleration by the B_θ field in the middle of our RACE apparatus. The initial magnetic field of the gun is established by discharging the solenoid capacitor bank through solenoids located outside the gun's outer electrode and inside its inner electrode. Eight magnetically driven gas valves admit roughly 1 atm cm^3 of gas. The gun's capacitor bank feeds the gun through a low-inductance array of coaxial cables and collector plates. Discharge currents typically have a 2-μs risetime and a 500-kA peak current.

In 1988, we improved our plasma-density diagnostics to measure total ring mass and the ring's internal density distribution. We improved the sensitivity of our HeNe interferometer to ~10^{-3} fringes and deployed a CO$_2$ interferometer to allow us to measure the ring's line-averaged electron density. Additional monochrometer measurements of visible radiation at the breach of the accelerator enabled us to determine that, under the conditions presented here, the accelerated ring was composed of nearly all hydrogen ions (O$^+$, C$^+$ ≤ several percent). Thus the ring mass could be estimated from the line-averaged electron density.

Using this estimated ring mass, trajectory calculations with RAC are in good agreement with measurements, more completely confirming the predicted acceleration process (Hammer *et al.*, 1988).

We initiated ring-focusing experiments in FY88 using a 4-m straight coaxial electrode and 2- and 3.8-m-long cone electrodes. These tests, in progress, have shown the expected basic ring-reflection trajectory in a cone and threefold compression in radius and magnetic field. A major improvement of the HAM two-dimensional MHD code was completed. HAM now uses a nonrectangular mesh, which allows calculations of ring motion in conical electrode regions. Preliminary results with this code show ring focusing as expected. Simulation of actual RACE-dimension rings, where $L_{ring}/L_{cone} = 0.4$, is in progress.

We also studied the use of a compact torus accelerator to generate intense bursts of soft x rays for simulating nuclear weapon effects. LASNEX calculations have been applied to the shock heating and radiation of a focused, accelerated plasma ring, and numerical acceleration calculations have been used to evaluate the scaling of accelerators up to a 100-MJ simulator. Such a simulator appears uniquely able to simulate nuclear weapon effects on whole warheads or satellite systems.

The discussion below summarizes our FY88 work. As a context for this work, Figure 1 shows schematically a compact-torus plasma ring being accelerated in our RACE experiment.

Magnetic field measurements made with probes arranged axially at the outer accelerator electrode confirm that the ring structure is preserved during acceleration. As shown in Figure 2, the ring evolves from a bell-shaped axial distribution when the acceleration field is weak ($z = 71$ cm) to one in which the gradients at the back of the ring are steepened by the B_θ acceleration force ($z = 264$ cm). Eddy-current variations near the probes are not corrected for and lead to the variations in signal height.

Three independent determinations of ring trajectory are consistent with our models. Figure 3 compares the ring trajectory measured by magnetic probes with the current sheath position determined from the accelerator inductance and with a zero-dimensional RAC calculation for a ring mass of 8 μg, determined from the HeNe interferometer. The agreement of these trajectory determinations confirms our predicted acceleration process.

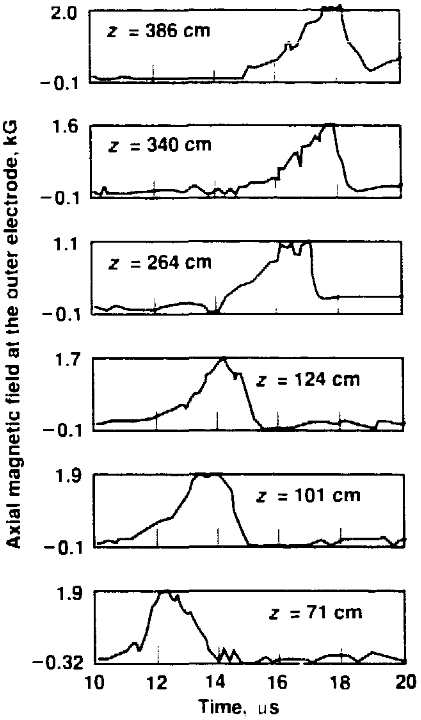

Figure 2. Time sequence of the axial magnetic field of an accelerated compact-torus plasma ring. The field is measured by magnetic probes located on the outer electrode and arrayed along z.

We have obtained more information on the internal structure of the accelerated ring and find it to be in qualitative agreement with MHD calculations using the HAM code. Figure 4a plots the measured axial field along with the accelerating B_θ field at $z = 124$ cm. The B_θ field distribution shows that the accelerator current flows at the back of the ring, indicating that the ring forms a high-conductivity moving short. The steepening of the gradients at the back of the ring and the ring's shorting are in qualitative agreement with MHD predictions of the accelerated ring's structure (adjusted B_θ curve). The HAM calculations have somewhat different initial conditions than the experiment.

Figure 4b shows the line-averaged electron density n_e and the B_z field at the outer electrode ($z = 124$ cm). For this case, the electron density remained below detectability for 40 μs after the ring's passage, indicating very little plasma ($n_e \leq 5 \times 10^{12}$ cm^{-3}) following the ring or evolved by electrode interactions with the ring or accelerated field. The magnitudes of B_z, B_θ, and n_e predicted by the HAM code in Figure 4 are adjusted in overall magnitude and scale length.

The data in Figure 4b are also in qualitative agreement with MHD calculations. Two features of this agreement, consistent with a varying acceleration field, are the tendency of B_z at the outer wall to trail n_e and for the n_e profile to also be shaped by acceleration. The trailing B_z results from an axial shift of the ring's back flux surfaces in response to the radial variation of the accelerating B_θ field ($B \propto 1/R$). The shaping of n_e, shown

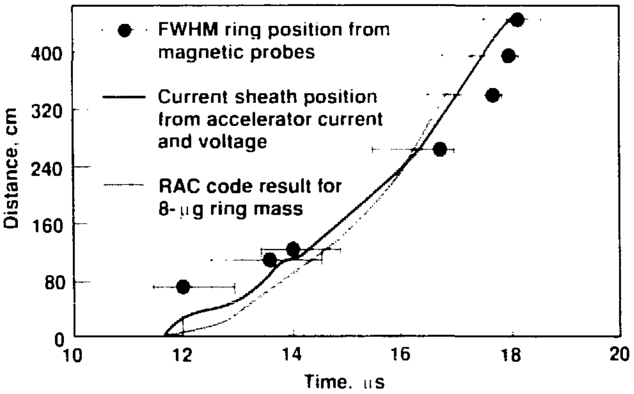

Figure 3. **Comparison of measured and calculated ring trajectories. The circles indicate peak ring fields measured by probes at the outer electrode, and the bars indicate half-amplitude points. The accelerating current sheath closely coincides with the ring B_z.**

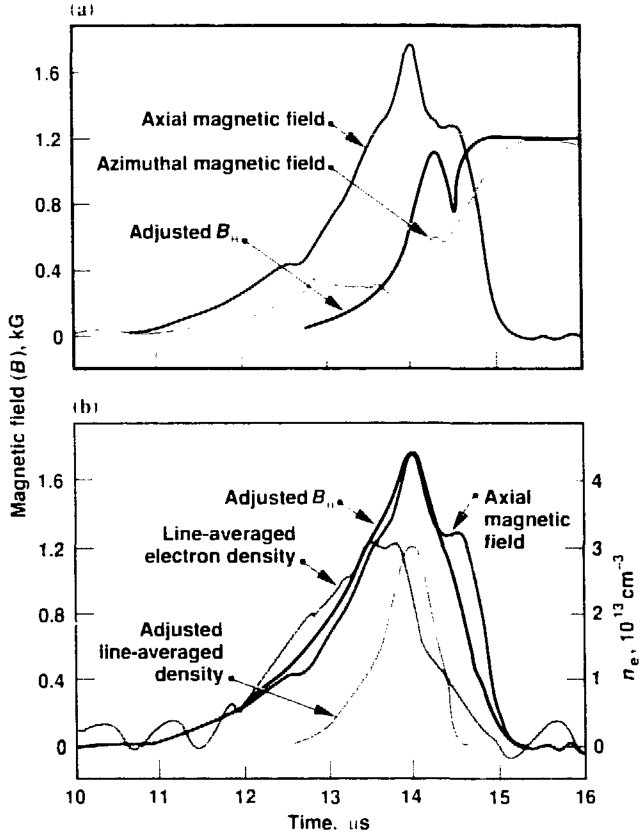

Figure 4. **(a) Axial magnetic and accelerating B_θ fields measured at the outer electrode (z = 124 cm). The adjusted calculation was made with the HAM two-dimensional MHD code. (b) Axial magnetic field at the outer electrode and line-averaged electron density measured at z = 124 cm. The adjusted B_θ and density curves were also calculated with HAM.**

most clearly in the code calculations, results from the accelerated plasma tending to "slump" to the rear of the ring. The degree of slumping depends on plasma temperature, which can differ significantly between experiment and simulation. The latter is shown for qualitative comparison.

We also conducted preliminary studies of ring focusing with 2- and 3.75-m-long cones attached to the 4-m straight acceleration section in RACE. Diagnostics for these studies were limited to magnetic field probes arrayed along the cone's outer electrode.

Figure 5 shows probe locations and the B_z field measured along the 2-m cone for a ring whose axial peak-field point penetrates to about z = 486 cm and whose head end reaches to about 509 cm. The peak field for this case increased by a factor of 2.6, and the radius compression reached 2.35. No clear reflection occurs.

On some shots, the ring clearly reflects from the cone (as expected from simple dynamics) and stops at the cone's entrance, where it decays over 100–200 μs. Figure 6 shows the trajectory of a ring that reflects from the 2-m cone at a radius compression ratio of 1.6. For this shot, the ring profile remained identifiably constant so that the ring length (FWHM) could be estimated along the trajectory. As can be seen, this length decreases as the reflection point is approached.

Analytic estimates and two-dimensional MHD calculations show that if the ring is adiabatically focused and β remains low, then $B_z/B_{z0} = C^2$ and $L_{ring0}/L_{ring} = C$. [B_{z0} and B_z are the initial and final (focused) axial magnetic fields, L_{ring0} and L_{ring} are the initial and final ring lengths, and C is the radial compression ratio.] Data for these two ratios versus C for both the 2- and 3.75-m cones have been obtained for a limited number of shots in which the ring is clearly self-similar during focusing. We find that for both cones, $L_{ringf}/L_{ring} = C^{-2}$ while $B_z/B_{z0} \cong C$, clearly deviating from adiabatic MHD compression. The source of this discrepancy is not yet known. However, we note that deviations from predicted focusing might be expected in this experiment for several reasons: $L_{ring}/L_{cone} \cong 0.3$ to 0.5 is not small, leading to nonadiabaticity; the ion gyro radius is comparable to the ring size; and any loss of ring mass or large slumping during focusing can push the ring beyond current-driven streaming instabilities, introducing large anomalous resistivity and rapid ring-field decay. These effects should be reduced (adiabaticity should increase) when, in FY89, a precompression cone is added at the beginning of the accelerator, and the gun/accelerator bank energies are increased.

The axisymmetric HAM code was extensively revised in FY88 to allow generalized quadrilateral zoning in a mixed Eulerian-Lagrangian mesh. The code's previous version was extremely useful for analyzing the operation of the magnetized coaxial gun and the subsequent formation of the compact-torus plasma rings. HAM calculations included the self-consistent establishment of the poloidal field structure by solenoidal field coils, gas flow from the pulse-gas valves into the interelectrode region, discharge of the gun bank, reconnection of the poloidal field around the gun-produced plasma to form isolated plasma rings, and acceleration of the rings by the discharge of a second capacitor bank.

The code's upgrade was motivated by the need for generalized zoning to simulate the effects of arbitrary electrode shapes and boundary conditions. We are now using the new code to analyze the compression of accelerated plasma rings in converging conical electrodes. These simulations will enhance our physical understanding

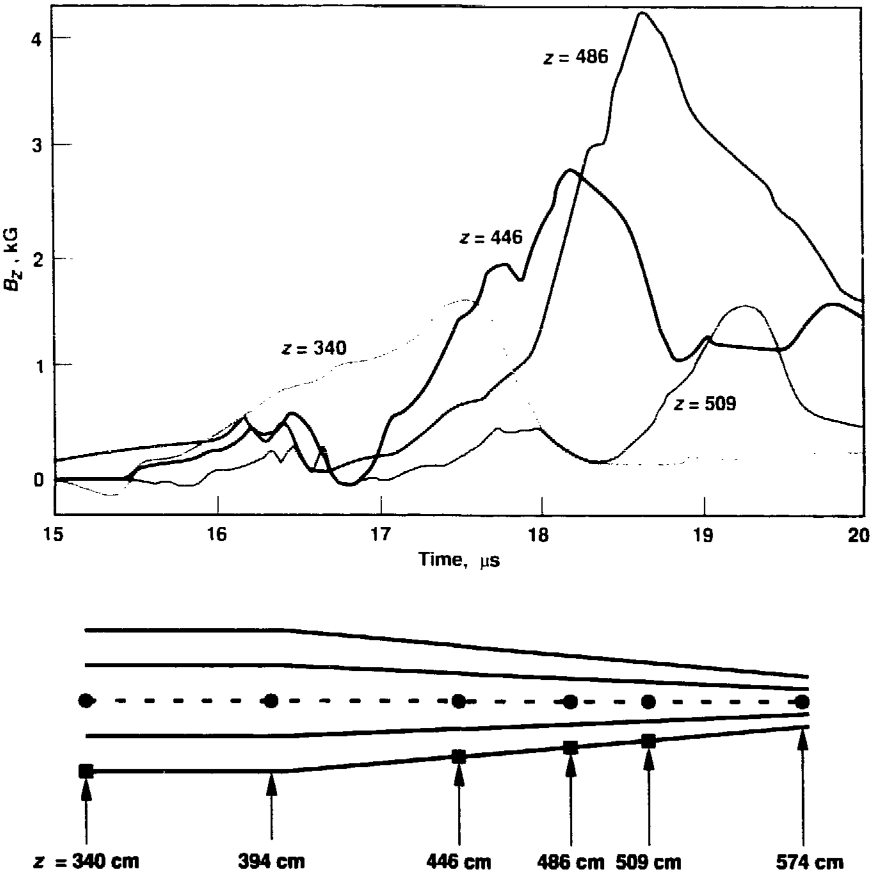

Figure 5. Measured B_z field at the outer electrode for an accelerated ring entering the 2-m focusing cone. The ring stagnates at about 486 cm, where the B_z field has increased by a factor of about 2.6 and the ring radius has decreased by a factor of 2.35. Probe locations (black squares) are shown at the bottom.

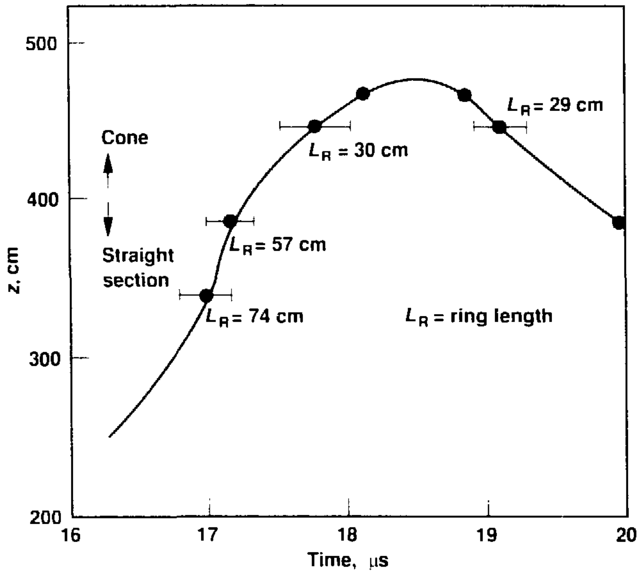

Figure 6. Trajectory of an accelerated ring (based on measured B_z field) that reflects in the 2-m cone at a radius compression ratio of 1.6. Ring length (L_R) decreases as the reflection point is approached.

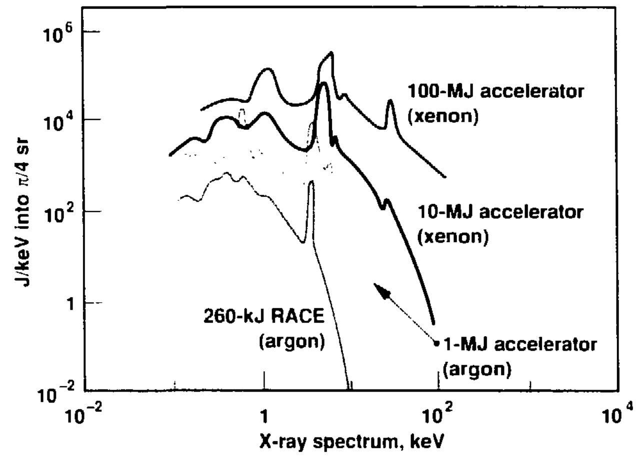

Figure 7. Calculated radiation spectra for rings accelerated over a range of energies from 260 kJ (RACE) to 100 MJ. The efficiency of acceleration $U_{kinetic}/U_{bank}$ is 0.5, and the ion species and ring mass are chosen to optimize the radiation output. With a 100-MJ accelerator bank, 22 MJ is radiated.

of ring behavior for various cone geometries, initial velocities at the cone entrance, and internal ring structures.

During FY88, we also evaluated the compact-torus accelerator as a soft-x-ray generator for simulating nuclear weapon effects. The basic process is to accelerate and focus a high-atomic-number ion ring plasma, which then impacts a solid surface, arresting the ring's kinetic energy and shock-heating the ions. If the focused plasma density is high enough, during the shock time ($T_i \cong$ 1 MeV), the ions will collisionally heat the electrons. The hot electrons strip the ions to high-charge states, which then efficiently radiate *K*- and *L*-shell excitation line spectra, along with plasma bremsstrahlung radiation. At focused ring speeds of 0.5–2 × 10^8 cm/s, typical of those already achieved in RACE, the kinetic energy is in gigajoules per gram. Thus the electrons may be heated to ~10 keV to radiate 10–30% of the ring's kinetic energy with a spectrum that peaks at 5–10 keV. To produce enough total radiated energy for testing whole weapon systems, we investigated scaling compact torus accelerators up to 100 MJ.

Figure 7 summarizes LASNEX calculations of the radiation produced by compact torus accelerators with accelerator bank energies from

260 kJ (RACE) to 100 MJ. For the 100-MJ accelerator, the total radiated energy is 22 MJ and the typical pulse width is 10–20 ns. Achieving the calculated radiation output shown in Figure 7 for RACE with argon-ion rings will place the experiment at the state-of-the-art level for soft-x-ray generators.

We used RAC to examine the scaling of compact torus accelerators. RAC calculates ring trajectory in straight and conical coaxial electrodes and includes electrode heating by radiation and eddy-current dissipation. It also calculates ring decay and plasma properties from radiation, ohmic heating, compression, and other energy flows. Figure 8 shows schematically the scale of accelerators from RACE (260 kJ) to 100 MJ. In each case, the expected limits on acceleration and ring decay have not been exceeded. We assume a precompression phase that couples the accelerator more efficiently to the low-voltage capacitor banks and also shortens the overall acceleration length. Precompression increases the peak field in the straight acceleration region; for the 10- and 100-MJ cases shown, this field reached 300 kG.

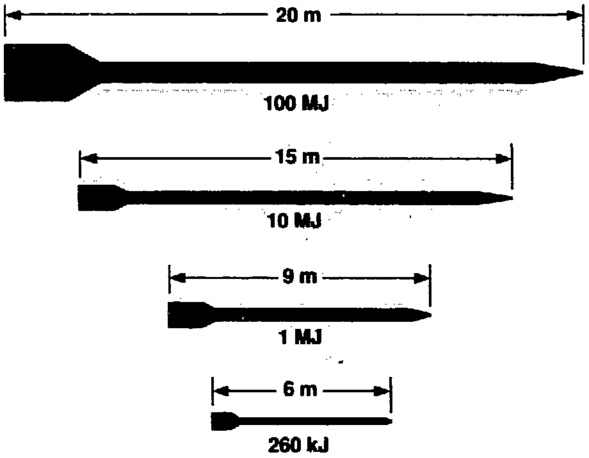

Figure 8. Scaling of compact torus accelerators from 260 kJ (RACE) to 100 MJ as soft-x-ray generators. All accelerators are assumed to use a precompression phase.

Cost as well as scalability is an important consideration for very-high-energy accelerators. We have designed and estimated the cost of the accelerators' capacitor banks (the primary electrical cost) using off-the-shelf capacitors. Since the discharge time is long (10 μs) and capacitor voltage is low (<500 kV), energy storage is relatively inexpensive and economies of scale are significant. A 100-MJ, 500-kV accelerator bank would cost about $35 million, or $0.35/J.

References

Hammer, J. H., C. W. Hartman, J. L. Eddleman, and H. S. McLean (1988), *Experimental Demonstration of Acceleration and Focusing of Magnetically Confined Plasma Rings*, Lawrence Livermore National Laboratory, Preprint UCRL-98988.

Hartman, C. W., and J. H. Hammer (1987), "The Compact Torus," *Institutional Research and Development*, Lawrence Livermore National Laboratory, Report UCRL-53689-87, pp. 102–107.

FY88 $1,000,000

Computer-Aided Design Tools for Very-Large-Scale Integration

Principal Investigator: W. S. Scott

The primary goal of the very-large-scale integration (VLSI) computer-aided design (CAD) portion of the Laboratory's efforts in supercomputer research and development is to create a vertically integrated CAD toolset to facilitate the design, manufacture, and testing of high-performance digital systems. We have placed particular emphasis on exploiting the manufacturing techniques developed by LLNL's laser pantography project, techniques that allow rapid fabrication of wafer-scale digital systems.

During FY88, we extended our previous work in developing tools to aid in the physical design (layout) of wafer-scale systems. In addition to completing the semiautomated hint router, we developed and demonstrated a fully automated router capable of exploiting two, three, or more wiring layers, each with its own electrical and physical characteristics, such as are available in hybrid wafer-scale and semicustom gate-array laser pantography processes. We also developed the key elements of a higher-level logical design tool for digital systems resynthesis—the automatic conversion of existing designs to such new implementation technologies as mapping a discrete board-level TTL (transistor-transistor logic) design into a hybrid wafer-scale semicustom CMOS (complementary metal-oxide semiconductor) version.

Design and Fabrication of Custom Integrated Circuits. Increasingly, builders of high-performance electronic systems are discovering the advantages of designing their own integrated circuit (IC) chips to implement these systems. Several methodologies have been developed for designing IC chips, ranging from semicustom approaches, in which the designer builds the chip from a collection of predesigned components, to fully custom approaches, in which the entire IC is designed from scratch. Three semicustom approaches—gate array, standard cell, and macrocell—and the fully custom approach are described more thoroughly in the box on page 129.

Recent technological advances, such as those provided by laser pantography (McWilliams and Tuckerman, 1985), have enabled collections of individual ICs to be assembled into wafer-scale systems. As a result, much higher packing densities are attainable than with the conventional approach of placing each chip in its own plastic or ceramic package and using a printed-circuit board to interconnect them. Wafer-scale systems created by laser pantography have much in common with standard-cell or macrocell styles used to create individual ICs, but they use ICs interconnected on a silicon wafer substrate instead of fixed transistor patterns on an individual chip.

Semiautomated Hint Router. In high-performance, custom IC designs, it is often necessary to route a few key signals along carefully chosen paths prior to the automatic routing of less performance-critical wires. To aid in this task, we have developed the hint router, an interactive maze router, as part of the Magic IC layout system (Arnold and Scott, 1988). The hint router is a flexible tool intended for use whenever tight or unusual constraints do not permit fully automatic routing. It has already been used in the layout of an 80,000-transistor CMOS chip (the "smart substrate" that was developed by our group and reported last year) as well as for routing the control signals of a 100,000-transistor, high-performance CMOS floating-point chip being developed by the UC Berkeley SPUR project.

Several new ideas for maze routing have been developed in the hint router. Hint layers permit the user to map out the general path of a route and pull the route in desired directions, while leaving details, such as obeying the layout width and spacing rules, to the router. Several additional routing heuristics were refined last year. Their use both improves the quality of routes in heavily congested designs and reduces the time it takes to complete those routes. The gross structure of the layout is now preprocessed to facilitate accurate cost-to-completion estimates during routing and hence to allow effective pruning of misdirected partial routes. A windowed search strategy slowly shifts the focus of the router from the start point toward the goal, permitting consideration of alternatives at all stages of routing without the penalty of exhaustive (exponential) blowup in highly congested regions. Finally, the general maze-routing algorithm has been extended to allow an arbitrary number of source and destination points, effectively allowing it to be used automatically to complete partially wired signal networks.

Multilayer Router. We have also implemented a fully automatic, gridless and channelless multilayer router as part of the Magic system. This router addresses several new routing problems arising from some of the expanded capabilities of laser pantography processes, particularly those of wafer-scale complexities (wiring feature sizes of a few micrometers but total problem sizes of 10 cm) and multiple, electrically different routing layers (four or more on a single silicon printed-circuit board).

This router incorporates three key ideas. First, it represent nets as rectilinear Steiner trees with floating segments. Segments of these Steiner trees correspond to wire segments of a net, and the relationship among segments defines the topology of the net. A floating segment is bound to a routing layer but not to a specific

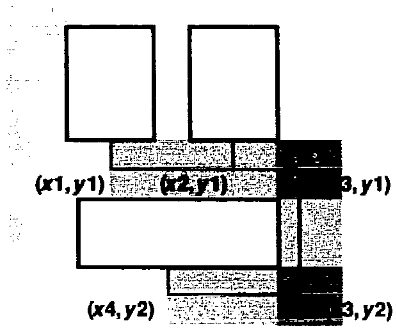

Figure 1. A rectilinear Steiner tree defining the course route of a three-terminal net. Shaded areas delineate ranges of floating segments.

Semicustom and Fully Custom Design Methodologies

Four common design methodologies constitute the range of choices for VLSI. Gate arrays (a) consist of rows of identical cells of transistors. The designer specifies which of a collection of standard metal interconnect patterns is to be placed atop each cell (thereby defining a given logical function) and how the terminals on each cell are to be connected. Gate arrays are the least expensive to fabricate since the underlying array of transistor cells can be mass-produced independently of the metal interconnect that is added later.

Standard-cell designs (b) also make use of standard logical functions, but they are not implemented atop an underlying array of identical transistor cells. Instead, the placement of cells within predefined rows or columns is under the control of the designer. Because the underlying transistor pattern can vary from cell to cell, standard-cell chips cannot be built atop prefabricated transistor arrays and are therefore more costly than gate arrays.

Designs using macrocells (c) offer still more flexibility than standard-cell designs. Macrocells are parameterizable, rectilinear blocks that are customized from a library of templates; they are connected either by abutment or by automatic routing.

In fully custom designs (d), there are no restrictions on the components; the designer is free to create new circuits and to lay them out in the best possible way. As a result, it is possible to achieve greater density with a fully custom design than with any of the other design styles.

(a) Gate array

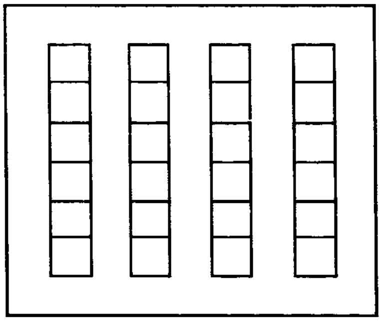

(b) Standard cell

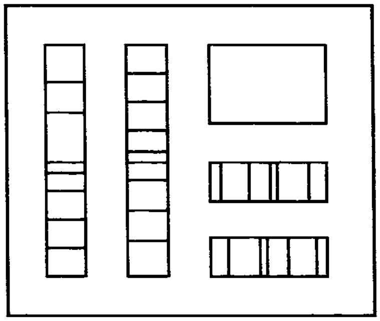

(c) Macrocell

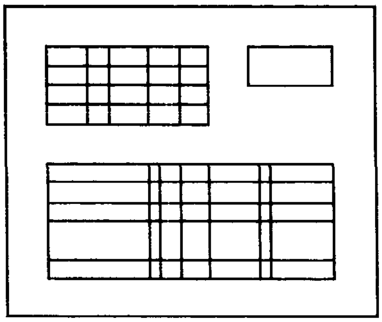

(d) Fully custom

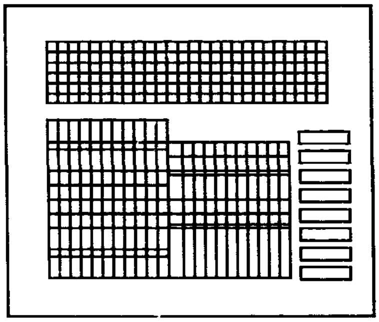

location within that routing layer; it may *float* within a range of values, as shown in Figure 1. As routing progresses, floating segments are bound to fixed locations. By preserving the floating segment representation throughout the routing process, it is easy to allow nets to be partially ripped up, enabling the router to explore alternate routes (to "change its mind") without incurring the end-game penalty of exponential runtime typical of traditional rip-up-and-retry routers.

Second, a routing scheduler applies a set of routing strategies to a queue of partially routed nets; each strategy attempts to further the routing of a net. Simple strategies are applied first, followed by more complex strategies to resolve more difficult problems. The orchestration of strategies is controlled by a finite-state machine, analogous to the controlling "expert" in the Weaver system, for example (Joobbani, 1986), but without the excessive runtime overhead typical of such general-purpose expert systems. Routing strategies are typically simple. They involve generating course routes, laying wires in routing regions, maze-routing through congested areas, and ripping up obstructing segments.

Third, a corner-stitched database (Ousterhout, 1984) represents obstacles and wiring as the routing progresses. Corner-stitching is a technique for representing two-dimensional objects. It provides a representation for such spatial relationships as adjacency that results in fast, efficient algorithms for searching for, creating, and deleting objects. By using corner-stitching, the router can both work with wires of varying widths and avoid preexisting wiring.

Our approach avoids several of the limitations characteristic of conventional routing methods:

- The router works on one net (as opposed to a channel) at a time, but it does not need to fully route a net before it advances to other nets. At any given time, a net may be partially routed or partially ripped up. The router thus has the flexibility to change its mind about the routing of a net as the routing problem is fleshed out.
- Because new course routes can be generated dynamically to avoid congested areas, generating course routes is a routing strategy, not a distinct routing phase.
- Connections may be made anywhere in a routing region, not only at its periphery, making it possible to route dense sea-of-gates or sea-of-transistors designs as well as more conventional, channelized standard-cell or gate-array designs.

We have successfully routed several large wafer-scale designs in times comparable to those required for single-chip designs—roughly 30 minutes of Sun-3 CPU time (Lunow, 1988.)

Digital Systems Resynthesis. The rapid prototyping and wafer-scale integration capabilities offered by laser pantography technology make it very attractive to have a tool to automatically convert existing designs into a form that can exploit that technology. The digital systems resynthesis effort aims to produce a conversion tool that will take (for example) an existing discrete-TTL design and reimplement it as (for example) semicustom CMOS circuits interconnected by a silicon printed-circuit board.

It is essential that we evaluate the tools we develop with realistic test cases. For this purpose, we have chosen a circuit design for a memory and input/output controller done as part of the Advanced Processor Project (APP). Because it consists of machine-readable schematics for both a discrete-TTL breadboard version and a pair of hand-designed CMOS gate arrays for a high-density version, this circuit provides us with both a starting point and a hand-generated end point for comparison.

During the past year, we have written a number of portions of the resynthesis system. The basic design for the digital systems resynthesis tool, called SECTAR (Self-Correcting Timing and Resynthesis), is complete. This system is based on network modification to ensure conformance to electrical design constraints (timing, power, fanout, etc.). SECTAR is made up of an incremental timing analyzer, a network extract-and-replace algorithm, and a simulated annealing optimizer that uses several network-modification techniques to transform a network into one that meets its functional criteria. SECTAR is designed to inform the engineer of trouble spots in cases where the tool could not conform to specified constraints.

Input to SECTAR is currently in a simple design-specification language, and the input interface has been designed to easily accommodate the integration of other design-specification languages (EDIF, VHDL). EDIF 2.0.0 is scheduled to be used because of industry's commitment to making it available for electrical design information transfer between tool sets. Valid Logic Systems will have an EDIF 2.0.0 reader and writer available late in 1988, which will allow SECTAR to operate on the APP test case.

We have also implemented the SECTAR database, which is tailored for quick traversal by the timing-analysis algorithm and for easy extraction and replacement of subnetworks. We have developed the following network transformation algorithms for use in SECTAR, as illustrated in Figure 2:

- Primitive function substitution (a). Simple replacement of input

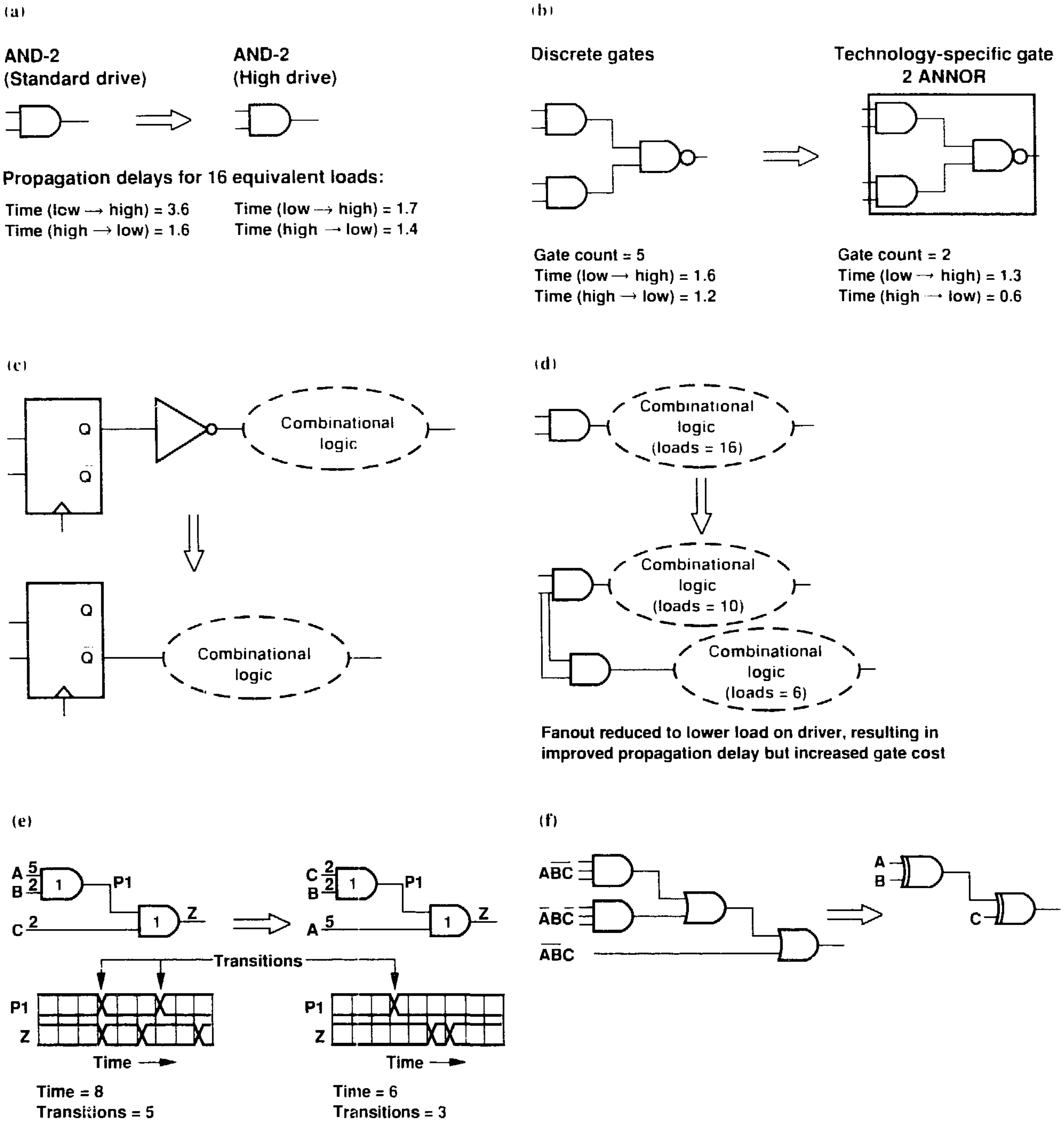

Figure 2. Six network-transformation algorithms used in SECTAR: (a) primitive function substitution, (b) macrofunction substitution, (c) logic negation, (d) logic duplication, (e) signal reordering, and (f) logic minimization. These algorithms are described in the text.

components by those in the target technology that best suit the needs of the circuit. This transformation automatically chooses, for example, whether to use high-power (and therefore high-speed) gates in appropriate situations.

- Macrofunction substitution (b). Graph-matching techniques map a subnetwork into a target-technology-specific component. These components are usually technology-specific, cost-effective combinations of gates.
- Logic negation (c). A subnetwork is negated to take advantage of an available complementary output of the driving subnetwork.
- Logic duplication (d). A subnetwork in the design is duplicated to improve the timing in an area by lowering the effective loading (fanout) of a node in the network.
- Signal reordering (e). The logic in a combinational subnetwork is reordered so that late-occurring signals are evaluated last, thus cutting down on the switching noise of the network.
- Logic minimization (f). A combinational subnetwork is minimized in order to realize the logic function in a minimal number of gates.

Future Work. Tools benefit from use, and CAD tools are no exception. The semiautomated hint router has already been distributed as part of the Magic IC layout system to a number of sites, where it has been used in the design of fully custom ICs. It will be part of a wide distribution of the Magic system that is currently scheduled for the spring of 1989.

Although the multilayer router has shown its usefulness in routing a variety of circuits, more experience is needed in its operation and performance before it will be ready for widespread distribution. In the coming year, we hope to use it on several semicustom and wafer-scale designs that span a range of fabrication technologies. New sea-of-gates and sea-of-transistors semicustom arrays also appear very well suited to our new router, and we hope to demonstrate its usefulness to these sorts of designs as well.

Work on SECTAR is still in progress. Next year, we expect to bring up a first version of the complete system and apply it to retargeting the breadboard version of the APP circuit into a CMOS gate array. After this retargeting, it will be possible to compare the results obtained by SECTAR with those of the manual retargeting that has just been completed. The experience gained from this real-world circuit should provide us with an excellent measure of the effectiveness of SECTAR as an automatic conversion and optimization tool.

References

Arnold, M. H., and W. S. Scott (1988). "An Interactive Maze Router with Hints," *Proc. 25th Design Automation Conf.* (IEEE, Association for Computing Machinery, Piscataway, NJ), 672–676.

Joobbani, R. (1986). *An Artificial Intelligence Approach to VLSI Routing* (Kluwer, Norwell, MA).

Lunow, R. E. (1988). "A Channelless, Multilayer Router," *Proc. 25th Design Automation Conf.* (IEEE, Association for Computing Machinery, Piscataway, NJ), 667–671.

McWilliams, B. M., and D. B. Tuckerman (1985). "Wafer-Scale Integration" and "Laser Pantography," *Energy and Technology Review*, Lawrence Livermore National Laboratory, Report UCRL-52000-85-12, pages 1–20.

Ousterhout, J. K. (1984). "Corner Stitching: A Data Structuring Technique for VLSI Layout Tools," *IEEE Trans. Computer-Aided Design*, **CAD-3** (1).

Fabricating Advanced Bipolar Transistors Using Two New Technologies

We are developing a fabrication process for robust, high-performance, bipolar transistors that incorporates the technologies of gas immersion laser doping and silicon-on-insulator epitaxial layer growth. The use of these two new technologies will increase the switching speed and radiation hardness of the transistors without reducing their manufacturability or yield.

Principal Investigators: B. M. McWilliams and K. H. Weiner
Co-Investigators: P. G. Carey* and T. W. Sigmon*

*Stanford University, Stanford, CA

The fabrication of highly integrated circuits is currently hampered by the formation of ultrashallow (<100-nm) impurity-doped regions and by the electrical isolation of individual transistors. To reach the next step in the design and manufacture of integrated circuits—ultralarge-scale integration (ULSI) and gigascale integration (GSI), with millions to billions of transistors per chip, respectively—we need a fabrication sequence that is as simple, precise, and defect-free as possible.

As integration levels increase, the conventional doping and isolation techniques of ion implantation and trench isolation become too complicated, and yields are markedly reduced. We are attempting to solve these doping and isolation problems by incorporating two new techniques—gas immersion laser doping (GILD) and silicon-on-insulator (SOI) epitaxial layer growth—into the standard integrated-circuit fabrication process. These two techniques should enable us to simplify shallow junction formation and transistor isolation, thereby reducing the cost and complexity of fabricating highly integrated circuits and expediting the introduction of economical ULSI and GSI chips into the marketplace.

The GILD process will make possible significant improvements in transistor performance. GILD can be used to form junctions of very precise depth (±10 nm), allowing the active base width of the device to be reduced from the 100 to150 nm possible with current processes to <50 nm, with no loss in yield and simpler processing. Since transistor switching speed is proportional to the square of the base width, the smaller base widths produced by GILD make possible four- to ninefold increases in speed. In addition, by using GILD in place of ion implantation, more favorable impurity profiles are achieved. Standard Gaussian impurity profiles are replaced by box-like, abrupt junctions similar to those obtained with molecular-beam epitaxy. The abrupt junction reduces base punch-through effects in the devices and lowers base resistance, which leads to improved device performance.

The use of SOI technology will produce transistors with performance and radiation immunity much improved over that of today's fastest transistors. These highly optimized transistors (with cutoff frequency $f_t \geq 20$ GHz) are approaching the maximum performance possible with current fabrication techniques on a semiconducting silicon substrate. The SOI process, however, replaces the semiconducting substrate with an electrically insulating substrate, thereby eliminating parasitic capacitance from the collector of the bipolar transistor to the substrate. Since this parasitic capacitance represents one-quarter to one-third of the total capacitance of the device, use of the SOI substrate will substantially increase transistor performance. In addition, the insulating substrate is much more immune to ionizing radiation, which can cause errors in circuit operation. Thus, by replacing silicon with an SOI substrate, both the transitor's performance and its radiation immunity will be increased.

Our overall project goals are to (1) develop GILD as an insertable process for current and future integrated-circuit fabrication processes, (2) develop an SOI technology suitable for fabricating high-performance, bipolar transistors, and (3) design and implement a fabrication process for robust, radiation-immune bipolar transistors for the custom integrated circuits required at LLNL.

We are also investigating the use of GILD to simplify and improve the fabrication and performance of the thin-film transistors (TFTs) used extensively in flat panel displays. In addition, GILD should offer a superior method to dope the source, drain and gate regions of metal-oxide semiconductor (MOS) devices, so we are working to incorporate GILD into the fabrication process for MOS transistors; this is a joint effort among LLNL, Stanford University, and the Semiconductor Research Corporation (SRC), Research Triangle, NC.

In the GILD process, a pulsed, ultraviolet (308-nm) excimer laser is used to melt the surface of the silicon substrate. Doping occurs when impurity atoms in the gas phase pyrolize on the heated surface and diffuse into the molten silicon. The molten layer regrows epitaxially, creating electrically activated, damage-free doped layers. Since diffusion occurs in the liquid phase, junction depth is limited by the penetration of the melt front into the silicon. By controlling the number of pulses and the laser energy, one can produce ultrashallow and very abrupt impurity profiles. In addition, since melt depth is a function of laser energy and the impurity profiles are abrupt, junction depths can be placed very accurately (±10 nm). Furthermore, because the doping process occurs in nanosecond time scales and the dopant is electrically active, high-temperature annealing is not required. This eliminates diffusion in the solid state. Consequently, placement of the emitter does not affect the base depth. With GILD (unlike diffusion processes), the relative junction depths may be varied independently, and base widths as narrow as 50 nm or less become possible. Process reproducibility is ensured by an array of *in situ* diagnostics incorporated within the laser doping equipment. Masking is achieved with conventional lithography; a thin aluminum or oxide film is applied to reflect the laser energy where doping is not desired. This combination of predictability, reproducibility, and compatibility with current fabrication processes makes GILD an ideal method for forming the active base and emitter regions in bipolar transistors.

During FY88, we concentrated on the fabrication of bipolar and MOS transistors using the GILD process. Significant progress was made toward the original goals, along with promising results in new, potentially high-leverage areas of advanced bipolar transistor fabrication. Notably this year, we precisely characterized the GILD process, made significant improvements in the GILD apparatus, and constructed a class 100 ultraclean area for GILD processing. We successfully fabricated very-low-leakage, ultrashallow p^+/n and n^+/p junctions using GILD and bipolar transistors using GILD and the simpler technique of ion implantation with laser redistribution (IILD). We also fabricated high-quality silicon and Ge_xSi_{1-x} epitaxial layers using GILD as well as submicron *n*-channel metal-oxide semiconductor (NMOS) and *p*-channel metal-oxide semiconductor (PMOS) transistors using GILD to form the source/drain regions. Below, we discuss the progress made in the fabrication of bipolar and MOS transistors and in epitaxial layer growth.

Bipolar Transistor Fabrication. The results achieved in fabricating bipolar transistors during this first year are very encouraging. We fabricated bipolar transistors using both the GILD process and the simpler but very powerful IILD

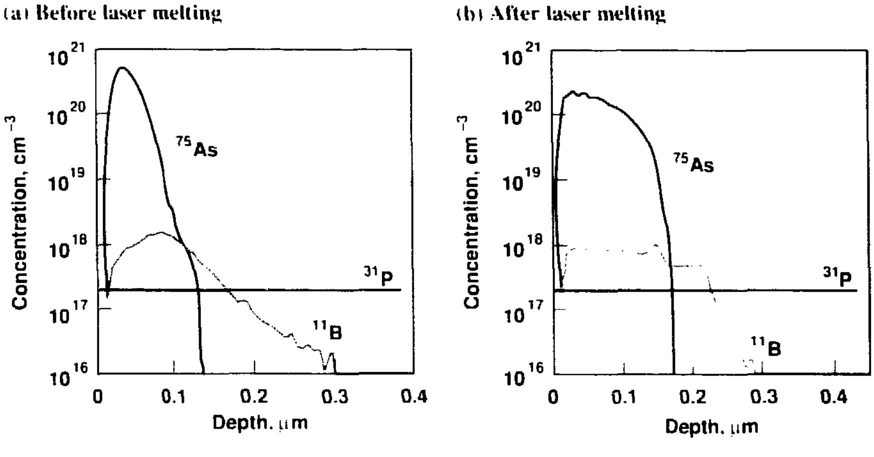

Figure 1. IILD ion-implantation profile before (a) and after (b) laser melting and ion redistribution. The base width is <70 nm. The ^{75}As and ^{11}B profiles were determined using secondary-ion mass spectroscopy with oxygen bombardment; the ^{31}P profile was determined by spreading resistance profilometry.

technique. IILD allows the immediate fabrication of narrow-base transistors using established high-performance bipolar processes. IILD combines the exceptional junction depth control of GILD with the accurate dose control of ion implantation. Transistors with base widths of 70 nm and maximum forward current gains of 100 have been fabricated using IILD. Figure 1 shows the results of the laser melting and ion redistribution, and Figure 2 shows the electrical characteristics for an IILD transistor with a 100-nm base width. Although problems with base-ion-dose control have limited GILD transistors to maximum current gains of 5, recent efforts to control the base-ion dose have been successful and we expect soon to be able to produce GILD bipolar transistors with improved forward current behavior.

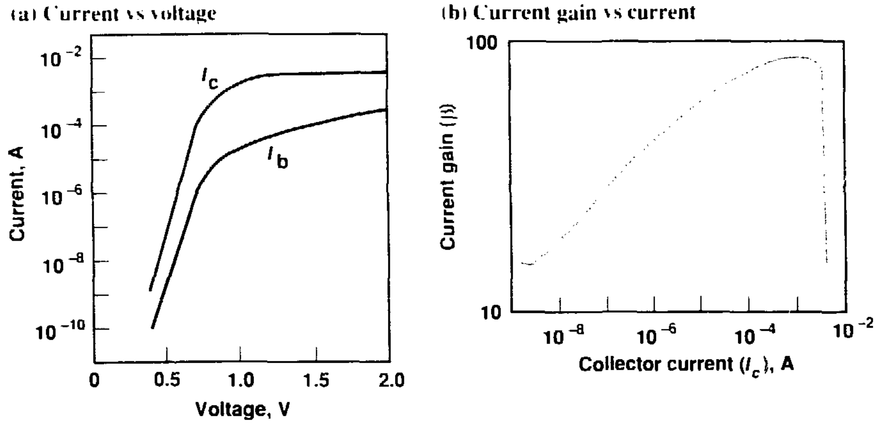
(a) Current vs voltage

(b) Current gain vs current

Figure 2. Electrical characteristics of an IILD transistor with a 100-nm base width. (a) current I vs voltage V, and (b) current gain β vs collector current I_C.

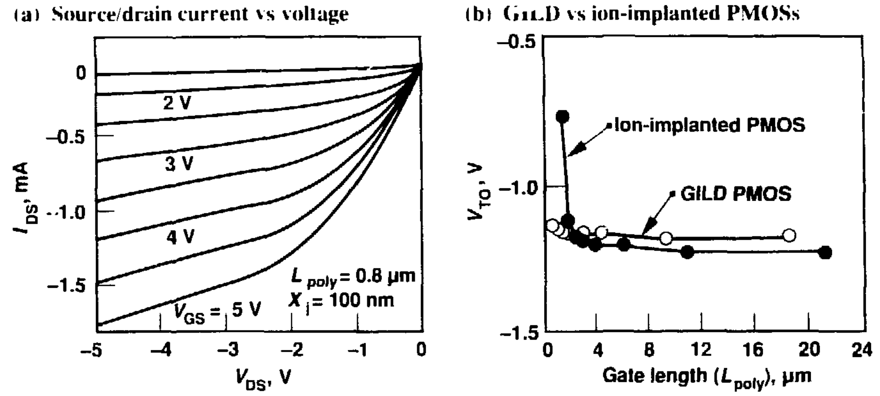
(a) Source/drain current vs voltage

(b) GILD vs ion-implanted PMOSs

Figure 3. Electrical characteristics of typical PMOS transistors fabricated using GILD. (a) Source/drain current I_{DS} vs source/drain voltage V_{DS} as a function of gate/source voltage V_{GS} of a GILD PMOS transistor. (b) Comparison of threshold voltage V_{TO} vs gate length L_{poly} for a PMOS transistor fabricated using GILD and one using ion implantation; the GILD device exhibits a maximum threshold shift of 2 mV.

CMOS Fabrication. GILD has been incorporated into the fabrication process for a complementary metal-oxide semiconductor (CMOS) device. Working at the LLNL GILD facility, T. W. Sigmon and P. G. Carey of Stanford University, under an SRC contract, produced submicron-size NMOS and PMOS transistors with excellent current/voltage characteristics. Figure 3a plots source/drain current vs source/drain voltage as a function of gate voltage for a typical PMOS transistor. Figure 3b compares plots of threshold voltage vs gate length for an ion-implanted transistor, used as a control device, and for a GILD transistor. Unlike the ion-implanted transistor, the GILD device shows no threshold shift even at submicron gate lengths. These results indicate that GILD is indeed a superior method for fabricating the ultrashallow impurity regions required in submicron-size transistors.

Epitaxial Layer Growth. High-performance bipolar transistors of the future are predicted to operate at switching speeds greater than 100 GHz. These devices will undoubtedly incorporate epitaxial layers for emitter and base structures. However, current methods of epitaxial layer growth do not allow the fabrication of high-quality layers while maintaining the ease of the planar silicon process. Without this capability, processing is severely hampered by the need for mesa isolation and other low-density, low-yield processes for electrically isolating the transistors. We have developed a GILD-based process for fabricating device-quality epitaxial layers on patterned substrates. This two-step process involves, first, depositing an amorphous silicon or germanium film and, then, using a laser to melt through the film to the silicon substrate. The substrate acts as a seed crystal from which the molten amorphous layer regrows as a single crystal. Figure 4 is a high-resolution transmission electron micrograph of the silicon/Ge_xSi_{1-x} interface. The interface exhibits no defects, indicating the high quality of the epitaxial layer. We have successfully grown very thin (24-nm) Ge_xSi_{1-x} epitaxial layers; this type of layer is ideal for use in the base region of heterojunction bipolar transistors. Silicon layers for use as emitters in both homo- and heterojunction devices have also been fabricated.

In FY89, we will increase the pace of our work to adapt the GILD and SOI technologies in the fabrication process for bipolar transistors. We plan to develop GILD equipment suitable for the fabrication of ULSI circuits. We will also work to incorporate a high-performance GILD process on an SOI substrate. The performance level for the bipolar transistors fabricated with these new techniques is targeted for a cut-off frequency f_t ≥ 15 GHz. GILD and SOI processes will also be incorporated into various MOS technologies. In particular, we will design and adapt SOI/MOS technology for the fabrication of MOS transistors in active-matrix liquid-crystal displays. In addition, we plan to explore the use of the GILD process to improve TFT fabrication by lowering the maximum process temperatures and by increasing the amount of dopant that is electrically active in the source/drain region. Lastly, we will investigate the advantages of SOI and GILD for fabricating image sensors; by simplifying their fabrication process, we should be able to increase the performance and yield of these detectors.

Figure 4. High-resolution, cross-sectional, transmission electron micrograph of the Si/$Ge_{0.18}Si_{0.82}$ interface. Note that the interface (dashed line) is perfectly crystalline, exhibiting no dislocations or point defects.

References

Abelson, J. R., K. B. Kim, K. H. Weiner, and T. W. Sigmon (1988), "Epitaxial Ge_xSi_{1-x}/Si (100) Structures Produced by Pulsed Laser Mixing of Evaporated Ge on Si (100) Substrates," *Appl. Phys. Lett.* **52** (3), 230–232.

Carey, P. G., K. H. Weiner, and T. W. Sigmon (1988), "A Shallow-Junction Submicrometer PMOS Process without High-Temperature Anneals," *Electron. Lett.* **9** (10), 542–544.

Weiner, K. H., B. M. McWilliams, and T. W. Sigmon (1988), "Measurements of Melt Depth Limited Diffusion in Gas Immersion Laser Doped Silicon Using an Improved Laser System," *Proc. of Symp. on Laser Processes for Microelectronic Applications*, J. J. Ritsko, D. J. Ehrlich, and M. Kashiwagi, Eds., Vol. 88-10, pp. 53–61.

Weiner, K. H., and T. W. Sigmon (1988), "Emitter and Base Fabrication in Advanced Bipolar Transistors Using Gas Immersion Laser Doping," *Proc. of the 1988 Bipolar Circuits and Technology Meeting*, J. Jopke, Ed. (IEEE), pp. 37–40.

I • R • & • D

Individual Awards

Lawrence Livermore National Laboratory

Individual Awards

R. A. Ward

The IR&D Individual Awards provide a means by which novel ideas can be given seed funding outside of the usual programmatic channels via grants awarded to individual LLNL investigators. The IR&D Research Committee focuses on highly leveraged projects that offer good potential of developing into self-sustaining programs. The concept of seed funding is extremely important in the committee's considerations of projects that will explore promising new directions for science and technology in areas relevant to the Laboratory's mission. The selection criteria for the FY88 proposals (consistent with Department of Energy guidelines) were:

- Scientific or technical quality.
- Impact on the Laboratory or the general scientific community.
- Leverage for future funding.

The FY88 Research Committee consisted of 19 members appointed by and reporting to the Director; the members represent the wide spectrum of scientific disciplines pursued at the Laboratory. After all written proposals were submitted, two committee members interviewed each principal investigator and then reported back to the full committee. The committee ranked each proposal in order of overall scientific excellence and pertinence to the Laboratory's scientific mission. Proposals were then funded in decreasing order of ranking until the available funds were exhausted. The descriptions below highlight a few representative proposals that were chosen for funding.

One project proposed the design, fabrication, and testing of micropole undulators to be used as insertion devices in synchrotron storage rings. The Lorentz force exerted by the periodic magnetic field inside the undulator causes the electrons to describe periodic oscillations as they are forced to undulate in microscopically prepared, spatially varying magnetic fields. As a result, the electrons accelerate over small distances (100 to 1000 μm) and produce very-high-energy, extremely monochromatic electromagnetic radiation.

In the biomedical and environmental sciences, researchers proposed to perform accelerator-mass-spectrometry measurements of carbon isotope ratios (^{14}C:^{13}C:^{12}C) in bottom-feeding marine microorganisms. Once the technique is perfected, they plan to study the basic food web to determine how petroleum and gas carbon are utilized by organisms in and around natural petroleum seeps on the ocean floor.

Researchers in engineering proposed to develop the modeling and technology necessary to design and analyze very small (micrometer-size) vacuum tubes. These devices would be fabricated on a small silicon wafer using semiconductor technology but would be tolerant of high temperatures, radiation, and high-voltage electrical transients.

Another project would determine the technical feasibility of using a cyclotron autoresonance maser (CARM) with an induction linear accelerator. The CARM is based on Doppler-shifted cyclotron resonance in a strong axial field guide, rather than on a wiggler, and gives much higher frequencies than the free-electron laser (in the range of 0.5 to 5 MeV). This allows the possibility of more compact, lower power modules for generating millimeter-wavelength radiation.

Several projects developed computer codes to model diverse physical processes. One project proposed to compile a theoretical understanding of high-temperature superconductors by applying methods and codes originally developed to study solid-state laser materials. The calculations would use the *ab initio* molecular orbital cluster method for clusters of several hundred ions and would be correlated with experimentally observed changes in critical temperature with oxygen vacancies and with high-pressure, diamond-anvil cell measurements being conducted at LLNL.

Another project proposed to build a prototype system for the simultaneous observation of up to 100 objects in an astronomical telescope. This automated system would use optical-fiber sensors, precisely positioned at the desired location on the telescope's focal plane; the light collected would be sent along the optical fibers to a spectrograph for analysis.

An all-time high of 151 proposals were submitted this year, requesting $19.8 million in funding, which included 2203 hours of time on the Laboratory's supercomputers. For FY88, 26 Individual Awards were granted, for a total of $3.353 million, with $112,000 for capital equipment.

Nuclear Magnetic Resonance Analysis and Molecular Modeling of Protamine

We are using nuclear magnetic resonance spectroscopy and innovative techniques in high-resolution computer graphics to study the structure of protamine. By identifying the normal DNA-protamine and interprotamine interactions present in fertile sperm, we will eventually be able to identify molecular defects responsible for certain types of human infertility.

Principal Investigator: R. L. Balhorn
Co-Investigators: R. Ward and N. Max

Protamine is a small DNA-binding protein that packages DNA inside the nucleus of mammalian sperm. As each spermatid in the mammalian testis differentiates into a mature sperm, approximately 10^9 protamine molecules are synthesized and deposited into its DNA, replacing the majority of existing chromosomal proteins. Although the molecular structure of the resulting DNA-protamine complex is not yet known, the positively charged center of the protamine molecule is thought to bind in the minor groove of one turn of DNA (10 base pairs), completely neutralizing its negatively charged phosphodiester backbone (Balhorn, 1984). Soon after binding, both ends of the protamine molecule fold inward and form crosslinks that interlock each protamine to its neighbor around the DNA helix. This charge neutralization and the subsequent formation of crosslinks between adjacent, folded protamines result in the inactivation of the sperm's genes and the packing of its DNA in a maximally condensed state.

The purpose of our investigation is to model DNA-protamine and protamine-protamine interactions and the packaging of DNA in mammalian sperm. Our work combines the expertise in molecular graphics that has been developed in the LLNL Computation Department, the nuclear magnetic resonance (NMR) capabilities now available in the Chemistry and Materials Science Department, and knowledge of the molecular structure of sperm chromatin gained in the Biomedical Sciences Division.

The four goals of our project are to:

- Model the binding of protamine to DNA and the folding of terminal peptides using a computer system developed at UC San Francisco.
- Refine our modeling of the DNA binding and folding interactions by using NMR.
- Produce a multistrand graphics model of the interactions of DNA and protamine in sperm chromatin. (This type of model can be used to assess existing experimental evidence and to facilitate the design of future experiments.)
- Explore the feasibility of using an energy-minimization software program to adjust certain molecular interactions (such as the binding of the polyarginine segment to DNA and protein folding).

We have completed the initial steps required to meet the goals involving molecular modeling. In particular, we have constructed graphically a small segment of the protamine molecule that binds to DNA. This segment, referred to as an anchoring unit, contains four arginine residues (see Figure 1).

We interactively manipulated the anchoring unit by computer, using an Evans and Sutherland Picture System and the UC San Francisco modeling program, MIDAS (Ferrin *et al.*, 1988), until the terminal amide groups were moved within 0.2 nm of the phosphates on five base pairs of DNA. Alternating arginines zig-zagged across the minor groove of DNA, crosslinking the phosphodiester strands. We determined the free energy of this structure, and we adjusted the conformation of the polyarginine molecule to yield a minimum free-energy value using the UC San Francisco program, BORN, run on a Cray computer. We then used the resulting minimized conformation as an initial step in a molecular-dynamics simulation with the UC San Francisco program, NEWTON.

During both the minimization step and the molecular-dynamics simulation, DNA was held rigidly in the B form, and only the protein was allowed to move. At every other time step in our simulation, we used the coordinates to produce a computer-animated film of the dynamics that were taking place. For this purpose, we developed a new shadow-casting program based on the Laboratory's ATOMLLL rendering program for molecular models. By using only a small segment of the DNA-protamine binding site, we were able to ensure that each step in the modeling and computing process worked correctly before we attempted to construct the entire DNA-protamine complex.

With respect to our work involving NMR spectroscopy, we isolated and purified protamine from bull sperm, modified the cysteines using methyl iodide, and then obtained proton NMR spectra for both the modified and unmodified proteins. In addition, we obtained spectra for each of the component amino acids. Four of the six synthetic peptides that correspond to specific fragments of the protamine molecule were also synthesized and purified. We have begun to assign the protons in protamine by comparing NMR spectra of individual amino acids with those of synthetic protamine fragments. Once all protons are assigned, we will then conduct computer analyses to identify coupled (neighboring)

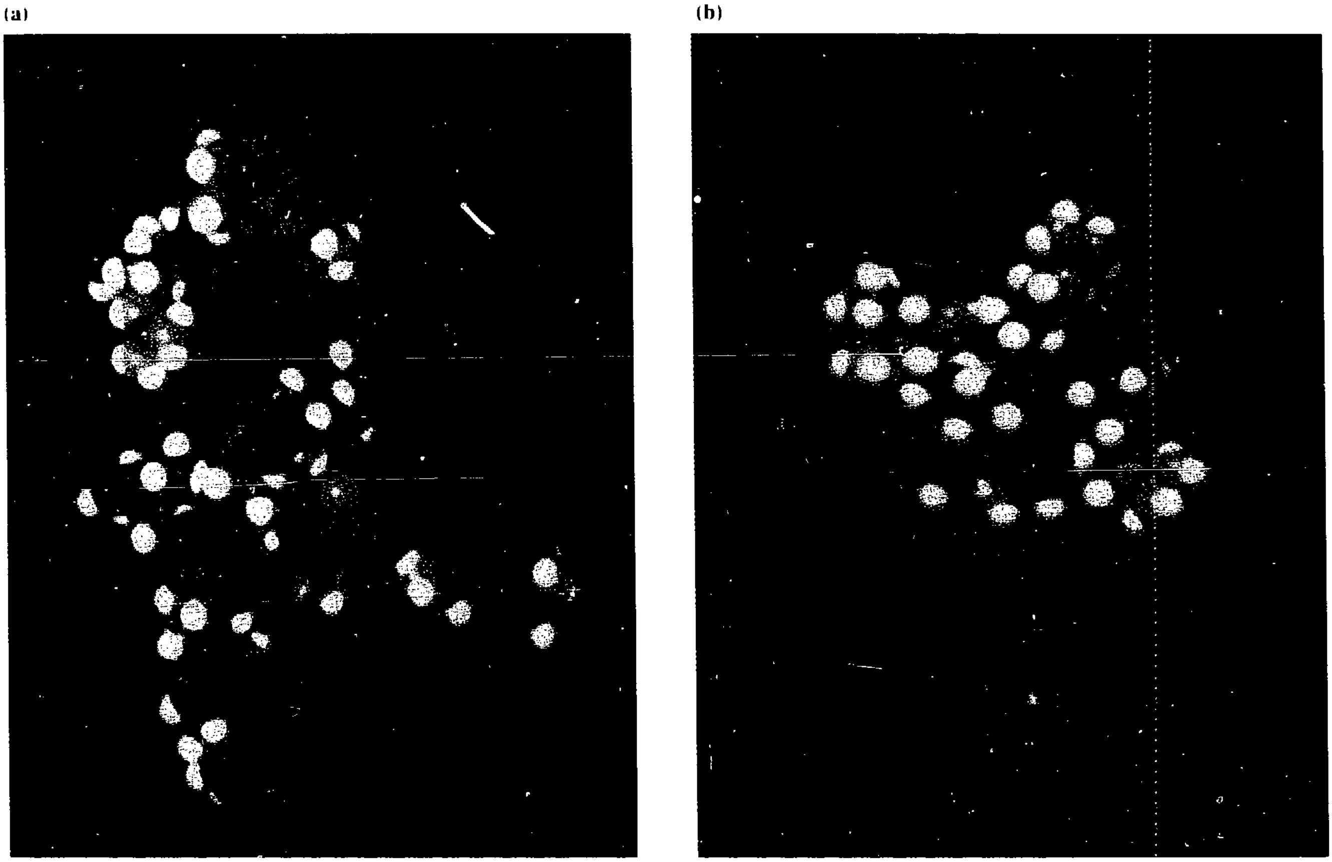

Figure 1. Computer-generated model of the interaction between a DNA-protamine binding unit (arg$_4$) and a segment of DNA. (a) The arg-arg-arg-arg peptide (top) and the DNA segment (bottom) shown as separate molecules. (b) Front view of the minor groove of DNA filled with the arg$_4$ peptide after rotating 90° to the right the DNA-peptide complex shown in (a).

protons in the same amino acid and interacting protons in different amino acids. We have prepared folded forms of the protamine molecule *in vitro* and are now separating and purifying these forms for subsequent NMR analysis. We have also prepared a covalently crosslinked protamine dimer in its two forms and are purifying them for analysis.

During FY89, we will concentrate on completing the identification of all unfolded protamine protons and on analyzing the spectra of naturally folded forms of protamine and folded synthetic peptides. By exploiting the nuclear Overhauser effect (which permits the identification and localization of protons in amino acids that are well separated in the peptide chain, but within 0.4 nm of one another in the folded molecule) and by modifying specific cysteines with radioactive (^{13}C) reagents, we should be able to map the location of amino acid residues within the amino- and carboxy-terminal folded domains.

We will use two approaches to locate the region of the protamine molecule that binds to DNA. The first approach involves constructing a synthetic DNA-protamine complex and monitoring the immobilization of specific amino acids after the protein binds to DNA. This approach requires the preparation of a soluble form of the DNA-protamine complex in a suitable solvent because the complex is insoluble in water. If a sufficiently soluble complex cannot be prepared, our second approach will be to attempt to obtain solid-state NMR spectra. Should both approaches fail to provide information on the location of the DNA-binding region, then we will use methyl glyoxal to chemically modify arginine residues of protamine not bound to DNA in intact sperm. The location of unbound arginines can then be determined by combining NMR spectroscopy and protein-sequencing techniques.

References

Balhorn, R. (1984). "A Model for the Structure of Chromatin in Mammalian Sperm." *J. Cell Biol.* **93**, 298–305.

Ferrin, T. E., C. C. Huang, L. E. Jarvis, and R. Langridge (1988). "The MIDAS Display System." *J. Mol. Graphics* **6**, 13–27.

FY88 $160,000

Application of Accelerator Mass Spectrometry to Marine Ecology

We are applying accelerator mass spectrometry to basic problems in marine science. Our ability to measure carbon-14 in microgram-size samples of carbon promises to advance our understanding of carbon cycling in the oceans.

Principal Investigator: R. B. Spies
Co-Investigator: J. Bauer

We are measuring the natural abundance of carbon-14 (^{14}C) in small samples of seawater, sediments, and marine organisms to elucidate aspects of the oceanic carbon cycle. One reason that ^{14}C is a useful tracer in the ocean derives from the fact that the carbon turnover time in oceans (500–1000 years) represents a significant fraction of the ^{14}C half-life (5730 years). Surface waters, where carbon is incorporated into the food web, are more nearly in equilibrium with the atmospheric source. New organic matter is, in general, significantly enriched in ^{14}C relative to deep-water organic matter. In addition, along the west coast of the U.S., persistent northwesterly winds in the spring and summer result in upwelling of deep, nutrient-rich, but ^{14}C-depleted, water (Robinson, 1981).

Conventional measurements of the abundance of ^{14}C by decay counting require several liters of seawater for the determination of inorganic carbon and 1 g of organic matter for organic carbon. Samples of marginal size often must be counted for several days to obtain an accurate determination. Thus, conventional techniques have limited the usefulness of using ^{14}C as a tracer. The separation and direct counting of carbon isotopes by accelerator mass spectrometry (AMS), on the other hand, allow us to use sample sizes as small as 20 to 30 µg and counting times of less than 1 hour. Early this year, we made the first measurements of ^{14}C content of dissolved inorganic carbon in sediment porewaters (samples obtained from the pores in sediment) using samples of 1 to 5 ml, the smallest seawater samples successfully analyzed for ^{14}C to date.

Although ^{14}C enters ocean surface waters mainly as CO_2, a key to better understanding of the oceanic carbon cycle is the cycling times of various forms of organic carbon. Recent evidence suggests that dissolved organic carbon in the ocean is relatively old (with a mean age of about 6000 years in the central North Pacific Ocean) and that a large fraction of such carbon appears to be only slowly decomposed by microbes (Williams and Druffel, 1987). It is clear that the cycling time of various classes of compounds comprising dissolved organic carbon needs to be investigated; because of the sample sizes that are practical to collect, such measurements can only be done with AMS. Our plan was to separate from seawater some specific classes of such compounds and then to measure the ^{14}C content.

We first used AMS to answer longstanding questions about fossil carbon cycling in the sediments of a shallow-water petroleum seep. In particular, we wished to know whether the higher population densities of some organisms in the sediments of the seep were due to the use of fossil carbon by the food web. Our previous investigations had strongly suggested this possibility. A dilution of modern carbon by fossil carbon in organisms from the sediments of the seep would constitute nearly irrefutable evidence of fossil carbon use.

Figure 1 shows the results of our radiocarbon analyses of total organic carbon in sediments, of dissolved inorganic carbon in porewater, of meiofauna (animals passing through a sieve with 0.5-mm openings), and of macrofauna (animals retained on a sieve with 0.5-mm openings). We obtained all samples from sediments of the Isla Vista petroleum seep located off the coast in the Santa Barbara Channel. The ^{14}C content of dissolved inorganic carbon in porewater shows a clear gradient due to the influence of fossil carbon. Station A, with the greatest active seepage, also has porewater with the greatest depletion of modern carbon. Station B has less seepage and more modern carbon. Station C has essentially no seepage and the most modern carbon. The depth profiles in each case are related to the influence of microbial metabolism, porewater pumping, diffusion into overlying seawater (which is nearly modern), and an upward flux of fossil CO_2 from the underlying, oil-bearing strata. Both meiofauna and macrofauna show a depletion of ^{14}C with increasing seepage. This relation indicates a dependence of the food web on fossil carbon use in Isla Vista sediments.

Our future plans include a time-series analysis (a series of tests over months) of ^{14}C content of dissolved inorganic carbon in seawater, phytoplankton, suspended particulate matter, total organic carbon in sediment, and benthic (bottom-dwelling) organisms from a coastal location in California that has both upwelling and non-upwelling seasons. Such data will help us to establish how organic matter is used over time on the California continental shelf and will serve as a reference for subsequent measurements of even more specific classes of organic matter, such as bacterial lipids.

References

Robinson, S. W. (1981). "Natural and Man-Made Radiocarbon as a Tracer for Coastal Upwelling Processes." *Amer. Geophys. Union Coastal Estuarine Sci.* **1**, 298–301.

Williams, P. N., and E. M. Druffel (1987). "Radiocarbon in Dissolved Organic Matter in the Central North Pacific Ocean." *Nature* **330**, 246–248.

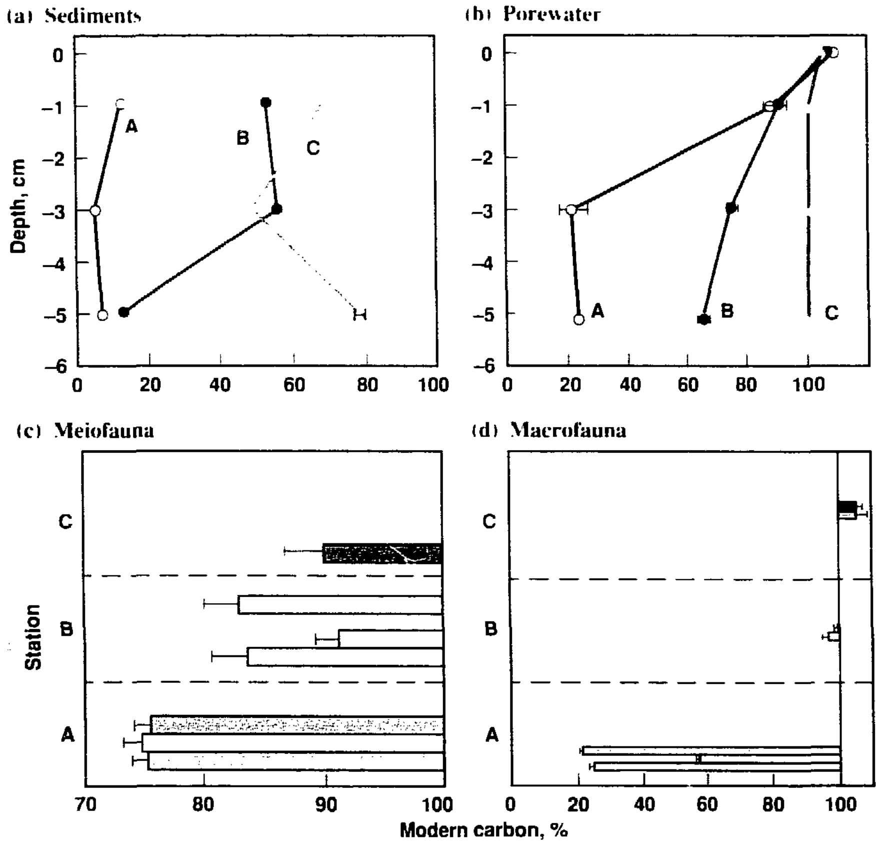

Figure 1. Natural abundances of ^{14}C, expressed as percent modern carbon, in (a) total organic carbon within sediments, (b) dissolved inorganic carbon within porewater, (c) four types of meiofauna, and (d) seven types of macrofauna. Sediments are from three stations with varying degrees of seepage near the Isla Vista petroleum seep. Data such as these indicate a dependence of the food web on fossil carbon.

FY88: $111,000

Fluorescence Detection and Quantification of Gene Expression

Principal Investigator: M. G. Pallavicini

We have developed fluorescence techniques to detect and quantify gene expression in individual cells. This capability allows us to track messenger RNA from a nucleus to cytoplasm, where it is translated into specific proteins, and to follow the movement of translated protein back to the nucleus. Such methods are useful for investigating selective gene expression in proliferating and differentiating systems and for **in situ** ***analyses of intracellular macromolecular traffic.***

The diverse nature of cell populations is based on the temporal and selective activation and expression of unique genes. We have developed the technology necessary to detect and quantify gene expression in individual cells by using three techniques: fluorescence *in situ* hybridization, quantitative image analysis, and flow cytometry.

We used recombinant Chinese hamster ovary cells containing elevated levels of DNA sequences that code for the c-myc protein. The c-myc protein is believed to play a role in the regulation of cell proliferation and differentiation. In our recombinant cells, expression of the c-myc sequences is regulated by temperature. Thus, when the cells are grown at 37°C , neither c-myc messenger RNA (mRNA) nor c-myc protein is produced. However, following exposure to 43°C, c-myc mRNA is generated (see Figure 1a). Upon return of the cells to 37°C, mRNA is then translated into the c-myc protein (see Figure 1b). Thus, the expression of both c-myc mRNA and c-myc protein can be experimentally manipulated in the cells, providing an excellent model system for developing techniques to measure and quantify gene expression.

We used flow cytometry and an immunofluorescence-based assay to quantify the amount of c-myc protein produced in cells that contained different levels of c-myc DNA sequences. We found that the level of production of c-myc protein was related to the number of c-myc sequences present in the chromosome. Although the c-myc protein is believed to play a role in regulating cell proliferation, our studies indicated that cell proliferation was independent of c-myc protein levels. We did, however, observe increased lethality in cells expressing c-myc protein at levels 20 to 40 times higher than normal. We also were able to follow the movement of the c-myc protein from cytoplasm to its functional domain, the nucleus.

To detect c-myc gene transcription, we used fluorescence *in situ* hybridization, a technique based on the formation of hybrids between complementary sequences of nucleic acid. In this technique, nucleic acid probes are first labeled with biotin and hybrized (with complementary sequences present within the cell) with biotinylated RNA probes. The resulting hybrids are detected using fluorescenated avidin, a protein with high affinity for biotin. We initially detected intracellular c-myc mRNA following hybridization with the biotinylated c-myc DNA probe. Although we were initially successful with this approach, it proved to be too variable for routine biological applications. We subsequently hybridized c-myc mRNA with biotinylated RNA c-myc probes, which were produced and characterized at LLNL. We found that RNA-RNA hybridization allowed for reproducible and sensitive message detection; that is, we were able to detect mRNA derived from transcription of 50 genomic copies. We analyzed both nuclear mRNA and cytoplasmic c-myc mRNA using this procedure.

Our work is the first demonstration of detecting nuclear mRNA using fluorescence *in situ* hybridization. We have already used image analysis to quantify total cellular fluorescence, and we will apply that technique in the future to separately analyze nuclear and cytoplasmic mRNA. We have also developed the capability to simultaneously label cells for a genomic sequence and its transcribed product. Thus, we now can measure both the copy number and expression of selected genes. This development has formed the basis for new research efforts in the Biomedical Sciences Division to investigate intracellular structural and molecular changes associated with gene activation *in situ*.

(a) C-myc mRNA

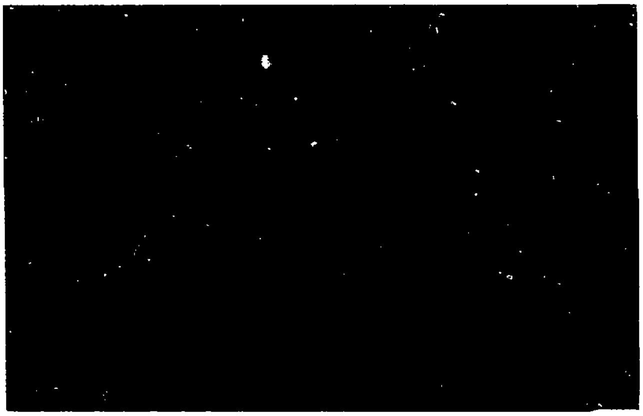

(b) C-myc protein

Figure 1. C-myc messenger RNA and protein in heated recombinant cells. (a) C-myc messenger RNA is visualized as a bright, tightly localized spot in the center of the nucleus. (b) C-myc protein is localized within the nucleus and appears as a relatively diffuse, yet distinct pattern. These cells were heated at 43°C for 20 minutes and then returned to 37°C for 4 hours to produce c-myc protein.

Reference

Wurm, F. K., A. Gwinn, O. Papoulas, M. G. Pallavicini, and R. E. Kingston (1987), "Use of a Transfected and Amplified *Drosophila* Heat Shock Promoter Construction for Inducible Production of Toxic Mouse C-myc Proteins in CHO Cells," in *Modern Approaches to Animal Cell Technology*, R. E. Spier and J. B. Griffiths, Eds. (Butterworth Publishers, Ltd., London), pp. 218–241.

Scanning Tunneling Microscopy

We have used our air-operated scanning tunneling microscope and other new techniques to image bare DNA without the metallic coating commonly required in transmission electron microscopy. We can determine the DNA structure with a resolution of ~1 nm, revealing for the first time its distinct helical structure through direct imaging.

Principal Investigator: W. L. Bell
Co-Investigators: R. Balhorn, T. Bebbe, W. J. Siekhaus, I. Wilson, and M. Salmeron*

*Lawrence Berkeley Laboratory
Berkeley, CA

Studies of the physical and electronic structure of surfaces on the scale of atoms is of central importance in understanding devices and processes in fields as diverse as semiconductor electronics, machining, polishing, surface chemistry, and biology. Until recently, most surface-sensitive techniques have been restricted to ultrahigh vacuum environments. The advent of the scanning tunneling microscope (STM) now provides us with the opportunity to study surface phenemona, such as corrosion, wetting, electrochemical deposition of metals, and catalysis on a variety of surfaces at normal operating pressures. Furthermore, STM can be used to image surfaces of biological molecules.

In last year's report, we showed the main features of the microscope we have built. We replaced the piezoelectric tripod with a cylindrical tube for greater speed and stability in manipulating the tunneling probe tip. In general, electric fields applied to the piezoelectric crystal tube through evaporated metallic contacts induce strain in the tube that moves the tip. The tube scanner provides a maximum tip range of 1000 nm in all directions with displacement control to better than 0.01 nm. We can acquire square pictures 10 nm on each side in less than 1 min.

To better understand the operation of our scanning tunneling microscope, imagine one atom at the end of an atomically sharp metallic needle close to the surface of a conducting material. For gap distances of 0.5 nm, an applied bias of several tens of millivolts induces current flow in the nanoampere range. Electrons flow across the gap because of the quantum-mechanical tunneling effect. The current typically decreases by one order of magnitude for every 0.1 nm in gap spacing.

We have used three operating modes: constant current, constant height, and local-barrier height. In

(a) STM image of DNA (< 10^6 bases) from calf thymus

Figure 1. (a) STM image of calf thymus obtained from Worthington Biochemical Corp. (Freehold, NJ). The highly polymerized thymus was dissolved overnight in aqueous 10-m*M* KCl (4.5 mg/ml). Aliquots of stock DNA solution were then diluted with 10-m*M* KCl to a working concentration of 1 mg/ml. We then evaporated one droplet in air on a freshly cleaved pyrolytic graphite substrate, which provides a

the constant current mode, for example, the needle is scanned across the surface laterally while its distance from the surface is adjusted to keep a constant tunneling current. We obtain a topographic image of the surface in the recorded trajectory of the tip.

Figure 1a is an image of DNA constructed from such a topograph. The intensity of the gray scale is proportional to the tip height, where white is high and black is low. This is a typical large-area (105 × 105-nm) image showing a DNA complex that makes many convolutions on a graphite surface. The pyrolytic graphite substrate provides a conductive surface with crystal planes atomically flat over hundreds of nanometers. Both isolated segments and overlapping, tangled segments of the DNA duplex are visible.

Figure 1b is another area of the DNA sample (34 × 34 nm) shown in Figure 1a. Biochemists expect that DNA appearing as a single strand will have a wide variety of pitch spacings. The appearance of the twisted ladder is evident in these images; however, no alternation in groove size is seen, as would be expected if the major and minor DNA grooves were resolved. The height of the DNA is between about 2 and 3 nm, as expected. The apparent width of the strand, which is ~6 nm, is caused by a convolution of the actual DNA width with the tip width.

Our STM images of biological molecules have a resolution far surpassing that of images obtained by any other technique. In addition, it is possible to fragment, attach, and remove simple organic molecules on the surface of graphite. We believe that similar manipulations can be performed on biological molecules. We anticipate that the revolution in the field of surface science that is being caused by STM and related techniques will be shortly followed by an even greater revolution in molecular biology and biophysics.

(b) STM image of spiraling, right-handed DNA from calf thymus

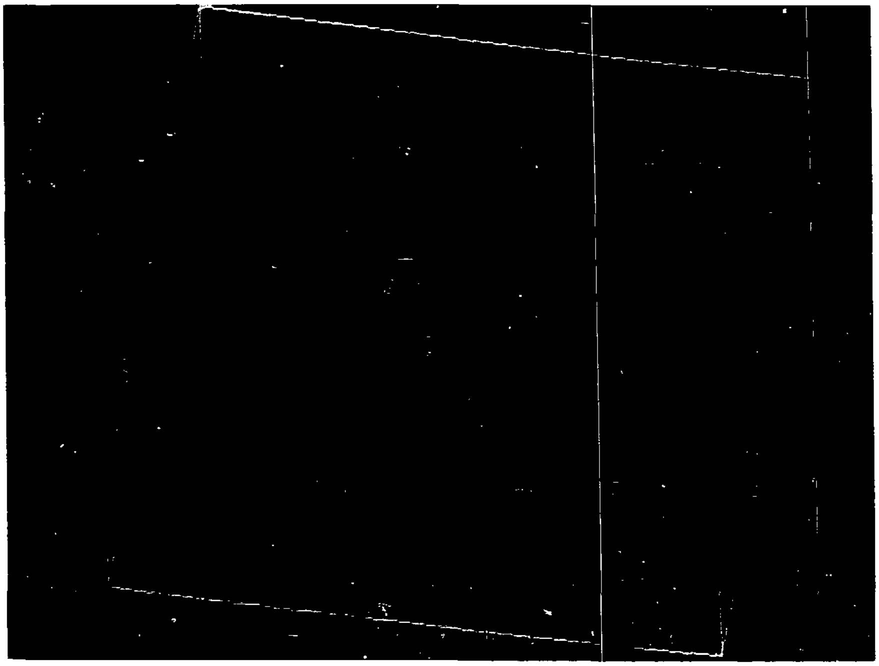

(c) DNA helix

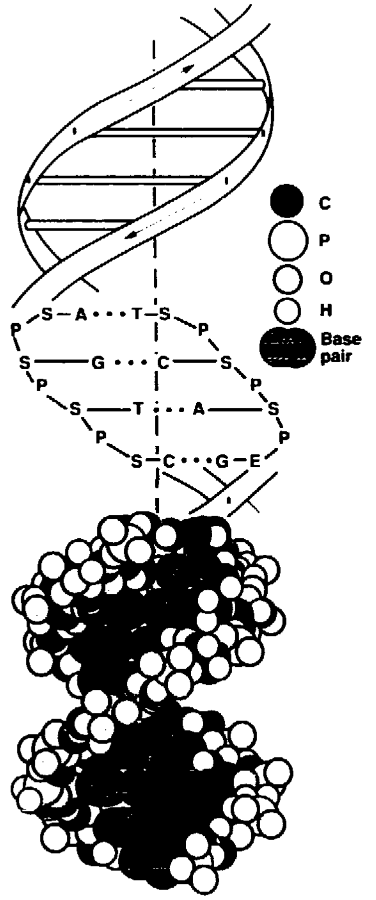

conductive surface with crystal planes atomically flat over hundreds of nanometers. This typical large-area image shows a DNA complex that makes many convolutions on the surface. Both isolated segments and overlapping, tangled segments of the DNA duplex are visible. This image is viewed from a perspective 45° above the plane and 20° clockwise in the plane. (b) Another area of the DNA sample taken within a few minutes of the image in (a). The spiraling, right-handed DNA structure is clearly visible. (c) Schematic of the helix of DNA for comparison.

FY88 $144 000

Synthesis of Dense Energetic Materials Using Polymer Supports

We have developed synthetic methods that will enable us to prepare larger-ring homologs of HMX and other new explosives related to HMX.

Principal Investigator: A. R. Mitchell

Our objective is to find new ways to synthesize high explosives that are more energetic than HMX (Coon, 1988). Figure 1 shows the structure of this important explosive, which has a density of 1.90 g/cm^3. Density is important because it is directly related to the Chapman-Jouguet (CJ) pressure P_{CJ}, the detonation property that principally determines the impulse delivered by an explosive:

$$P_{CJ} = \rho_0 D^2/(K + 1) \ .$$

where ρ_0 is the initial density of the explosive, D is the detonation velocity, and K is the adiabatic expansion coefficient of the chemical reaction product gases at the CJ state. Because the detonation velocity and the adiabatic expansion coefficient both increase linearly with the initial density, P_{CJ} is proportional to the initial density squared. Therefore, to develop more powerful explosives, we must identify energetic materials with very high densities (Tarver, 1979).

Nielsen (1973) predicted higher densities than that of HMX for the compound's larger-ring homologs, estimating a maximum of 2.09 g/cm^3 for the twelve- to fourteen-member rings (I, n = 6, 7). Attempts by researchers to prepare such compounds have been unsuccessful, thus indicating the need for alternative synthetic strategies.

Our general approach is illustrated in Figure 2. At the start of this investigation, we obtained only six- and eight-member rings (III or V, n = 3, 4) when using either carboxamides (II, R = CH_3) or urethanes (IV, R′ = CH_3O) in reaction b. Furthermore, although carboxamide derivatives (III) could be nitrolyzed to I, urethane derivatives (V) failed to yield I in reaction c (Gilbert *et al.*, 1976).

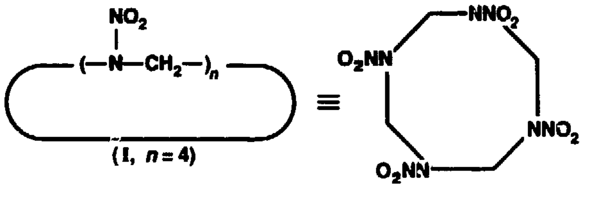

Figure 1. Two structural representations of HMX (I, *n* = 4), which is an important military explosive. The number of methylenenitramino groups is represented by *n*. HMX is a cyclic methylenenitramine with an eight-member ring and a density of 1.90 g/cm^3.

The discovery of derivatives that would allow the formation of larger ring systems (n > 4) was critical to the success of the project. We reinvestigated the use of urethanes with a focus on the more acid-labile derivatives. We found that we could use urethanes derived from *tert*-butanol, which are normally employed as *tert*-butyloxycarbonyl (BOC) protecting groups in peptide synthesis (Barany and Merrifield, 1979). In Figure 2, R′ in such urethanes (IV) would be $(CH_3)_3CO$. Especially noteworthy are the mild reaction conditions required for nitrolysis of the BOC group.

In an analogous fashion, we prepared and investigated the use of polymeric urethanes derived from benzhydryl alcohol bonded to 1% cross-linked polystyrene. In this case, R′ in Figure 2 was $(C_6H_5)_2CHO$. The polymer derivatives were designed to have chemical reactivity similar to the BOC group and possibly act as templates that would favor the formation of larger ring systems (Mitchell and Merrifield, 1985).

Low-molecular-weight and polymeric urethanes reacted as shown in Figure 3. The formation of ten- and twelve-member cyclic methyleneimine derivatives (III, n = 5, 6) was demonstrated by chemical-ionization mass spectrometry in reaction mixtures also containing the known six- and eight-member ring compounds (III, n = 3, 4). Not surprisingly, the trimer VI, in contrast to the monomer II, promoted the production of larger cyclic products (III, n = 5, 6).

In conclusion, we have developed a synthesis for precursors that will enable us to prepare larger-ring homologs of HMX. In addition, we discovered a mild nitrolysis reaction that should improve our ability to synthesize new explosives.

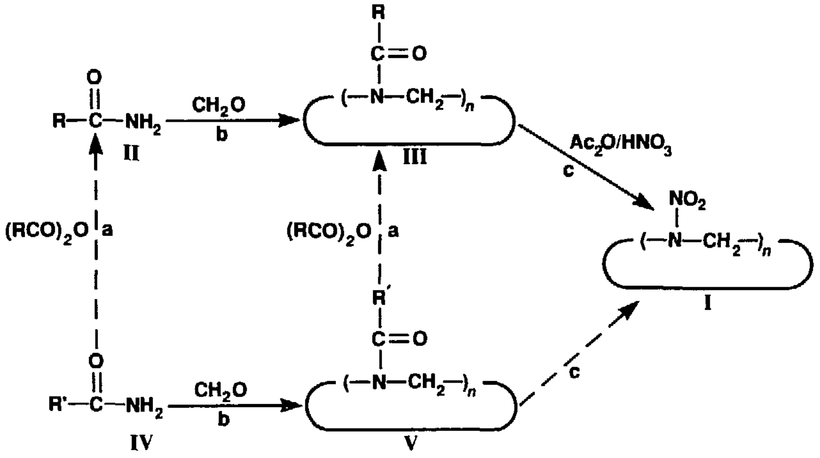

Figure 2. General approaches to the synthesis of cyclic methylenenitramines (I). Carboxamides (II, R = alkyl) or urethanes (IV, R′ = alkoxy) are used. Urethanes can be converted to carboxamides (reaction a). Ring formation (reaction b) followed by nitrolysis (reaction c) yields I. Dashed arrows denote reactions unknown at the start of the investigation.

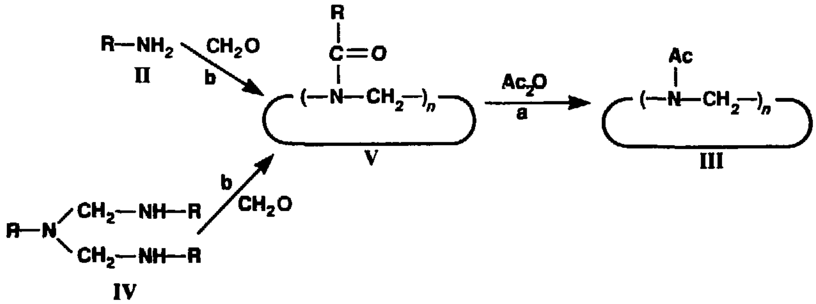

Figure 3. Formation of acetylated cyclic methyleneimines (III) from monomer (II) and trimer (VI) urethanes via ring formation (reaction b) and acetolysis (reaction a). R is *tert*-butyloxycarbonyl or 1% cross-linked polystyrene incorporating benzhydryloxycarbonyl groups.

References

Barany, G., and R. B. Merrifield (1979). "Solid-Phase Peptide Synthesis," in *The Peptides*, E. Gross and J. Meienhofer, Eds. (Academic Press, NY), Vol. 2, pp. 1–284.

Coon, C. L. (1988). "Synthesis of Energetic Materials," in *Energy and Technology Review*, Lawrence Livermore National Laboratory, Report UCRL-52000-88-1 2 (January February 1988).

Gilbert, E. E., J. R. Leccacorvi, and M. Warman (1976). "The Preparation of RDX from 1,3,5-Triacylhexahydro-s-triazines," in *Industrial and Laboratory Nitrations*, L. F. Albright and C. Hanson, Eds. (ACS Symposium Series 22, American Chemical Society, Washington, D.C.), pp. 327–340.

Mitchell, A. R., and R. B. Merrifield (1985). "Peptide Cyclizations on Polystyrene Supports: A Study of Intrasite and Intersite Reactions," in *Peptides: Structures and Function*, C. M. Deber, V. J. Hruby, and K. D. Kopple, Eds. (Pierce, Rockford, IL), pp. 289–292.

Nielsen, A. T. (1973). *Calculation of Densities of Fuels and Explosives from Molar Volume Additive Increments*, Naval Weapons Center, China Lake, CA, NWC Technical Publication No. 5452.

Tarver, C. M. (1979). "Density Estimations for Explosives and Related Compounds Using the Group Additivity Approach," *J. Chem. Eng. Data* **24**, 136.

FY88 $157,000

Multilayer Gratings for $\Delta n = 0$ Spectroscopy

We have developed ways to fabricate and characterize normal-incidence, multilayer focusing gratings for moderate- to high-resolution spectroscopy in the wavelength range of 5–50 nm. We will use these gratings to study the emission spectra of foil-excited heavy-ion beams from accelerators, particularly the $1s_{1/2}2p_{1/2}3P_0 \rightarrow 1s_{1/2}2s_{1/2}3S_1$ transition in helium-like ions.

Principal Investigators: T. W. Barbee, Jr., and D. D. Dietrich
Co-Investigators: J. Bixler and R. Marrus*

---

*University of California, Berkeley.

Our overall objective is to apply normal-incidence multilayer diffraction gratings, which allow moderate- to high-resolution spectroscopy in the spectral wavelength range of 5–50 nm, to the study of heavy-ion beams. Simple, flat, multilayer coatings are manmade depth-periodic structures that have been experimentally shown to have normal-incidence reflectivities in excess of 30% over the spectral range of 10–25 nm (see Figure 1a). These reflectivities are two to three orders of magnitude larger than those attainable with traditional single-layer coatings. Code calculations of multilayer reflectivities for 5–10-nm and 25–50-nm light predict similar performance. Although these measurements are for flat multilayers (Trail *et al.*, 1988), we have obtained similar reflectivities for multilayer structures synthesized onto spherical substrates with radii from 0.5–4.0 m (see Figure 1b).

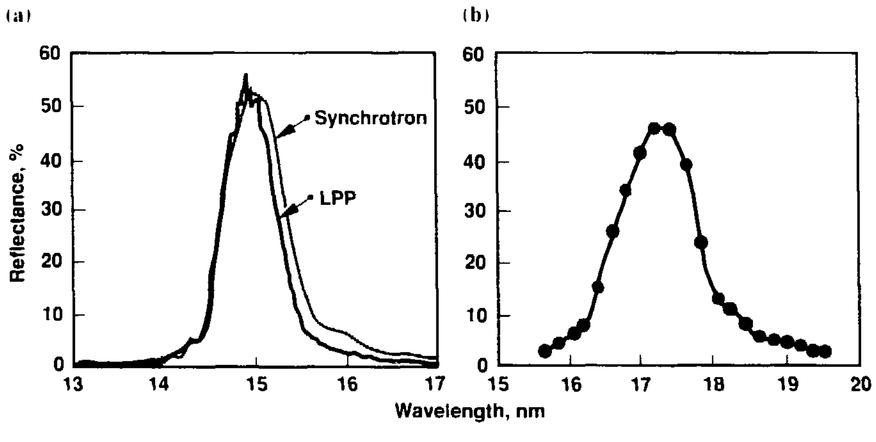

Figure 1. Measured reflectivity of (a) a flat molybdenum-silicon multilayer (7.8-nm period) at normal incidence, using both synchrotron radiation and light generated by laser-produced plasma (LPP) and (b) a molybdenum-silicon multilayer (9.31-nm period) deposited onto a concave, 1-m-radius, superpolished substrate, measured at 15° off normal incidence. The measured reflectivity (48%) in (b) compares well with our calculation (54%).

Diffraction gratings, used as substrates for multilayer deposition in our study, are in-plane microstructures that have been used as spectroscopic elements for over eight decades. Convolution of the diffractive properties of these two periodic structures (the grating and the multilayer) result in specific design criteria for multilayer diffraction gratings.

During FY88, the first year of our two-year study, we acquired a McPherson 225 vacuum spectrometer and tested it with a standard 1200-line/mm, 1-m-radius, iridium-coated blazed grating. We also fabricated two multilayer gratings. Both a 1200-line/mm, 1-m-radius holographic grating and a 1200-line/mm, blazed replica grating were coated with a molybdenum/silicon multilayer designed to reflect 15.5-nm light at normal incidence. The holographic grating operated in second pseudoblaze order and the blazed grating in third order at this wavelength. Characterization of these gratings is still incomplete because of interference from strong first-order dispersed lines excited in the plasma source used. Grating

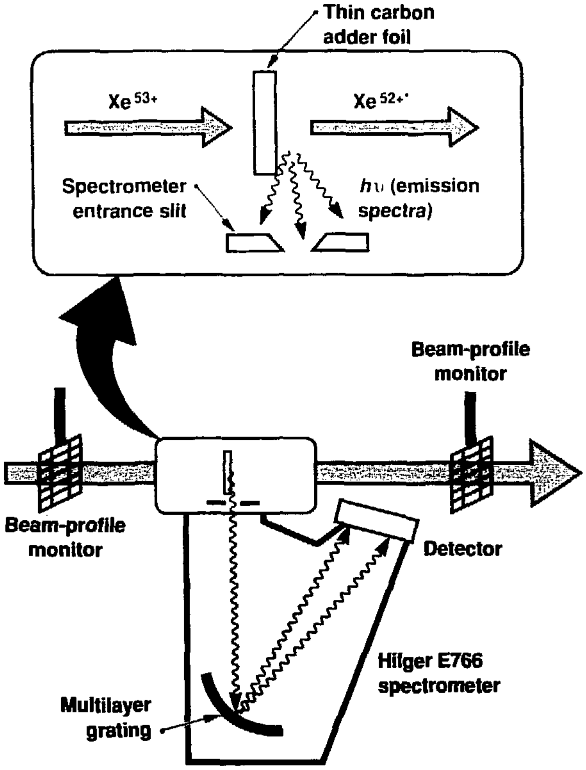

Figure 2. Schematic of our experiment at the GANIL accelerator, showing the normal-incidence spectrometer, adder foil, and ion beam.

resolution as determined from these first-order lines (1500 to 2500) was as expected.

In April 1988, we ran a preliminary experiment at the GANIL accelerator complex in Caen, France, to measure the energy of the $1s_{1/2}2p_{1/2}{}^3P_0 \rightarrow 1s_{1/2}2s_{1/2}{}^3S_1$ transition in helium-like xenon. In this experiment, a beam of helium-like Xe^{52+} was passed through a thin carbon foil placed in front of a normal-incidence spectrometer (see Figure 2). We observed a weak spectral line at the expected energy (83.4 eV). However, since this was a parasitic experiment, we did not have time to reproduce our results or explicitly verify the line's spectral order.

This transition in xenon is analogous to the Lamb-shift $2s_{1/2} \rightarrow 2p_{1/2}$ transition in hydrogenic ions. It occurs at 15.4 nm (Drake, 1988), with quantum electrodynamic (QED) corrections accounting for 8% (6.5 eV) of the total 83.4-eV transition energy. Our goal is to measure the wavelength of this transition to ±0.05 nm, which requires knowing the angle between the ion beam and the spectrometer to only 1 mrad. The resulting measurement of the Lamb shift will then have a 0.4% (0.03-eV) uncertainty level. Current Lamb-shift measurements are at the 10% uncertainty level and exist only for much lower Z [18 for $n = 2$ (Gould and Marrus, 1983) and 36 for $n = 1$ (Tavernier *et al.*, 1985)]. At 0.4% uncertainty, we would be sensitive to additional QED effects (estimated at 0.168 eV) due to the extra electron.

We are currently completing a facility at LLNL to unambiguously measure the absolute reflectivity of these gratings in any spectral order. We are also setting up a normal-incidence spectrometer in Cave H at the Lawrence Berkeley Laboratory SuperHILAC. We have requested beamtime on the Michigan State University (MSU) cyclotron, a new accelerator that promises to duplicate the performance of the GANIL one. We expect to perform experiments on xenon at MSU after our initial SuperHILAC experiments on iron. We also expect to run experiments using a helium-like uranium beam at the new SIS/ESR accelerator facility in Darmstadt, West Germany, when it becomes available in late 1989.

References

Drake, G. W. F. (1988). "Theoretical Energies for the $n = 1$ and 2 States of the Helium Isoelectronic Sequence up to $Z = 100$." *Can. J. Phys.* **66**, 586.

Gould, H., and R. Marrus (1983). "Lamb Shift and the Lifetime of the $2^2S_{1/2}$ State of Hydrogenlike Argon ($Z = 18$). *Phys. Rev. A* **28**, 2001.

Tavernier, M., J. P. Briand, P. Indelicato, D. Liesen, and P. Richard (1985). "Measurement of the (1S) Lamb Shift of Hydrogenlike Krypton." *J. Phys. B* **18**, L327.

Trail, J. A., R. L. Byer, and T. W. Barbee, Jr. (1988). "Measurement of Soft X-Ray Multilayer Mirror Reflectance at Normal Incidence Using Laser Produced Plasmas." *Appl. Phys. Lett.* **52**, 269.

FY88 $12,000

Monte Carlo Atomic Kinetics Calculations

Principal Investigators: J. R. Albritton, B. G. Wilson, and T. Thomson

We are working on a computer program that employs a Monte Carlo approach to determining the ionization and excitation distribution of the dominant atomic configurations in local-thermodynamic-equilibrium (LTE) and non-LTE plasmas.

The absorption and emission of radiation by atomic electrons are important in the calculation of energy transport in plasmas. Direct evaluation of these contributions is difficult because of the multiplicity of atomic configurations that must be accounted for. The Monte Carlo method is a new alternative to exhaustive search schemes and to schemes involving a limited or preselected ensemble of atoms (Albritton, 1986). Its principal virtue is its well-known ability to realize solutions, efficiently and without bias, to multivariate problems that are difficult to formulate and solve rigorously.

The Monte Carlo method uses direct numerical simulation of the transitions of an atom in its ambient plasma and radiation field. Starting with a definite initial configuration (given by the occupation of all the atom's quantum levels) and the rates for transitions to all accessible configurations, the code casts random numbers to determine the lifetime of the configuration and to choose a transition to a new configuration. Diagnostic information is recorded, and the "test" atom is advanced to the new configuration. The test atom randomly but rapidly "walks" from the initial configuration to sample those configurations that are the most probable—those in which it is likely to spend the most time.

We are now implementing the transition processes of radiative and collisional excitation and deexcitation, ionization and recombination, and Auger and resonant-capture transitions. The large amount of microphysical information required, such as the energy levels and matrix elements, is being provided by a relativistic, self-consistent field model (Liberman and Albritton, 1984).

References

Albritton, J. R. (1986). "Monte Carlo Calculation of Non-LTE Line Radiation." *Laser Program Annual Report 85*, Lawrence Livermore National Laboratory, Report UCRL-50021-85, pp. 2-53–2-59.

Liberman, D. A., and J. R. Albritton (1984), "Rapid Calculation of Properties of Plasma Atoms and Ions." *Laser Program Annual Report 84*, Lawrence Livermore National Laboratory, Report UCRL-50021-84, pp. 3-66–3-68.

FY88 $198,000

Micropole Undulator Insertion Devices

Principal Investigator: A. Toor
Co-Investigators: P. Csonka,* J. Hunter, R. Hornady, R. Tatchyn,† D. Whelan, and G. Westenskow**

*Institute of Theoretical Science, University of Oregon, Eugene
†Stanford Synchrotron Radiation Laboratory, Stanford University, CA
**Hughes Aircraft Company, Los Angeles, CA

We have developed two prototype micropole undulator insertion devices to demonstrate a new class of high-brightness x-ray sources. In experiments conducted on the LLNL 150-MeV linear accelerator, we demonstrated the first-ever production of photons from submillimeter-period undulators. Installation of either of these devices on the Bates linear accelerator at the Massachusetts Institute of Technology would produce tens of milliwatts of monoenergetic soft x rays, thus providing an x-ray source that is competitive with bending magnets installed on high-energy electron storage rings.

As recently as last year, the feasibility of scaling undulator insertion devices to submillimeter periods was highly controversial and believed by many to be impossible. Nevertheless, the theoretical[1] benefits of such devices were obvious. Installed on high-energy electron storage rings, such insertion devices would produce monochromatic x-ray beams with significantly higher brightness than currently attainable in the laboratory by any other means. We have investigated theoretically the scaling limits for micropole undulator (MPUs) and believe that 100-μm period devices with 10^4 periods are achievable. Such devices would provide a new class of high-brightness, monochromatic x-ray sources.

Our research this year has focused on the development of two prototype designs for MPUs using two different technologies to address the issues in building spatially coherent structures with 10^4 periods. In the first design, the periodic magnetic structure is machined in a single, monolithic block of material; the MPU is biased with an external magnetic field and cooled with liquid nitrogen. We used the LLNL 150-MeV linear accelerator (linac) to measure the intensity and angular distribution of 66-eV photons radiated by 75-MeV electrons passing through a 706-μm-period undulator 35 periods long. These experiments were the first to produce photons from submillimeter-period undulators. The advantage of this type of MPU is that ion-milling of anisotropic materials such as NdFe(B) or $SmCo_5$ can produce very-short-period (~50-μm) devices with lithographic accuracy, thereby simplifying the technical challenge to fabricate MPUs with 10^4 periods. The major disadvantage is the bulk associated with the bias magnets and the active cooling that is required to dissipate the electrical energy needed to produce the bias field.

The second design is a laminar MPU for which each "pole" piece is a stack of thin magnetized wafers with alternating magnetic polarity. A prototype of this design was assembled from NdFe(B) wafers with 54 periods of 986 μm (i.e., a total of 216 magnets). In a second series of experiments using the LLNL linac, we generated 70-eV photons and characterized the radiated photon intensity as a function of photon energy and angle (Figure 1). The advantage of this laminar design is that it does not require a bias field with the attendant cooling apparatus; thus it can be remotely positioned and scanned in vacuum using manipulators with micrometer accuracy. Disadvantages of this design are associated with the handling and characterizing of a large number of separate fragile components whose internal magnetic forces approach the inherent strength of the materials.

The measured performance of both MPU prototypes was in agreement with our theoretical predictions. With both types of MPUs, we found that the frequency, intensity, and angular distribution of the photon output were limited by the electron-beam characteristics (e.g., energy, current, emissivity) of the accelerator and by the resolution of our diagnostics.

During this work, we discovered that the field strength of NdFe(B) decreases with decreasing thickness below ~1 mm as a result of surface effects due either to oxides or to machining. Therefore, $SmCo_5$ (which was demonstrated not to exhibit this property) was used to fabricate two additional laminar prototypes: a 494-μm, 120-period MPU, and a 253-μm, 248-period MPU, both of which are ready for testing. Theoretical field-strength uniformity and phase criteria coupled with the measured values of field and thickness for each wafer currently limit the number of periods attainable with 250-μm $SmCo_5$ wafers to about 1000, or four times that of our largest prototype MPU.

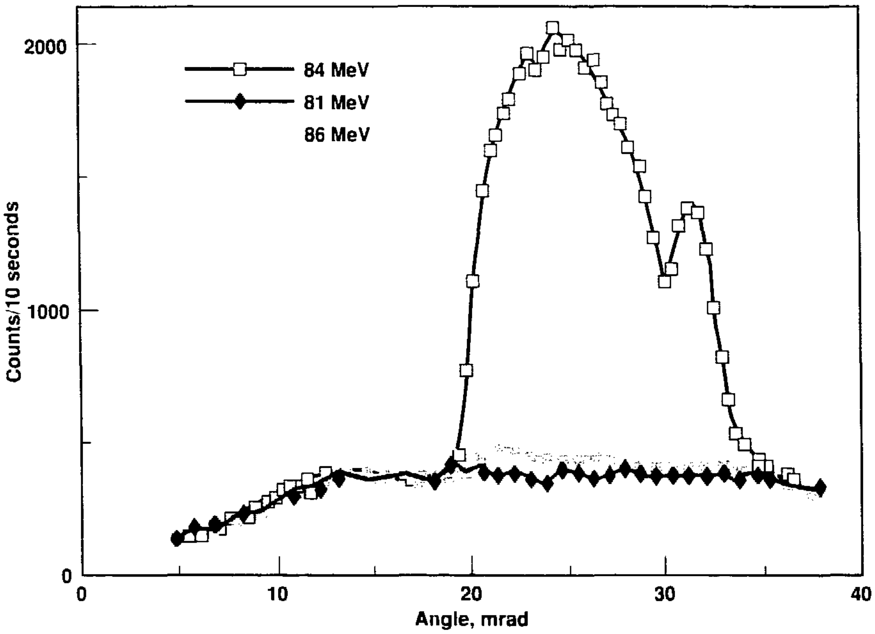

Figure 1. Angular distribution of radiated photons for the NdFe(B) 986-μm laminar MPU at three electron energies. These data show that a ±3% change in electron energy moves the radiated photons out of the diagnostic's bandpass, thereby eliminating the possibility that the detected photon origin is due to some other process (bremsstrahlung, or channeling radiation).

The LLNL linac does not have low enough emittance to allow us to adequately test the performance scaling of the 250-μm MPUs. Thus, we must either upgrade the LLNL linac (which is being considered by the Physics Department) or travel to the Bates linac at the Massachusetts Institute of Technology or the Race Track Microtron accelerator at the National Bureau of Standards (which is currently under construction).

Installed on the Bates linac, either of our two prototype MPUs would radiate narrowband, ~10–25-keV x rays at the tens-of-milliwatt level. This would provide a high-brightness x-ray source facility [spectral brilliance greater than 10^{14} photons/(s·mm·mr·1% bandwidth)] that is competitive with the bending magnets installed on high-energy electron storage rings.

FY88 $137,000

Pressure Effects in High-Temperature Superconductors

Principal Investigator: B. Bonner
Co-Investigators: M. Young, R. Reichlin, F. Ryerson, and G. Smith

We are probing the nature of high-temperature superconductivity in cuprate oxide (Cu-O) materials. By comparing the pressure dependence of the superconducting transition to that for related optical and vibrational properties, we should be able to identify aspects of the electronic or phonon structure that are critical to superconductivity.

Pressure-enhanced superconductivity appears to be a general property of high-temperature superconducting (HTSC) materials. This pressure effect, believed to result from an underlying change in structure or in the mechanism that mediates pair formation, has yet to be explained by theory. We are investigating this effect by comparing experimental observations with theoretical simulations in which the ionic spacings are reduced to model the pressure effect.

We used the diamond-anvil cell to study the optical properties of single crystals of Y-Ba-Cu-O (supplied by J. Z. Liu, Argonne National Laboratory) at high pressure. When pressure is increased to 22 GPa, there is a 300% rise in near-infrared normal-state reflectivity, indicating increased oscillator strength (Figure 1). This suggests that the density or mobility of the free charge carriers increases with pressure, implying more metallic behavior that must be treated theoretically.

Reflectivity data in the mid-infrared show a weak spectral feature near 0.4 eV that we attribute to an exciton or to a Cu-O charge-transfer excitation that shifts only slightly with pressure to 20 GPa. Additional mid-infrared measurements of diffuse reflectance at atmospheric pressure have clearly demonstrated that such data are useful indicators of annealing history and oxygen content for the Y-Ba-Cu-O system.

Also this year, we applied high-pressure synthesis techniques to La-Cu-O (the parent HTSC system), which is not ordinarily a superconductor. By annealing this material in oxygen overpressures of 20–300 MPa, we produced a superconductor at $T_c = 18$ K. Extensive characterization efforts are under way to identify the structural changes associated with this effect.

Next year, we will extend our optical measurements to observations of Raman backscattering, beginning with normal-state measurements for yttrium compounds to 25 GPa. Pressure shifts of the vibrational frequencies for oxygen will be compared to predictions from *ab initio* cluster simulations. We will use x-ray diffraction to measure changes in cell dimensions with increasing pressure for yttrium- and lanthanum-based superconductors to see if changes in the Cu-O plane separation can explain the observed pressure effect.

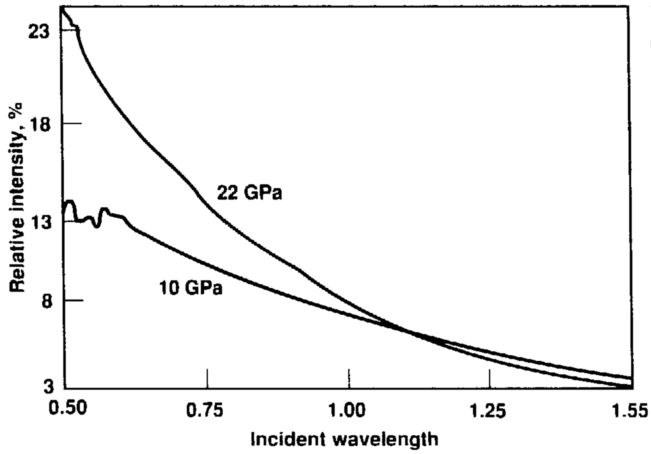

Figure 1. Pressure causes large increases in near-infrared normal-state reflectivity for superconducting Y-Ba-Cu-O. Data were collected at 300 K.

Using Geochemical Modeling to Investigate the Paleoecology of Closed Basin Lakes in the East African Rift During the Plio-Pleistocene

Principal Investigator: K. J. Jackson

Modern geochemical modeling codes have been advanced to the point that we can evaluate quantitatively the chemical interactions between mineral phases present in sediment samples and the solutions from which they precipitated. Our project was to collect water and sediment samples from the closed-basin lakes in the East African Rift Valley and to use the EQ3/6 code to ascertain the kinds of geologic and climatic events that might have produced the observed mineral phases. The lake water chemistry in the East African Rift Valley is of special interest because this is the area in which many of the most important discoveries of early-hominid remains have been made.

We proposed to use trends in the composition of water samples collected from closed basin lakes in the East African Rift Valley (Figure 1), together with observed differences among the mineral phases precipitated from these lakes, to gain insight into changes in lake water chemistry that occurred during the Plio-Pleistocene. By illustrating the systematic dependence of chemically precipitated mineral phases on the compositional variations in water chemistry in the modern lakes, we hoped to be able to model how the mineral assemblages present in sedimentary rocks formed during the Pliocene and Pleistocene provide a record of the changes in water chemistry that occurred during those epochs.

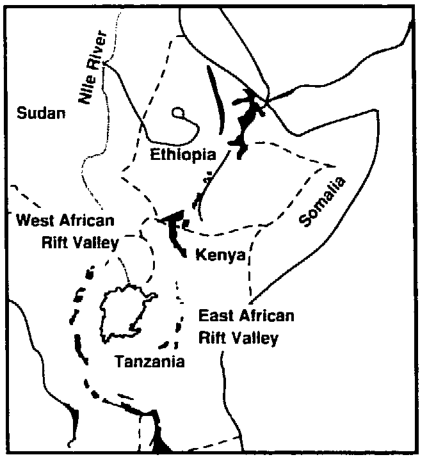

Figure 1. Map showing the location of the East African Rift Valley, the area in which many important early-hominid remains have been found.

Past compositional changes in lake water chemistry in this region are of special interest because of the impact they would have had on the paleoecology of the East African Rift Valley—the area in which many of the most important early-hominid remains have been found. Changes in the chemistry of lake waters in the geologically recent past have apparently been responsible for environmental fluctuations in which a number of lacustrine (lake-dwelling) species have alternately flourished and died off. Molluscs and fish that might have been important sources of food for early hominids are among these species.

By coupling recent advances in theoretical geochemistry with corresponding advances in of geochemical modeling codes like EQ3/6, it is now possible to evaluate quantitatively the chemical equilibria between the mineral phases present in lake sediments and the aqueous solutions from which they precipitated. The identity and relative proportions of the various minerals found in Plio-Pleistocene lake sediments would have served as the input constraints for the geochemical modeling codes. From the code calculations, we hoped to be able to ascertain the kinds of geologic and climatic events that might have provided for the observed changes in mineral assemblages and variations in lake water chemistry.

In order to carry out this project, a research permit from the government of Kenya was needed. However, no permit was granted in time, and therefore the proposed project could not be done in FY88.

FY88: $195,000

Atmospheric Compensation Algorithms for Imaging

We are developing algorithms for imaging astronomical objects and man-made satellites to the diffraction limit imposed by a collecting telescope instead of that imposed by the atmosphere. Our work will benefit the scientific and defense communities by reducing or eliminating resolution-limiting effects of atmospheric turbulence.

Principal Investigator: J. P. Fitch
Co-Investigators: T. W. Lawrence and D. M. Goodman

The world's largest telescopes, such as the 5-m Hale telescope on Palomar Mountain in southern California, have a theoretical diffraction-limited resolution of about 0.1 µrad. In practice, however, these instruments are limited by the turbulent atmosphere to a 5.0-µrad resolution, the diffraction limit of a 10-cm telescope. The limitation is suffered by all ground-based telescopes and severely hampers our ability to image distant objects. Recent advances in short-exposure imaging technology and computer postprocessing algorithms could provide a method for imaging astronomical objects and man-made satellites to the diffraction limit imposed by the telescope instead of that imposed by the atmosphere. In addition to the immediate impact on existing telescopes, sparse optical arrays hundreds of meters in diameter could be constructed to image higher-altitude earth-orbiting satellites. The new atmospheric-compensated arrays could potentially revolutionize astronomy.

Our approach is based on a class of nonstandard imaging techniques that have been applied successfully by radio astronomers. The turbulence-induced effects of the atmosphere on the object image can be frozen if the image-exposure time is reduced below the correlation time of refractive index fluctuations (1 to 10 ms, depending on wind velocity). Short-exposure images captured this way are a random superposition of diffraction-limited images of the object. Each short-exposure interference pattern, called a speckle image, is analogous to the speckle seen with coherent laser light. Procedures for extracting object information from a sequence of speckle images are collectively referred to as speckle interferometry. These techniques have been successfully applied by the astronomical community to image star clusters; however, no algorithms have been demonstrated for imaging extended objects through the atmosphere.

We met the following major objectives this year:

- To conduct a scaled, horizontal-path imaging experiment and to investigate image reconstruction of known objects under realistic atmospheric conditions and illumination levels.
- To conduct a comprehensive numerical simulation of the speckle imaging process and to extend this simulation, backed by experimental validation, to a complete range of imaging scenarios.
- To implement state-of-the-art image reconstruction algorithms used in the astronomical community and to investigate ways to statistically optimize the reconstruction process.

The summer months on Mt. Diablo in northern California afforded excellent access to a range of horizontal path lengths from about 1 to 3.5 km. We used a 0.5-m telescope designed by our group, a low-noise, 512 × 512 charge-coupled device (CCD) array controlled by a MicroVax data-acquisition system, and a white-light illumination target board. Data from an unresolved point reference on the target indicated turbulence levels in the range D/r_0 = 15 to 25 for a 1.2-km path, where D/r_0 is the ratio of the telescope diameter to the coherence scale length in the atmosphere. This ratio characterizes the amount of degradation introduced by the fluctuations, such that a value of 15 means that the resolution of the telescope is degraded by a factor of 15 by the atmosphere.

We obtained data with illumination levels simulating signals expected for objects between low earth orbit (300 km) and high earth orbit (1000 km). We also obtained data with various bandwidths and exposure times. Analysis of the data is now under way, and we are planning to continue the experiment later next spring to extend the range of imaging conditions.

A complete simulation of the speckle imaging process is now operational. The computer-based atmospheric simulator allows input objects to be propagated through an isoplanatic atmosphere with arbitrary values of r_0. Objects are received by a telescope with a pupil function defined as the superposition of circular apertures varying in size and with arbitrary obscurations. In addition, the simulator includes noise sources resulting from Poisson photon statistics (arising from the randomness associated with the quantum nature of light) and nonideal photon detection. The speckle images we simulated of a point reference and objects used in the experiment compare quite well with experimental data. In addition, a reconstructed image from several simulated speckle frames also compares well with experimental results, thus addressing the goal of detailed validation. Our future plans for the simulator include a survey of a variety of satellite imaging conditions.

We have implemented state-of-the-art algorithms for image reconstruction to process both experimental and simulated speckle images. The algorithms are:

- The Labeyrie technique for Fourier magnitude estimation.
- A bispectral (triple-correlation) technique for Fourier phase estimation.
- The Gerchberg-Saxton-Fienup Fourier-iteration technique for nonlinear imposition of object constraints.

We have applied a combination of these techniques and a new algorithm developed at LLNL to reconstruct extended objects with both binary and gray-scale intensity features at illumination levels of low-earth-orbit satellites. These are the first reconstructions of extended objects degraded by atmospheric turbulence using speckle imaging. This work constitutes a first-order demonstration that speckle imaging of satellites is indeed feasible. Figure 1 is an example of one of the many objects we reconstructed from experimental data.

Because none of the techniques listed above is optimal in a statistical sense, we are now attempting to produce an optimization-based algorithm for image reconstruction that directly imposes positivity and support constraints on the image. That is, the final image must be positive in value everywhere and occupy a finite region of space. In addition to statistical appeal, our development of an optimal algorithm is motivated by preliminary indications that the techniques we have used to date do not effectively reconstruct objects with an increased dynamic range of intensity features. Our continuing analysis will address this problem in more detail, extending reconstruction performance to include objects illuminated at high earth orbit and eventually at 40,000 km.

(a) Recorded image **(b) Processed image**

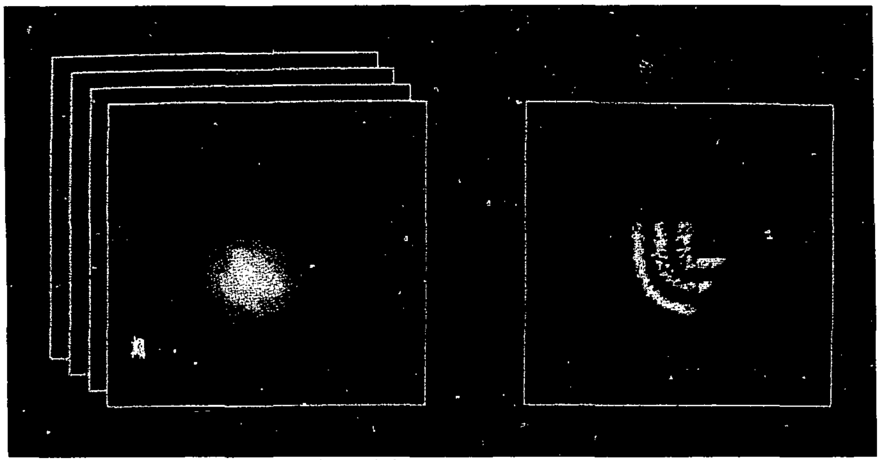

Figure 1. Reconstruction of a test target using speckle interferometry. (a) One of a set of 400 speckle images recorded by our CCD camera mounted on the 0.5-m telescope. The telescope was located at Curry Point in the foothills of Mt. Diablo. The target, a 3-cm cutout of the Laboratory logo illuminated with a high-intensity light bulb, was located on a hill 1.2 km away. The image, captured with a 5-ns exposure time, shows the degrading effects of the atmosphere. (b) The result of processing the 400 speckle images using the three algorithms described in the text. Comparison with (a) underscores the power of our technique in reconstructing diffraction-limited detail about an object.

FY88 $162,000

Thermally and Ion-Assisted Etching of Tungsten and Molybdenum

Principal Investigator: D. E. Miller
Co-Investigators: W. J. Siekhaus and M. Balooch*

*University of California, Berkeley

We are investigating the kinetics of etching tungsten and molybdenum by chlorine alone and with simultaneous argon-ion bombardment. The reactions are directly related to plasma and ion-beam etching processes needed to form patterned tungsten and molydenum films for future microelectronics and x-ray optical microstructures.

Refractory metals are increasingly used as interconnections and gates in microelectronic devices and integrated circuits. One reason for their growing use is that metals, such as tungsten and molybdenum, have high temperature stability with high conductivity and amenability to dry-etch patterning. Multilayer and superlattice microstructures containing these metals are proving to be vital components of extremely efficient and novel x-ray optics. However, fundamental etching studies of these metals, including those using molecular chlorine, have not previously been done.

Modulated molecular-beam mass spectrometry allows us to determine the elementary steps of the overall heterogeneous etching (or deposition) reaction. The steps include adsorption of a reactant with or without dissociation, surface reaction of adsorbed species, surface or bulk diffusion of intermediate species, and desorption (or deposition) of products. Moreover, modulated-beam experiments can yield quantitative rate constants for the elementary steps in addition to a mechanistic interpretation of the reaction itself. Our previous investigations with modulated molecular beams determined specific mechanisms for hydrogen and chlorine reactions with gallium arsenide and silicon, respectively (Balooch *et al.*, 1986; Olander *et al.*, 1987).

Our immediate objectives were to determine the:

- Etching rates of tungsten and molybdenum with temperature, reactant flux (beam intensity), and reactant degree of dissociation.
- Principal reaction products.
- Kinetics and mechanisms of the overall etching reaction with and without simultaneous ion bombardment.

The goals during the second phase of our research included measuring the effect of oxygen additions, which is a common industrial practice in fluorine-based plasma processing. We also wished to investigate the silicides of tungsten and molybdenum.

In seqential sets of experiments, we achieved the first two objectives listed above for both tungsten and molybdenum. With extensive calculations based on the experimental data, we found satisfactory kinetic models for the thermally assisted etching of both metals without ion assist. The results for tungsten etching by atomic and molecular chlorine are described in detail elsewhere (Balooch *et al.*, 1988a). Our more recent assessment of data on the molybdenum reaction with chlorine showed many similarities to the tungsten data; however, we observed a markedly increased influence of adsorbed reactant diffusion in the overall reaction sequence over the temperature range of 900 to 1250 K. Our molybdenum experiments included measurements of the chlorine reaction with a modulated argon-ion beam using multiscaling to improve data collection compared to techniques for our earlier tungsten work. We have summarized our findings on the kinetics of molybdenum etching by atomic and molecular chlorine (Balooch *et al.*, 1988b), and we are now preparing for publication a detailed description of chlorine-molybdenum reaction kinetics.

To summarize our work, we studied etching reactions of tungsten and molybdenum with atomic and molecular chlorine, both with and without simultaneous 4-kV argon-ion bombardment. Surface temperatures ranged from 300 to 1500 K without ion assist, while the simultaneous argon-ion beam was modulated during steady chlorine impingement with surface temperatures held at 300 K. Beam intensities for molecular chlorine were 5×10^{15} to 3×10^{17} molecules/cm^2·s; the atomic chlorine beam effused from a separate radiofrequency discharge chamber.

The main reaction products up to 1000 K were $WCl_{[illegible]}$ and $MoCl_2$, respectively. For tungsten and molybdenum surfaces hotter than 1000 K, atomic chlorine was the dominant species. Dissociation of molecular chlorine was the only reaction detected above 1300 K. The reaction probability at 300 K was about 0.1% for molecular chlorine, while atomic chlorine yielded etch rates higher by a factor of 10 across the temperature range from ambient to 1000 K. With argon-ion assist, we found some increase in the reaction probability of tungsten with chlorine, but we have not yet obtained a reliable quantitative comparison. For molybdenum on the other hand, we observed an increase in etching by one order of magnitude, as shown in Figure 1.

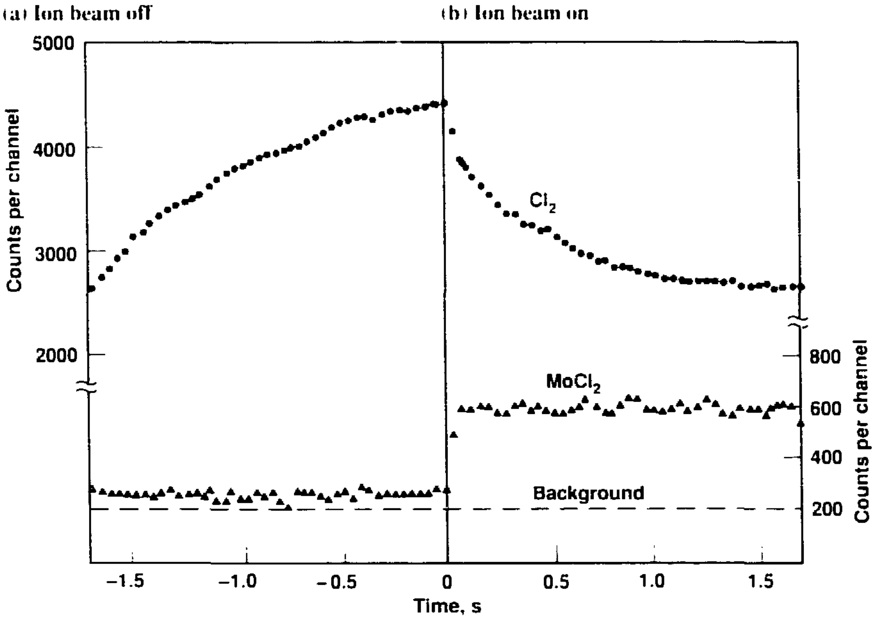

Figure 1. Reflected (i.e., unreacted) chlorine (color) and molybdenum dichloride (black) intensities (a) without and (b) with argon-ion assist at room temperature. In this experiment, the argon-ion beam intensity was 10^{14} ions/cm^2-s using 4.4-kV argon-ion bombardment, and the surface temperature was 300 K. After background subtraction, these data show that simultaneous ion bombardment produces a 10× enhancement of molybdenum etching by chlorine.

A key goal for future research is to acquire experimental data on product velocity distributions. Such data will enable us to investigate mechanisms responsible for the significant ion-beam enhancement of chlorine etching in refractory metals. In anticipation of such experiments, we have designed and purchased a new reaction chamber and mass spectroscopic apparatus that will allow us to obtain time-of-flight measurements on etching products.

References

Balooch, M., D. R. Olander, and W. J. Siekhaus (1986). "The Thermal and Ion-Assisted Reactions of GaAs(100) with Molecular Chlorine," *J. Vac. Sci. Technol.* **B4**, 794.

Balooch, M., D. S. Fischl, D. R. Olander, and W. J. Siekhaus (1988a). "The Kinetics of Tungsten Etching by Atomic and Molecular Chlorine," *J. Electrochem. Soc.* **135**, 2090.

Balooch, M., D. R. Olander, W. J. Siekhaus, and D. E. Miller (1988b). "The Kinetics of Molybdenum Etching by Atomic and Molecular Chlorine," *Proc. Fifth Workshop on Tungsten and Other Refractory Metals for VLSI Applications* (Mat. Res. Soc., Pittsburgh, PA).

Olander, D. R., M. Balooch, J. Abrefah, and W. J. Siekhaus (1987). "Modulated Molecular-Beam Studies of the Surface Chemistry of Silicon Reaction with Reactive Gases," *J. Vac. Sci. Technol.* **B5**, 1404.

Miniature Vacuum Tubes for Harsh Environments

We are establishing the modeling and technology necessary to build and analyze miniature, integrated vacuum tubes for use in electronic devices operating in hazardous environments.

Principal Investigators: W. J. Orvis, C. F. McConaghy, D. R. Ciarlo, and J. H. Yee

Miniature vacuum tubes are vacuum-switching and power-control devices analogous to existing vacuum tubes. What makes them unique by today's standards is that they are micrometer-size devices, they are constructed on a semiconductor wafer using fabrication techniques specific for integrated circuits, and they employ field emission rather than thermionic emission to generate charge carriers. Compared to existing semiconductors, miniature vacuum tubes should operate faster and be much more tolerant of high temperatures and radiation. Such characteristics make them strong candidates for use in power and control applications in nuclear and high-temperature environments (e.g., in weapon systems, nuclear reactors, fusion reactors, and satellites).

A millimeter-size thermionic vacuum tube developed at Los Alamos National Laboratory has now been subjected to 10^7 neutrons/cm^2 and 2.5×10^8 rad (Si) with no degradation. These levels are 1000 to 10,000 times larger than the levels that destroy silicon devices. We expect our device to have a similar tolerance to radiation and heat.

In semiconductor devices, the velocity of an electron is about 10^7 cm/s. Electrons saturate because they are moving through a solid, and collisions with atoms in that solid restrict the velocity. Because the velocity is saturated, increasing the applied voltage will not speed up the device. In a vacuum device, on the other hand, charge-carrier transport occurs in a vacuum, where the electron velocity saturates at the speed of light (3×10^{10} cm/s), which is considerably faster that the velocity in silicon. While the velocity of an electron is important in determining a device's speed, the device's capacitance is also important and must be kept low for high-speed operation. A device's capacitance can be controlled by design considerations rather than by considerations of electron physics, as is the case for electron velocity. With these considerations in mind, we expect that miniature vacuum tubes can operate 10 to 100 times faster than conventional silicon devices.

During FY88, we designed and built two variations of a proof-of-principle device to integrate the necessary fabrication methods and to determine the operating characteristics. Our first vacuum tube is an encapsulated, field-emission vacuum triode; our second is a field-emission vacuum diode with an anode-to-cathode spacing of 2 µm.

The vacuum triode consists of a silicon wafer on which is etched a pyramid-shaped silicon field emitter. The field emitter is buried in phosphorus-doped silicon dioxide glass. On top of the glass is a layer of polysilicon with a hole forming the grid. Locating this grid layer accurately required that we develop new alignment methods to ensure that the hole was precisely centered over the field emitter. The structure is then buried once again in glass and another layer of polysilicon to form the anode. At this step of fabrication, we have a structure that is filled with glass rather than a vacuum. We then etch away the glass from under the anode and grid, leaving a miniature vacuum tube (see Figure 1). The use of the glass sacrificial layer to

Figure 1. Encapsulated field-emission vacuum triode. Such devices should prove to be faster than conventional semiconductors and more tolerant of high temperatures and radiation. The novel fabrication procedures are described in the text.

produce three-dimensional structures is a new technique developed at UC Berkeley. Because the technique is new and therefore not well characterized, we must determine deposition and etch rates experimentally.

Our second device is based on the vacuum triode; however it omits the grid and the second layer of glass to produce a vacuum diode. We developed the diode so that we could begin testing field emitters before we completed fabrication of the vacuum triode. We recently performed a fabrication run of vacuum diodes and have now begun testing. While we have measured currents in our diodes that could be due to field emission, we have not yet verified that fact.

Our modeling effort is focused on examining field enhancement near the tip of the field emitter and on simulating device operation. The modeling has been productive in that we were able to identify several problems before a device was actually fabricated. We will simulate device operation to verify the existence of field emission and to predict device output characteristics. Such modeling efforts will also give us a design tool for future device engineering.

We have presented more detailed versions of our work in two papers at the First International Vacuum Microelectronics Conference, in Williamsburg, VA. Next year, we will continue to develop the design of miniature vacuum tubes and attempt to demonstrate both thermal and radiation hardness. At the completion of our project, we expect to have the capability to design and fabricate miniature vacuum switching and control devices and to predict their operational characteristics.

FY88 $150,000

Development of an Induction Linac Cyclotron Autoresonance Maser

We are investigating the design of a CARM (cyclotron autoresonance maser) amplifier that can generate gigawatt peak power levels at millimeter wavelengths by using an induction linear accelerator injector as the beam source. This device may supplement or provide an alternative to the microwave free-electron laser for heating fusion plasmas.

Principal Investigator: M. Caplan
Co-Investigators: J. K. Boyd, A. Salop,*
R. R. Stone, and C. Thorington†

*386 Creekside Dr., Palo Alto, CA 94306.
†11689 MacDonald St.,
Culver City, CA 90230.

The only operational cyclotron autoresonance maser (CARM) is in the Soviet Union (Botvinnik *et al.*, 1982), where output powers of 10 MW at 125 GHz, with 30-ns, 0.5-MeV beam pulses at 1 kA have been achieved. Efficiency was only 2%, however, due to poor beam quality and lack of magnetic tapering. We believe that great improvements in performance can be made by using the high-brightness beams and tapering techniques that proved so successful in the LLNL microwave free-electron laser (FEL). With improved effiency, the CARM could become an alternative microwave source for heating fusion plasmas. During FY88, our efforts were directed toward developing new computational techniques for analyzing the beamline and interaction circuit of a CARM and a conceptual design for a CARM amplifier. We also conducted a performance-cost analysis for the proposed CARM as compared to the FEL.

To improve our ability to analyze the CARM beamline, we developed and brought on line a variable-mesh electron-gun design program (CRMGUN) based on earlier versions with no self-magnetic field (Caplan and Thorington, 1981). With CRMGUN, we can analyze beam dynamics, including self-consistent radial and axial space-charge forces, within the large variation of scale lengths occurring as the beam is compressed from a 12.7-cm cathode at 14 G to a 0.5-cm diameter at 22.8 kG.

We also developed a quasi-three-dimensional beam-dynamics code (WIGCRM) from an earlier version with no self-magnetic fields (Neilson *et al.*, 1985). WIGCRM uses fast-Fourier transforms to solve Poisson's equation at every axial position. This code is useful for modeling nonsymmetric transverse space-charge forces in the beam as it corkscrews from the helical wiggler to the interaction region; it can also be used to model the emittance growth in the drift region. In addition, we developed a three-dimensional CARM interaction code (CARMRP), based on earlier gyrotron TWT codes (Salop and Caplan, 1986), which includes a self-tapering algorithm adapted from a technique used in FEL codes for monitoring a trapped resonant particle.

Another objective for FY88 was to develop a conceptual design for a CARM amplifier based on typical beamlines that now exist or will exist at LLNL's Accelerator Research Center (ARC). The design is also compatible with an existing superconducting magnet at the Massachusetts Institute of Technology. We developed a first set of blueprint drawings showing all internal dimensions of a beam-pipe transmission system, circuit, and beam dump. We also determined the positions and settings that will be required for the 34 magnets to focus the beam into the high-field region without wall interception. Figure 1 is a schematic drawing of the CARM amplifier, indicating key design parameters; Table 1 gives the amplifier's predicted performance.

In conducting a performance-cost trade-off study for the proposed CARM as compared to the FEL at 280 GHz, we found that for a total average power above 5 MW, a number of CARMs operating at 2 MeV and 2 kA would be more expensive than a single 10-MeV FEL. However, below 5 MW, CARMs become relatively much less expensive because wiggler constraints prevent the FEL from operating at lower voltages for lower power. CARMs could also become competitive at higher power (above 5 MW) if they could operate at higher current. However, we do not know at present whether CARMs could maintain high efficiency in the presence of the increased beam emittance resulting from increased space charge.

This project will continue into FY89. Our main objective next year will be to design a proof-of-principle experiment, which could be performed in the ARC. That experiment will most likely test a CARM oscillator using Bragg resonators. The CARM circuit and accompanying drift sections will be fabricated and cold-tested. We will also continue work on designing magnet coil configurations that minimize beam emittance.

References

Botvinnik, I. E., V. L. Bratman, A. B. Volkov, G. G. Denison, B. D. Kal'chugin, and M. M. Ofitserov (1982). "Cyclotron-Autoresonance Maser with a Wavelength of 2.4 mm." *Sov. Tech. Phys. Lett.* **9** (11), 506–507.

Caplan, M., and C. Thorington (1981). "Improved Computer Modelling of Magnetic Injection Guns for Gyrotrons." *Intl. J. Electronics* **51** (4), 415, 426.

Neilson, J., M. Caplan, N. Lopez, and K. Felch (1985). "Simulation of Space-Charge Effects on Velocity Spread in Gyro Devices." *International Electron Devices Meeting, Technical Digest* (IEEE, New York, NY), 184–187.

Salop, A., and M. Caplan (1986). "Self-Consistent Field Large Signal Analysis of Gyroklystron." *Intl. J. Electronics* **61** (6), 1005–1024.

Table 1. **Predicted performance for the 280-GHz CARM amplifier.**

Parameter	Predicted value
Peak output power, GW	2
Average power, MW	2
Tapered efficiency, %	50
Gain, dB	60
Transverse velocity spread, %	5–10
Axial velocity spread, %	0.2–0.4

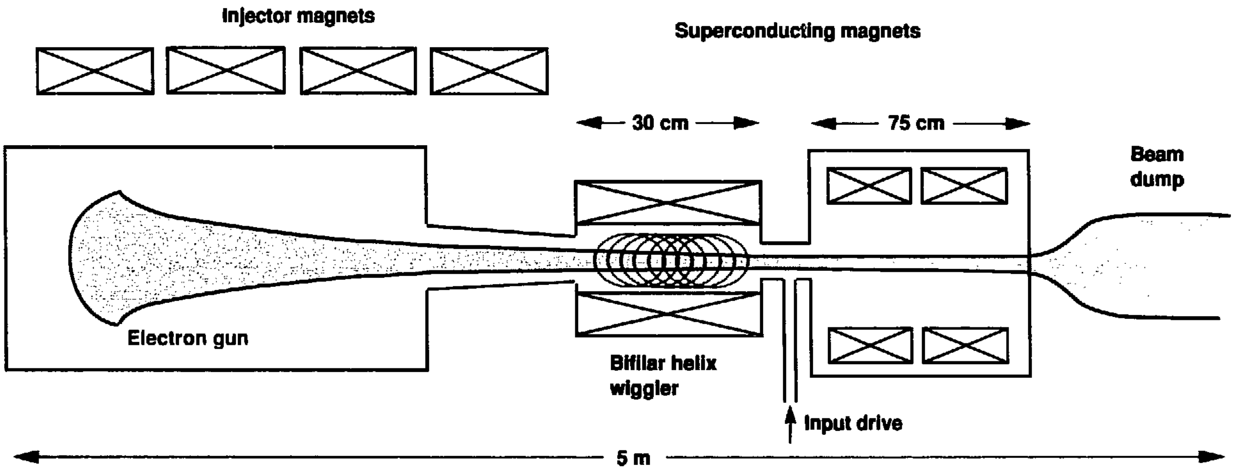

Injector
Cathode = 12.7 cm diameter
Cathode field = 14 G
Voltage = 2 MeV
Current = 2 kA

Wiggler
Axial field = 10 kG
Wiggler field = 35 G
Beam radius = 0.24 cm
Pitch = 5 cm

Circuit
Axial field = 22.8 kG
Beam radius = 0.24 cm
Pipe radius = 0.3137
Perpendicular/parallel velocity = 0.2 – 0.3
Mode = HE_{11} or TE_{11}

Figure 1. Schematic diagram of a 280-GHz CARM amplifier. Key design parameters are listed below the corresponding section of the amplifier.

FY88: $97,000

Generation of High Electrical Potentials in Plasma for Application to the Mirrortron

We have assembled experimental apparatus and performed theoretical analyses in preparation for a proof of principle of the Mirrortron, a new concept for a high-energy ion accelerator.

Principal Investigator: **R. F. Post**
Co-Investigators: **S. Douglass,[*] T. Weisgraber,[†] and S. Fallabella**

[*] University of California, Davis.
[†] University of California, San Diego.

The Mirrortron concept is based on our substantial understanding of the mirror confinement of plasmas gained from years of research at LLNL and other laboratories. Mirror theory predicts that if a mirror-confined plasma containing multi-MeV electrons and low-temperature ions is subjected to a rapidly rising and spatially localized, pulsed magnetic field (a pulsed, local mirror), then a local region of high (megavolt) positive potential will be generated. Repetition of this process down a linear array of mirror cells synchronized with the passage of a bunched ion beam would result in a kind of plasma linac (linear accelerator). What distinguishes the Mirrortron from conventional ion linacs is the much higher acceleration gradients that we should be able to achieve. In addition, the Mirrortron is distinct from other accelerator ideas that are based on plasma space-charge fields because of the precise spatial control and focusing character of the electric fields that should be achievable. Such control arises because the spatial distribution of accelerating electric fields is determined by the spatial distribution of the pulsed mirror field, the characteristics of which should be precisely controllable from outside the plasma.

Because the plasma density required to produce megavolt potentials in a plasma is relatively low, several methods for creating the hot electron plasma needed in the Mirrortron are available. Previous methods include cyclotron-resonant microwave heating and slow magnetic compression. The most demanding technological requirement of the Mirrortron is, therefore, generation of the fast-pulse mirrors. Fortunately, major advances have occurred in this area associated with the development of high-power switching techniques for use in induction linacs (such as the Advanced Test Accelerator) and for other purposes.

The objective of our experiment during Phase I is to generate and characterize a low-density, hot-electron plasma created in a 150-cm-long cylindrical resonator located within a dc magnetic field of the mirror type. We will use continuous-wave microwave power at two frequencies, 2.4 and 4.0 GHz, to excite electric-field modes in the cavity resonator and to create and heat the plasma to temperatures on the order of 250 keV. During Phase II, we will apply a pulsed mirror field (~30-ns risetime) to the plasma and measure the transient potential using a probing electron beam shot down the central axis of the plasma.

We have assembled and conducted preliminary tests on all necessary equipment for Phase I, including the diagnostic apparatus needed to measure plasma characteristics. We have completed the design, fabrication, and testing of a prototype pulser for implementation of Phase II. Our pulser uses Blumlein transmission lines and is fabricated from copper foil and Mylar film; the switching action is performed by mechanical penetration of a sharp metallic point through a replaceable element. This pulser more than met our required specifications, exhibiting pulse risetimes on the order of 2 ns. We have also made progress in terms of theory. We have developed a computer code that traces the trajectory (position and velocity) of an electron or ion beam down the magnetic axis through the space-charge field. This code is useful for both the diagnostic portion of Phase II and for predictions of acceleration in the Mirrortron.

FY88 $207,000

Microcalorimeters for X-Ray Spectroscopy

Principal Investigator: E. Silver
Co-Investigators: S. Labov, F. Goulding,*
N. Madden,* D. Landis,* J. Beeman,*
E. Haller,* and J. Rutledge†

*Lawrence Berkeley Laboratory,
Berkeley, CA
†University of California, Irvine

We are developing new x-ray spectrometers that take advantage of the small heat capacity of their materials at cryogenic temperature to measure the temperature rise associated with the absorption of a single x-ray photon. When operated between 0.1 and 0.3 K, these microcalorimeters will offer the broad bandwidth capability of photoelectric detectors, nearly 100% efficiency between 1 and 10 keV, and the high resolving power of Bragg-crystal x-ray spectrometers.

Cryogenic calorimeters offer high resolving power and sensitivity. Detection of dark matter in the universe and high-resolution stellar x-ray spectroscopy are notable examples of their application. We began an experimental effort two years ago to develop resistive microcalorimeters for studying the x-ray emission from laboratory and astrophysical plasmas.

In principle, an x-ray calorimeter may be any material that exhibits a perceptible temperature increase after it absorbs a single photon. For the temperature rise to be measurably large, the material must possess a small heat capacity. This can be achieved below 1.0 K in crystals with small dimensions, since the volume heat capacity of an ideal crystal drops with the third power of temperature.

Using well-developed infrared bolometric techniques as the foundation for our work, we have constructed prototype calorimeter/spectrometer refrigeration systems to operate at 1.4 and 0.3 K. We have fabricated and studied the properties of both monolithic and composite calorimeters.

In monolithic devices, a single material functions as both x-ray absorber and thermometer. To date, we have fabricated and tested wafers of single-crystal germanium, which have been doped via neutron-induced transmutation. The dopant level defines a well-characterized variation between the sample resistance and temperature.

An x-ray spectrum obtained with a 0.1 × 0.1 × 0.01-cm monolithic germanium sample is shown in Figure 1a. The calorimeter was cooled to 0.3 K and irradiated by a radioactive source of americium-241, which produces neptunium *L* x rays, and fluorescent copper x rays from the backing in the source container. The source also contains some iron-55. The 320-eV resolution is within 20% of that predicted for this device and these operating conditions. Further improvements in resolution will require a reduction in heat capacity, achieved by changing either the materials or the size of the device or by lowering the device temperature.

A spectrum obtained with a much smaller germanium sample (0.025 × 0.01 × 0.01 cm) is shown in Figure 1b. This spectrum shows the manganese $K\alpha$ and $K\beta$ emission lines near 6 keV, which are produced by a source of iron-55. The resolution of 80 eV is 40% better than the best resolution achievable with a lithium-drifted silicon detector (Silver *et al.*, 1988).

We are also developing composite microcalorimeters, in which the x-ray absorber and thermometer are two distinct materials. In our composite design, a thin-film germanium-gold alloy thermometer is evaporated onto a sapphire substrate. The excellent thermal contact between the evaporated thin film and the sapphire should make the thermalization time of this device 50–100 times faster than conventional composite calorimeters used for infrared astronomy. Furthermore, the heat capacity of this device is dominated by the sapphire absorber rather than by the thermistor as in conventional composite designs. We have successfully measured the heat capacity and the time response of a composite calorimeter at 1.0 K. Our measured heat capacity agrees with previous measurements of sapphire to within 10%.

We have also worked on adiabatic demagnetization refrigerators for use in the laboratory and eventually in space. A temperature of <0.05 K has been achieved, and the hold time at 0.1 K is more than 12 hours. To achieve a resolving power of 1000 at an operating temperature of 0.1 K requires a temperature stability of

±8 μK. We have begun work on developing a microprocessor-based servo-control system that will adjust the superconducting magnet current, and thereby the temperature, of the calorimeter to the desired precision. A low-resolution prototype of this controller has been tested, and a stability of ±20 μK has already been achieved. We are confident that the new control system will provide the required temperature stability.

Finally, we have started an investigation of an innovative concept that takes advantage of the temperature dependence of the dielectric constant in ferroelectric materials. A dielectric calorimeter operated with a charge-sensitive preamplifier would have many potential advantages over traditional resistive devices, not the least of which is the reduction of Johnson noise. This would make the energy resolution for photon-counting spectroscopy limited only to the phonon noise. This would also increase the sensitivity over a broader frequency range than is possible with resistive devices, opening the way for development of detectors that can handle higher count rates.

We have fabricated a dielectric-calorimeter proof-of-principle device from strontium-titanate glass ceramic and have operated it at 1.4 K (Silver *et al.*, 1989). We obtained a pulse response from this calorimeter by irradiating it with a short burst of infrared radiation. This response demonstrates that calorimetry with dielectrics is indeed possible. We have obtained two years of funding from the National Aeronautics and Space Administration's Innovative Research Program to continue development of this device.

References

Silver, E., S. Labov, D. Landis, N. Madden, F. Goulding, J. Beeman, E. Heller, J. Rutledge, G. Bernstein, and P. Timbie (1988). "High-Resolution X-Ray Spectroscopy of Cosmic Particles," *Proc. IAU Colloq. 115*, Cambridge, MA, August 22–25 (in press).

Silver, E., S. Labov, F. Goulding, N. Madden, D. Landis, and J. Beeman (1989). *A New Microcalorimeter Concept for Photon-Counting X-Ray Spectroscopy*, Lawrence Livermore National Laboratory, Preprint UCRL-99996; accepted for publication in *Nucl. Instrum. Meth.*

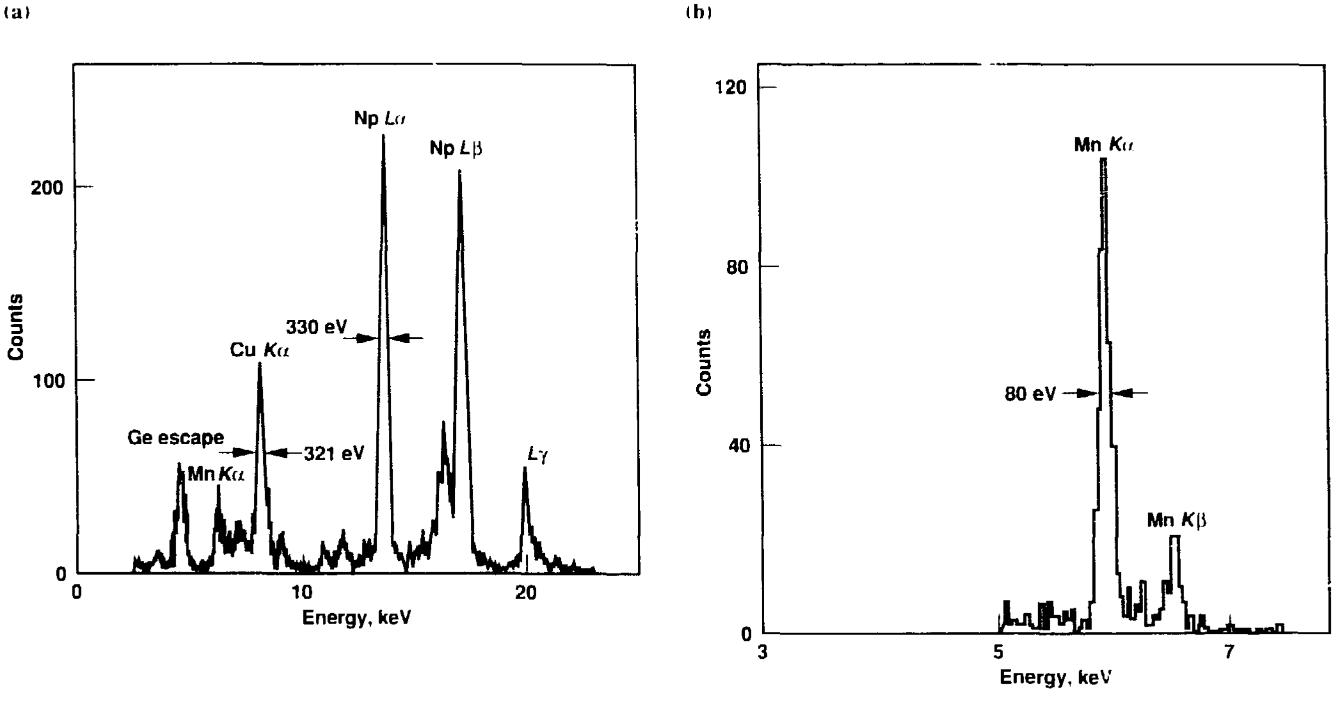

Figure 1. X-ray spectra measured with two monolithic germanium microcalorimeters at 0.3 K. (a) The larger device (crystal dimensions are 0.1 × 0.1 × 0.01 cm); the resolution of this device is within 20% of that predicted for these operating conditions. (b) The smaller device (crystal dimensions are 0.025 × 0.01 × 0.01 cm); the resolution of this device is 40% better than that achievable with a lithium-drifted silicon detector.

FY88 $71,000

Chaos in Amplified Spontaneous Emission

Principal Investigator: J. C. Garrison
Co-Investigators: H. Nathel and
R. Y. Chiao*

*University of California, Berkeley.

We have developed a vector theory of electromagnetic polarization dynamics in media consisting of polar molecules. Numerical simulations to locate the parameter range in which polarization chaos can occur are under way. Our experimental searches will use streak-camera polarimetry that has been demonstrated in the laboratory.

Amplified spontaneous emission (ASE) is the basis for x-ray laser action and occurs naturally in other laser media. Dyes are convenient for ASE experiments, and they are particularly useful for the study of chaos, i.e., the apparently random changes in the polarization or intensity of ASE radiation. Chaotic behavior in ASE is interesting in itself and has practical implications for laser physics.

Dye molecules are polar in that they have definite orientations in space; therefore, the response of a medium depends on the polarization of ASE light. To include this effect, we have augmented our previous theory (Garrison *et al.*, 1988) with a generalized Debye model in which collisions cause the molecular-orientation unit vector to diffuse on the unit sphere at a rate inferred from experiments on induced molecular polarization (Nathel, 1986). For our dyes, the orientational diffusion rate is comparable to the stimulated emission rate and to the inverse of the light transit time across an experimental sample. Under these circumstances, chaotic behavior can be expected in the polarization of the ASE field.

As a first step, we are working on the relatively simple problem of an external signal injected into a dye medium in which an inverted molecular population has been produced by laser pumping. We wrote a numerical simulation program for this case and are now searching for parameter values leading to chaos.

We set up a streak camera with 100-ps resolution for time-resolved polarimetry, and we obtained a master dye oscillator for use in future injection experiments. Figure 1 shows a schematic of our initial ASE experiment. Pump radiation was linearly polarized either transversely (perpendicular to the propagation axis of the ASE beam) or longitudinally (parallel to the ASE axis). In preliminary experiments, we found that transverse pump polarization produced ASE linearly polarized in the same direction. However, for longitudinal pump polarization, there was no preferred ASE polarization direction, and the ASE was unpolarized within the time resolution of the streak camera. This result suggests a form of chaos in which the polarization of the ASE beam wanders rapidly over the Poincaré sphere. This effect might show up as rapid intensity switchings between the fields of the streak camera image, corresponding to different states of polarization. Another possibility would be intermittency, i.e., periods of fixed polarization interrupted by interludes of rapid wandering. Neither switching nor intermittency were seen for the limited range of parameters in this experiment. We will next apply our technique in injection seeding experiments with the master dye oscillator.

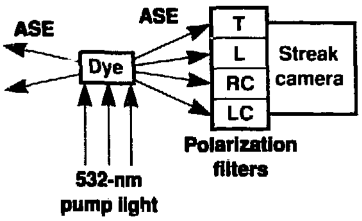

Figure 1. Experimental setup for time-resolved polarimetry. The polarization filters transmit transverse (T), longitudinal (L), right circular (RC), and left circular (LC) polarizations.

References

Garrison, J. C., H. Nathel, and R. Y. Chiao (1988). "Quantum Theory of Amplified Spontaneous Emission: Scaling Properties," *J. Opt. Soc. Amer.* **B5**, 1528.

Nathel, H. (1986). *Development and Application of a High-Powered Broadly Tunable Picosecond Source*, Lawrence Berkeley Laboratory, Berkeley, CA, Report 20446.

FY88 $63,000

Algorithms for the Lamb Shift in High-Z Hydrogen- and Helium-Like Ions

We have reformulated the calculation of the electron radiative self-energy in high-Z hydrogen-like ions. We also developed a quantum electrodynamics approximation scheme that systematically incorporates radiative corrections into the structure of high-Z helium-like ions.

Principal Investigator: N. J. Snyderman

The experimental measurement of the Lamb shift in atomic hydrogen (the $\sim 10^{-6}$-eV splitting of the $2s_{1/2}$ and $2p_{1/2}$ levels that are degenerate in relativistic quantum mechanics) stimulated the development of quantum electrodynamics (QED). For hydrogen-like uranium, on which experiments will be done in the near future, the Lamb shift is expected to be ~100 eV. Since $Z\alpha$ (the nuclear charge times and fine-structure constant) for uranium is no longer the small parameter for perturbative expansion that it is for hydrogen, new calculational methods are required. Because of the magnitude of QED radiative corrections to the inner shells of high-Z atoms, they are no longer small corrections but are necessary for an accurate understanding of the atomic structure of highly stripped ions.

Our objectives were twofold: to explore ways to simplify the calculation of the electron radiative self-energy in high-Z hydrogen-like ions, and to begin to understand how to incorporate this self-energy into multielectron atomic structure by studying it in helium-like ions.

For the hydrogen-like self-energy, we reformulated the calculation in two ways and obtained renormalized algorithms appropriate for computer implementation. In our first algorithm, the best features of the two existing methods for calculating K-shell self-energy were synthesized. (Only one of these methods could obtain the L-shell result.) However, this algorithm still shares with the previous methods the numerical difficulty of obtaining the answer as a small difference of two large numbers. It requires two radial integrations, a partial wave summation, and a photon-frequency integration. In our second algorithm, the subtraction is eliminated at the expense of two additional radial integrations. These new algorithms may be able to calculate M-shell self-energy.

Since the self-energy calculation is most sensitive to distances of the order of the electron Compton wavelength (lc = *h*/*mc*) from the nucleus, penetration by additional bound electrons within this distance (the Bohr radius is $\lambda_c/Z\alpha$) screens the nuclear charge and thus modifies the hydrogenic result. For helium-like ions, this screening, as well as the energy levels in general, can be calculated by QED perturbation theory in the background nuclear Coulomb field. We have derived renormalized formulas appropriate for computer implementation for all Feynman graphs of order α^2: these formulas account for electron correlations and screening corrections to the Lamb shift. In principle, their evaluation will give the energy levels of helium-like uranium to ~0.1 eV (1 part in 10^6) if detailed nuclear-structure corrections can be shown to be small enough. The helium-like system offers a conceptually clean foundation on which to build an accurate understanding of high-Z ions with few electrons.

References

Brown, G. E., J. S. Langer, and G. W. Schaefer (1959). "Lamb Shift of a Tightly Bound Electron." *Proc. Roy. Soc. London. Ser.* A **251**, 105.

Mohr, P. J. (1974). "Self-Energy Radiative Corrections in Hydrogen-Like Systems." *Ann. Phys. (N.Y.)* **88**, 26.

Mohr, P. J. (1982). "Self-Energy of the $n = 2$ States in a Strong Coulomb Field." *Phys. Rev.* A **26**, 2338.

Mohr, P. J. (1985). "Quantum Electrodynamics of High-Z Few Electron Atoms." *Phys. Rev.* A **32**, 1949.

Snyderman, N. J. (1988). *Relativistic Atomic Structure I*. Lawrence Livermore National Laboratory, Report UCID-21577.

Stewart, R. E., and C. J. Hailey (1986). *Lamb Shift Measurements in Uranium*. Lawrence Livermore National Laboratory, Report UCRL-63689-86

Density Fluctuations in the Big Bang and the Dark Matter Problem

Principal Investigators: G. Fuller, C. Alcock, and G. J. Mathews

We have investigated the production of density fluctuations in the early universe from a phase transition between unconfined quark-gluon plasma and a gas of bound hadrons. Our calculations show that the universe may be closed by ordinary baryons, a result that differs from the standard model of the Big Bang which requires massive neutrinos or other exotic, weakly interacting particles for closure.

A central question in modern astrophysics is the dark matter problem: if the universe is closed (as most astrophysicists believe), then up to 99% of the mass of the universe is in unseen "dark" matter. It has been thought that this matter cannot be ordinary baryons (e.g., neutrons, protons, and other heavy nuclear particles) because, if it were, the process of primordial nucleosynthesis in a standard, homogeneous, Big Bang would seriously underproduce deuterium.

We are investigating (Alcock *et al.*, 1987; Fuller *et al.*, 1988) an alternative to the standard Big Bang model. Our work has focused on (1) the production of density fluctuations in the primordial quark-hadron transition, (2) the subsequent evolution of these fluctuations, including their effects on primordial nucleosynthesis, and (3) a reconciliation between the abundances of the light elements predicted in a universe closed by baryons and their observed abundances in the galaxy.

When the universe is at a temperature greater than $T_c \approx$ 100 MeV, it consists of a plasma of unconfined quarks, gluons, and other light particles (T_c is the phase-coexistence temperature). Present theoretical analyses point to a weak first-order phase transition from the unconfined plasma to a confined gas of hadrons (protons, neutrons, pions, hyperons, etc.). Since the solubility of the baryon number is higher in the quark phase than in the hadron phase, the small net baryon number in the universe tends to be concentrated in lumps that correspond to the shrinking bubbles of quark-gluon plasma. We have done detailed baryon-number transport calculations for this epoch to ascertain the spatial distributions and shapes of the fluctuations left over after the quark-gluon bubbles have shrunk away and the entire universe has been converted to bound hadrons.

As the universe expands and cools after the quark-hadron transition, the fluctuations tend to be preserved until the temperature falls below the weak-interaction decoupling temperature $T_{wk} \approx 1$ MeV. Subsequently, the neutrons begin to diffuse out of the fluctuations, so that by the time the temperature has fallen low enough for nucleosynthesis to begin ($T_{nuc} \approx 0.1$ MeV), the universe consists of dense proton-rich regions and tenuous neutron-rich regions.

Our efforts to model the process of nucleosynthesis are complicated by the fact that as neutrons are used up in nuclear reactions in the high-density regions, neutrons diffuse back in from the low-density areas. Furthermore, this neutron-diffusion time scale is comparable to the nucleosynthesis time scale. We find that for an appreciable range of the parameters that characterize the fluctuations, our models yield D, ^{3}He, and ^{4}He abundances that are in agreement with observations, even if the universe is closed by baryons. However, ^{7}Li seems to be overproduced relative to the standard Big Bang by a factor of 50.

The ^{7}Li overproduction is potentially a problem for this model. We plan to study the ^{7}Li abundance evolution in the galaxy to see whether current observations could be compatible with a high primordial ^{7}Li abundance.

References

Alcock, C. R., G. M. Fuller, and G. J. Mathews (1987), *Astrophys. J.* **320**, 439.
Fuller, G. M., G. J. Mathews, and C. R. Alcock (1988), *Phys. Rev. D* **37**, 1380.

FY88: $269,000

Multiphoton Ionization of Atoms in Strong Fields

We are investigating the role of bound-state resonances in the multiphoton and above-threshold ionization of atoms in strong laser fields.

Principal Investigators: M. D. Perry, A. Szöke, and O. L. Landen

The goal of our research is to understand the response of an atom to an applied field with a strength comparable to that of the atomic Coulomb field. Such an applied field is too strong to be considered a weak perturbation on the atomic system. Our work in FY88 continues earlier studies on the multiphoton ionization of atoms subjected to strong laser fields.

Multiphoton ionization of an atom by an intense laser field is the process by which the atom is ionized by absorbing two or more photons from the laser field, each single photon having an energy that is insufficient to ionize. The process may be purely nonresonant or it may be enhanced by an intermediate resonance. At low laser intensities (<10^{12} W/cm^2), both nonresonant and resonantly enhanced multiphoton ionization are well described by perturbation theory. As the strength of the applied field increases, several phenomena emerge that cannot be explained within the framework of lowest-order perturbation theory. Examples include the well-known phenomenon of tunneling ionization and the more recently observed above-threshold ionization, defined as that occurring when an atom absorbs more photons than the minimum required for ionization.

Our initial work on nonresonant multiphoton ionization (Perry *et al.*, 1988b) shows that the tunneling ionization theory of Keldysh, Faisal, and Reiss predicts reasonably accurate values of the ionization probability of neutral atoms at a given laser intensity. We extended this theory to account for distortion of the outgoing electron by the Coulomb field of the residual ion and found remarkable agreement between the theoretical and experimental results with no adjustable parameters (Perry *et al.*, 1988c).

Exploiting the tunability of our short-pulse, dye-laser system, we investigated the influence of intermediate resonances on the multiphoton ionization probability (Landen *et al.*, 1987). We observed significant resonant enhancement in the multiphoton ionization of krypton near the $4d'$ and $5d$ manifolds at intensities approaching 10^{14} W/cm^2 (Figure 1). Using a two-level-plus-continuum model of the krypton atom, we were able to deduce the three-photon excitation rate to members of the $4d'$ and $5d$ manifolds. We were also able to determine the photoionization cross sections and ac Stark shifts of these states (Landen *et al.*, 1987; Perry and Landen, 1988).

In FY88, we began measuring the energy distribution of the electrons emitted during multiphoton ionization in addition to the ion charge states produced. This work extended our ability to make quantitative measurements of atomic parameters because the energy with which the photoelectron is detected is a direct measurement of the laser intensity at which it is produced (Perry *et al.*, 1988a). This phenomenon is a result of the

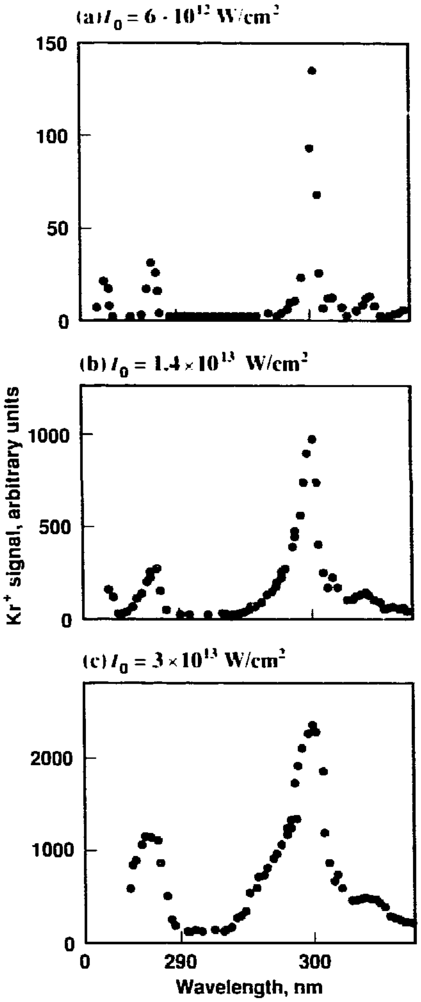

Figure 1. Relative yield of singly charged krypton ions as a function of laser wavelength at various peak intensities. Vertical lines mark the field-free positions of dipole-allowed, three-photon resonances in neutral krypton.

(a) Resonance positions

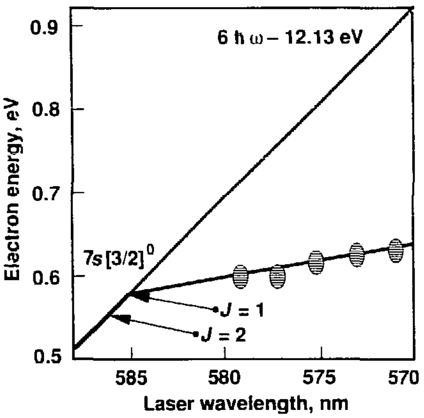

(b) Observed spectrum

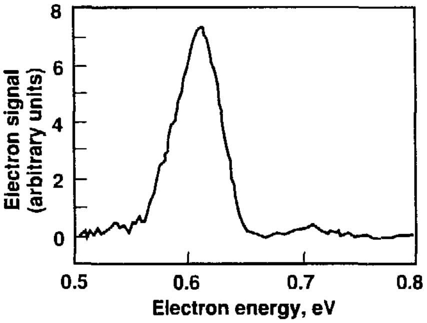

Figure 2. (a) The observed position of the resonances originating in the $7s[3/2]^0$ levels of xenon. The nearly horizontal line corresponds to an ac Stark shift equal to that of a free electron. The Stark shift is in good agreement with the observed shift of the resonance position. (b) One of the observed spectra.

ponderomotive potential present at the laser focus, which alters the ionization potential of the atom according to

$$IP(I) \sim IP(0) + U_p(I) \ ,$$

where $IP(0)$ is the ionization potential of the atom in the absence of the field and $U_p(I) = 9.33 \times 10^{-14}$ I (W/cm^2) λ^2 (μm) is the intensity-dependent ponderomotive potential in electron volts (Szöke, 1985).

The shift in the ionization potential of the atom from its field-free value can be observed only by using lasers that have a pulse width significantly shorter than the time required for the electron to leave the laser focus. For the vast majority of experiments, the pulse width would have to be in the picosecond or subpicosecond range. The shifts were easily observable with our short-pulse, dye-laser system. By tuning the frequency of the laser near-allowed five- and six-photon resonances, we obtained a direct measurement of the shifts of the intermediate levels as a function of laser intensity (Szöke *et al.*, 1988). Figure 2 shows the results of our measurements.

This area of research continues to expand as experimental capabilities improve and higher laser intensities become available. One recent, important advance was the nonperturbative production of extremely high harmonics of the incident laser light with surprisingly high conversion efficiency. By using a tunable laser to generate such harmonics in pulsed gas jets, one might obtain an efficient, compact source of tunable extreme-ultraviolet radiation with a source brightness equal to that of a synchrotron. A study of this phenomenon and further investigation of resonantly enhanced multiphoton ionization using extremely high-resolution photoelectron spectroscopy constitute our work in this field for the next year.

References

Landen, O. L., M. D. Perry, and E. M. Campbell (1987), *Phys. Rev. Lett.*, **59**, 2558.

Perry, M. D., and O. L. Landen (1988), *Phys. Rev. A*, **38**, 2815.

Perry, M. D., O. L. Landen, and A. Szöke (1988a), Lawrence Livermore National Laboratory, Report UCRL-98960.

Perry, M. D., O. L. Landen, A. Szöke, and E. M. Campbell (1988b), *Phys. Rev. A*, **37**, 747.

Perry, M. D., A. Szöke, O. L. Landen, and E. M. Campbell (1988c), *Phys. Rev. Lett.*, **60**, 1270.

Szöke, A. (1985), *J. Phys. B*, **18**, L427.

Szöke, A., O. L. Landen, and M. D. Perry (1988), Lawrence Livermore National Laboratory, Preprint UCRL-99422.

FY88: $119,000

Atomic Physics Studies at the LBL ECRIS

Principal Investigator: P. O. Egan
Co-Investigators: S. Chantrenne and M. H. Prior*

*Lawrence Berkeley Laboratory,
Berkeley, CA.

We are measuring cross sections for electron-impact excitation in multiply charged ions with an electron-energy-loss spectrometer. The spectrometer, along with a connecting atomic physics beamline, has been built at the Lawrence Berkeley Laboratory electron cyclotron resonance ion source (ECRIS).

Electron-impact excitation of multiply charged ions is an important process in many of the high-temperature plasmas studied at LLNL, such as those in laser and astrophysics work. However, there are virtually no experimental data on excitation cross sections for ions more than singly or doubly ionized. This lack forces us to rely on theoretical calculations for cross sections. For instance, the inclusion of complex, indirect processes (recombination-excitation-autoionization) for a simple system such as lithium-like oxygen (O^{5+}) is predicted to change the cross sections for dipole forbidden processes by a factor of four near threshold, yet this effect has never been verified experimentally.

We have built a low-energy, atomic physics beamline at the Lawrence Berkeley Laboratory (LBL) ECRIS so that we can measure electron-impact excitations in multicharged ions (see Figure 1). The cross sections will be measured with a merged-beam, electron-energy-loss spectrometer (EELS) that we have also built as part of this project.

The ECRIS is a relatively new development in ion-source technology that produces high currents (1–10 μA) of highly stripped ions. The source itself is essentially a magnetic mirror plasma that is heated solely by microwaves at the electron cyclotron resonance frequency. Originally developed as an injector for nuclear physics experiments at the cyclotron, ECRIS has become a useful tool for atomic physics with our addition of a low-energy (10-keV) beamline that runs parasitically on the cyclotron.

With EELS (Figure 2), we can measure the electrons that lose energy after excitation and hence determine the cross sections not only for optically allowed but also for optically forbidden transitions. EELS uses trochoidal analyzers (crossed electric and magnetic fields) to merge an electron beam with the ion beam from ECRIS and then to demerge the electrons and analyze their energy. The long merged-beam interaction region and the use of a position-sensitive detector increase the sensitivity of EELS over more conventional techniques used for singly ionized systems. Also, EELS detects all electrons that interact, rather than just a small fraction of fluorescent photons, increasing the counting efficiency and broadening the number of excitations that can be observed by allowing us to look at states that do not have a dipole-allowed transition back to the ground state.

EELS was installed at ECRIS in the spring of 1988; it can be seen in the foreground of Figure 1. Initial beam tests with multiply charged ions have shown that the currents and beam-spot sizes are as expected; for example, we can produce several microamperes of O^{5+} in a 2-mm-diam, 20-cm-long interaction region. The ion beam has been successfully merged in this region with a 100-eV electron beam.

The major challenge that faces the project now is to separate the signal of energy-loss electrons, which is expected to be about several hundred counts per second, from extraneous background counts in the detector that arise from other processes producing low-energy electrons. For example, even in the spectrometer's ultrahigh vacuum ($\sim 4 \times 10^{-8}$ Pa), the electron and ion beams interact with the background gas to ionize it, giving a low-energy electron signal that can mask the true signal. Or, a poorly tuned ion beam can scrape on an aperture, again producing unwanted low-energy electrons.

Our present experimental effort at LBL is directed toward finding the beam operating conditions that minimize such background effects. In addition, we are studying other ways to improve the experiment's signal-to-noise ratio. One approach is to redesign the trochoidal analyzers to avoid beam aberrations and add more pumping capacity to reduce the residual-gas problem.

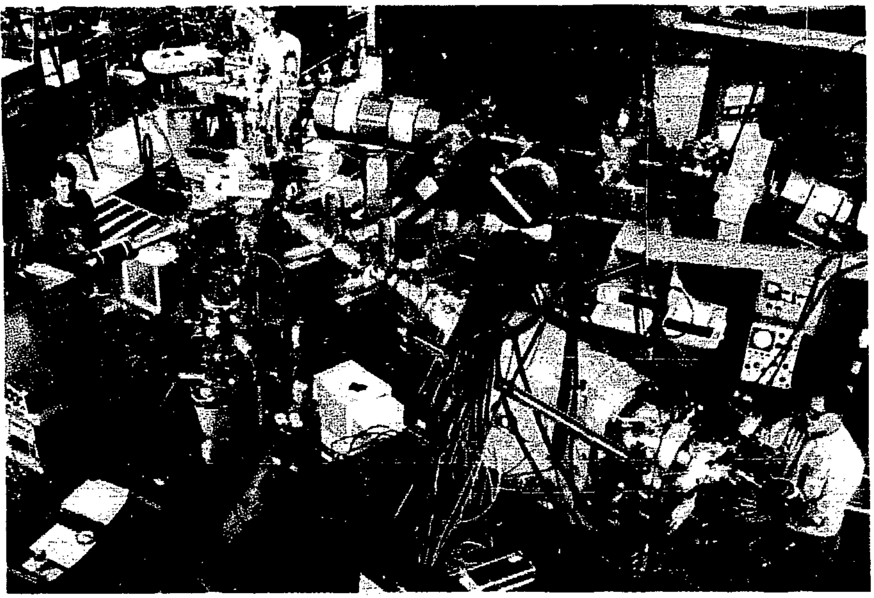

Figure 1. Atomic physics area at ECRIS. The source is in the upper left corner of the photograph; the atomic physics beamline and EELS are in the foreground.

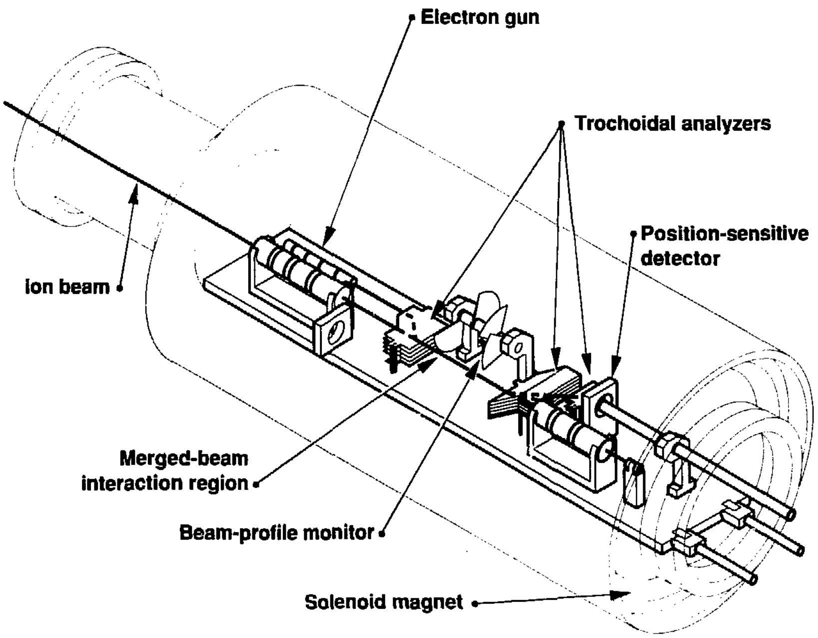

Figure 2. Electron-energy-loss spectrometer (EELS). An electron beam from the electron gun merges with an ion beam from ECRIS at the first trochoidal analyzer. A second analyzer extracts the electrons, and the position-sensitive detector measures those electrons that have lost energy by exciting ions in the merged-beam interaction region.

An important corollary to the experiment is to model the exact behavior of low-energy electrons in complex electric and magnetic fields. We have developed a set of computer codes that allows us to solve the problem of merging the two beams without imparting unwanted transverse energy to the electron beam. These codes are also used to model the expected low-energy electron trajectories in the analyzer plates and the resulting signal on the detector.

Our initial plans were to measure the cross section for $n = 2 \rightarrow n = 3$ excitation in lithium-like oxygen and then to continue to explore the lithium-like sequence at higher Z. Since these cross sections are rather small, typically 10^{-18} cm^2, it will be difficult to study the systematics or parameters of the experiment with the present background-noise level. Instead, we now intend to concentrate on the $Dn = 0$ transitions in the O^{5+} system, where the cross sections are closer to 10^{-16} cm^2; this will improve the signal-to-noise ratio and allow us to better understand the systematics.

Reference

Clark, D. J., *et al.* (1989). "The Atomic Physics Facility at the LBL ECR Source." *Nucl. Instrum. Meth.* (in press).

X-Ray Spectroscopy of Highly Ionized Atoms

We used axial observation of a recoil-ion source to produce x-ray spectra of highly charged ions with the best resolution achieved to date.

Principal Investigators: D. Dietrich and J. Silver*
Co-Investigators: A. Simionovici, W. Hallett,* J. M. Laming,* and S. Lea*

*Clarendon Laboratory, Oxford University, England.

By bombarding a monatomic gas with a very highly charged, fast-ion beam, one can produce slow, electronically excited, highly charged ions in sufficient quantities to allow very precise x-ray spectroscopy. We take advantage of the directed nature of these recoil ions to obtain spectra of hydrogen-like and helium-like argon ions with very high resolution.

Such ions are produced in collisions with impact parameters of the order of the "radius" of the 1*s* electron orbit. The angular deviation from scattering perpendicular to the incident ion beam is very small: for example, in an Ar^{16+} recoil-ion source produced by bombarding argon gas with 2-GeV U^{70+} ions, it is a mere 1 mrad. This produces Doppler shifts of only 0.1 ppm, some three orders of magnitude smaller than with perpendicular viewing, so that the Doppler widths are characteristic of the temperature of the gas from which the ions were formed.

Several experiments using this technique were performed at Oxford's 10-MV tandem accelerator (Laming and Silver, 1987) and recently at the Lawrence Berkeley Laboratory's SuperHILAC. A stripped beam of gold or xenon at 8.6-MeV/amu was directed into a 1-m-long argon-gas target maintained at 1 Torr. A slit at the end of the target formed the entrance to a Johann x-ray spectrometer. The spectrum was normalized to the charge collected from the ion beam.

Figure 1 shows two x-ray spectra taken with different entrance-slit widths (and therefore different resolutions) for the $1s^2\,{}^1S_0{-}1s2p\,{}^{1,3}P$ transitions in helium-like argon. The spectrum taken at a low resolution of ~2000 (a) has the characteristic appearance seen in earlier work. By reducing the width of the entrance slit, we obtained higher resolution. The best resolution achieved was ~5000 for the $1s^2\,{}^1S_0{-}1s2P\,{}^1P_1$ transition of helium-like Ar^{16+} (b), which exceeds that obtained by Deslattes *et al.* (1984), the best-resolved published spectrum of this ion. Unfortunately, the statistical quality of our spectra is not as good: as resolution improves, our spectra break into a number of lines which we believe are satellites to helium-like transitions arising from ions of lower charge. One reason for this could be the different excitation of the spectra. In Deslattes *et al.*, very highly charged uranium ions were used to generate the recoil ions. We were unable to use the SuperHILAC's intense uranium beam, which would have given a higher yield of helium-like argon and a lower yield of satellites.

We conclude, therefore, that our new technique gives the best resolution achieved to date in the x-ray spectroscopy of highly charged ions. However, further work with incident beams of uranium ions is required if we are to properly compare this technique with other work or to apply it to accurate measurement in the ions studied.

References

Deslattes, R. D., H. F. Beyer, and F. Folkmann (1984), *J. Phys.* **B17**, L689.

Laming, J. M. and J. D. Silver (1987), *Phys. Lett. A* **123**, 395.

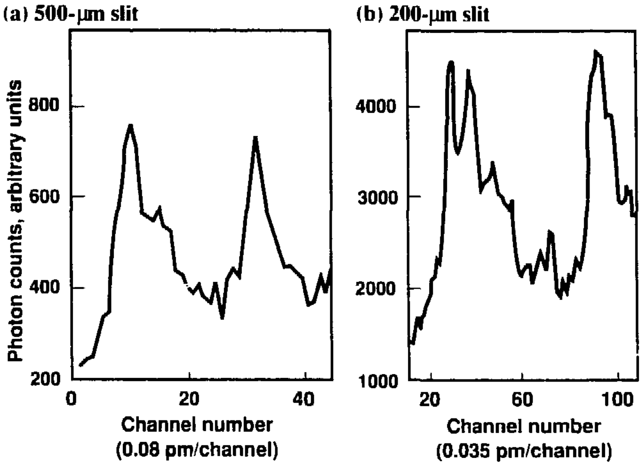

Figure 1. Two x-ray spectra for $1s^2\,{}^1S_0{-}1s2p\,{}^{1,3}P$ transitions in helium-like argon. (a) A 500-µm entrance slit yields a resolution of 2000. (b) A 200-µm entrance slit produces a resolution of 5000; note the increased detail in peak features.

A Multiple-Object Spectrograph for Astronomical Observations

An instrument is being developed for use on the 120-in. telescope at Lick Observatory that will permit simultaneous acquisition and observation of up to 100 object spectra over a 1-deg field of view. The resulting increase in telescope efficiency will allow us to conduct research that would otherwise be impossible using conventional instruments.

Principal Investigator: C. J. Hailey
Co-Investigators: J. P. Brodie,* and R. E. Stewart

*Lick Observatory, University of California, Santa Cruz.

All of the world's major telescopes are oversubscribed, especially for nighttime viewing. Observations with conventional telescopes focus on one object or specific region of the sky at a time. If, however, the spectra of many objects could be observed simultaneously, telescope efficiency would be dramatically increased.

We are building a multiple-object spectrograph (MOS) to observe separately many individual objects in the telescope's 1-deg field of view. Up to 100 optical fibers can be individually positioned to collect light from objects of interest. The input end of each fiber is placed at the focal plane of the telescope; the output end mates with the input slit of a spectrograph, which is coupled to an image intensifier.

The quality of the spectrographic results depends greatly on the

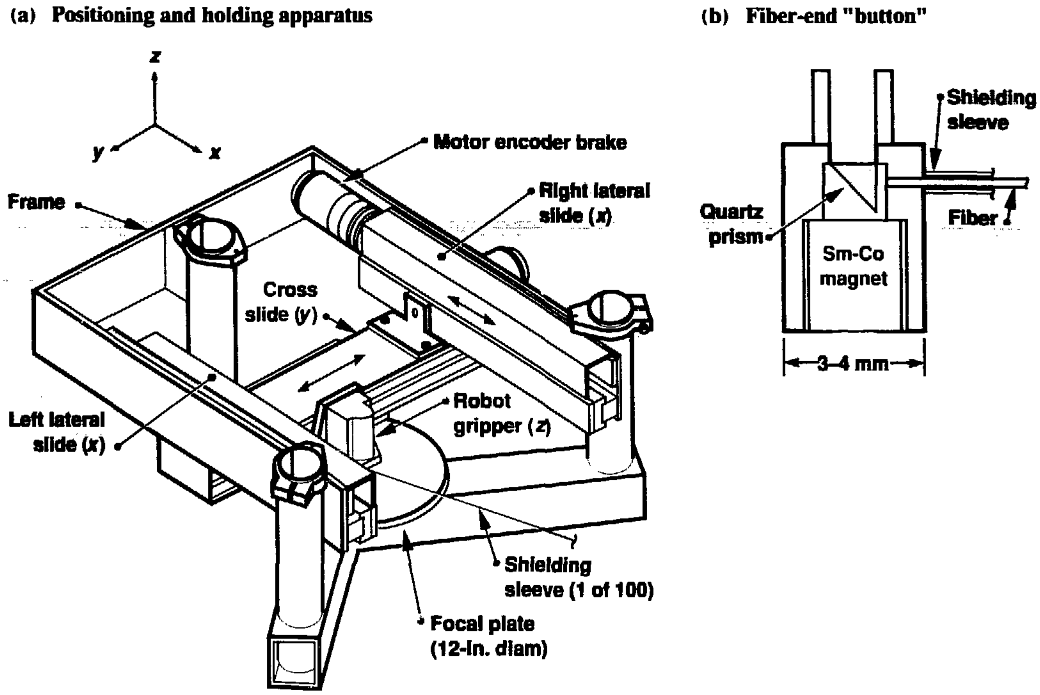
(a) Positioning and holding apparatus

(b) Fiber-end "button"

Figure 1. Diagram of the apparatus for positioning and holding the optical-fiber ends (a). Up to 100 fibers can be positioned and focused to collect spectra. Lateral sliders (*x* motion) hold a cross slide (*y* motion) between them. A robot gripper (*z* motion) lifts and emplaces the fiber "button" (b) on the focal plate of the MOS. A magnet in the base of the button holds it securely on the focal plate.

precision with which the fiber end can be pointed at the object to be observed. Each fiber end must be positioned with an accuracy of greater than 10 µm in order to properly collect the light of the object of interest. We have built a positioning and holding system that is accurate to better than 10 µm in any orientation. This apparatus (Figure 1a) uses a robot gripper for three-dimensional positioning of the fiber ends; each fiber end is mounted in a "button" (Figure 1b).

The light collected by each optical fiber is detected by a spectrograph, which is coupled to an image intensifier. We have built and conducted preliminary tests on a large-area optical image intensifier with good quantum efficiency. The large-format detector is essential for simultaneously recording the spectra of many objects in real time.

Additional research has been done to develop techniques for accurately positioning and mounting the prism and film in the "button." This is essential to ensure maximum efficiency in the coupling of light to the spectrograph. It requires use of sophisticated, interactive laser-alignment and micromanipulation techniques.

Finally, we have carefully studied the effects of atmospheric dispersion on our ability to perform precision spectroscopy, and have developed the necessary techniques to compensate for this effect.

With the fabrication of our spectrograph/camera nearing completion, we expect to begin evaluating the MOS at Lick Observatory in early FY89.

FY88 $115,000

Theoretical Studies of High-Temperature Superconductors

Principal Investigators: N. Winter and M. Ross

We are using advanced calculational methods to determine the electronic structure of $La_{2-\delta}Sr_{\delta}CuO_4$, $YBa_2Cu_3O_{7-\delta}$, and related new superconductors and thereby gain a better understanding of the mechanisms responsible for superconductivity in these materials. The theoretical models developed in this study will also help us to predict new superconducting materials.

To understand the mechanisms responsible for high-temperature superconductivity, we must be able to calculate accurately the electronic structure in a superconducting material, including the effects of electron correlation, electron phonon interactions, and electron-spin coupling. The goal of this research is to determine the electronic structure of $La_{2-\delta}Sr_{\delta}CuO_4$, $YBa_2Cu_3O_{7-\delta}$, and related compounds using advanced theoretical methods and computer codes.

Specifically, we are using an *ab initio* Hartree-Fock (HF) cluster approach that calculates the exchange interactions, instead of approximating them as is done in the more conventional electron-band-theory calculations. By including configuration interaction (CI), we can incorporate the electron-correlation and spin-coupling effects that are important in high-temperature superconducting materials.

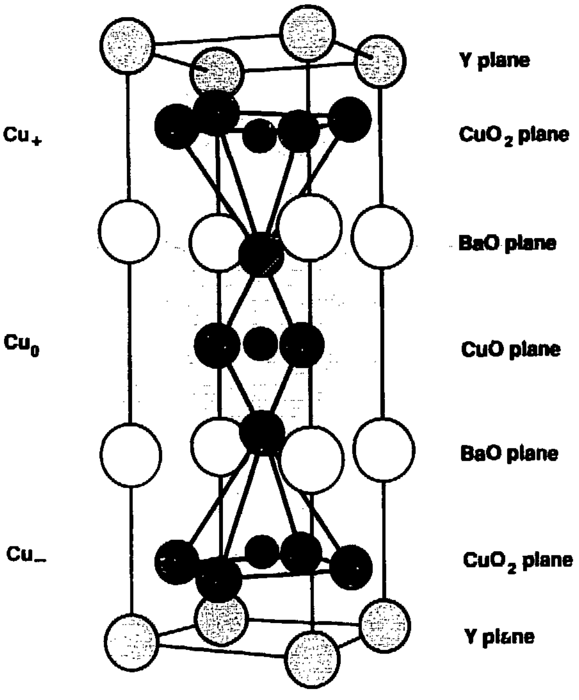

Figure 1. The unit cell structure for $YBa_2Cu_3O_7$. The three Cu sites in the unit cell (Cu_+, Cu_0, and Cu_-) are shown in color.

We began by studying $YBa_2Cu_3O_7$, one of the more promising high-temperature superconductors; its orthorhombic unit cell structure is shown in Figure 1. Assigning formal charges to the ions and imposing charge neutrality requires that of the three Cu ions in the unit cell (Cu_+, Cu_0, and Cu_-), one must be trivalent and the remaining two must be divalent. This can be described by a CI wavefunction Ψ of the form

$$\Psi = c_0 \,|\, Cu_+^{2+}\, Cu_0^{3+}\, Cu_-^{2+} >$$
$$+\, c_+ \,|\, Cu_+^{3+}\, Cu_0^{2+}\, Cu_-^{2+} >$$
$$+\, c_- \,|\, Cu_+^{2+}\, Cu_0^{2+}\, Cu_-^{3+} > .$$
$$\Psi = c_0\Psi_0 + c_+\Psi_+ + c_-\Psi_- .$$

where c_0 and $c_\pm$ are mixing coefficients that determine the amount of trivalent character at each Cu site. The four O^{2-} ions surrounding each Cu site are not shown explicitly above but are included in the calculations.

The $\Psi_\pm$ components of the ground-state wavefunction represent charge-transfer configurations where an electron has moved from one of the CuO_2 planes to the CuO chain, leaving behind a mobile hole, which gives rise to the intrinsic metallic behavior observed in $YBa_2Cu_3O_7$. This is in sharp contrast to the results obtained from band theory, which predict that strong bonding and antibonding interactions between Cu^{2+} and O^{2-} orbitals give rise to the metallic nature of the CuO_2 planes.

The values of the mixing coefficients c_i are related to the carrier density. Charge transfer within the CuO_2 planes is also included but does not lead to charge carriers.

The CuO chains evidently serve as a reservoir of holes for the CuO_2 planes. This helps explain the observed sensitivity of the superconducting transition temperature of $YBa_2Cu_3O_{7-\delta}$ to the integrity of the CuO chains. The role of the CuO chains is similar to that of the Sr^{2+} ions in doped $La_{2-\delta}Sr_{\delta}CuO_4$ and the BiO and TlO planes in the Bi-Ca/Sr-Cu-O and Tl-Ca/Ba-Cu-O superconductors.

To obtain a qualitative understanding of the nature of the CuO bonds when Cu has a 2+ or 3+ valence, we made HF molecular-orbital calculations on the linear cluster O-Cu-O-Cu-O-Cu-O. We found that a net charge on the cluster of 2–, appropriate for the CuO_2 planes of La_2CuO_4 or $YBa_2Cu_3O_7$, corresponds to a formal valence of O^{2-} and Cu^{2+}. Also, a net charge of 1+ corresponds to oxidation of the Cu ions to the 3+ valence, which is consistent with the CuO chains in $YBa_2Cu_3O_7$. The $3d$, $4s$, and $4p$ orbitals on the Cu ions and the filled $2p$ orbitals on the O ions participate in the formation of bonds and/or charge transfer; thus, calculated charges can differ significantly from these formal charges.

Initially, each Cu^{2+} ion has eight closed-shell electrons and one open-shell electron with the configuration $3d^9 4s^0 4p^0$. In terms of the atomic orbitals, this leads to the following configurations:

(a) $d^9 4s^0 4p^0 2p^6$

(b) $d^9 4s^1 4p^0 2p^5$

(c) $d^9 4s^0 4p^1 2p^5$

(d) $d^{10} 4s^0 4p^0 2p^5$

The HF wavefunction is dominated by configuration (a), with contributions from (b) and (c) that allow the O^{2-} ions to stabilize their filled $2p$ shell by hybridizing with the empty $4s$ and $4p$ orbitals. A population analysis of the HF wavefunction shows that the three singly occupied levels in the cluster correspond to Cu $3d$ orbitals. The holes are not constrained to the Cu^{2+} $3d$ orbitals but can transfer to the O^{2-} $2p$ orbitals by mixing with configuration (d). There is little evidence of this in the high-spin-coupled planar or linear clusters due to the unfavorable exchange interaction between O^1 $(2p^5)$ and its second near-neighbor $Cu^{2+}(3d^9)$. The singly occupied $3d$ orbitals on Cu^{2+} can be coupled antiferromagnetically to give the ground-state electronic structure observed for the CuO_2 planes in La_2CuO_4 and $YBa_2Cu_3O_6$. In this case, the open-shell electrons are singlet-coupled, and the contribution from configuration (d) increases. This has been verified by calculating the nuclear quadrupole resonance lines for the Cu sites and comparing to experiment.

By removing three open-shell electrons from the cluster, we investigated the bonding in O-Cu($3d^8$)-O-Cu($3d^8$)-O-Cu($3d^8$)-O chains. In this case, the O^{2-} ions *do* strongly hybridize with the empty $3d$ orbitals on the Cu^{3+}. The total gross populations indicate that ~0.65 electrons are transferred to the Cu^{3+}, with the majority going into the $3d$ orbital. In contrast, only ~0.1 electrons are transferred to the Cu^{2+} in calculations on O-Cu($3d^9$)-O-Cu($3d^9$)-O-Cu($3d^9$)-O.

Another, more realistic calculation was carried out that included all the valence electrons in the unit cell cluster (see Figure 1) plus those from the near-neighbor ions in surrounding cells. By including the valence electrons from adjacent ions, we were able to impose the correct boundary conditions on the ions that are only partially in the cell. The population analysis of the HF wavefunction predicts the following atomic charges:

Y planes: $Y^{2.92+}$

CuO_2 planes: $Cu^{1.40+}$ $O_x^{1.64-}$ $O_y^{1.66-}$

BaO planes: $Ba^{1.97+}$ $O^{1.45-}$

CuO chains: $Cu^{1.35+}$ $O^{1.40-}$

The Cu-O bonding is indicative of Cu $3d^8$ in the chains and of Cu $3d^9$ in the planes.

We are now using these cluster wavefunctions to calculate the nuclear quadrupole and nuclear magnetic resonance spectra of $^{63,65}Cu$ and ^{17}O, as well as vibrational frequencies, positron anihilation cross sections, and Mossbauer spectra. These wavefunctions will also serve as a starting point for the CI calculation of the real-space pairing energies of the mobile holes in the CuO_2 planes.

FY88 $175,000

Laser Cooling of Positronium

Principal Investigator: K.-P. Ziock
Co-Investigators: C. D. Dermer, E. P. Liang, R. Howell, K. M. Jones,* and F. Magnotta

We apply the technique of laser cooling to positronium produced at the LLNL linac. Cooling improves the accuracy of fundamental measurements on positronium; it is also necessary for the creation of a gas-phase Bose-Einstein condensate—a new state of matter that may allow the stimulated production of annihilation gamma radiation.

Positronium (Ps) is the hydrogen-like bound state of an electron-positron pair. The study of Ps is complicated by the small amount available, its short lifetime (142 ns for the longest-lived ground state), and its high thermal velocity (~10^7 cm/s). Our goal is to take room-temperature Ps produced at the LLNL electron linear accelerator (linac) and use laser cooling to lower its temperature to ~1 K.

Precise measurements of the fundamental properties of Ps are currently limited by its high thermal velocity. Ps cooled to near absolute zero would help solve this problem. It has also been suggested that a new state of matter—a low-density Bose-Einstein condensate—might form from the gas phase of cold Ps. Stimulated annihilation gamma radiation could be produced using such a condensate (Liang and Dermer, 1988).

The ground state of Ps consists of a short-lived (125-ps) singlet and a longer-lived (142-ns) triplet spin state. We perform cooling on the 1^3s–2^3p transition of Ps due to the longer lifetime of the triplet state. This involves irradiating half the Doppler profile of the cooling transition with broadband laser light tuned to frequencies below the resonance frequence. For optimum cooling, the laser must produce high-intensity, broadband, ultraviolet light (~0.7 nm FWHM, 243 nm) with a duration of approximately one triplet lifetime and with a sharp cut-off at the high-frequency edge.

This year, we verified that we could create a light pulse with the required frequency and intensity profiles; we also verified that no unexpected losses occur from the Ps cooling transition. We used the frequency-doubled output of an excimer-pumped dye laser, modified to give the desired bandwidtn. Laser light is passed in front of a heated copper target that is being exposed to the linac's low-energy positron beam. Thermal Ps boils off the heated copper surface. The interaction region, where the laser beam passes through the resulting Ps gas, is monitored with a collimated gamma-ray detector to measure the annihilation radiation from the Ps.

The laser light affects the Ps annihilation rate in two ways. First, excitation to states with longer annihilation lifetimes decreases the overall Ps annihilation rate. Second, the weak ~200-G magnetic field used to focus the positron beam causes a slight mixing of the singlet and triplet spin states of excited-state Ps but leaves the ground state unaffected. Any Ps in the singlet excited state decays to the singlet ground state, from which it annihilates in 125 ps; this increases the observed Ps annihilation rate. We use the change in annihilation rate resulting from these two effects to monitor the degree of optical saturation of the $1s$–$2p$ transition.

Both laser-on and laser-off annihilation time profiles are recorded. The laser-off profile provides the background spectrum; the difference between the laser-on and laser-off profiles shows the effect of the laser. The increase in annihilation rate due to the laser and the magnetic field is clearly visible in the spectra in Figure 1. Examination of the effects of laser intensity, polarization, and magnetic field strength on such time profiles reveals that we have indeed attained sufficient laser intensity in a bandwidth required for cooling. This work also represents the first time that any $1s$–$2p$ transition in Ps has been optically saturated

We also developed a method for determining the degree of cooling achieved. This measurement is

---

*Williams College, Williamstown, MA.

performed by exciting the cold Ps out of the $2p$ state into higher-lying (Rydberg) levels. Near the end of the cooling pulse, we expose the Ps to narrow-bandwidth red light that is tuned to interact only with the cooled atoms. The (cooled) Ps excited by the red light is detected, using field ionization, and a comparison of the amount of Ps excited with and without the cooling laser pulse provides a measure of the number of cooled Ps atoms.

In a preliminary test of this technique, we achieved excitation of Ps to the $n = 13$–15 excited states. The system was simultaneously exposed to ultraviolet light tuned to the 1^3s–2^3p transition and to red light from a second dye laser. The variation of the annihilation rate as a function of red-laser frequency was used to verify excitation to the Rydberg levels. A characteristic signature of the annihilation time profile was observed when the red light was tuned to a $2p$–nD resonance. This represents the first time that any excited state of Ps other than the $n = 2$ level has been observed.

All of our work to date has been done with a 10-ns-pulse laser. For cooling to occur, the excited state must decay spontaneously about 50 times. Thus, the 3.2-ns decay lifetime of the Ps excited state requires a laser-pulse duration of approximately 150 ns. In the coming year, we will install a new laser with the required longer pulse duration. We will then perform experiments to cool Ps, first in one and then in three dimensions.

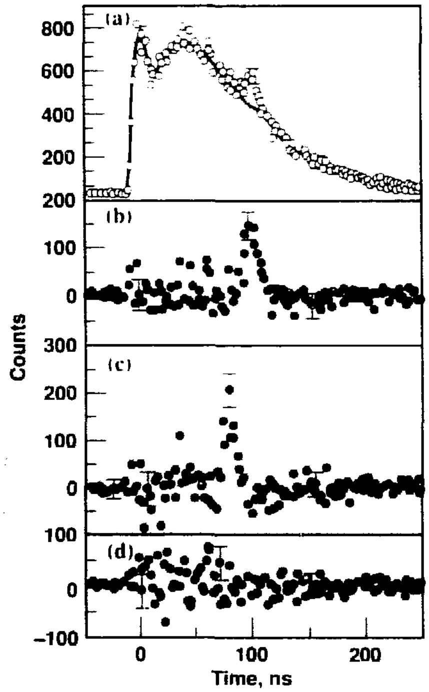

Figure 1. Typical Ps annihilation time profiles. In (a), the solid black curve is the laser-off profile; the open circles give the laser-on profile (laser pulsed at 90 ns, with a 200-G magnetic field). Represenative 1σ error bars are shown for two points in the laser-on spectrum; errors for the laser-off spectrum are less than the width of the line. (b) Difference spectrum obtained by subtracting the laser-off spectrum from the laser-on spectrum in (a). (c) Difference spectrum as in (b) but with the laser pulsed 20 ns earlier. (d) Difference spectrum as in (c) but with the laser detuned 1 nm to the red of the 1^3s–2^3p transition; the laser peaks approximately where the representative 1σ error bar is given at 70 ns.

References

Dermer, C. D., R. H. Howell, K. M. Jones, E. P. Liang, F. Magnotta, and K. P. Ziock (1988). *Photoexcitation and Cooling of Positronium*. Lawrence Livermore National Laboratory, Preprint UCRL-98775.

Liang, E. P., and C. D. Dermer (1988). "Laser Cooling of Positronium," *Opt. Comm* **65**, 419.

Ziock, K. P., C. D. Dermer, R. H. Howell, F. Magnotta, and K. M. Jones (1988). *Optical Saturation of the 1^3s–2^3p Transition in Positronium*. Lawrence Livermore National Laboratory, Preprint UCRL-100160.

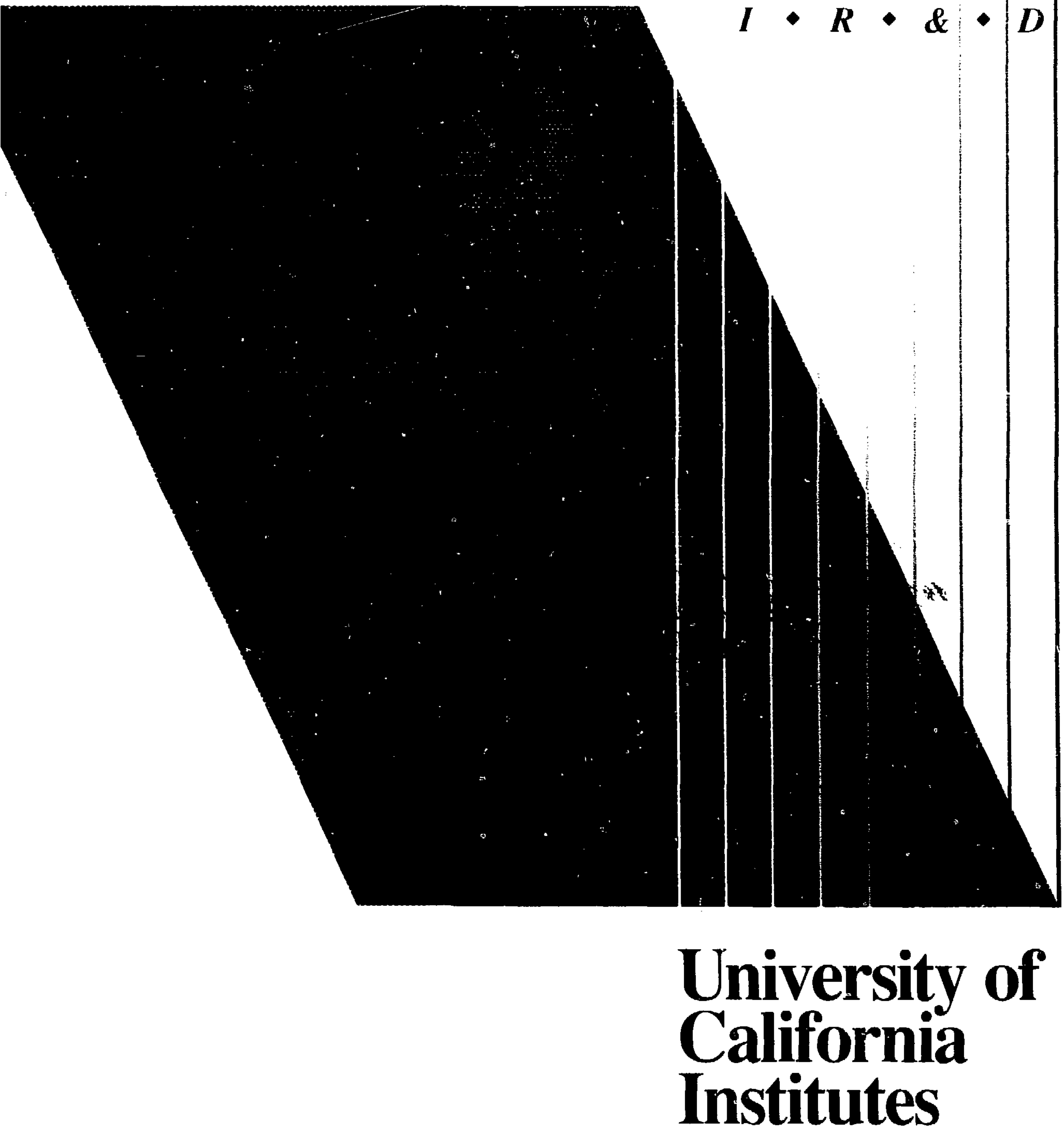

I ◆ R ◆ & ◆ D

University of California Institutes

Lawrence Livermore National Laboratory

University of California Institutes

C. E. Max

Several University of California (UC) advisory committees have recently reiterated the importance of increased scientific collaboration among staff members at the national laboratories and scientists at UC campuses. The latest contract between the Department of Energy and UC re-emphasizes the importance of such collaboration. This type of interaction has advantages for Laboratory staff members, who gain professional enrichment, closer contacts with the academic community, and expertise in fields that are under-represented at the national laboratories. Likewise, such collaboration has advantages for UC researchers, who obtain access to unique Laboratory facilities and expertise, particularly in applied fields. In recent years, several joint UC-LLNL Institutes and Programs have been established with the goal of enhancing campus-Laboratory collaboration in areas of overlapping interests and expertise.

The four current UC-LLNL joint Institutes, which are at various stages of maturity, are:

- The LLNL branch of the Institute of Geophysics and Planetary Physics, approved by the Regents in 1982 as the fifth branch of a University-wide Multicampus Research Unit.
- The Institute for Scientific Computing Research, a new project undertaken jointly by the LLNL Computation Department and participants from UC Berkeley.
- The Plasma Physics Research Institute, a new project in collaboration with the College of Engineering, UC Davis.
- The Program for Analytical Cytology, approved by the Regents in 1982 as a joint program of LLNL and UC San Francisco.

All of these joint programs are currently functioning at LLNL, sponsoring collaborative research, postdoctoral and student researchers, workshops, and seminars. At present, the first and last collaborative projects listed above receive funds from the system-wide administration of UC, as well as from other campuses, LLNL, and national funding sources. The system-wide funding is used to sponsor small awards to UC researchers for collaborative projects with LLNL.

Institute of Geophysics and Planetary Physics

C. E. Max

The LLNL branch of the Institute of Geophysics and Planetary Physics (IGPP) was established by the UC Regents in 1982. Its purpose is to make LLNL's unique facilities and expertise in geosciences and astrophysics available to outside researchers, primarily those associated with UC. The program also broadens the scientific horizon of LLNL researchers by encouraging collaborative and interdisciplinary work with University scientists. At present, the IGPP at LLNL has three research centers:

- The Center for Geosciences, headed by G. Zandt.
- The Astrophysics Research Center, headed by C. Alcock.
- The Center for High-Pressure Sciences, headed by W. Nellis.

The IGPP also has administrative responsibility for the new UC Accelerator Mass Spectrometry Program at LLNL.

The IR&D Program provides funding for IGPP administrative and secretarial costs at LLNL and provides one-half the salaries of the three Center heads. The LLNL Physics and Earth Sciences Departments contribute scientific and technical personnel to the IGPP.

At the core of the IGPP branch at LLNL is a group of research grants open to scientists from all UC campuses. These peer-reviewed grants (jointly funded by the UC Regents and by the IR&D Program) have been awarded annually since FY83. Typical grants range from $5,000 to $20,000 and are used for research in seismology, geochemistry, cosmochemistry, high-pressure physics, and astrophysics. In recent years, we have received about twice as many qualified proposals as we can support (see Figure 1).

The grants help support visiting graduate and postgraduate researchers, experimental facilities for visiting researchers, and supercomputer time. The opportunity for University faculty and students to use LLNL's supercomputers has been a prominent component of the program.

Several advanced facilities are available to researchers visiting the IGPP at LLNL. The Center for Geosciences has a variety of digital, broadband

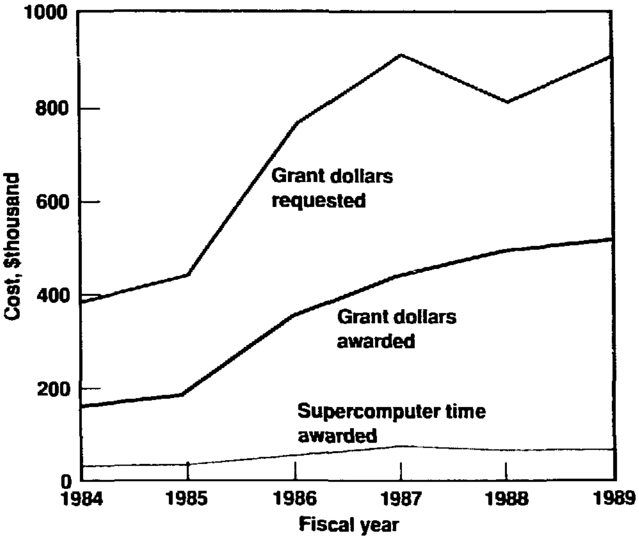

Figure 1. IGPP funding from LLNL since FY84 and cost of supercomputer time awarded to campus researchers as part of the collaborative projects.

seismographic equipment. The Astrophysics Research Center maintains a state-of-the-art image-processing facility for analyzing and displaying astronomical data. The Center for High-Pressure Sciences has two light-gas guns, several diamond-anvil-cell laboratories, a piston-cylinder apparatus, and facilities for synthesizing and characterizing specimens at high temperatures and pressures.

For data analysis, powerful LLNL-developed geophysical software can be run on a network of Sun workstations. Researchers also have access to the Cray supercomputers of the National Magnetic Fusion Energy Computer Center. The Crays can be accessed through a local node in one of the IGPP-LLNL buildings and are at present used most extensively by the Astrophysics Research Center.

In addition to providing grants for campus researchers, the IGPP strives to provide an intellectual focal point for UC-LLNL interactions. To further this goal, the IGPP runs a weekly seminar series, helps host University visitors for periods ranging from a few days to a full sabbatical year, and sponsors conferences and workshops.

The high scientific productivity for IGPP-sponsored collaborations is evidenced by the volume of publications that have resulted from IGPP research at LLNL (Figure 2). In all, about 135 IGPP papers have been published since 1983.

In FY88, the Laboratory's IGPP received $1,454,000 in IR&D operating funds plus $57,000 for capital equipment.

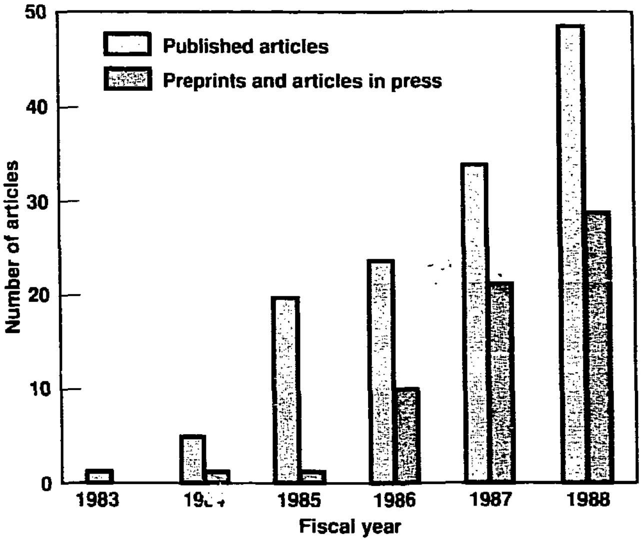

Figure 2. History of IGPP publications (refereed journal articles and published conference proceedings)

Analysis of the Mt. Lewis Earthquake and Prior Activity (1980–1986) Using Digital Seismic Data

Changes in the coda quality factor may precede the occurrence of large earthquakes. We determined the coda quality factor and studied its dependence on lapse time and distance for earthquakes within 10 km of the 1986 Mt. Lewis main shock to search for precursory temporal changes associated with this moderate-magnitude event.

Principal Investigator: K. C. McNally*
Co-Investigators: G. Zandt and G. Nelson*

*University of California, Santa Cruz.

The coda, or temporal decay in seismic energy arriving after the main ray-arrival, is a measure of the attenuation of the medium through which seismic waves from an earthquake propagate. This measure is quantified by the coda quality factor Q_c, which is a function of frequency and is related to inverse attenuation. Several previous studies have indicated that temporal variations in coda Q precede and accompany the occurrence of large earthquakes. The March 31, 1986, Mt. Lewis earthquake (magnitude 5.7) in Fremont, California, presented us with an opportunity to study this phenomenon with an extensive data set obtained by the Lawrence Livermore Seismic Network (LLSN).

We determined coda Q for earthquakes that occurred from 1980 through 1987 within 10 km of the Mt. Lewis main shock. The coda Q was determined at three stations located within 10 km of the main shock using the Sato (1977) single-scattering formulation. We observed that coda Q increases with lapse time and that three distinct decay slopes are commonly obtained in the lapse-time range of 2–20 s and greater. Within the confines of the single-scattering model, we have modeled this increase as being due to:

- Increasing intrinsic Q in the upper mantle.
- Scattering into surface waves in the uppermost crust.
- Increased scattering strength in the uppermost crust.

The lapse-time range of 5–12 s excludes both the complicated early coda and possible upper-mantle scattering. We find that coda Q has a local minimum in the standard error when computed over the lapse-time range of 5–12 s. Our finding may signify that different parameters apply to scattering outside this lapse-time window. In this range, the average coda Q measured at station CDV at 6 Hz was 135; however, the value exhibits significant variation, with both temporal and spatial dependence.

Coda Q also exhibits a dependence on distance from the main shock and time before and after the main shock. We found that, for events within 5 km of the main shock, attenuation ($1/Q_c$) at 6 Hz was 63% higher (Q_c = 100) 15 months before the main shock occurred, began to decrease nine months before the main shock, and reached a low (Q_c = 160) six months after the main shock. Coda Q also exhibits a dependence on the distance of the source epicenter from the main shock epicenter. Attenuation was highest for sources closest to the main shock (Q_c = 114), decreased to a minimum at a distance of 6–8 km from the main shock (Q_c = 167), then increased to a distance of 14 km (Q_c = 125), beyond which we have no data. The aftershock had a radius of 5 km, which is slightly smaller than the radius of the area with smallest attenuation.

Our results imply that temporal changes in coda Q may be associated with the occurrence of moderate-magnitude earthquakes. However, the distance dependence that is also present complicates the usefulness of this measure as a tool for earthquake prediction.

Reference

Sato, H. (1977). "Energy Propagation Including Scattering Effects: Single Isotropic Scattering Approximation," *J. Phys. Earth* **25**, 27

Mapping Changes of Crustal Heterogeneities

Principal Investigator: R. S. Wu*
Co-Investigators: G. Zandt and G. Nelson*

---

*University of California, Santa Cruz.

We have used the Lawrence Livermore Seismic Network to determine changes in the coda duration as a function of distance and time before and after the magnitude-5.7 Mt. Lewis earthquake.

The temporal changes of coda Q (Q_c) and coda duration of foreshocks and aftershocks associated with a major earthquake are the subject of many reports from around the world. Most observations, however, are based on one or two stations, and the results are often contradictory. The Lawrence Livermore Seismic Network (LLSN) provides an excellent opportunity to study temporal variations in coda duration, postulated to be an earthquake precursor, because of the dense distribution of stations and events around the main shock zone of the March 31, 1986, Mt. Lewis earthquake (magnitude 5.7) located near Fremont, California.

We grouped the 25 stations of the LLSN into three rings based on their distances from the epicenter of the Mt. Lewis earthquake:

- Ring 0 extends from 0 to 15 km.
- Ring 1 extends from 15 to 25 km.
- Ring 2 extends from 25 to 38 km.

We used earthquakes occurring from the beginning of 1980 to April, 1987, with depths ≥5 km and epicentral distances <10 km from the main shock to study temporal changes in coda duration. We used as the reference background the USGS magnitude that was derived from the average log T_c (the logarithmic coda duration) over stations in a broad area. We then plotted the difference between the average log T_c for each ring and the background log T_c versus time to study temporal changes of the scattering coefficient of crustal heterogeneities sampled by coda waves recorded by stations in different rings. We found an increase of average T_c starting about 2 years before the main shock. After the main shock, the average T_c decreased gradually. The anomaly of T_c was more pronounced for rings 0 and 1 than for ring 2.

Teleseismic-Converted Waves in the Long Valley Caldera

We are using teleseismic P-to-S-converted seismic waves to determine locations and configurations of magma bodies beneath the Long Valley Caldera.

Principal Investigator: W. Prothero, Jr.*
Co-Investigators: G. Zandt and L. Steck*

*University of California, Santa Barbara.

Teleseismic *P* (compressional) waves impinging on a velocity discontinuity, such as the interface between solid and semimolten rock, generate converted *S* (shear) waves. Such converted *P*-to-*S* waves provide direct evidence on the location and velocity contrast of the causative interface. We recorded teleseismic *P* waves in an active volcanic area to search for converted waves and to assess the utility of converted waves in the identification of magma bodies.

Data for our study were recorded on a combined Lawrence Livermore National Laboratory/UC Santa Barbara seismic array located on the northwest shoulder of the resurgent dome of the Long Valley Caldera in eastern California. Using array-analysis techniques, we have shown that the large, delayed arrivals seen on horizontal components are converted shear waves. These phases originate from beneath the western moat, a region identified by other researchers as possibly containing magma bodies. We also found that direct *P* waves are perturbed from expected great-circle back-azimuths, most likely by the same structure as that generating the shear waves. We are now determining station corrections to remove the effect of near-surface velocity variations on our array-analysis techniques. Such corrections will allow more accurate estimates of the locations of converting interfaces.

Crustal Fault Zone Study with the Lawrence Livermore Seismic Network

We are studying earthquake-generated seismic waves in crustal fault zones to search for waveguide effects that may provide valuable diagnostic measures of fault properties.

Principal Investigator: J. Vidale*
Co-Investigators: G. Zandt, G. Nelson,*
and D. Garcia-Gonzales*

---

*University of California, Santa Cruz.

The zone of material up to a few kilometers wide around major strike-slip faults has been hypothesized to have compressional and shear velocities that are lower than those of the surrounding material by 10–40%. The waves that travel in the fault zone or low-velocity channel can provide important diagnostic observations of the fault zone.

We examined the waveguide effects from earthquake-generated seismic waves traveling along a fault zone with data from the Lawrence Livermore Seismic Network located in the east San Francisco Bay area. *SH* waveforms (horizontally polarized shear waves) for paths that follow the fault trace are quite similar to waveforms for paths that cut across the fault zone. These observations suggest a much narrower or less anomalous fault zone than has been proposed for the Calaveras fault in other locations and for the San Andreas fault near Bear Valley.

We have developed a novel scheme to compute travel time to determine whether there are indications of a low-velocity fault zone in the travel times to the stations near the Calaveras fault. The travel times are consistent with 10% lower-velocity material in the fault zone than on either side. Surprisingly, however, the results are not mathematically unique. Nevertheless, the scheme for travel-time analysis has proven to be quite useful. We are currently using the scheme for windowing finite-difference calculations, Kirchhoff migration, and tests of the resolution of tomographic inversions.

Seismic Attenuation from Earthquake and Explosion Sources

We are investigating the attenuation of regional seismic waves and comparing the high-frequency content of explosions with that of earthquakes in western Nevada.

Principal Investigator: S. Hough*
Co-Investigators: J. Anderson† and H. Patton

*Institute of Geophysics and Planetary Physics, University of California, San Diego.
†Scripps Institution of Oceanography, University of California, San Diego.

We are studying the attenuation of regional seismic waves at frequencies between 1 and 15 Hz and at epicentral distances from 20 to 250 km in western Nevada. Following the method of Hough *et al.* (1988), we parameterize the asymptote of the high-frequency acceleration spectrum by a two-parameter model. We interpret the model parameters in terms of a simplified two-layer model for seismic-wave attenuation Q and relate the observed model parameters to Q_i and Q_d, the frequency-independent and the frequency-dependent components of the coda quality factor Q, respectively. We obtain total Q (Q_t) by $1/Q_t = 1/Q_i + 1/Q_d$. In the top 5 km of the crust, we obtained a Q_i of ~67. We have no resolution of Q_d in the near-surface layers.

Comparing our results to those from previously published Q studies in the Basin and Range region, we find that our estimate of Q_t in the shallow crust is consistent with shear-wave Q at close distances, as determined by Patton and Taylor (1984) and Chavez and Priestley (1985). For depths greater than 5 km, we obtain Q_t that increases from ~150 at 1 Hz to ~600 at 15 Hz. This estimate of Q_t is consistent with coda Q reported by Singh and Herrmann (1983) and with Q determined from the L_g phase (shear waves propagating in the crustal layers) reported by Chavez and Priestly (1986) (see Figure 1). This result suggests that both coda Q and Q determined from L_g are insensitive to near-surface contributions to attenuation.

In addition to our results on attenuation, we compared the high-frequency content of explosions with that of earthquakes. Our results from S waves are similar to results for P_g waves (compressional waves propagating in the crustal layers) by Chael (1988), who found that the P_g wave spectra from explosions are depleted in high-frequency energy with respect to earthquake spectra. Taylor *et al.* (1988) compared spectral energy at 1–2 Hz with energy at 6–8 Hz for earthquakes and explosions. These researchers found relative depletion of the higher frequencies for explosion sources, especially for L_g waves. This result is also consistent with those in the present study. The combined results indicate that spectral differences between explosion and earthquake sources observed at regional distances may be an important discriminant in the seismic verification of compliance with nuclear test-ban treaties.

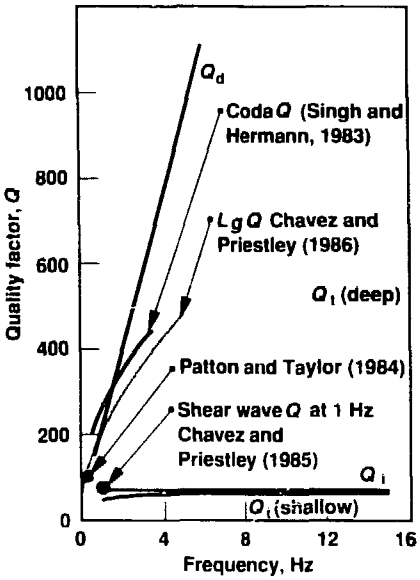

Figure 1. Summary of variation of quality factor *Q* in the Basin and Range. See text for a more detailed interpretation of these data.

References

Chael, E. P. (1988), *Geophys. Res. Lett.* **15**, 625.

Chavez, D. E., and K. F. Priestley (1985), *Bull. Seism. Soc. Amer.* **74**, 1583

Chavez, D. E., and K. F. Priestley (1986), *Geophys. Res. Lett.* **13**, 551.

Hough, S. E., J. G. Anderson, J. Brune, F. Vernon, III, J. Berger, J. Fletcher, L. Haar, T. Hanks, and L. Baker (1988), *Bull. Seism. Soc. Amer.* **78**, 672

Patton, H. J., and S. R. Taylor (1984), *J. Geophys. Res.* **89**, 6929-6940.

Singh, S., and R. B. Hermann (1983), *J. Geophys. Res.* **88**, 527

Taylor, S. R., N. W. Sherman, and M. D. Denny (1988), *Bull. Seism. Soc. Amer.* **78**, 1563

Crustal Genesis and Recycling in Northwestern Mexico

We are studying silicic volcanic rocks in northwestern Mexico to determine the mechanisms responsible for their origin.

Principal Investigator: K. Cameron*
Co-Investigators: S. Niemeyer and G. Nimz*

---

*University of California, Santa Cruz.

The largest Cenozoic rhyolite province in the world occurs in western Mexico. If these silicic volcanic rocks originated by fractional crystallization of mantle-derived basaltic magmas, then their extrusion marked a major Cenozoic crust-forming event. Alternatively, the rhyolites may largely represent melting and recycling of preexisting continental crust.

Our analyses have established that the mid-Cenozoic rhyolites overlap in strontium and neodymium isotopic compositions with coeval basaltic rocks. The basaltic rocks, in turn, have strontium, neodymium, and lead isotopic ratios similar to those of mantle pyroxenites, demonstrating that crustal assimilation is not required to explain their isotopic compositions. About two-thirds of the granulite-facies xenoliths we have analyzed from Mexico appear to be Precambrian basement, and they have neodymium and/or strontium isotopic ratios that differ greatly from those in Cenozoic volcanic rocks. The remaining xenoliths, mostly cumulate mafic granulites, are isotopically indistinguishable from the Cenozoic volcanic rocks. These mafic granulites may be the first recognized samples of several-kilometer-thick, cumulate-dominated, mid-Cenozoic crust that formed during the fractionation of the basalt-to-rhyolite series.

Geologic Application of Discrete-Particle Models for Earth Materials

We are combining the results of physical experiments with those of discrete-particle computer models to simulate mechanisms of flow in granular material for applications in which experiments would be impractical.

Principal Investigator: R. Shreve*
Co-Investigators: O. Walton and T. Drake*

Flow of granular material is important in a variety of scientific and engineering studies. Examples from the earth sciences include avalanches, pyroclastic flows, and impact cratering. Examples of some engineering applications are the industrial transport of coal and other particulates, fluidized-bed technologies, and proposed designs for inertially confined fusion reactors.

Experimental studies of the flow of granular material in progress at UC Los Angeles and the discrete-particle computer models developed by the Granular Solids Flow Project at LLNL are providing a unique opportunity for mutually beneficial collaborative research. Our physical experiments provide a means of calibrating, validating, and refining the computer models, which can then be used to simulate flows that are experimentally impractical.

We have completed our experiments comparing collision-dominated grain flow performed at UC Los Angeles and discrete-particle computer simulations performed at LLNL. We directed most of our recent work toward the sensitivity analyses of computer simulations to flow parameters, such as friction coefficients between flow particles and flow and boundary particles, number density of particles per unit length of a channel, and spacing of parallel walls that confine particles to essentially two dimensions.

At LLNL, we are currently transferring the computer code to Sun workstations. Many of the graphics capabilities readily available on the Cray will be implemented on those workstations. We are also exploring new ways of visualizing the experimental results obtained at UC Los Angeles and LLNL.

At UC Los Angeles, we are conducting physical experiments using geologic materials to determine several parameters for the simulations, including the coefficients of friction and restitution. Our previous computer experiments and available theory indicate that flows of geologic materials should not be sensitive to choices of these parameters. Thus, we should be able to proceed rapidly to our proposed simulations of the development of eolian (wind-borne) slipface deposits. After we understand the uniform-grain-size eolian system as a first, relatively simple geologic application, we envision using the model to investigate a variety of problems in sedimentologic sorting. The lengthy process of validating and calibrating our computer simulations should earn exciting scientific dividends.

---

*University of California, Los Angeles.

Isotopic Analysis of Microscopic Domains in Garnet Porphyroblasts from Sri Lanka

Our results on electron microprobe analysis of garnets from Sri Lanka suggest that more than one episode of metamorphism affected these specimens.

Principal Investigator: J. Reynolds*
Co-Investigators: W. Glassley and
J. J. Irwin*

---

*University of California, Berkeley.

The purpose of our project is to establish the pressure-temperature-time history of high-grade metamorphic rocks from Sri Lanka. To do so, we are integrating etrologic studies conducted at LLNL with microanalysis of argon sotopes at UC Berkeley. We selected from a large collection of amples of high-grade metamorphic rocks obtained from Sri Lanka a few specimens of garnet and feldspar that best illustrate variations in temperature and pressure of formation of different parts of single crystals. Electron microprobe study of the garnets indicates that the rims of some crystals contain more iron and less calcium than the cores of the same crystals. These data indicate that the rims of some crystals formed at a considerably lower pressure than the cores. This finding implies that more than one episode of metamorphism may have affected these rocks. The pronounced compositional variations observed in these garnets, combined with their large grain size, make the specimens ideal for laser-microprobe argon-isotope analysis.

Trace-Element and Isotope Geochemistry of Cretaceous/Tertiary Boundary Sediments

We have developed a new approach for identifying the sedimentary minerals responsible for trace-element concentrations associated with the end of the Cretaceous period. This should enable us to resolve the controversy surrounding the volcanic-versus-impact origin of anomalous geochemical concentrations.

Principal Investigator: S. Margolis*
Co-Investigators: G. P. Russ, III, and E. Doehne*

*University of California, Davis.

We have analyzed trace elements and stable isotopes in a series of sediment samples crossing the Cretaceous/Tertiary (K/T) boundary and obtained from critical sections at Zumaya and Sopelano, Spain. Our aim is to distinguish extraterrestrial versus volcanic or authigenic concentration of the platinum group and other elements in K/T boundary transitional sediments. These sediments have been shown to contain evidence for the stepwise extinction of several groups of marine invertebrates associated with negative oxygen and carbon isotope excursions occurring during the last million years of the Cretaceous period. The isotope excursions have been interpreted to indicate major changes in ocean thermal regime, circulation, and ecosystems that may be related to multiple "events" during the Late Cretaceous.

Our results to date on the petrographic and geochemical analyses of the Late Cretaceous and Early Paleocene sediments indicate that diagenesis has affected the trace-element geochemistry and stable-isotope compositions at Zumaya. The degree of diagenetic alteration is correlated with lithology. The best-preserved samples are soft marls with high clay contents and limestones that have undergone early, permeability-reducing marine cementation. More porous sandstones and bedding-place veins show the greatest alteration and depleted stable-isotope values.

Platinum and nickel grains perhaps represent the first direct evidence of siderophile-rich minerals at the K/T boundary. The presence of spinels and nickel-rich particles as inclusions in aluminosilicate spherules from Zumaya suggests an original, nondiagenetic origin for the spherules. The chemistry and morphology of the platinum grains, spinels, spherules, and nickel-rich grains most closely match chondritic fireball or ablation debris. This finding suggests that a substantial portion of any proposed K/T bolide(s) may have burned up in the earth's atmosphere. A volcanic origin for the boundary particles is incompatible with the chemistry of the Zumaya particles. Chalcophile elements appear to have an authigenic origin and may be derived from seawater or an early diagenetic enrichment.

Our research represents a new approach in trying to directly identify the sedimentary mineral components that are responsible for trace-element concentrations associated with the K/T boundary. These techniques are currently being used on several other well-preserved marine and terrestrial K/T sections. Such applications may provide valuable information that could resolve the controversy surrounding the possibility of multiple K/T boundary events. the volcanic-versus-impact origin for anomalous geochemical concentrations, and the relation of these factors to biotic extinctions.

Nondestructive Gamma-Ray Analysis of Uranium-Series Nuclides in Volcanic Rocks

We are investigating the use of nondestructive techniques to analyze uranium-series nuclides in an effort to understand the extent and time scale of chemical fractionation in volcanic processes.

Principal Investigator: J. D. Macdougall*
Co-Investigators: R. Finkel and K. Rubin*

---

*Scripps Institution of Oceanography, University of California, San Diego.

The aim of our work has been to assess the feasibility of nondestructive measurements using the Ge(Li) detectors belonging to the LLNL Nuclear Chemistry Division to analyze uranium-series nuclides in young volcanic rocks. Earlier work indicated that, for samples having uranium concentrations in the parts-per-million range, this method would be most useful for measurement of ^{228}Ra, ^{226}Ra, and ^{228}Th. Rapid and reliable radium measurement is important in our studies. With its approximately 1600-year half-life, ^{226}Ra is ideally suited to the investigation of processes occurring in magma chambers of young volcanoes because it has the same time scale as the processes of interest. Moreover, radium is a chemical analog of barium, an important trace element in geochemical modeling; ^{228}Ra is especially useful for very young volcanic rocks. The ^{228}Ra/^{232}Th disequilibrium could provide evidence of recent fractionation accompanying or immediately preceding volcanic eruption.

Over the past year, we have successfully completed nondestructive measurements of ^{226}Ra using Ge(Li) detectors. Our measured activities generally agree with those we determined using the destructive radon-emanation technique at the Scripps Institution of Oceanography. Such measurements help constrain the extent and time scale of chemical fractionation in volcanic processes. We plan to extend our work to samples with lower activity levels.

Stable Isotope Ratios of Reactive Metals in Seawater

We are obtaining precise measurements of lead isotope ratios as a means for tracing the origin and flux of contaminant leads in the biosphere.

Principal Investigator: A. R. Flegal*
Co-Investigator: S. Niemeyer

*University of California, Santa Cruz.

Our objectives were to improve the analytical capabilities at LLNL for accurate measurements of stable lead isotopic compositions in small (1-ng) lead samples. In addition, we sought to use those measurements to study the biochemical cycle of lead in the marine environment. We require precise measurements of lead isotopic compositions because most concentrations of lead in seawater are $<5 \times 10^{-12}$ mol/kg, and isotopic ratios must be accurate to at least four significant figures for environmental research. Measurements of the isotopic composition of lead are extremely useful because they provide a fingerprint of its origins and may be used to trace the flux of contaminant leads in the biosphere.

We have developed ultraclean techniques for measurements using thermal-ionization mass spectrometry of stable lead isotopic compositions in water samples. The lead concentrations in the samples are one part per 10^{12}. We are using these geochemical fingerprints to identify sources of contaminant leads in the Great Lakes, the Antarctic, and the North Pacific (see Figure 1). Fluxes of industrial lead currently account for more than 95% of the total lead fluxes to those three systems. We are also investigating the applicability of our measurements as tracers of associated contamination, including that arising from acid rain.

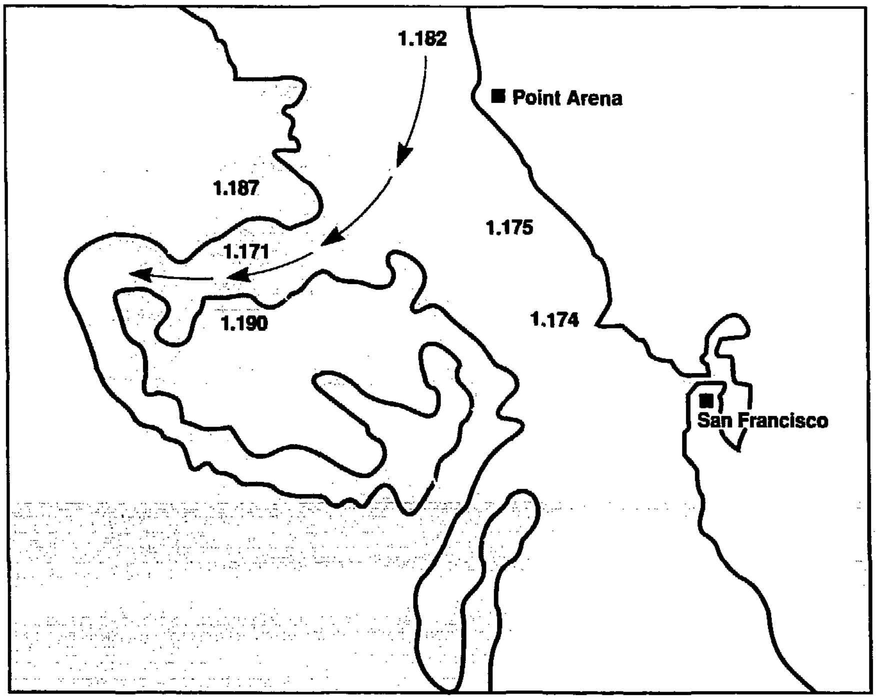

Figure 1. Ratios of ^{206}Pb to ^{207}Pb from surface waters in an upwelling filament (colored arrows) off the coast of central California. The filament outline is derived from satellite imagery of the thermal boundary.

Multiwavelength Study of the Continuum in Active Galactic Nuclei

We are attempting to explain the radiation continuum, from infrared through gamma rays, of active galactic nuclei by combining a model for the accretion-disk spectrum with a model for a nonthermal source surrounding a black hole.

Principal Investigator: M. Malkan*
Co-Investigator: D. Band

---

*University of California, Los Angeles.

How trillions of solar luminosities are released within a light day of the center of an active galactic nucleus (AGN) has not yet been determined. In the standard theoretical scenario, material accretes through an accretion disk onto a massive black hole, which powers a surrounding source of x rays and gamma rays. Our goal was to combine a model for the accretion-disk spectrum with a model for a nonthermal source surrounding the black hole to explain the radiation continuum. We fit observed spectra to derive the basic quantities that characterize the source, such as mass of the black hole and radius of the nonthermal source. With these quantities, we can investigate the physics of the central engine.

We modeled the continua, from infrared through gamma rays, of an AGN by combining the accretion disk of Malkan and Sun with the nonthermal source model of Band (1987). The accretion-disk model adds relativistic effects to the emission from an optically thick, geometrically thin accretion disk. In the nonthermal source model, relativistic electrons radiate the infrared continuum by synchrotron emission and the x-ray spectrum by inverse Compton scattering of ultraviolet photons from the accretion disk. The electron distribution consists of a flat ($\gamma^{-2.4}$), low-energy component and a steeper ($\gamma^{-3.4}$), high-energy component, where $\gamma = E/mc^2$ is the electron Lorentz factor.

We found that the typical AGN in our sample has a black hole of mass $\sim 4 \times 10^8$ $M_\odot$ at its center (where $M_\odot$ is the solar mass), a total thermal and nonthermal luminosity of about one-half the Eddington luminosity, and an accretion rate of ~0.4 $M_\odot$ per year. The high accretion rate indicates that the approximation of a thin accretion disk is only marginally acceptable. Because the AGN lifetime is short, $\sim 10^9$ years, the activity in a given galactic nucleus is short-lived compared to the age of the universe.

The nonthermal source has a radius of $\sim 2 \times 10^{15}$ cm, a relativistic electron density of $\sim 5 \times 10^6$ cm^{-3}, and a magnetic field of ~200 G. Consequently, the photon and magnetic fields are in rough equipartition, while the relativistic electron energy density is smaller by a factor of 10^3. In an inhomogeneous source, the electron density could be greater. The luminosities of the nonthermal infrared, ultraviolet accretion disk and the nonthermal x-ray to gamma-ray continua are comparable. Our combined model of an accretion disk and a nonthermal source reproduces quite well the observed spectra of the ten AGN we have studied so far.

References

Band, D. L. (1987). "On Nonthermal Models for Active Galactic Nuclei." *Astrophys. J.* **321**, 80.

Band, D. L., and M. A. Malkan (1988), *Synthesis of Accretion Disk and Nonthermal Source Models for Active Galactic Nuclei*, Lawrence Livermore National Laboratory, Preprint UCRL-97451.

Modeling Supernova Spectra

Principal Investigator: S. Woosley*
Co-Investigators: T. Axelrod, P. Pinto,*
and D. Hartmann*

We are modeling the energy budget, spectra, and other features of the February 1987 supernova in the Large Magellanic Cloud after obtaining high-resolution images of that Type II event.

The term "supernova" refers to the giant explosions of aging, massive stars. The most spectacular event in the history of the study of supernovas occurred in February 1987. This event was the supernova in our neighboring galaxy, the Large Magellanic Cloud (LMC), and is known to astrophysicists as SN 1987A.

We traveled to Christchurch, New Zealand, in April 1987 to observe SN 1987A in the infrared using the NASA Kuiper Airborne Observatory. We obtained high-quality spectra during the April flights that covered the region from 3–11 µm at energy resolutions of 3000 km/s. In addition, we observed the argon 6.9-µm and nickel 6.6-µm lines at high resolution (300 km/s).

The resulting profiles showed both asymmetric tails to the red end of the spectrum and an overall red shift of the profiles in excess of the LMC recession velocity. We have explained the red line shifts and asymmetries observed in the infrared as the effect of radiative transfer through an expanding cloud of electrons. Model profiles fit to the data yielded an electron column depth at 400 days, which agrees with predictions of models for radioactive-decay ionization.

We have also continued our work on modeling the energy budget and emergent spectra of ejecta from SN 1987A. We have produced synthetic spectra from self-consistent models of the ejecta, which include all elements and ionization stages observed in SN 1987A and in other supernovas. These models agree reasonably well with infrared observations, especially of low-ionization infrared lines of nickel, argon, and cobalt. We are beginning our work on optically thick line calculations for earlier-time spectra of SN 1987A; however, few results are yet available. Finally, we are now working with researchers at the Cerro Tololo Inter-American Observatory in Chile in an effort to match recent optical observations because the optical spectrum of SN 1987A increasingly resembles the Type Ib supernova spectra that Chilean researchers investigated previously.

---

*University of California, Santa Cruz.

Neutron-Rich Nucleosynthesis

We are examining the nucleosynthesis of neutron-rich matter and the interaction of neutrinos with various shells of heavy elements ejected during a Type II supernova explosion.

Principal Investigator: S. Woosley*
Co-Investigators: G. Mathews and D. Hartmann*

---

*University of California, Santa Cruz.

One of the principal problems in nucleosynthesis continues to be the origin of *r*-process nuclei, which are nuclei that are more massive than iron and have neutron-to-proton ratios that are higher than average. The *r* process is a proposed mechanism for making such nuclei by rapidly growing seeds of iron in an environment that is rich in neutrons. General trends and requirements are known, but despite enormous efforts invested during the last 30 years, a specific site that renders the requisite neutron flux, temperature, and time scale is still lacking. We have combined the special expertise at LLNL and UC Santa Cruz in this area to carry out two studies relevant to the *r* process: nucleosynthesis of neutron-rich matter in nuclear statistical equilibrium (NSE), and neutrino-induced neutron spallation.

Abundances in NSE are sensitive to uncertainties in the partition functions at finite temperature, nuclear-force parameterization, Coulomb shifts in strongly coupled plasmas, freeze-out corrections, nuclear binding energies, and other effects. We have studied the sensitivity to nuclear binding properties because they enter the calculations exponentially in the nuclear Saha equation. The binding energies of experimentally inaccessible nuclei are determined by an extrapolation scheme that relies on a nuclear mass law. Errors associated with this method increase with distance from the valley of β stability, which refers to those isotopes (defined by atomic mass and atomic number) that do not decay by emission of an electron or positron or the capture of a positron. We calculated neutron-rich equilibrium mass fractions. Final abundances were calculated after β decay to the stable isotopes. Concentrating on the abundances of those isotopes that exhibit strong meteoritic isotopic-abundance anomalies, we conclude that neutron-rich equilibrium abundances are uncertain by a factor of about two. Our earlier conclusions (Hartmann *et al.*, 1988) were that nucleosynthesis of ^{48}Ca, ^{50}Ti, ^{54}Cr, and ^{64}Ni occurs within neutron-rich zones that have achieved NSE. These conclusions have been confirmed by recent high-precision measurements of meteoritic isotopic anomalies (Birck and Lugmair, 1988).

We also studied the interaction of neutrinos with the various shells of heavy elements ejected in a Type II supernova, such as SN 1987A. Here, inelastic neutral-current neutrino scattering on nuclei in or near their ground state can lead to the excitation of particle-unbound states that decay by neutron or proton emission. For specific calibration, we adopted initial radii and densities for a 20-M. star. This choice of mass is a representative value for supernovas responsible for producing the solar abundance set and has the additional advantage of affording direct comparison with abundances that might ultimately be measured in SN 1987A. We found that the resulting abundance yields are extremely sensitive to the radius of the interaction zone. Our preliminary results indicate that the neutrino-induced *r* process does not yield abundances comparable to the observed *r*-process elements in the solar system because neutron densities are too low.

References

Birck, J. L., and G. W. Lugmair (1988). "Nickel and Chromium Isotopes in Allende Inclusions." *Earth and Planet. Sci. Lett.* **90**, 131.

Hartmann, D., S. E. Woosley, and M. F. El Eid (1988). "Nucleosynthesis in Neutron Rich Supernova Ejecta." *Astrophys. J.* **297**, 837.

High-Spatial-Resolution Detectors for Hard-X-Ray Imaging

We are investigating a new phototube and various geometries for a device that could be used to obtain useful astrophysical data on cosmic hard-x-ray sources.

Principal Investigator: S. Kahn*
Co-Investigator: O. Siegmund* and C. Hailey

*Space Sciences Laboratory, University of California, Berkeley.

The aim of our study was to investigate the feasibility of using a high-spatial-resolution image intensifier coupled to an alkali-halide scintillator crystal for hard-x-ray imaging. Computer modeling in support of this effort would determine if the observation of cosmic x-ray sources could be done with high enough sensitivity to yield an astrophysically useful instrument.

The design we have adopted is quite different from the one we originally proposed. The original design involved an image intensifier that was available at LLNL. This device, however, proved to have disappointing energy resolution.

We became aware of a phototube that was commercially available and could image a multiphoton input. Its large area (16 cm^2) and lack of optical-fiber faceplate suggested that it might make a good imaging unit for the x-ray imaging spectrometer (XRIS). We evaluated one of these tubes coupled to scintillator crystals and obtained good energy and spatial resolution (~10% and ~1.5 mm at 100 keV). Thus, the XRIS with an imaging-proportional (IP) counter could serve as the basis for a balloon payload without need for optical-fiber couplers. Although we would have to array many of these tubes, their low cost makes this process feasible.

We performed additional studies on the new phototube to understand the scaling of spatial resolution with crystal thickness and x-ray energy. We used crystals both with and without entrance windows. The difference between geometries can be substantial in that each can modify the width of the light cloud reaching the photocathode and, hence, the spatial resolution. We successfully modeled our results for a crystal with a window. Our results for crystals without entrance windows are much better than might be naively expected from our model. We hope to better understand this surprising outcome in the future.

We have also evaluated the science that could be done with XRIS. We used our experimental results as input for the computer model to determine sensitivities of the XRIS payload for a variety of potential cosmic hard-x-ray sources. It is now clear that XRIS can be used to study the center of our galaxy and giant clusters of galaxies at photon energies that are greater than those previously possible.

Measurement of Optical Fibers to be Used in Multiobject Spectroscopy

We have characterized the properties of stepped-index, fused-silica, UV-transmitting optical fibers that are candidates for use in a multiobject spectrograph.

Principal Investigator: J. P. Brodie
Co-Investigator: C. J. Hailey

The goal of this project is to develop a spectroscopic instrument that will dramatically increase the efficiency of the 120-in. telescope at the UC Lick Observatory. Currently, astronomical spectra are collected one object at a time. A multiobject spectrograph is being developed that will collect light from 100 separate optical fibers located on the focal plane of the telescope and channel the light to a floor-mounted spectrometer 30 m away. The ability to gather 100 spectra simultaneously will permit new projects that require large statistical samples of astronomical spectra.

A crucial issue in the development of this instrument is the performance of the optical fibers that channel the light to the spectrograph. The light transmission of these fibers must be high enough to ensure good sensitivity of the instrument. Also important is the focal ratio degradation of the fibers, which is the change in the effective speed of the telescope output beam after light passes through the fibers. Focal ratio degradation results from the presence of microbends in the fibers, stresses on the fiber ends, and facial roughness. Thus, the way in which the optical fibers are polished and mounted is very important.

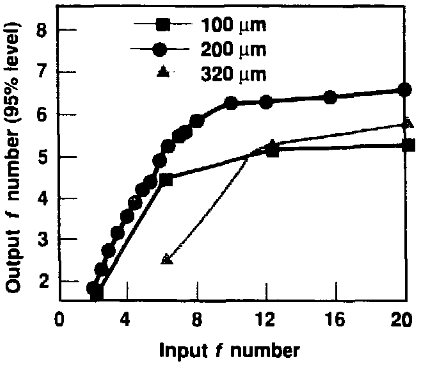

Figure 1. Output for various input *f* numbers for three fiber diameters. The relatively low value for the 320-µm core fiber may be a result of a stressed end mounting.

Typical data on focal ratio degradation are shown in Figure 1. The data indicate that the 100-µm-diam core fibers, which are best matched to the Lick stellar seeing disk, would greatly degrade the beam *f* number. The data also show that the specially polished and mounted, 200-µm-diam core fibers will produce an output beam that will not significantly degrade the Lick prime focus input beam (slightly faster than *f*/5).

We have selected and characterized optical fibers which, when properly mounted and polished, are acceptable in terms of fiber focal ratio degradation and optical and UV transmission. Our experiments have produced key data that have enabled us to optimize the design of the multiobject spectrograph.

Astrophysical Studies of CNO Isotopes

We are combining theory with observations to help explain the history of element production in our galaxy, particularly that of carbon, nitrogen, and oxygen.

Principal Investigator: M. Jura*
Co-Investigators: D. Dearborn and I. Hawkins

---

*University of California, Los Angeles.

In qualitative terms, it is well established that most of the material heavier than helium was synthesized in stars rather than in the Big Bang. However, quantitative details of the process of nucleosynthesis, and the resultant chemical evolution of the galaxy, are still uncertain. In particular, because carbon, nitrogen, and oxygen are the most abundant elements after hydrogen and helium, and because the carbon-nitrogen-oxygen (CNO) tricycle is so important as an energy source within stars, we have concentrated our efforts on understanding the abundances of these three species.

We used stellar evolution and nucleosynthesis computer codes to calculate $^{12}C/^{13}C$, $^{16}O/^{17}O$, and $^{16}O/^{18}O$ abundance ratios on the surfaces of stars with masses in the range 0.8 to 25 $M_\odot$. We compared the predicted surface-oxygen ratios in these stars to existing observations to set more stringent limits on the destruction rates of ^{17}O and ^{18}O, via the reactions $^{17}O\,(p,\alpha)\,^{14}N$ and $^{18}O\,(p,\alpha)\,^{15}N$, which are theoretically uncertain by up to two orders of magnitude. In addition, the behavior of our calculated oxygen abundance ratios can be used as a sensitive observational test of the depth of convection in stars whose measured carbon isotope ratios agree with the $^{12}C/^{13}C$ values predicted by our models. This serves as evidence that observed oxygen-abundance ratios are the consequence of normal stellar evolution followed by convective mixing that brings material from the star's interior to the surface, and that the star has not suffered additional nonconvective mixing processes. This objective is important because it can lead to a better understanding of which stars undergo more extensive convective mixing of material and are thus the major contributors of processed elements to the interstellar medium.

We are now preparing for publication the results of our calculations of a grid of models of stars with masses in the range 0.8 to 25 $M_\odot$ to obtain carbon and oxygen isotope ratios, in particular $^{12}C/^{13}C$, $^{16}O/^{17}O$, and $^{16}O/^{18}O$. In evolved models of stars up to 15 $M_\odot$, we found that after hydrogen exhaustion in the core and a first dredge-up of material, surface $^{12}C/^{13}C$ ratios are on the order of 22, which is considerably lower than the solar value of 89. The enhanced ^{13}C abundance can be understood in terms of an incomplete CNO cycle operating in a thin shell outside the hydrogen-burning core in the main sequence phase. Here, the temperature is hot enough to burn ^{12}C to ^{13}C but not to ^{14}N. These predicted carbon isotope ratios are, thus, the consequence of normal stellar processing followed by convective mixing.

The $^{16}O/^{17}O$ surface ratios were found to decrease from the solar value of 2600 to 800, 106, and 62, for the 1.3-, 2.0-, and 3.0-$M_\odot$ stars, respectively. Implementation of two extreme theoretical destruction rates of ^{17}O and ^{18}O in the nucleosynthesis of models evolved through the first dredge-up does not change the ratios predicted above because the convective layer has not had a chance to dig deeper into the star and reach more processed material.

We pushed the computational evolution past helium ignition in the more massive stars, using the two extreme choices of ^{17}O destruction rates. After comparing our calculations with infrared CO observations of red giant photospheres, we conclude that the higher destruction rate is the more appropriate choice. Our results also suggest that theory and observation can be reconciled only if the convection layer in stars of masses less than 3 $M_\odot$ attains a depth that is somewhat less than that previously calculated. By performing a similar analysis, we have found that the lower ^{18}O destruction rate is clearly more consistent with the observations.

The Interface of Astrophysics and Particle Physics

We are developing an interdisciplinary approach to astrophysical problems in an attempt to understand the nature of dark matter in the universe.

Principal Investigator: J. Silk*
Co-Investigators: D. Dearborn and G. Raffelt*

---

*University of California, Berkeley.

Our goal is to explore the interface of astrophysics and particle physics in cosmology. Constraints from the cosmological production of helium and deuterium and from the observed extreme isotropy of cosmic microwave background radiation may have effectively eliminated ordinary baryonic matter as a candidate for pervasive dark matter. Our new approach provides plausible elementary-particle candidates for the dark matter that pervades our universe and promises to account for the extreme isotropy of cosmic blackbody radiation, now known to be more than 3 parts in 105 on scales ranging from 5 arc-minutes up to 90 deg. It tentatively accounts for the origin of the fluctuations from which galaxies and galaxy clusters formed. Our aim is to develop a coordinated, interdisciplinary approach to astrophysical problems, involving input from particle physics, with emphasis on constraining the nature of dark matter.

The theory of stellar evolution, in conjunction with observational data, yields important information on the nature and distribution of particle dark matter in the universe. We can, for example, use low-mass stars as a probe for dark matter in galactic nuclei, then review astrophysical axion bounds to understand constraints on the possible interpretation of the cosmic microwave background distortion in terms of late particle decays. Thus, the observed lifetimes of horizontal branch stars yield an upper bound of 3×10^{-50} cm^2 for the process $\gamma + {}^4\mathrm{He} \rightarrow {}^4\mathrm{He} + X^\circ$ involving some hypothetical boson X°. This result excludes a recent interpretation of the angular distribution of the IMB and Kamioka signals of neutrinos from SN 1987A in terms of the coherent scattering process $X^\circ + {}^{16}\mathrm{O} \rightarrow {}^{16}\mathrm{O} + \gamma$.

The observation of a neutrino pulse from SN 1987A constrains the production of light, exotic particles in the protoneutron star. We are investigating recently derived bounds on axion parameters, the strength of right-handed weak currents, Dirac masses of neutrinos, neutrino magnetic-dipole moments, and bounds on the neutrino-majoron coupling.

Plasma Astrophysics

Principal Investigator: J. Arons*
Co-Investigators: R. Klein, A. B. Langdon, C. Max, D. Alsop,* D. Burnard,* Y. Gallant,* D. Hartmann,† S. Woosley,† and A. Zachary**

*University of California, Berkeley.
†University of California, Santa Cruz.
**University of Chicago, Illinois.

We are attempting to understand the origin of nonthermal energy in astrophysical systems.

The first goal of our research project was to study the basic physics of relativistic shock waves in electron-positron plasmas, with application to the origin of synchrotron emission in supernova remnants powered by pulsars and to the nonthermal emission from jets emanating from active galactic nuclei. Part of this effort was oriented toward modeling the electromagnetic waves created as part of the shock structure because these waves provide the conduit for energy into nonthermal particles. In this work, we made use of an existing LLNL plasma-simulation computer code whose properties are ideally suited to studying the electromagnetic phenomena associated with relativistic shocks.

Our second research goal was to investigate the physics of accretion onto the polar caps of magnetized neutron stars when radiation pressure is the dominant effect controlling the deceleration of plasma. This effort is directed primarily toward understanding the temporal fluctuations and polarimetric content of the emergent radiation observed in x-ray binary stars. These values provide powerful diagnostics into the flow structure and magnetic fields of accreting neutron stars. Our research in this area made use of radiation hydrodynamics and radiation-transfer computer codes that were developed at LLNL for this work.

We have completed a study of the cyclotron-reprocessing efficiency of gamma rays in the outer magnetosphere of a magnetized neutron star under conditions appropriate to sources of gamma-ray bursts. In this work, we attempted to model the optical and ultraviolet emission from isolated, old neutron stars undergoing gamma-ray bursts. All other models for this phenomenon require a surrounding disk or a companion star as the site of the reprocessing material.

We have also completed a study of the propagation of a low-density beam of ions through a magnetized plasma. The goal of this work was to understand the excitation of large-amplitude hydromagnetic waves upstream from a collisionless shock and to compare this effect with satellite measurements made upstream of the earth's bow shock.

Finally, we have studied the role of cosmic rays upstream of a supernova remnant's shock wave in the excitation of large-amplitude density fluctuations in the interstellar medium. In this research, we were interested in a possible explanation for the pockets of strong scintillation observed in the radio flux of pulsars.

Fractal Dust Grains

We are using the discrete-dipole approximation to study absorption and scattering properties of fractal dust grains in the solar system.

Principal Investigator: E. Wright*
Co-Investigators: C. Alcock and I. Hawkins

*University of California, Los Angeles.

A significant proportion of dust particles in the solar system are loose aggregations with low mean density. These structures can best be described using fractal geometry, which is known to be appropriate for particles that grow by slow aggregation. Traditional models of optical and infrared absorption and scattering by interstellar grains have considered only solid particles with simple topologies. The objective in our project was to study the absorption and scattering properties of fractal dust grains. We have now made substantial progress toward this objective.

We used the discrete-dipole approximation, in which many small regions of one grain are described using interacting dipoles to model the interaction of the grain with radiation. We have found that fractal grains have much greater cross sections for interaction with radiation than do solid grains with similar masses, as shown in Figure 1. This result is potentially of great importance because fractal dust grains may dominate the infrared background radiation in some of the channels of the Cosmic Background Explorer Satellite, which is scheduled for launch in 1989.

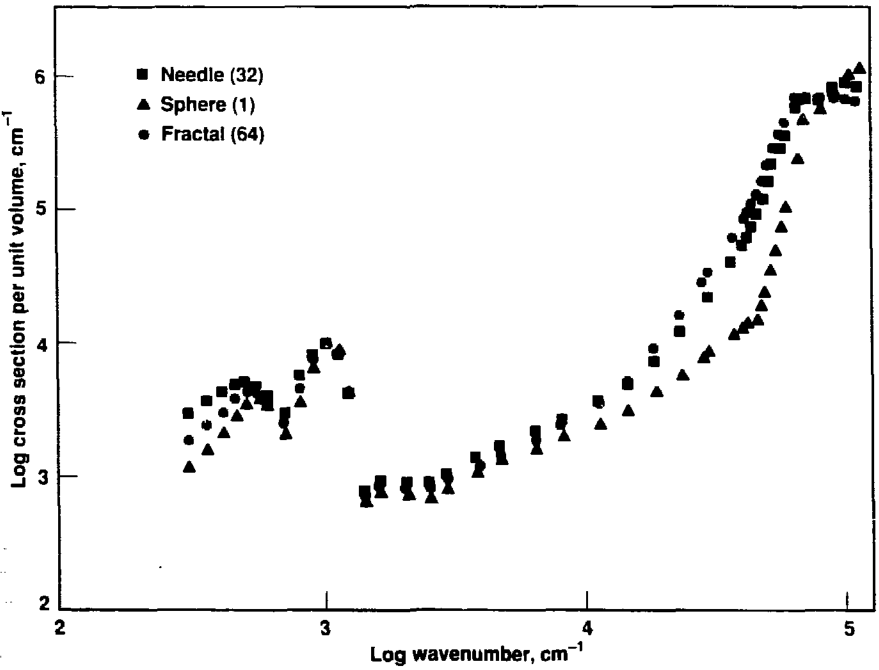

Figure 1. Cross section per unit volume of solid material as a function of wavenumber for grains of three different shapes: needles, spheres, and fractals. Numbers in parentheses are the number of unit cells used in the construction of the grains.

Statistical Mechanics and Phase Equilibria of Ionic and Geophysical Systems at High Pressure

We are using computer simulations to model liquid silicates in an effort to understand their behavior under extreme pressure.

Principal Investigator: M. Bukowinski*
Co-Investigators: M. Ross and L. Stixrude*

*University of California, Berkeley

Recent discussions of the chemical and thermal evolution of the earth's interior have been influenced considerably by the realization that, at pressures in excess of those corresponding to depths of about 200 km, the density of magmas might exceed that of crystal phases with which they are in equilibrium. If this concept is true, it would place an upper bound on the depth from which certain magmas can rise to the surface, and it may suggest that there are significant compositional differences between the lower and upper mantles. Evidence for dense liquids comes mainly from shock-wave data and is not entirely conclusive. The main purpose of our project is to model liquid silicates and to obtain information on the behavior of these liquids when they are subjected to pressure. Indeed, detailed structural information can be obtained only through computer simulations.

We investigated the effect of pressure on the structure of tetrahedrally bonded liquid SiO_2 by using Monte Carlo simulations based on a covalent potential model of tetrahedral Si-O bonding. The simulated liquid has zero-pressure density, structure, and compressibility that are in good agreement with experimental observations. The corresponding properties and known equations of state of the crystalline phases are also reproduced accurately. The liquid compresses by a continuous rearrangement, of the intermediate-range order, as evidenced by a tightening of the ring-size distribution around six-membered rings. Effective Si-O coordinations of greater than four were not observed even at 50 GPa of pressure; the first and second coordination shells remain distinct. Hence, a change in local bonding that increases the number of Si-O bonds per silicon atom, e.g., a rehybridization of silicon orbitals, seems to be required to achieve coordinations higher than four in liquid SiO_2. Even though the coordination number of the model liquid does not exceed four, its density surpasses that of all tetrahedral crystal phases by 60 GPa. SiO_2 glass has a measured density 10% higher than the model liquid at high pressure, suggesting the presence of sixfold coordination in the glass.

Dynamic High-Pressure Synthesis of High-Temperature Superconductors and Ferromagnets

We are attempting to fabricate high-critical-current-density conductors by means of shock compaction of new copper oxides and shock synthesis of new high-critical-temperature materials.

Principal Investigator: M. B. Maple*
Co-Investigators: W. Nellis, J. Neumeier,* C. Seaman,* and J. Markert*

*University of California, San Diego.

We have used high dynamic pressure, generated by the LLNL two-stage light-gas gun, to synthesize (Neumeier *et al.*, 1988) and compact (Nellis *et al.*, 1988) superconducting materials. We are attempting to produce superconductors with high critical temperature (T_c), high critical current density (J_c), and high upper critical magnetic field (H_{c2}). We have achieved dynamic pressures up to 1 Mbar, temperatures up to a few thousand kelvins, pressure quench rates up to 10^{12} bar/s, and thermal quench rates up to 10^9 K/s.

Our principal goals are to fabricate high-J_c conductors by means of shock compaction of the new high-T_c copper oxides and shock synthesis of new high-T_c materials. Shock compaction of powders has the potential to produce high J_c because compressive energy is deposited heterogeneously at grain boundaries, the region limiting J_c. All specimens were prepared and then characterized at UC San Diego before and after processing with the LLNL two-stage light-gas gun.

Shock-compacted specimens of $YBa_2Cu_3O_{7-\delta}$ and $HoBa_2Cu_3O_{7-\delta}$ powder mixed with 30- and 50-vol% silver powder were prepared via the light-gas gun in the pressure range of 3–22 GPa. Subsequent measurements of magnetic susceptibility on specimens compacted from small (<28-µm) and large (>180-µm) powders showed that bulk superconductivity is retained in this pressure range, with T_c onsets unchanged at 91 K, but with an apparent broadening of the transition. Measurements of electrical resistivity revealed a change in slope at 60 and/or 90 K for most samples. We observed a complete resistive transition at T_c = 90 K only after a specimen was annealed at 890°C in oxygen.

We have also prepared samples of the high-T_c copper-oxide superconductors $Bi_2Sr_2CaCu_2O$ (T_c = 88 K) and $Tl_2Ba_2Ca_2Cu_3O$ (T_c = 121 K) and have performed preliminary shock compaction experiments on these materials. Our results to date suggest that oxygenation of the intergranular region, either by postprocessing or *in situ* sources, is necessary to produce high J_c. Once the process for achieving high J_c is developed using 0.2-g research-size specimens, the process could be scaled up in length using the high-explosive technology available at LLNL.

References

Nellis, W.J., M. B. Maple, and T. H. Geballe (1988), "Synthesis of Metastable Superconductors by High Dynamic Pressure," *SPIE, Multifunctional Materials* (SPIE, Bellingham, WA) **878**, 2.

Neumeier, J. J., W. J. Nellis, M. B. Maple, M. S. Torikachvili, K. N. Yang, J. M. Ferreira, L. T. Summers, J. I. Miller, and B. C. Sales (1989), "Metastable A15 Phase Nb_3Si Synthesized by High Dynamic Pressure," *High Pressure Res.* **1** (3) (in press).

Melting and Other Phase Transitions of Solids at High Pressures

We are measuring phase transitions at high pressures in diamond-anvil cells and are modeling equations of state of simple solids.

Principal Investigator: **M. Nicol***
Co-Investigators: **D. Young, M. Ross, and B. Baer***

---

*University of California, Los Angeles.

Melting and solid-solid phase transitions reflect delicate energy balances between two phases of condensed matter. Thus, predicted pressures and temperatures of phase transitions are sensitive tests of statistical-mechanical models for both phases. Our project couples the expertise available at UC Los Angeles in measuring phase transitions at high pressures in diamond-anvil cells with LLNL expertise in modeling equations of state, especially melting curves of simple solids.

We have worked on several one-component systems (including Ar, N_2, O_2) and are extending this work to mixtures. Near room temperature, we have determined the $(O_2)_x:(N_2)_{1-x}$ P-x diagram to more than 10 GPa, where x is the molar oxygen concentration and P is pressure. We have also made measurements to pressures of 35 GPa for a few compositions. We have discovered a new phase of the N_2-O_2 system at pressures above 11 GPa, the properties of which emphasize the differences among O_2-O_2, O_2-N_2, and N_2-N_2 interactions.

Mixtures of N_2 and O_2 in diamond-anvil cells are being characterized by Raman spectra of the vibrons and, when possible, lattice vibrations to determine the room-temperature isotherm of the binary P-T-x phase diagram (T is temperature). We surveyed samples with compositions of 5, 15, 25, 35, 50, 65, 75 and 90 mol% O_2 to pressures of at least 10 GPa. In addition, we studied several compositions at pressures as high as 34 GPa. Below 10 GPa, the two components appear to be highly miscible. For N_2-rich samples, the vibron spectra of the cubic δ-N_2 phase suggest nonrandom mixing. The effects are especially noticeable above 11 GPa. It appears that O_2 molecules preferentially occupy one of the sites and that the preference varies with pressure and/or composition.

Conductivity of Mantle Rocks at Subsolidus Temperatures

We have measured the electrical conductivity of dunite, a representative mineral, to assist in the interpretation of data from sea-floor sounding.

Principal Investigator: S. Constable*
Co-Investigator: A. Duba

*Institute of Geophysics and Planetary Physics, University of California, San Diego.

Data on electrical conductivity of rock at high temperature below the sea floor are needed to interpret electromagnetic sounding data obtained from sea-floor controlled-source sounding (Cox *et al.*, 1988). Dunite is a representative mineral for this purpose. We measured the electrical conductivities of several samples of dunite from Jackson County, North Carolina, having minor (<10%) pyroxene and a grain size of approximately 1 mm. Our measurements encompassed the temperature range of 20 to 1200°C. We controlled the oxygen fugacity (fO_2) in the measurement environment by passing a CO_2:CO mix through the conductivity cell.

The conductivity of dunite is much less than that of other ultramafic rocks reported in the literature and is comparable to single crystals of olivine of similar composition. Although our measurements were not made under pressure, the effect of cracking due to thermal cycling was not evident in the highly reproducible results on reversible conductivity. Some hysteresis, amounting to 0.3 log units at most, appears to be dependent on heating and cooling rates and on fO_2. This result suggests changes in defect density and type as a function of temperature at fixed gas mix, although reversible reactions between olivine and other phases in the rock and on the grain boundaries might also affect conductivity.

It has been often suggested that values for single-crystal conductivity might be smaller than those for polycrystalline materials because of enhanced conduction along grain boundaries and the effects of phases other than olivine in the upper mantle. Our results do not support this notion.

Reference

Cox, C. S., S. C. Constable, A. D. Chave, and S. C. Webb (1988). "Controlled Source Electromagnetic Sounding of the Oceanic Lithosphere," *Nature* **320**, 52.

Measurement of Elastic Constants up to 2000 K

We have modified an existing apparatus and designed a new device to extend the limit of elastic-constant temperature measurements from 1700 to 2000 K.

Principal Investigator: T. Goto*
Co-Investigator: A. Duba

*Institute of Geophysics and Planetary Physics, University of California, Los Angeles.

Knowledge of high-temperature elastic properties of minerals is needed for an understanding of the physics of the deep earth. In this domain, high temperatures are those well above the Debye temperature, which is the temperature above which all thermal vibrations of a crystal lattice are excited. Because Debye temperatures of representative minerals range from 600 to 1100 K, data on elastic constants for temperatures well above 1000 K are of current geophysical interest.

The object of our project was to extend the limit of elastic-constant temperature measurements from 1700 to 2000 K. For non-iron-containing silicates, our problem was to extend previous measurements by modifying the existing experimental apparatus. For iron-bearing minerals, on the other hand, our problem was to design a new device that could stabilize the partial pressure of oxygen surrounding a sample to a low level as the temperature increased.

Our previous success in obtaining 1700 K for elasticity measurements was due to separation of transducers from the sample by long polycrystalline corundum buffer rods. The rods allowed the transducer to remain at less than 1000 K while the specimen attained higher temperatures. By redesigning our buffer rods to accommodate some distortion without destroying alignment, we performed experiments on Al_2O_3 up to 1825 K (Goto and Anderson, 1988). Increasing the temperature to 2000 K will require buffer rods made of zirconia. In addition, we have designed an apparatus to control the fugacity of our iron-containing sample at higher temperature and are now building this apparatus.

Reference

Goto, T., and O. L. Anderson (1988), "An Apparatus for Measuring Elastic Constants of Single Crystals by a Resonance Technique up to 1825 K," *Rev. Sci. Inst.* **59**, 1405.

Emission Spectra from Simple Shocked Solids

We are testing the use of molecular and vibrational spectroscopy for analyzing the chemistry of shock decomposition in simple molecular systems.

Principal Investigator: M. Nicol*
Co-Investigators: N. C. Holmes, H.-C. Cynn,* and S. Johnson*

---

*University of California, Los Angeles.

We are using the expertise available at UC Los Angeles in chemistry and spectroscopy at high pressures as well as that at LLNL in shock-wave generation and diagnostics to investigate the chemistry that occurs during shock compression of simple organic molecules. Our purpose is to understand the equations of state (EOS), transport properties, and chemical kinetics of planetary interiors.

Shock-wave studies of the EOSs of simple molecular compunds (CO, CH_4, C_6H_6, and N_2) suggest that these materials decompose at high shock pressures and temperatures. More complex organic compounds, including high explosives, also decompose during shock compression. Interpretations of the EOS data depend critically on assumptions about the products formed, their individual EOSs, and the rates of formation of the reaction products. Molecular spectroscopy might be used to identify products and intermediates of reactions and, in favorable cases, reaction kinetics. Thus, the goal of our project is to test the value of molecular electronic and vibrational spectroscopy for analyzing the chemistry of shock decomposition in simple molecular systems.

We have shown that for single- and double-shocked benzene specimens, the emission spectra are simply broad and thermal in character (Nicol *et al.*, 1988). Evidently, most of the reaction products are generated in their ground electronic states. This finding suggests that a technique that probes ground-state populations, such as absorption spectroscopy, may be usefully applied.

We have recently developed a new, double-beam, absorption spectroscopic instrument for use in shock-compression experiments. This instrument uses optical fibers for sample illumination and detection of the absorption signal. In our previous work on emission spectroscopy, we learned that closed-beam, lensless systems are preferable for shock experiments. We obtain the absorption spectrum with a novel dual-array, linear-diode-array detector. This detector allows simultaneous recording of the light input to the specimen holder and the light that passes twice through the shocked sample. The system can be gated to allow a time resolution of about 50 ns. We also added several photomultiplier detectors in narrow-wavelength bands to record the time dependence of the absorption.

Our preliminary results indicate that adequate spectra can be obtained on a single-shot basis in shock experiments on water and benzene. The time dependence of the signals agrees quantitatively with an optical model of the system as the shock moves through the sample. We plan to conduct experiments with this new apparatus in early 1989 to observe Mie scattering from carbon particles formed during shock decomposition of benzene.

Reference

Nicol, M., S. W. Johnson, and N. C. Holmes (1988), "Shock-Chemistry of Benzene as Revealed by Spectra From and Behind the Shock Front," *Shock Waves in Condensed Matter—1987*, S. C. Schmidt and N. C. Holmes, Eds. (North-Holland, Amsterdam), p. 99.

Transition-Metal Oxides and Silicates at Ultrahigh Pressures

After compressing Fe_2SiO_4 to pressures up to 85 GPa, we have discovered a new type of metastable glass at 300 K and have documented changes in optical and electrical properties as it is converted continuously to an amorphous state.

Principal Investigator: R. Jeanloz*
Co-Investigators: R. Reichlin, S. Martin,
Q. Williams,* and E. Knittle*

---

*University of California, Berkeley.

Experiments on fayalite (Fe_2SiO_4) to 30 GPa have suggested that this material might become metallic at a pressure of 80 GPa (Mao and Bell, 1972). Because of the importance of understanding the nature of the Fe-O bond at conditions in the earth's deep mantle, we compressed Fe_2SiO_4 up to 85 GPa. We discovered a new type of metastable glass at high pressures and at 300 K. Crystalline fayalite amorphizes at 41 ± 5 GPa, resulting in a significant change in electrical properties. Extrapolations of our results indicate that metallization of the glassy phase would not occur until pressures above 300 GPa, which are much higher than expected previously.

Because of its highly refractory nature, amorphous Fe_2SiO_4 has been produced only once before by conventional techniques (splat quenching). We found from Fourier-transform infrared spectroscopy that the pressure-amorphized fayalite is distinctly different in structure from the conventional (splat-quenched) glass. Our study is the first to document the changes in optical and electrical properties of a crystal as it is converted continuously to an amorphous state. We have demonstrated that novel glasses can be produced by high pressure.

Reference

Mao, H. K., and P. M. Bell (1972), "Electrical Conductivity and the Red Shift of Absorption in Olivine and Spinel at High Pressure," *Science* **176**, 403.

Institute for Scientific Computing Research

N. G. Smiriga

The Institute for Scientific Computing Research (ISCR) supports collaborative research in scientific computing between UC and LLNL. The goals of the Institute are to advance the state of the art in computer science and to foster research that strengthens the ties between the related disciplines of computer science and scientific computing.

Through the ISCR, LLNL's expertise in scientific computing and its computational facilities are made available to University researchers. The Institute also provides professional enrichment for LLNL scientists by encouraging collaborative and interdisciplinary work. Currently, the ISCR interacts mainly with faculty and students from UC Berkeley, UC Davis, and UC Los Angeles.

In FY88, the IR&D Program provided the ISCR with funding to support two postdoctoral fellows and to cover the Institute's administrative and secretarial costs. The ISCR also received substantial contributions from LLNL's Computation Department. During FY88, the ISCR supported three postdoctoral fellows who were jointly funded by the IR&D Program, the Physics Department, and the Computation Department.

Two of the ISCR postdoctoral fellows are performing research in computational fluid dynamics. Computational fluid dynamics is an essential element in many of the computer simulations of physical phenomena performed at the Laboratory. The topics under investigation include vortex methods to solve the incompressible Navier-Stokes equations and numerical simulation of self-similar shock refraction.

The third postdoctoral fellow is working on physics algorithms for massively parallel computers and on computer models of motion detection in vertebrate retina.

The ISCR organized two workshops in FY88. One examined the SISAL language; SISAL is a functional programming language designed to facilitate the writing and debugging of scientific applications on parallel processors. The second workshop had the dual objectives of bringing into focus the various research efforts on artificial neural networks scattered throughout the UC system and identifying research activities within LLNL that could benefit from the emerging technology of artificial neural networks.

Also during FY88, two conference rooms adjacent to the ISCR were renovated; the work was completed in January 1988. Since then, the Institute has been able to host seminars on a regular basis.

The ISCR received $185,000 in IR&D funds for FY88.

Physics Algorithms for Massively Parallel Computers

Principal Investigator: M. Colvin
Co-Investigators: A. Ladd, D. Frenkel,* G. Sugiyama, and B. Alder

*FOM Institute of Atomic and Molecular Physics, The Netherlands.

Most computational physics algorithms can be implemented on computers with up to several dozen processors, but these methods are unsuitable for the massively parallel computers (with hundreds or thousands of processors) that will be needed to simulate large-scale chemical or biological systems. We are developing algorithms for a variety of physics problems designed specifically for the massively parallel computers that will be available in the coming years.

There is much current interest in the use of lattice gas methods for solving the incompressible Navier-Stokes equations. The simplicity and regular structure of these methods makes them ideally suited for massively parallel computers. We first applied lattice gas methods to the simulation of two-dimensional Brownian motion. Our approach was to model the relatively slow motion of the solid particles using molecular dynamics and to model the fluid phase with a lattice gas (Ladd *et al.*, 1988) This algorithm has worked extremely well. At low solid densities, the theoretical results for the drag forces and suspension viscosity are reproduced correctly. Moreover, this algorithm is extremely fast, even on conventional computer architectures: systems with several hundred solid particles could be simulated on a desktop workstation. The results for the two-dimensional suspensions are so encouraging that we are extending the model to three dimensions.

We also applied lattice gas methods to the simulation of diffusion-limited aggregation (DLA). Experimental and theoretical studies have shown that under certain conditions, crystals grow into low-density, self-similar structures that can be characterized by a fractal dimension. Most DLA simulations model only the motions of the aggregating particles and ignore the potentially important hydrodynamic interactions between the growing crystal and the solvent. We developed a lattice gas model that accurately models the interaction of the solvent with the crystal and the aggregating particles and yields crystals with fractal dimensions in good agreement with experimental results (Figure 1).

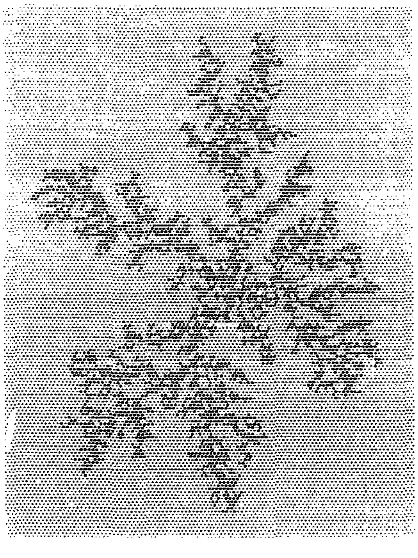

Figure 1. Crystal "grown" using the lattice gas model of diffusion-limited aggregation with simulated hydrodynamic interactions. The fractal dimension of the crystal in this simulation is 1.65, in good agreement with experimental results.

We also examined the application of quantum chemical calculations on parallel computers. Although such methods (used for the *ab initio* calculation of chemical properties of small molecules) have been adapted to parallel computers (Whiteside *et al.*, 1987), the large data sets and tightly coupled iterative algorithms severely constrain the number of processors that can be used efficiently. To overcome this difficulty, we are studying an alternative method, called quantum Monte Carlo (QMC), involving the stochastic evolution of electron configurations. In QMC, chemical properties are calculated by averaging over many random walks (typically millions). Since these random walks are independent, QMC is naturally adaptable to parallel computers with any plausible number of processors.

References

Ladd, A. J. C., M. E. Colvin, and D. Frenkel (1988), *Phys. Rev. Lett.* **60**, 975–978.

Whiteside, R. A., J. S. Binkley, M. E. Colvin, and H. F. Schaefer, III (1987), *J. Chem. Phys.* **86**, 2185–2193.

Computer Model of Motion Detection in the Vertebrate Retina

Principal Investigators: M. Colvin and F. Eeckman
Co-Investigators: Prof. F. Werblin,* G. Maguire,* P. Lukasiewicz,* J. Sasinowski,* and T. Axelrod

*University of California, Berkeley.

A computer model of the retina of the eye would make it possible to test hypotheses about retina function and would help in the design of synthetic motion-detection systems As the first step toward such a model, we have developed a detailed simulation of the small functional units believed to mediate movement detection in the retina of the Tiger Salamander.

The detection of motion, either to locate prey or to detect hostile predators, is one of the most important functions of the visual system. There is evidence that in many animals, motion detection takes place in the retina. Research over the past century has yielded a wealth of anatomical and physiological data about the retina, but we still do not have a complete understanding of how the retina transforms visual data. A detailed computer model of the retina, based on existing data, could provide an important framework for new experimental data and would allow the testing of hypotheses about retina function. Such a computer model would also be very useful in suggesting design principles for synthetic motion-detection systems.

Our goal is to develop a general computer model of the vertebrate retina. As the first step, we have developed a detailed simulation of the small functional units believed to mediate movement detection in the retina of the Tiger Salamander. These so-called movement-gated subunits consist of three cell types, two of which are responsible for detecting the arrival or departure of the target while the third acts as a lateral inhibitory element. Our present simulation consists of an interactive neural network program that closely mimics the response of each of the various cell types (see Figure 1). The model exhibits behavior that is consistent with known biological data and acts as a movement detector with preferred and null-target directions.

We are presently extending our model to simulate an interacting two-dimensional array of these subunits. Future work will involve a more detailed simulation of the individual neurons and the inclusion of more retinal cell types.

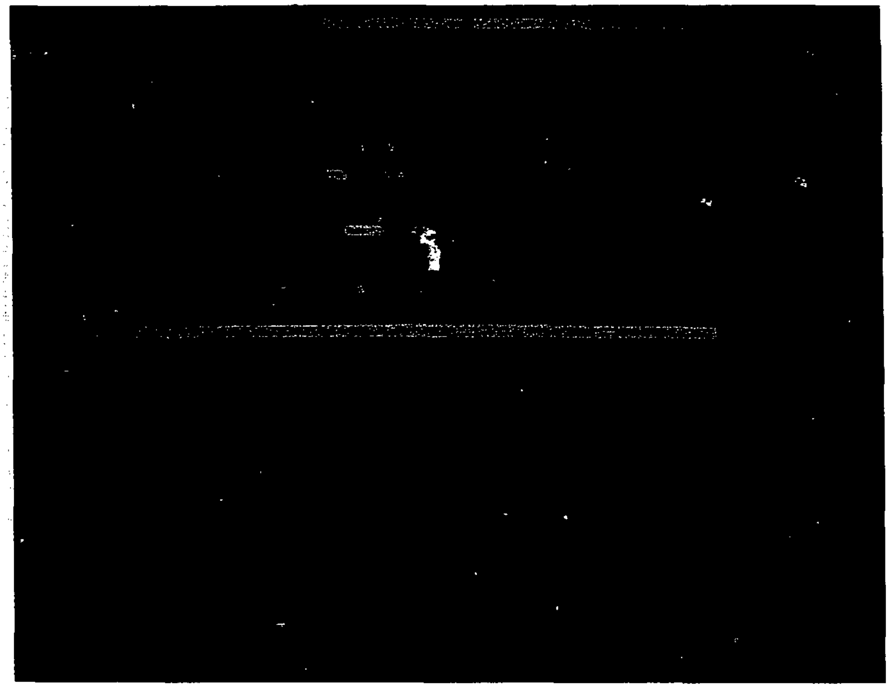

Figure 1. Photograph of the computer screen showing our interactive computer model of the motion-detection subunit in the retina. The rectangular and octagonal boxes represent different retinal neurons; their levels of excitation are denoted by the different colors. The excitation levels are also displayed in oscilloscope traces at the bottom of the screen.

Advanced Algorithms in Computational Fluid Dynamics

Our work on computational fluid dynamics has focused on two different areas: development of fast vortex methods for viscous incompressible fluid flow, and computation of the refraction of a shock wave at an oblique interface between two inviscid compressible gases.

Principal Investigator: E. G. Puckett
Co-Investigators: S. Baden,[*] P. Colella, L. F. Henderson,[†] and M. Welcome

[*]Lawrence Berkeley Laboratory, Berkeley, CA.
[†]University of Sydney, Australia.

Many problems in physics require the modeling of fluid flows. We may be able to address a number of these by using vortex methods to solve the incompressible Navier-Stokes equations. Vortex methods are particle methods that carry information about the vorticity in the flow being modeled and allow particles to be concentrated in regions of high vorticity. Their principal drawback is the amount of computational effort needed to compute the velocity field induced by the particles.

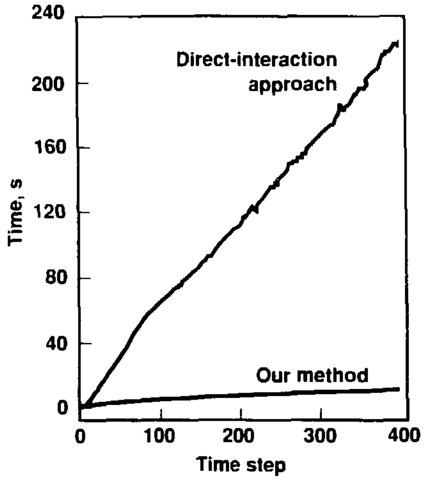

Figure 1. Comparison of computational speed for our hybrid vortex method and a conventional direct-interaction approach for calculating viscous incompressible flow. Our method is at least ten times faster.

We have developed a fast vortex method for modeling viscous, incompressible flow in a box. This is the first fast implementation of a fully viscous, hybrid vortex method. Vortex sheets are generated to model vorticity production near boundaries, and these subsequently diffuse into the interior of the computational domain, where they are converted into vortex blobs (Chorin, 1973 and 1978). Our approach is a modification of Anderson's (1986) method of local corrections (MLC), extended to include viscous effects. Compared to traditional implementations of the vortex method, our method is at least ten times faster (Figure 1). This work has established the feasibility of doing large, detailed computations using the hybrid vortex method.

We are also investigating the self-similar refraction of a shock wave by an oblique interface between two gases. Our initial effort was to compute the case in which the fluid containing the incident shock has a lower sound speed than the fluid on the other side of the interface (the slow-fast case). We used a version of the adaptive-mesh-refinement algorithm of Berger and Colella (1988), coupled with a multifluid algorithm to handle the interface between the two gases. We have obtained excellent agreement with the experimental results reported in Abd-el-Fattah and Henderson (1978) and have been able to correlate the experimentally observed wave patterns to the inviscid nonlinear waves in the calculation.

References

Abd-el-Fattah, A. M., and L. F. Henderson (1978), "Shock Waves at a Slow-Fast Gas Interface," *J. Fluid Mech.* **89**, 79–85.

Anderson, C. (1986), "A Method of Local Corrections for Computing the Velocity Field Due to a Distribution of Vortex Blobs," *J. Comp. Phys.* **62**, 111–123.

Berger, M. J., and P. Colella (1988), *Local Adaptive Mesh Refinement for Shock Hydrodynamics*, Lawrence Livermore National Laboratory, Preprint UCRL-97196.

Chorin, A. J. (1973), "Numerical Study of Slightly Viscous Flow," *J. Fluid Mech.* **57**, 795–796.

Chorin, A. J. (1978), "Vortex Sheet Approximation of Boundary Layers," *J. Comp. Phys.* **27**, 428–442.

Plasma Physics Research Institute

J. Killeen

The Plasma Physics Research Institute (PPRI) was established in 1987 as a joint UC-LLNL organization. Its purpose is to strengthen basic and applied research in plasma science throughout the University. The PPRI makes the facilities and expertise of LLNL more available to campus scholars in fields of interest to the Institute. Research on fundamental issues in plasma physics is its primary focus. The PPRI receives support from the IR&D Program, from the Department of Applied Science at UC Davis, and from other LLNL programs.

In FY88, the program of the PPRI consisted of three elements:

- The Davis Diverted Tokamak.
- A joint LLNL-UC Berkeley particle-simulation project.
- A summer program sponsoring research by a visiting scientist on radiofrequency (rf) heating and current drive in tokamaks.

The Davis Diverted Tokamak is so named because it employs a magnetic field configured to divert (eliminate) unstable edge plasmas, thus creating a more coherent plasma. This magnetic field is called a divertor. The design of the tokamak was guided by the Tokamak Simulation Code (TSC), provided by Princeton Plasma Physics Laboratory. Our investigations will focus on how the divertor affects the confinement and stability of the plasma.

Our particle-simulation project consists of adding new capabilities to the one-dimensional, relativistic, electrostatic particle code TESS. This code makes it possible to simulate particle confinement in simple and tandem-mirror plasmas. In FY88, we added models that simulate energy diffusion in the plasma and plasma heating by charge-exchange and impact-ionization processes.

The FY88 summer program sponsored the development of a computer code to simulate parametric instabilities in tokamak plasmas penetrated by lower-hybrid rf waves.

These projects will be continued in FY89, and several new ones will be started, including the following:

- Theoretical and computational plasma astrophysics (UC Berkeley).
- Statistical dynamics of multi-field models for plasma turbulence (UC San Diego).
- Numerical simulation of rf experiments in the ionosphere (UCLA).
- Basic plasma physics research in inertial confinement fusion (UC Davis).
- Nighttime ionospheric cavitons generated by high-frequency radio waves (UCLA).

In FY88, the PPRI received $150,000 in IR&D funds.

The Davis Diverted Tokamak

In the Davis Diverted Tokamak, a magnetic field is used to divert or eliminate unstable edge plasmas, thus creating a more coherent plasma. We are studying how the divertor affects the confinement and stability of the plasma.

Principal Investigators: D. Hwang*
Co-Investigators: D. E. Shumaker, K. Mizuno,* G. Dimonte, B. I. Cohen, D. Flittner,* and T. Hillyer*

*University of California, Davis.

In FY88, we made progress on the construction and assembly of the Davis Diverted Tokamak (DDT). The DDT is now ready for experimental operation. We obtained two X-band, tunable (8.6–9.5-GHz) microwave transmitter systems capable of delivering 250 kW each for up to 2 µs. We also obtained microwave diagnostic and transport equipment to deliver power into the DDT vacuum chamber. Electrical power has been installed in the laboratory, and we are currently installing the microwave systems, which should be operational by the end of 1988. We designed an initial set of plasma and microwave diagnostics, including electromagnetic loop probes and Langmuir probes; these will be fabricated at UC Davis. We also built a discharge-plasma source to produce the low-density plasma required to match the frequency range of the X-band microwave sources.

The use of a magnetic field as a divertor has been shown to enhance the plasma containment properties of a tokamak. However, the introduction of divertors causes axisymmetric plasma instability to become a problem. Up to now, this instability has been corrected by using passive conductors and active feedback systems, both of which can be costly. Experimental results in the literature show that the axisymmetric instability is nonlinear and grows on a time scale corresponding to the *L*/*R* time of the plasma (L = inductance and R = resistance). Recent experiments have shown that lower-hybrid rf waves can control the profile of the plasma current and thus modify the resistance and inductance of the plasma.

In FY89, we will conduct experiments using lower-hybrid current drive to remedy the axisymmetric instability. Lower-hybrid current drive has been shown to produce electron distributions that appear to contain an anisotropic high-energy tail. This condition could produce a plasma that is less collisional, and thus lower in resistivity, on the outside. For a given loop voltage, such plasma parameters should lead to a redistribution of the current, with a large fraction of the current flowing on the plasma surface. This change in the current profile will produce a large change in the plasma inductance.

Our lower-hybrid stabilization experiments will be conducted with a 50-kW klystron system, used at 800 MHz at the Princeton Plasma Physics Laboratory. The Princeton data show that this system is capable of modifying the plasma current up to an electron density of about $1 \times 10^{13}/\text{cm}^3$. This density is ideally suited for the DDT since the operating density range is about $1 \times 10^{13}/\text{cm}^3$.

We also plan to use the DDT facility to investigate beat-wave current drive. In this type of experiment, two counterstreaming electromagnetic waves mix nonlinearly to generate plasma waves that, in turn, produce directed energetic electrons through Landau damping. This investigation will provide a basis for future microwave tokamak experiments utilizing millimeter-induction, free-electron lasers. For sake of economy, we will tailor these experiments around our X-band microwave sources, which were available on the surplus market and which produce sufficiently short wavelengths for geometric optics to apply.

Joint LLNL/UCB Particle-Simulation Project

We are adding new capabilities to the TESS particle-simulation code.

Principal Investigator: R. Procassini*
Co-Investigators: E. Morse,*
C. K. Birdsall,* J. Cummings,* and
B. I. Cohen

---

*University of California, Berkeley.

The one-dimensional (axial), relativistic, electrostatic particle code TESS makes it possible to simulate particle confinement in simple and tandem-mirror plasmas. In FY88, we made a number of advances in the development of TESS. Specifically, we added:

- A quasilinear, radiofrequency energy diffusion model for both ion-cyclotron resonance plasma heating and relativistic electron-cyclotron resonance plasma heating.
- A neutral-beam injection model that simulates plasma heating via charge-exchange and impact-ionization processes.

The balance of TESS consists of a basic electrostatic particle code, which uses a direct implicit scheme to advance particle trajectories and field quantities, and a Monte Carlo, binary, particle-collision model. The code has been used to investigate the collisional loss processes in an auxiliary-heated, tandem-mirror plasma.

In FY89, we plan to modify TESS to allow the kinetic simulation of plasma-surface interactions at the divertor plate of a tokamak. The code will then be capable of studying the effects of recycled plasma on the collector-sheath potential drop and will provide a self-consistent simulation of plate erosion due to sputtering and redeposition of sputtered material.

Intense Lower-Hybrid Wave Penetration into Magnetized Fusion Plasma

In the summer of 1988, the PPRI sponsored research by a visiting scientist on radiofrequency heating and current drive in tokamaks.

Principal Investigator: M. Porkolab*

*Massachusetts Institute of Technology, Cambridge, MA.

The prospect of achieving intense, pulsed radiofrequency waves in the X-band regime (8–10 GHz) with a relativistic klystron creates new possibilities for lower-hybrid wave penetration in high-temperature, reactor-grade, magnetized fusion plasma. For example, the steady-state version of the International Thermonuclear Experimental Reactor (ITER), which is now being studied by an international group of scientists at Garching, Federal Republic of Germany, yields tens of megawatts of lower-hybrid power for driving toroidal currents. Although, to date, lower-hybrid power has produced the most impressive toroidal current-drive results by noninductive means, its applicability in reactor-grade plasmas is thought to be restricted to the plasma periphery because of Landau damping at electron temperatures greater than 15 keV. Nevertheless, high-intensity, lower-hybrid waves may, in fact, penetrate to the core of the tokamak plasma by flattening the electron-distribution function, thereby reducing Landau damping.

An important issue connected with this wave penetration is the potential severity of nonlinear effects, such as parametric instabilities. In FY88, the PPRI Summer Program sponsored the development of a code that simulates such nonlinear phenomena, even in the presence of very intense electric fields (about 200 kV/cm). Under these conditions, the commonly used theory of weak parametric instabilities is not satisfied. The results of our calculations have been reported (Killeen, 1988).

Reference

Killeen, J. (1988), *The Plasma Physics Research Institute, Annual Review*, Lawrence Livermore National Laboratory, internal report. (Readers wishing to obtain copies of this document should contact the author.)

Program for Analytical Cytology

B. H. Mayall

The Program for Analytical Cytology (PAC) fosters collaborative research, promotes scientific progress, and facilitates technology transfer in the field of analytical cytology. By means of analytical cytology, we can quantify the properties of individual cells and investigate the distribution of such properties across a population of cells, rather than merely measuring in a test tube the average characteristics of many cells. The PAC serves as a scientific and institutional bridge between LLNL and campuses of the University of California, particularly UC San Francisco. As a result of PAC projects, we are seeing benefits to the biomedical research community, primarily at UC San Francisco, and increasingly at the Berkeley, Davis, and Los Angeles campuses. PAC activities are contributing significantly to the diagnosis, understanding, and treatment of many diseases, and have made UC San Francisco a world leader in clinical applications of analytical cytology.

The PAC uses funding from the UC Regents to award many small grants for innovative and collaborative research projects. LLNL and UC San Francisco provide matching funds primarily to support administration and teaching; additional gifts from industry support postdoctoral fellows. The PAC awards permit researchers to collect preliminary data and to demonstrate the feasibility of their investigations. More than one-half of the PAC awards have evolved into ongoing projects. Grants from the National Institutes of Health now support the mature collaborative research projects of proven potential.

Early in FY88, the future of the PAC research grants was uncertain because the University of California defined new guidelines for distributing nuclear science funds. The University initiated the Institutional Collaborative Research Program (INCOR) and invited applicants to compete for INCOR funding; the PAC was one of only four proposals approved for funding. This reflects recognition of past achievements by the PAC, the need for nuclear science funds to continue and strengthen the PAC mini-award program, and the potential for the PAC to make substantial contributions in the future.

A primary scientific interest of the PAC is to advance image cytometry at LLNL and its application at UC campuses. Image cytometry combines optical microscopy and digital image processing in a quantitative approach that permits detailed analysis of large numbers of cells prepared on a glass slide. This technique is emerging as a crucial approach for analytical cytology, and LLNL is pioneering many of the new applications of image cytometry.

In the following short articles, we highlight five PAC efforts during FY88. The first two are based on application of the glycophorin-A (GPA) assay developed at LLNL. This assay is an extraordinarily sensitive test that uses monoclonal antibodies against the M and N types of GPA, the two variant types found on the surface of human red blood cells. One project uses this assay to monitor changes associated with the aging of red blood cells. The other uses this assay to monitor mutations induced in cancer patients undergoing chemotherapy with mutagenic drugs. In the third article, LLNL approaches to quantifying the DNA content of tumor cells are applied in human breast cancer to evaluate progression of the disease, to find the stage at which major changes occur in cellular DNA content, and to relate such changes to the clinical course of the disease. The project described in the fourth article uses cytokinetic techniques to analyze the proliferative behavior of human brain tumors and to relate their cellular proliferation to the clinical outcome. In the final project, basic techniques of analytical cytology are used to investigate fundamental mechanisms of the body's immunologic defenses.

The Program for Analytical Cytology received $190,000 in IR&D funds in FY88.

Red Cell Density and Aging

We are developing transfusion products enriched with low-density red cells that may increase the transfusion interval for patients with chronic anemia.

Principal Investigator: L. Corash*
Co-Investigators: R. Langlois, R. Jensen, and M. Clark*

*University of California, San Francisco

The purpose of our project is to determine if cellular density increases progressively as red cells age *in vivo*. If density is proven to be an age-dependent characteristic, then separating red cells by density from whole blood may provide a means to prepare transfusion products depleted of old red cells and enriched with young cells. Such enhanced products could reduce the frequency of transfusion for patients with chronic anemia and could reduce the toxicity associated with excessive iron accumulation during long-term transfusions.

We have developed a technique in which red cells bearing the glycophorin-A (GPA) antigenic phenotype NN can be identified when mixed with either GPA MN or GPA MM cells. The M antigen can be detected using a monoclonal antibody directed against the M phenotype. Patients with chronic, stable anemia and either the MM or MN phenotype are transfused with NN red cells, and the density distribution of these cells is followed as the transfused cells age *in vivo*. In this way, the effect of *in vivo* aging on red cell density can be examined. After initial studies with unfractionated red cells, density-dependent cohorts of NN cells are prepared and transfused into MM or MN recipients to measure the survival and density distribution of low- and high-density cells. If we confirm that low-density red cells survive in the circulation longer than the unfractionated cells, then units of such cells will be used for transfusion support of patients with chronic anemia to confirm that the transfusion interval can be increased under clinical conditions.

The specific aims of this project are to:

- Use monoclonal antibodies directed against the M and N types of GPA to detect small numbers of NN red cells among a larger population of MN red cells.
- Prepare *in vitro* mixtures of NN and MN cells that mimic the proportions of these cell types in an *in vivo* human transfusion experiment in which NN cells will be transfused into MN individuals.
- Examine the concentration of N and M types of GPA on red cells of various densities after density-dependent fractionation (necessary to ascertain whether concentrations of these surface antigens vary with cell density).

This year, we instituted the GPA assay in our laboratory and demonstrated that we could detect NN cells mixed with MN cells in a ratio of 1:2000, well within the working limits required to perform our proposed experiments. We also showed that we could isolate either high- or low-density NN cohorts, mix them with unfractionated MN red cells, and then detect expected numbers of NN cells in the correct density fraction after density-gradient centrifugation. After adapting the technique for detecting small numbers of NN cells mixed with MM or MN cells, we prepared artificial mixtures of MN and NN cells, separated them into density-dependent fractions, and determined the coefficient of variation for detection of a 1:2000 mixture of NN and MN cells. This coefficient was less than 5%, an acceptable level.

Our first patient had myelodysplasia with a stable, chronic transfusion requirement. The patient, whose red cell phenotype was MN, was transfused with unfractionated NN cells. We obtained 5-ml blood samples weekly for analysis of density distribution of the transfused NN cells as they aged *in vivo*. The density distribution of the recipient's autologous NM-positive cells was stable, and we detected the transfused NN-positive cells with adequate precision. We then used red cell fractions enriched with either low- or high-density cells. We are evaluating a new cell-separation system to ensure that it can provide cell fractions that are adequately enriched with low- and high-density cells.

We are now seeking other patients with the correct clinical state to participate in the project. Our work may provide the potential for improved transfusion support of patients with chronic anemia and a new means to measure red cell survival.

Detecting Somatic Cell Mutations Using the Glycophorin-A Assay

We have found evidence of the in vivo *induction of null variant red cells in blood samples from cancer patients undergoing chemotherapy with mutagenic drugs.*

Principal Investigator: S. Saks*
Co-Investigators: W. L. Bigbee, R. H. Jensen, E. C. Cadman,* and H. Jaffe*

*University of California, San Francisco.

LLNL scientists have recently developed a new human *in vivo* somatic cell mutation assay based on immunologic detection and flow-sorter enumeration of variant red cells that fail to express a normally present cell-surface antigen. We are applying this assay to blood samples from cancer patients undergoing chemotherapy with mutagenic drugs. Our aim is to validate the genetic basis of the assay by determining whether elevated frequencies of glycophorin-A (GPA) "null" cells can be demonstrated in these individuals.

We screened cancer patients of the Oncology Clinics at UC San Francisco for individuals with the required clinical histories who were undergoing appropriate chemotherapy. We compared the frequency of GPA variant red cells in blood samples from patients treated with several classes of mutagenic chemotherapy with the variant cell frequency observed in normal subjects.

Blood samples from 85 cancer patients were encoded to ensure anonymity in a blind study. Because the GPA assay requires blood of the heterozygous MN type, samples were first serotyped using commercial anti-M and anti-N sera. Because 52% of the general population are MN heterozygotes, we expected about one-half of the patients to have the required MN blood type. Blood samples from 41 patients were typed as MN and run in the assay; after eliminating patients with incomplete clinical histories or confirmation of recent blood transfusion, the study population was reduced to 30 individuals.

The patients were diagnosed with a variety of malignancies, including breast cancer, colon cancer, Hodgkin's disease, and malignant melanoma. Treatments included a variety of mutagenic agents, such as adriamycin, bleomycin, *cis*-platinum, and dicarbazine, and sometimes involved other non- or weakly mutagenic agents. In addition to each patient's current chemotherapy treatment, we obtained other clinical data and collected blood samples at random times before, during, and after chemotherapy.

Red cells from MN samples were labeled with monoclonal antibodies and analyzed on a dual-beam sorter using the 1W1 version of our GPA assay. This version measures the frequency of variant cells that have lost expression of the GPA(M) allele while retaining expression of the sister GPA(N) allele. Data were calculated as the frequency of N null-variant cells per million normal cells, which we call the variant frequency.

For statistical analysis, samples were placed into a pretherapy group and four other groups defined by the time a sample was obtained relative to the course of treatment. Table 1 shows a generally consistent and statistically significant effect of

Table 1. GPA variant frequencies in UC San Francisco patients.

Sample group	Days	Samples	Variant frequency per million cells: Range	Median	Mean ± SD*	$p^{\dagger}$
Pretherapy	—	22	4 – 23	11.0	11.9 ± 5.4	—
Early therapy	4 – 93	15	2 – 171	19.0	32.1 ± 41.7	0.004
Late therapy	120 – 335	11	5 – 53	36.0	31.7 ± 17.3	0.001
Early post-therapy	12 – 101	6	29 – 120	40.0	56.5 ± 34.0	<0.001
Late post-therapy	132 – 4126	6	2 – 26	21.0	17.8 ± 8.7	0.030

*Standard deviation.

[†] Mann-Whitney statistic compared to all pretherapy cohorts.

chemotherapy, despite the heterogeneous patient population. Variant frequencies increased during therapy, reached a maximum of about fivefold over the pretherapy level at or shortly after the end of therapy, and then declined to near pretherapy levels within six months. Thus, our study provides clear evidence of the induction *in vivo* of null variant red cells by mutagenic chemotherapy. The time of appearance and persistence of induced variants suggests that cells at maximum risk for mutagenic damage by these agents are the rapidly cycling erythroid precursor population.

We are now studying breast cancer patients receiving standardized treatments with adriamycin and cyclophosphamide. We also plan to study patients receiving other agents thought to be stem-cell mutagens. Some cancer patients receiving chemotherapy with mutagens are at excess risk of secondary cancer, mainly acute leukemia and lymphoma. Thus, certain chemotherapeutic agents may induce a carcinogenic potential from persistent *in vivo* mutational damage to hemopoietic stem cells. If *in vivo* mutagenesis is related to cancer risk, then quantification of induced *in vivo* somatic cell mutation using the GPA assay may become a predictor of the ultimate risk of developing malignancy.

Reference

Bigbee, W. L., R. G. Langlois, R. H. Jensen, A. W. Wyrobek, and R. B. Everson (1987). "Chemotherapy with Mutagenic Agents Elevates the *In Vivo* Frequency of Glycophorin A 'Null' Variant Erythrocytes." *Environ. Mutagen.* **9** (8), 14.

Viability of Primary Human Breast Cancers

We have found that hyperdiploid cells usually do not grow in cell culture, whereas diploid breast cancer cells proliferate well. Failure to see hyperdiploid cells cultured from breast cancers is due to their poor viability.

Principal Investigator: H. S. Smith*
Co-Investigators: J. W. Gray, B. H. Mayall, and B.-M. Ljung†

*University of California, San Francisco, and Peralta Cancer Research Institute, Oakland, CA.
†University of California, San Francisco.

The goal of our study was to characterize the properties of hyperdiploid populations found in many breast cancers. Hyperdiploidy refers to cells containing more than 46 chromosomes, the human diploid number. We wanted to challenge suggestions that the diploid cells cultured from breast cancers are nonmalignant in origin because it seemed possible that another isolation technique might readily detect true cancer cells, those with hyperdiploid DNA contents.

Much evidence suggests that the cells responsible for metastatic breast cancer are aneuploid (nondiploid). Hence, the ability to isolate those cells capable of metastatic growth from primary breast cancers is important for both a clinical and a basic understanding of the disease process. However, there is a paradox in that many breast cancers contain a large proportion of cells with hyperdiploid DNA content. In contrast, cells cultured from primary breast cancers are uniformly diploid. It is essential to understand where in the process of isolation or culture the aneuploid cells are lost.

We used image cytometric techniques rather than flow systems for our studies because of the limited number of cells available for study. We evaluated specimens for DNA content before and after different isolation procedures. Populations isolated by gentle mechanical dissociation were enriched in hyperdiploid cells, whereas populations isolated from the same breast carcinomas by enzymatic digestion were enriched for diploid populations. We found that the mechanically dissociated material grew poorly in culture. Further studies of this phenomenon revealed that the majority of cells in most mechanically dissociated samples were nonviable by dye exclusion. In contrast, the enzymatically digested material was uniformly viable.

Subsequent experiments revealed that the nonviable cells were not an artifact of sample preparation or of the time delay from commencement of surgery to specimen acquisition in the research laboratory. Tumor cells acquired by fine-needle aspiration cytology prior to surgery and assayed immediately also contained a variable but often sizable proportion of nonviable cells.

We conclude that hyperdiploid cells are not readily cultured from primary breast cancers because few of them are viable. Techniques that enrich for hyperdiploid cells also enrich for nonviable cells, whereas techniques that enrich for viable cells favor diploid populations. Therefore, regardless of the technique used, only a small subpopulation of viable cells is hyperdiploid. Thus, viable aneuploid populations, which have been hypothesized to represent those cancer cells capable of metastatic growth, are actually only a small component of most breast cancers.

References

Dairkee, S. H., B. H. Mayall, H. S. Smith, and A. J. Hackett (1987). "A Marker that Predicts Early Recurrence of Breast Cancer" (letter). *Lancet* **8532**, 514.

Smith, H. S., B.-M. Ljung, B. H. Mayall, S. S. Sylvester, and A. J. Hackett (1987). "Cellular Manifestations of Human Breast Cancer." *Cellular and Molecular Biology of Experimental Mammary Cancer.* D. Medina, W. Kidwell, G. Heppner, and E. Anderson, Eds. (Plenum Press, New York, NY).

Smith, H. S., S. H. Dairkee , B.-M. Ljung, B. H. Mayall, S. S. Sylvester, and A. J. Hackett (1986). "Clonal Manifestations of Human Breast Cancer." Ce*llular and Modular Biology of Experimental Mammary Cancer*. D. Medine, W. Kedwell, G. Heppner, and E. Anderson, Eds. (Plenum Press, New York, NY).

Smith, H. S., S. R. Wolman, G. Auer, and A. J. Hackett (1986). "Cell Culture Studies: A Perspective on Malignant Progression of Human Breast Cancer." *Breast Cancer: Origins, Detection, and Treatment.* M. A. Rich, J. C. Hager, and J. Taylor-Papadimitriou, Eds. (Martinus Nijhoff, Boston, MA), pp. 31–49.

Human Brain Tumors Classified by Cytometry

For patients with brain tumors, we are developing and evaluating BrdUrd-labeling procedures to measure cellular predictors of tumor growth.

Principal Investigator: J. Murovic*
Co-Investigators: J. W. Gray and T. Hoshino*

---

*University of California, San Francisco.

Because brain tumors grow within a closed cavity, fatality depends critically on the size or rate of tumor growth. Biological determination of the degree of cellular abnormality in primary brain tumors has been important in estimating the prognosis of patients and predicting the effects of drugs and radiation on the tumor. Quantification of the proliferative capacity of tumors with flow cytometry and immunocytochemistry will greatly enhance our ability to predict tumor behavior.

Our objective was to develop an improved bromodeoxyuridine (BrdUrd) staining procedure and multivariate analysis on human specimens and to establish the protocol of BrdUrd administration. The goal was to measure cellular predictors of tumor growth (e.g., rate of DNA synthesis, cell cycle time, growth fraction) and to correlate these findings with serial computed tomography scans.

Sixteen patients with brain tumors were given a 30–60-min intravenous infusion of BrdUrd at 200 mg/m^2. Fragments from biopsied tumor specimens were divided into two portions. One portion was dissociated into single cells, stained with fluorescein isothiocyanate (FITC), using anti-BrdUrd monoclonal antibody as the first antibody, stained with propidium iodide (for DNA), and then analyzed by flow cytometry. We calculated the labeling index (LI) as the number of FITC-labeled cells expressed as the percentage of total cells analyzed. The other portion was stained with immunoperoxidase using anti-BrdUrd monoclonal antibody as the first antibody. We calculated the LI of these tissue sections in two ways: from selected areas in which the labeled cells were evenly distributed, and from the entire tissue section. The LIs obtained by flow cytometry correlated closely with those from entire tissue sections and were usually lower than the LIs from selected areas of tissue sections. The LIs determined by flow cytometry also correlated well with those from selected areas of tissue sections. Thus, the flow-cytometry-derived LI and the tissue-derived LI provide useful information for predicting biological behavior of individual tumors and for designing treatment regimens for patients with brain tumors. Different standards, however, must be used to interpret the LIs obtained by these two methods.

We also analyzed paraffin-embedded specimens of brain tumors from 256 patients who had received an intravenous infusion of BrdUrd during craniotomy. We used DNA flow cytometry to determine the modal population. A single G1 peak indicates a unimodal DNA population; two or more G1 peaks indicate a multimodal population. Most pituitary tumors and moderately anaplastic astrocytomas had unimodal DNA populations, whereas a higher percentage of other slow-growing tumors had multimodal populations. A similarly high percentage of the rapidly growing brain tumors also had multimodal populations. In most tumor groups, however, the percent of tumors with multimodal DNA populations did not correlate with the BrdUrd labeling index or the percent of BrdUrd-labeled cells. Thus, analysis of DNA distribution by flow cytometry may provide information about the degree of heterogeneity and the biological behavior of individual brain tumors, but the results do not necessarily correlate with the rate of tumor growth or the prognosis in individual patients.

References

Cho, K. G., T. Nagashima, S. Barnwell, and T. Hoshino (1988), "Flow Cytometric Determination of Model DNA Population in Relation to Proliferative Potential of Human Intracranial Neoplasms," *J. Neurosurg.* **68**, 588–592.

Nagashima, R., T. Hoshino, K. G. Cho, M. Senegor, F. Waldman, and K. Nomura (1988), "Comparison of Bromodeoxyuridine Labeling Indices from Tissue Sections and Flow Cytometry of Brain Tumors," *J. Neurosurg.* **68**, 388–392.

Molecular Regulation of Complement Activation

We are using analytical cytology to investigate complement mechanisms that are of fundamental importance to the body's immunologic defenses against many bacterial infections.

Principal Investigator: G. A. Jarvis*
Co-Investigators: R. Langlois and
J. M. Griffiss*

---

*University of California, San Francisco.

The primary immunologic barrier to bacterial infection depends on a two-step process. First, antibodies from the host recognize and attach to antigens on the surface of bacteria. Second, a system of proteins, known as complement, recognizes the antibody-antigen complex and kills the antibody-coated bacteria by lysing its membrane. For infection by the bacteria *Neisseria meningitidis*, resistance to disease is correlated with the formation of strain-specific bactericidal activity. The mechanism is antibody-dependent, complement-mediated immune lysis. The classical pathway (CP) of complement activation has long been assumed to be the principal effector pathway.

Recently however, two human families with multiple cases of fatal, fulminant (group B, C, and Y) meningococcal infection have been identified. These cases suggest that the alternative complement pathway (ACP) is important for protection against meningococcal disease. In addition, fully encapsulated (group B) meningococci and K1 *Escherichia coli*, in the absence of host-acquired immunity, have been found to resist the activity of the ACP. Resistance was dependent on production of an identical K polysaccharide homopolymer of sialic acid by both organisms.

Our objective was to define the contribution of the ACP to host defense against gram-negative infection and to understand the ACP regulatory role of K polysaccharides using *E. coli* and *N. meningitidis* as target cells as models. We hypothesized that production of K polysaccharides reduces ACP activation with variable degrees of efficiency related to quantitative and structural differences, and that a specific antibody augments ACP activation by either the increased efficiency or extent of ACP activation.

Our specific aims were twofold. First, we attempted to determine whether there are quantitative differences in the capacity of K polysaccharides of different structural or chemical families to regulate ACP activation. We used flow cytometry to quantify K polysaccharide expression by and ACP component binding to bacteria. Second, we used flow cytometry to determine the effect of K polysaccharide antibody on the kinetics of binding ACP components to specific groups of *N. meningitidis* and *E. coli*.

We used a fluorescein-labeled anti-K polysaccharide monoclone and a FACS II flow cytometer. We found interstrain differences in the quantity of K polysaccharide produced by various strains of group B *N. meningitidis*. We also found intrastrain differences in K polysaccharide production depending on the growth phase of the bacterial cell. Thus, we can group strains based on the quantity of K polysaccharide they produce. We also identified subpopulations of cells that produced exceptionally high amounts of K polysaccharide, a finding that led us to propose that this group of high-producer cells resists killing by complement in the blood and produces septicemia.

In *N. gonorrhoeae*, we used a FACS II flow cytometer and a monoclonal antibody directed at a lipo-oligosaccharide (LOS) epitope (antigenic determinant) to define the dynamics of LOS expression over time. LOS is an important molecule for the serum resistance of this organism. We found a reduction in fluorescence (monoclonal binding) in the entire population as growth progressed from 2 to 8 hours in culture. This result indicates that the density of LOS expression was a function of the time of growth and that variable LOS expression at the single-cell level may affect the outcome of the bacterial-complement interaction.

In other work, we concluded that the degree to which strains of *N. meningitidis* are lysed and killed in human serum is a function of strain-specific binding of properdin, which is one of the initiators of ACP. Our most recent investigations used flow cytometry to quantify simultaneously K polysaccharide production by and complement component binding to *N. meningitidis*. We found, for two group B strains, a correlation between increased K polysaccharide production and decreased complement C3 deposition. These investigations confirm the importance of ACP in defending the host against *N. meningitidis* infection.

References

Apicella, M. A., M. Shero, G. A. Jarvis, J. M Griffiss, R. E. Mandrell, and H. Schneider (1987). "Phenotypic Variation in Epitope Expression of the Neisseria Gonorrhoeae Lipooligosaccharide." *Infect Immun* **55**, 1755–1761.

Jarvis, G. A., H. Schneider, M. K. Albertson, and J. M. Griffiss (1988). "Strain-Specific Directed Binding of Properdin Accounts for Variable Lysis of Neisseria Gonorrhoeae." *Gonococci and Meningococci*, J. T. Poolman *et al.*, Eds. (Martinus Nijhoff, Dordrecht, The Netherlands).

I ◆ R ◆ & ◆ D

Resource Requirements
& Author Index

Lawrence Livermore National Laboratory

FY88 Budget

Institutional Research and Development Program

	FY88 actual cost, thousands of dollars
Exploratory Research	$ 5,464
Biotechnology	99
Chemistry and Materials Science	1,003
Computation	728
Earth Sciences	876
Engineering	498
Nuclear Chemistry	750
Physics	2,010
Director's Initiatives	6,495
Biotechnology	710
Energy Research	110
Beam Research	773
Lasers	2,150
Compact Torus	1,252*
Supercomputer Research and Development	1,500
Individual Awards	3,241†
26 projects funded in FY88	
31 grants projected for FY89	
University of California Institutes	1,979
Institute of Geophysics and Planetary Physics	1,454**
Institute for Scientific Computing Research	185
Plasma Physics Research Institute	150
Program for Analytical Cytology	190
IR&D Administration	339††
Totals	
Capital Equipment	$ 180
Operating Costs	$18,018

---

*The Compact Torus Director's Initiative received an additional $11,000 for capital equipment, for a total of $1,263,000.

†Individual researchers were awarded an additional $112,000 for capital equipment, for a total of $3,353,000.

**The Institute of Geophysics and Planetary Physics received an additional $57,000 for capital equipment, for a total of $1,511,000.

††Cost includes *IR&D Annual Report FY87*, salaries, and administrative expenses.

Author Index